

Loughborough University  
Institutional Repository

---

*Density-based unstructured  
simulations of gas-turbine  
combustor flows*

This item was submitted to Loughborough University's Institutional Repository by the/an author.

**Additional Information:**

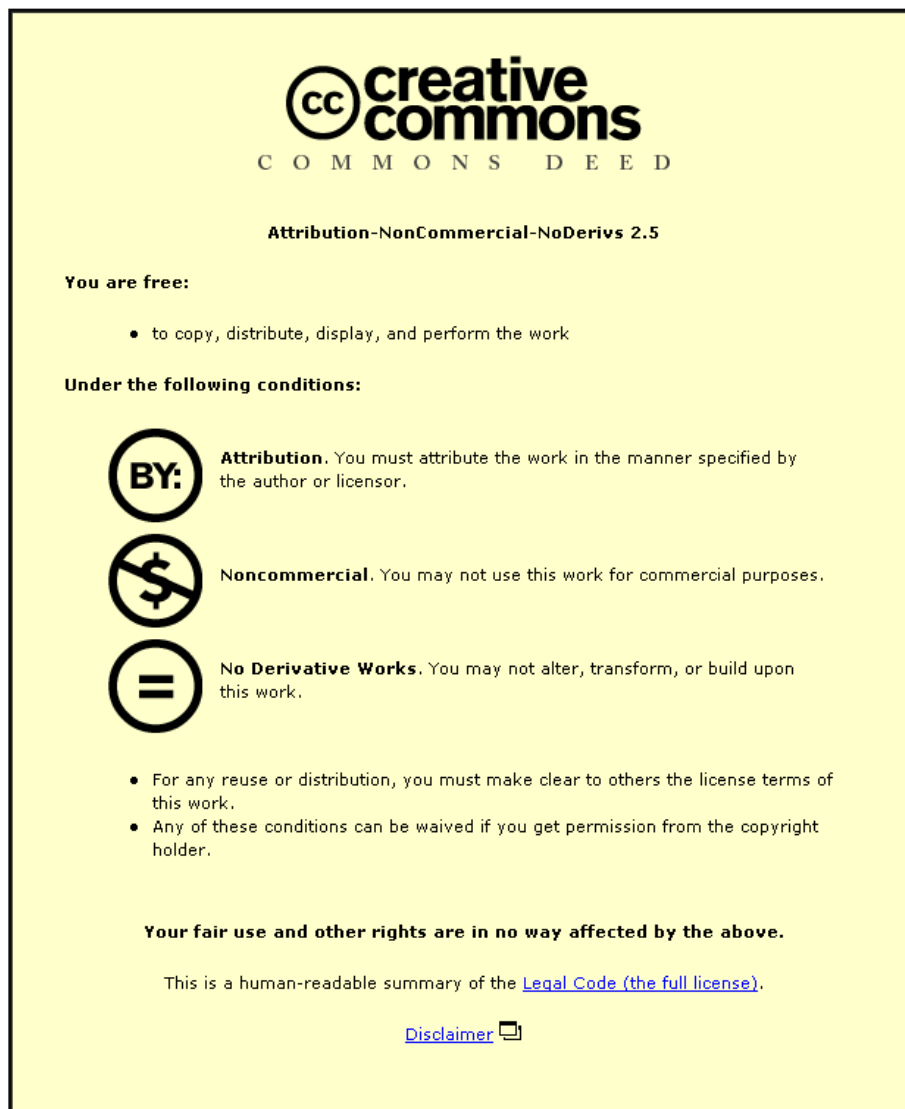
- A Doctoral Thesis. Submitted in partial fulfilment of the requirements for the award of Doctor of Philosophy of Loughborough University.

**Metadata Record:** <https://dspace.lboro.ac.uk/2134/13892>

**Publisher:** © A. N. Almutlaq

Please cite the published version.

This item was submitted to Loughborough University as a PhD thesis by the author and is made available in the Institutional Repository (<https://dspace.lboro.ac.uk/>) under the following Creative Commons Licence conditions.



For the full text of this licence, please go to:  
<http://creativecommons.org/licenses/by-nc-nd/2.5/>



# University Library

Author/Filing Title Almutlag, A.N.

Class Mark T

Please note that fines are charged on ALL overdue items.

**OR REFERENCE ONLY**

0403603803







# **Density-Based Unstructured Simulation of Gas-Turbine Combustor Flows**


By

Ahmed Nasser Almutlaq, MSc (Hons)

A Doctoral Thesis

Submitted in partial fulfilment of the requirements for the award of  
Doctor of Philosophy of Loughborough University  
30th March 2007

© A. N. Almutlaq, 2007

	Leeds University Purchase Library
Date	6/2008
Class	T
Acc No:	0403603803

## Abstract

The goal of the present work was to identify and implement modifications to a density-based unstructured RANS CFD algorithm, as typically used in turbomachinery flows (represented here via the Rolls-Royce 'Hydra' code), for application to low Mach number gas-turbine combustor flows. The basic algorithm was modified to make it suitable for combustor relevant problems. Fixed velocity and centreline boundary conditions were added using a characteristic based method. Conserved scalar mean and variance transport equations were introduced to predict scalar mixing in reacting flows. Finally, a flamelet thermochemistry model for turbulent non-premixed combustion with an assumed shape pdf for turbulence-chemistry interaction was incorporated. A method was identified whereby the temperature/density provided by the combustion model was coupled directly back into the momentum equations rather than from the energy equation.

Three different test cases were used to validate the numerical capabilities of the modified code, for isothermal and reacting flows on different grid types. The first case was the jet in confined cross flow associated with combustor liner-dilution jet-core flow interaction. The second was the swirling flow through a multi-stream swirler. These cases represent the main aerodynamic features of combustor primary zones. The third case was a methane-fueled coaxial jet combustor to assess the combustion model implementation. This study revealed that, via appropriate modifications, an unstructured density-based approach can be utilised to simulate combustor flows. It also demonstrated that unstructured meshes employing non-hexahedral elements were inefficient at accurate capture of flow processes in regions combining rapid mixing and strong convection at angles to cell edges. The final version of the algorithm demonstrated that low Mach RANS reacting flow simulations, commonly performed using a pressure-based approach, can successfully be reproduced using a density-based approach.

**Keywords:** Gas-Turbine Combustor, Density-based, Unstructured Grids, Jet in Cross Flow, Swirler, Non-premixed, Combustion Modelling.

## Acknowledgement

First and foremost, I would like to express my appreciation to Prof. James McGuirk and Dr. Gary Page for having presented me with the opportunity to carry out this project and for their patience, encouragement, support and guidance throughout the duration of my research.

The completion of this thesis would not have been possible without many collaborators involved in this project and I would like to take this opportunity to thank them all for their role. I would like to thank Dr. Dave Hollis and Dr. Nicola Hughes for providing me with necessary experimental data which formed a very important part of this thesis. I would also like to thank Dr. Leigh Lapworth of Rolls-Royce and Dr. Mamdud Huessien for having supplied and helped me with the use and understanding of the Hydra code.

During over 4 years in Loughborough, I have been involved in many fruitful discussions among many friends and colleagues who have influenced my views on a number of topics. I would like to take this opportunity to thank them for sharing their views and ideas with me. In particular, I would like to thank Dr. Chris Priddin, Dr. Qinling Li, Dr. Indi Tristante, Dr. Mehriar Dianat and Dr. Dachung Jiang. Thanks and appreciations also should go to Dr. Bowen Zhong of Cambridge University UTC and Dr. Salvador Navarro-Martinez of Imperial College combustion group.

Finally, I would like to thank Prof. John Chew of Surrey University and Dr. Zhiyin Yang of Loughborough University for examining this thesis.

My postgraduate studies would not have been possible without the generous financial support by the Saudi Ministry of Defence and Aviation (MODA) and the Rolls-Royce Company.

*To my wife, our sons and daughter*

# Contents

<b>Abstract</b> .....	i
<b>Acknowledgement</b> .....	ii
<b>Dedication</b> .....	iii
<b>List of Figures</b> .....	viii
<b>Nomenclature</b> .....	xvi
<b>1. Introduction</b> .....	1
1.1 Background and Motivation.....	1
1.2 Combustor Flow Characteristics.....	9
1.3 Previous Experimental and Numerical Studies.....	13
1.4 Summary of Current Literature.....	26
1.5 Objectives of the Present Study.....	27
1.6 Outline of the Thesis.....	29
<b>2. Mathematical Methodology and Numerical Techniques of the Basic Hydra Code</b> .....	31
2.1 Introduction.....	31
2.2 Equations of fluid motion.....	32
2.3 Turbulence Modelling.....	36
2.4 Finite Volume and Spatial Discretisation.....	41

2.4.1 Control volume definition.....	41
2.4.2 Convective flux.....	45
2.4.3 Diffusive flux.....	50
2.4.4 Discretisation of turbulence model equations.....	51
2.5 Integration Scheme.....	54
2.5.1 Mean flow equations.....	54
2.5.2 Turbulence model equations.....	56
2.7 Preconditioning.....	61
2.8 Multigrid Method.....	63
2.9 Boundary Conditions.....	65
2.9.1 Free stream boundary condition.....	65
2.9.2 Solid walls and symmetry boundary conditions.....	65
2.9.3 Subsonic inflow/outflow boundary condition.....	67
2.9.4 Periodic boundary condition.....	68
2.10 Flow Solver Overview.....	68
<b>3. Modifications to the Basic Hydra Code.....</b>	<b>72</b>
3.1 Introduction.....	72
3.2 Fixed Velocity Inlet Boundary Condition.....	74
3.2.1 Riemann invariant boundary condition (RINV).....	76
3.2.2 Velocity and temperature boundary condition (VIN).....	78
3.2.3 Validation test case.....	79
3.3 Periodicity and Centreline Boundary Condition.....	87

3.4 Reacting Flow Modelling.....	91
3.5 Convective Error Analysis and Estimation.....	94
3.5.1 Scalar transport test problem.....	96
3.6 Conserved Scalar Implementation and Validation.....	109
3.6.1 Validation test case.....	112
<b>4. Jet in Confined Cross Flow (JICCF).....</b>	<b>116</b>
4.1 Background Review.....	116
4.2 Numerical Investigations Review.....	121
4.3 Previous Experimental and Numerical Work on the Selected Test Case.....	127
4.4 Present Unstructured Mesh Numerical Predictions.....	135
4.5 Conclusions and Discussions.....	164
<b>5. Multi Stream Swirling Flow (MSSF).....</b>	<b>168</b>
5.1 Background Review.....	168
5.2 Review of Previous Swirling Flow Studies.....	172
5.3 Previous Experimental and Numerical Work on the Selected Test Case.....	179
5.4 Solid geometry modelling and Grid Generation.....	185
5.5 Unstructured Mesh Predictions, Comparisons and Discussions.....	199
<b>6. Non-premixed Turbulent Combustion Modelling.....</b>	<b>216</b>
6.1 Introduction.....	216
6.2 Conserved Scalar Modelling.....	219



6.3 Implementation of the Presumed $\beta$ -PDF Model.....	222
6.4 Model Testing and Validation.....	227
<b>7. Conclusions and Recommendations.....</b>	<b>242</b>
7.1 Summary of Results.....	242
7.2 Recommendations for Future work.....	246
<b>Appendix A.....</b>	<b>248</b>
<b>References.....</b>	<b>252</b>

## List of Figures

1.1 Aircraft engine layout [1].....	3
1.2 Integrated RANS simulation of gas turbine engine [24].....	8
1.3 Annular type combustor [30].....	11
1.4 Combustor airflow distributions [30].....	11
1.5 Combustor general airflow patterns [30].....	12
1.6 Koutmos and McGuirk experimental combustor geometry [35].....	14
1.7 Combustor split computational zones [36].....	16
1.8 Unstructured Computational grids [37].....	16
1.9 Geometry of Tsao et al. gas turbine combustor model [45].....	20
1.10 Experimental test section and numerical grid of Spencer's model [46].....	21
1.11 Multi-stream swirler geometry.....	22
1.12 Gas-turbine combustor of GE 90 turbofan engine [51].....	24
1.13 Davoudzadeh et al. experimental gas turbine combustor model [52].....	25
2.1 Average and fluctuating quantities for turbulent flow.....	37
2.2 Control volume types.....	42
2.3 Median dual control volume in triangular mesh.....	43
2.4 One dimensional reconstruction stencil.....	48
2.5 Schematic representation of Hydra user suit.....	70

2.6	Flowchart of Hydra nonlinear solver.....	71
3.1	Periodicity in turbomachinery [26].....	74
3.2	Nomenclature used with the velocity inlet boundary condition.....	78
3.3	Nozzle geometry and computational mesh.....	81
3.4	Mach number contours (RINV).....	82
3.5	Mach number contours (VIN).....	83
3.6	Velocity distribution along the axis, $U_{IN}=40$ m/s.....	84
3.7	Mach number distribution along the axis, $U_{IN}=40$ m/s.....	84
3.8	Velocity distribution along the axis, $U_{IN}=100$ m/s.....	85
3.9	Mach number distribution along the axis, $U_{IN}=100$ m/s.....	85
3.10	Convergence history.....	86
3.11	Periodic setup for $90^\circ$ sector of cylindrical domain.....	88
3.12	Convergence history.....	89
3.13	Axial velocity distribution.....	90
3.14	Combustion modelling approaches.....	93
3.15	Streamlines of the fixed velocity flow field.....	98
3.16	Various grid types and CVs.....	98
3.17	Scalar field contours (central differencing scheme and $21 \times 11$ coarse grid).....	100
3.18	Scalar field contours (upwind differencing scheme and $21 \times 11$ coarse grid).....	101
3.19	Influence of grid type and size on the global error.....	101
3.20	Scalar distribution along $y=0.2$ horizontal line.....	104

3.21 Flow angle along $y=0.2$ horizontal line.....	105
3.22 Centred (no smoothing terms).....	105
3.23 Upwind (second difference term only).....	106
3.24 Wiggles associated with scalar contours on CDS and coarse grids.....	106
3.25 Fourth difference term only.....	107
3.26 Blend of second and fourth difference ( $\epsilon^{(2)} = 0.5$ ).....	108
3.27 System with single inlet stream of fuel and oxidizer.....	110
3.28 The system of coaxial (fuel-air) jets.....	113
3.29 Scalar variable contours and particle tracks.....	114
3.30 Axial variation of concentration mean along centreline.....	115
3.31 Radial variation of concentration variance at $z/R_j = 28$ .....	115
3.32 Radial variation of concentration variance at $z/R_j = 40$ .....	115
4.1 JICF various structures [113].....	117
4.2 Jet penetration as a function of ( $J$ ) [116].....	120
4.3 Opposed jets in confined cross flow in a rectangular duct [133].....	122
4.4 Numerical hexahedral grid at x-y and y-z plane [134].....	123
4.5 Computational mesh of coupled combustor geometry [137].....	126
4.6 Schematic of the experimental setup [46].....	129
4.7 Test section dimensions and nomenclature.....	130
4.8 Particle tracks on symmetry plane [46].....	132
4.9 Numerical and experimental velocity profiles on the axial plane of symmetry [46, 138].....	133
4.10 Velocity profiles at port exit	

(Experimental and structured predictions vs. RANS structured) [46, 138].....	134
4.11 Turbulent kinetic energy at port exit (Experimental measurements vs. RANS structured predictions) [46, 138].....	134
4.12 Computational domain (60° sector with single port).....	136
4.13 Tetrahedral computational grid.....	137
4.14 Hexahedral computational grid.....	138
4.15 Flow particle tracks using Fluent with hexahedral grids.....	140
4.16 Flow particle tracks using Fluent with tetrahedral grids.....	140
4.17 Velocity distribution using Fluent with hexahedral grid.....	143
4.18 Velocity distribution using Fluent with tetrahedral grids.....	144
4.19 Velocity radial profiles (Experimental measurements vs. Fluent with hexahedral grid).....	145
4.20 Velocity radial profiles (Experimental measurements vs. Fluent with tetrahedral grid).....	146
4.21 Velocity radial profiles (RANS structured predictions vs. Fluent with hexahedral grid).....	147
4.22 Velocity radial profiles (RANS structured predictions vs. Fluent with tetrahedral grid).....	148
4.23 Velocity profiles at port exit (Experimental and structured predictions vs. Fluent with hexahedral grid)....	149
4.24 Velocity profiles at port exit (Experimental and structured predictions vs. Fluent with tetrahedral grid)....	149
4.25 Turbulent kinetic energy at port exit (Experimental measurements vs. Fluent with hexahedral grid).....	150
4.26 Turbulent kinetic energy at port exit (Experimental measurements vs. Fluent with tetrahedral grid).....	150

4.27 Velocity field predictions and flow particle tracks using Hydra with purely tetrahedral grid.....	154
4.28 Tetrahedral-prismatic grid in the port region.....	155
4.29 Velocity field prediction and flow particle tracks using Hydra with tetrahedral-prismatic grid.....	155
4.30 Velocity radial profiles at the annulus (Hydra purely tetrahedral vs. tetrahedral-prismatic grid).....	156
4.31 Inlet velocity profile with different boundary conditions.....	156
4.32 Velocity field prediction and particle tracks using Hydra with velocity inlet boundary condition and various types of grids.....	157
4.33 Velocity radial profiles (Experimental measurements vs. Hydra with tetrahedral-prismatic grid).....	158
4.34 Velocity radial profiles (Experimental data vs. Hydra with hexahedral grid).....	159
4.35 Velocity profiles at port exit (Experimental data vs. Hydra with tetrahedral-prismatic grid).....	160
4.36 Velocity profiles at port exit (Experimental data vs. Hydra with hexahedral grid).....	160
4.37 Turbulent kinetic energy at port exit (Experimental data vs. Hydra with hexahedral grid).....	161
4.38 Turbulent kinetic energy at port exit (Experimental data vs. Hydra with tetrahedral-prismatic grid).....	161
4.39 Port radial velocity contours and locally refined grids.....	162
4.40 Port exit velocity profiles (Experimental vs. different sizes of locally refined hexahedral grids).....	163
4.41 Turbulent kinetic energy at port exit (Experimental vs. different sizes of locally refined hexahedral grids).....	164
4.42 The various structures of the predicted JICCF flow.....	166

4.43 Flow particle tracks as predicted by Hydra.....	166
4.44 Velocity contours as predicted by Hydra.....	167
5.1 Various types of swirl generator.....	170
5.2 Structure of Recirculation Region in Swirling Annular Jet [143].....	171
5.3 Details of So et al. swirler geometry.....	173
5.5 Computational domain of Widmann et al. swirl generator [155].....	176
5.6 A schematic of the geometry and grid used by Guo et al. [156].....	177
5.7 Schematic layout of the movable block burner.....	178
5.8 Computational grid for location number 3 of the burner.....	178
5.9 Swirler model components.....	182
5.10 Experimental testing setup.....	183
5.11 Streamline contours of the flow downstream the swirler exit [48].....	183
5.12 Experimental data vs. structured grid predictions at ( $x/D=0.05$ ) [48].....	184
5.13 Various parts of the swirler solid model.....	189
5.14 Swirler solid model side, rear and front views.....	190
5.15 Longitudinal cross-section along the whole solid model.....	191
5.16 The $45^\circ$ sector and the four meshing zones.....	192
5.17 The tetrahedral surface mesh at the inlet of swirl passages.....	193
5.18 The tetrahedral computational grid.....	193
5.19 Surface meshes of the swirler components.....	197
5.21 Axial cross-sections through the computational domain.....	198
5.22 Illustrative sketch for the flow features at swirl exit region.....	201

5.23 Velocity magnitude contours calculated on tetrahedral grids using Fluent solver with the k- $\epsilon$ turbulence model.....	206
5.24 Velocity magnitude contours calculated using Fluent solver on tetrahedral grids with the RST model.....	207
5.25 Fluent predictions at ( $x/D= 0.05$ ) on tetrahedral grid with the k- $\epsilon$ turbulence model.....	208
5.26 Fluent predictions at ( $x/D= 0.05$ ) on tetrahedral grids with the RST model.....	209
5.27 Fluent predictions on tetrahedral fine grid vs. the experimental data at ( $x/D= 0.05$ ).....	210
5.28 The predicted particle tracks of the flow along the computational domain....	211
5.29 Velocity magnitude contours calculated on hexahedral grid.....	212
5.30 Hydra and Fluent predictions on hexahedral grid vs. the experimental data at ( $x/D= 0.05$ ).....	213
5.31 Longitudinal cross-section along the hexahedral computational grid.....	214
5.32 Hydra predicted streamlines along the computational domain.....	214
5.33 Examples of poor grid quality.....	215
6.1 The main blocks of the implementation procedure.....	226
6.2 Shapes of the calculated $\beta$ -PDF.....	227
6.3 Schematic of the coaxial jet combustor experiment.....	233
6.4 Hydra predictions of the axial velocity contours in comparisons with the previous predictions and the experimental data.....	234
6.5 Radial profiles of temperature.....	235
6.6 Radial profiles of CO mass fraction.....	236
6.7 Radial profiles of axial velocity.....	237



6.8 Radial profiles of mixture fraction.....	238
6.9 Radial profiles of temperature.....	239
6.10 Temperature as a function of mixture fraction from equilibrium and fast chemistry state relationships [179].....	240
6.11 Temperature as a function of mixture fraction from equilibrium and steady flamelet solutions relationships [179].....	240
6.12 Radial profiles of CO mass fraction.....	241

# Nomenclature

## Latin Characters

$A$	Inviscid flux Jacobian matrix; Area, (m <sup>2</sup> )
$A_t$	Turbulent flux Jacobian matrix
$B$	Viscous flux Jacobian
$a$	Speed of sound, (m/s)
$C_D$	Discharge coefficient
$C_p$	Specific heat at constant pressure, J/(Kg. K)
$C_r$	Craya-Curtet number
$C_v$	Specific heat at constant volume, J/(Kg. K)
$C_{g1}$	Constant in transport equation of mixture fraction variance, $C_{g1}=2.0$
$C_{g2}$	Constant in transport equation of mixture fraction variance, $C_{g1}=2.8$
$C_1$	Turbulent model constant, $C_1=1.44$
$C_2$	Turbulent model constant, $C_2=1.92$
$C_\mu$	Turbulent model constant, $C_\mu=0.09$
$D_a$	Damkohler number
$E$	Total internal energy, (m <sup>2</sup> /s <sup>2</sup> )
$e$	Internal energy, (m <sup>2</sup> /s <sup>2</sup> )

$F$	Flux vector
$f$	Mixture fraction
$H$	Total enthalpy, $\text{m}^2/\text{s}^2$
$h$	Static enthalpy, $\text{m}^2/\text{s}^2$
$I$	Identity matrix
$J$	Momentum flux ratio
$J^k$	Molecular diffusive flux of the specie $k$
$k$	Turbulent kinetic energy, $(\text{m}^2/\text{s}^2)$
$k$	Thermal conductivity, $(\text{m Kg}/\text{s}^3 \text{K})$
$M$	Mach number; Molecular weight
$M_x$	Swirler axial flux of axial momentum
$M_\theta$	Axial flux of swirl momentum
$m_k$	Mass fraction of specie $k$
$\dot{m}$	Mass flux, $(\text{Kg}/\text{s})$
$L()$	Pseudo-Laplacian operator
$n$	Normal vector
$P$	Preconditioner matrix; Probability Density Function
$Pr$	Prandtl number
$p$	Static pressure, $(\text{N}/\text{m}^2)$
$Q$	Conservative variables matrix
$q$	Heat flux

$R$	Gas constant, $R=287.04 \text{ J/kg.K}$ Radius, (m)
$Re$	Reynolds number
$R_r$	Residual operator
$R^-$	Riemann invariant in negative direction
$R^+$	Riemann invariant in positive direction
$S$	Source term vector
$s$	Entropy, ( $\text{m}^2/\text{s}^2$ )
$s$	Reaction stoichiometric coefficient
$T$	Temperature, (K)
$T, T^{-1}$	Eigen vector matrix and matrix inverse
$t$	Time, (s)
$u$	Axial velocity component, (m/s)
$V$	Velocity vector
$v$	Radial axial velocity, (m/s)
$w$	Circumferential velocity, (m/s)
$x$	Cartesian coordinate direction, (m)
$Y_k$	Mass fraction of specie $k$
$y$	Cartesian coordinate direction, (m)
$y^+$	Non-dimensional distance to the wall
$z$	Cartesian coordinate direction, (m)

## Greek

$\gamma$	Specific heat ratio, $\gamma = 1.4$
$\rho$	Density, (kg/m <sup>3</sup> )
$\Lambda$	Eigen value matrix
$\mu$	Dynamic molecular viscosity, (kg/m.s)
$\mu_t$	Eddy viscosity, (kg/m.s)
$v$	Kinematic viscosity, (m <sup>2</sup> /s) Cartesian velocity component, (m/s)
$\phi$	Nozzle diameter
$\phi$	Scalar variable
$\varepsilon$	Turbulent dissipation rate, (m <sup>2</sup> /s <sup>3</sup> )
$\Psi$	Flux limiter function
$\kappa$	von Karman constant, $\kappa = 0.41$
$\tau$	Shear stress, (N/m <sup>2</sup> )
$\lambda$	Eigenvalue, (m/s)
$\sigma_k$	Turbulent model coefficient, $\sigma_k = 1.0$
$\sigma_\varepsilon$	Turbulent model coefficient, $\sigma_\varepsilon = 1.3$
$\dot{\omega}_k$	Mass reaction of specie $k$ rate per unit volume
$\theta$	Mixing characteristic parameter
$\Omega$	Control volume

## Subscript

c	Core
IN	Inflow condition
i	Index
j	Jet, Cell index
n	Normal vector direction
OUT	Outflow condition
t	Turbulent
x	x-direction
y	y-direction
z	z-direction

## Superscript

C	Convective flux
D	Diffusive flux
I	Inviscid fluxes
k	Species index
V	Viscous fluxes
Lp	Linear-preserving
-	Evaluated at left state
+	Evaluated at right state
'	Fluctuating part of Reynolds-decomposed variable

“ Fluctuating part of Favre-decomposed variable

## Acronym

CDS	Central differencing scheme
CFD	Computational fluid dynamics
CTRZ	Central toroidal recirculation zone
JICF	Jet in cross flow
JICCF	Jet in confined cross flow
LDA	Laser Doppler Anemometer
LES	Large Eddy Simulation
NASA	National Aeronautics and Space Administration
ND	Numerical diffusion
OGV	Outlet Guide Vane
PDF	Probability density function
PVC	Precessing vortex core
QUICK	Quadratic Upwind Interpolation for Convective Kinetics
RANS	Reynolds-Averaged Navier Stokes
RINV	Riemann invariant
RST	Reynolds stress turbulence model
SIMPLE	Semi-Implicit Method for Pressure Linked Equations
UDS	Upwind differencing scheme
VIN	Velocity inlet

# Chapter 1

## Introduction

### 1.1 Background and Motivation

Computational fluid dynamics (CFD) has become an essential tool in solving many engineering problems especially for aerothermodynamics applications. In many cases CFD modeling possesses advantages over experimental modeling due to its low cost, high efficiency and ability to simulate realistic conditions. Reliable CFD predictions speed up the technological advancement of automotive and aeronautical design (e.g. gas turbine engine, turbomachinery and combustors) as well as the prediction of environmental and biological flows. However, advances in some fields have been limited due to the complexity of equipment geometries and flow phenomena such as turbulence and chemical reaction. During the last three decades, great efforts have been invested to develop CFD techniques to overcome these difficulties and lower the computational cost. Various algorithms and mathematical models have been developed to improve accuracy and minimise simulation time.

Aircraft gas turbine engines represent one of the most challenging aerothermodynamics problems for which accurate simulations of the flow, combustion and flow/structure interactions are very important in order to meet the requirements of high performance, efficiency and the strict environmental regulations on the gas emissions. For a long time, engine design has been



dependent on extensive test rig and full engine experiments over a wide range of operating conditions, which are, however, expensive and time consuming. Three dimensional CFD simulation is the only possible way to minimize the cost and reduce the number of experiments. Figure 1.1 shows a typical modern advanced aeroengine, a Rolls-Royce Trent 900, which consists of a fan and a two-stage compressor that raise the air pressure by around a factor of 30, a combustor in which fuel is injected and burned to produce high temperature gases, and a three stage turbine that extracts mechanical energy from the high temperature high pressure gases. The high pressure and intermediate pressure turbines drive the two compressor stages, and the final low pressure turbine drives the fan. The large fan at the inlet supplies airflow to both a by-pass stream and a core (hot) stream, both of which contribute to engine thrust. In such a modern engine, a significant fraction of the compressor flow is bled off to bypass the combustor and flows inside the turbine blades to cool them, and then out through the blade surface to provide a cool protective film that prevents melting of the blades by the very hot combustion gases. Some compressor air ( $\sim 900\text{K}$ ) is also used to control the temperature of the combustor walls against the high flame temperature ( $\sim 2300\text{K}$ ). This complexity presents a large variety of flow phenomena encountered in the engine flow path including turbulent, reacting, non-reacting, single and two-phase, high speed and low speed flows which all impact on the optimum component design. Each engine component is subjected to differing combinations of these flow complexities which lead to different specialised and optimized simulation approaches according to the flow characteristics in each component.

In the turbomachinery parts of the engine the flow field is characterized by single phase flow at both high Reynolds numbers and high Mach numbers without chemical reaction. In addition, boundary layers and shear layers are usually thin with a large portion of the flow being essentially inviscid, and recirculation zones are by design arranged to be absent or small. Accurate prediction of this kind of flow requires precise description of the turbulent boundary layers around the blade

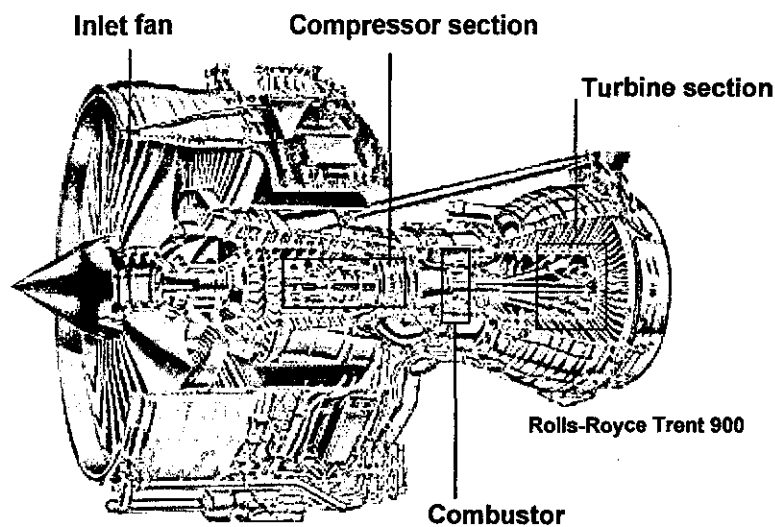


Figure 1.1 Aircraft engine layout [1]

with tip gap and leakage flow effects. Typically, flow solvers for turbomachinery applications are based on the Reynolds Averaged Navier Stokes (RANS) approach developed from solvers discretised to have good performance for 3D Euler equations at high Mach number (strongly compressible flow) [2, 3]. In the RANS approach, the unsteady flow field is ensemble averaged, thereby removing all dependence on the details of unsteady turbulent structures and creating extra terms that describe the statistical moments of the turbulent fluctuations (i.e. Reynolds stresses). A turbulence model becomes necessary to model these extra terms which represent the portion of the mean momentum transport that has been removed during the averaging process. In order to deliver accurate solutions and due to the complexity of the flows in turbomachinery, various turbulence models and parameters in these models have to be developed and calibrated. For turbomachinery flows, the importance of avoiding separation (stall) from blade aerofoil sections has encouraged turbulence model selection based on optimum representation of turbulent boundary layer behavior in adverse pressure gradients, e.g. Spalart-Allmaras model [4], rather than more general models for free shear layers and recirculating flows. Over a long period of time (~ 30 years) separating

boundary layer flow has been the subject of a large number of investigations. Model development and turbulence model constants calibration are well developed, and hence, the flow solvers used for turbomachinery deliver reasonably good performance and acceptably accurate results for flow simulations which are similar to the calibration test cases [4, 5].

The computational methods used to solve compressible turbomachinery flows are usually classified as density-based methods. These methods treat the continuity equation as a transport equation for the density as a primary variable and then calculate the pressure as a secondary variable using the equation of state. It is also most common in this type of CFD algorithm to adopt an unsteady or time-marching schematic algorithm for the coupled set of governing equations. Density-based methods have a disadvantage for low Mach number or nearly incompressible flows when the density variation vanishes and therefore pressure variation in space cannot be easily and accurately calculated [6]. To deal with this problem the artificial compressibility method has been used where a fictitious density term is added to the time derivative term in the continuity equation. A time-marching method is then used to calculate the pressure through a fictitious equation of state [7]. A further problem with density-based methods is that they suffer from limitations of small time steps, due to equations stiffness, when solving low Mach number flows which causes convergence rates to deteriorate. To remedy this problem, several approaches to eliminate the system stiffness by normalizing the eigenvalues through time-derivative preconditioning have been proposed and shown to improve the convergence rate significantly [8-10].

In stark contrast to the above, the flow in and around the combustor is very different to the turbomachinery parts of the engine. It is characterised by low Mach, essentially incompressible flow. Inside the combustor itself the mixing of the fuel and air has to be controlled to allow flame stability, rapid heat release, complete combustion with low emission of unburned fuel, CO and NO<sub>x</sub> and an acceptable

temperature profile at the combustor exit. In the region close to the fuel injector, gas/liquid two phase flows are also present but this is not addressed further in the present discussion. Over the past two decades researchers have developed gas turbine combustor computational methods which, because of the low Mach number characteristics, have avoided the complications mentioned above with density-based time-marching CFD methods and used pressure-based steady state RANS methods which have proven a successful way to analyse combustors and gain insight regarding their design and performance. The internal combustor flow patterns that are needed to achieve this lead to large recirculation regions, extremely high turbulence levels (~100 %) and a flow field in which static pressure is essentially constant but large gas density changes still occur due to temperature and species variations. It is easy to see that these characteristics are significantly different to turbomachinery flows, and hence it is not surprisingly that a different computational methodology has developed. These differences lie in both CFD algorithms and turbulence model areas.

In pressure-based methods the equations of motions are typically solved (again in contrast to the compressible turbomachinery approach) in an uncoupled or segregated way, relying on diagonal dominance for convergence. The basic idea of these methods is that the momentum equations are first solved using a guessed pressure field, resulting in a tentative velocity field. An equation for the pressure correction field is obtained via manipulation of the momentum and continuity equations. This equation is solved to obtain the pressure correction, and the velocities are then corrected to satisfy the continuity equation [11, 12]. When using these methods, the computer time required to solve the pressure correction equation is often a sizeable fraction of the total computational effort (about 80% of the total CPU time [13]). This is because the pressure-correction equation, which has the form of an anisotropic elliptic equation, is diffusion dominated, whereas the other equations are convection dominated. To improve the convergence rate, the multigrid technique has been found to be useful. The basic idea of multigrid

strategy is to accelerate the solution of a set of fine grid equations by computing corrections on a coarser grid; further details can be reviewed in [14].

As well as the algorithmic differences already addressed, the very different flow field associated with combustor flow (jet free shear layers, large recirculation zones, high swirl) has led to a preference for RANS turbulence models which are more general and more advanced than those for turbomachinery flows, typically two equation models such as  $k-\epsilon$  and Reynolds stress models [4, 5]. As an aside, apart from the major differences between density-based, compressible and pressure-based, incompressible formulations between turbomachinery and combustor CFD methodologies, it can be noted that much current interest in the turbulent mixing aspects of combustors is aimed at replacing RANS methods by Large Eddy Simulation (LES) methods [15, 16]. The reason for this is that the large scale eddy motions in a combustor play a much greater role in internal mixing over the whole combustor volume than they do in wall-dominated blade flows. However, these developments are still in the research stage and the vast majority of combustor design calculations in industry still retain the RANS approach.

Flow solvers, solution techniques and turbulence model selection constitute the major part of overall CFD methodology. Grid type is another important element which plays an important role in algorithm efficiency and solution accuracy. The structured grid approach facilitates the use of direct addressing techniques in the algorithms used to compute convective, viscous and energy fluxes at cell interfaces, and, hence, the solution of the flow field itself. These techniques are relatively simple to code and are readily vectorizable. The structured (or multi-block structured) approach also leads to grids of high quality e.g. low levels of grid skewness, controllable cell aspect ratios. However, an inherent disadvantage of the structured grid approach is the resultant need for excessive spatial resolution of the flow field in low-gradient regions in order to adequately resolve the flow field in high-gradient regions. This disadvantage often results in a compromise situation

for the global resolution of the flow field, with the degree of the compromise dictated by available computer memory. The solution to this situation is accomplished through the use of an unstructured grid approach which allows local choice of element type (hexahedral, tetrahedral, prism, etc) and thus allows adequate grid resolution in high-gradient regions (local refinement) without over resolving the low-gradient regions. The disadvantages of the unstructured approach are that grid quality is not so easily maintained (which can affect accuracy), and the need for indirect addressing in the solution algorithms, which necessarily leads to more complicated programming techniques and greater CPU time per grid point, when compared to the structured grid. The extra computational costs associated with unstructured meshes may be worthwhile in order to allow more rapid analysis of geometrically complex problems (faster grid generation), and many commercial CFD codes now use unstructured grid formulations. The ability to resolve the high-gradient regions of the flow field, while remaining within reasonable computer memory requirements makes the unstructured grid approach attractive for complex turbomachinery and combustor calculations. It is interesting to note, however that in general (there are of course exceptions), the "industry standard" CFD approach to turbomachinery has been the unstructured approach [17, 18], whereas the equivalent approach for gas turbine combustors is still the block-structured approach [19, 20].

The above discussion has identified that currently there are two quite different CFD methodologies in place which are both reasonably successful and widely used for turbomachinery blading and combustor calculations. However, the increasing computational resources and the improved efficiency of CFD techniques are now beginning to allow prediction of the interaction between single components or a coupled calculation of more than one component. One approach to this in the current context is to use two separate solvers, one optimized for the turbomachinery, and the other for the combustor. These are executed simultaneously, each computing a portion of the flow and exchanging flow

information at the component interfaces. This new approach has the distinct advantage of building upon the experience and validation that has been put into the individual codes during their development. It provides the possibility of running simulations in different domains at different time steps and provides a high degree of flexibility. Figure 1.2 shows one of the recent trials to simulate the whole gas turbine engine. Further details about such integrated simulation of aircraft gas turbine engines can be found in [21-24].

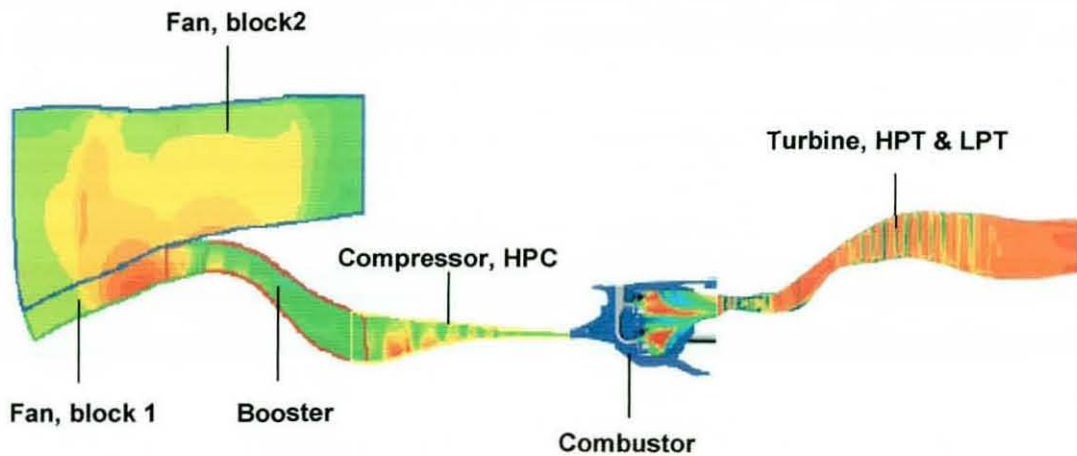


Figure 1.2 Integrated RANS simulation of gas turbine engine [24]

The above trend towards a more integrated simulation approach is the main motivation behind this work. Differently to the approach followed in [21-25], the question to be addressed in the current thesis is: can the same CFD methodology be used for both turbomachinery and combustor components of the engine?, this will be studied by investigating the use of a typical turbomachinery code (time-marching, density-based, unstructured) applied to combustor relevant flows. Hydra, a Rolls-Royce unstructured compressible RANS flow solver has been used extensively in aerodynamic optimization of turbomachinery and many other engine components such as lobed mixers, OGVs, nacelles, fans and intakes [25-29]. Predictions showed high accuracy compared to experimental data and participated



significantly in component design enhancement efforts [28, 29]. The Hydra solver has been enhanced with a multigrid acceleration scheme and a low Mach number preconditioner in order to increase its robustness, yielding a satisfactory convergence at all flow speeds. The unstructured grid capabilities of Hydra have enabled rapid analysis, especially in redesign and optimization processes and demonstrated potential advantages for coupling components and resolving flow features. As yet, however, the accuracy of predicting complex combustor flows using a code such as Hydra has not been proven. The main goal of this work therefore is to explore the use of the Hydra code when applied to typical combustor flow problems and extend the solver capability to simulate reacting flows typical of main gas turbine combustor flows. Achieving this goal can be considered as an important step towards engine integrated simulation approach. Since the route being followed is to start with a typical turbomachinery CFD code and apply this to combustor-like flows, the next step is to extract a detailed understanding of the typical fluid mechanics of gas turbine combustor flows.

## 1.2 Combustor Flow Characteristics

Ideally, gas turbine engines operate on the principle of the Brayton cycle, where compressed air is mixed with fuel and burned in the combustor under essentially constant pressure conditions [30-32]. The resulting high temperature, high pressure gas is expanded through high and low pressure turbines, forcing them to rotate and power the fan and compressor systems through connecting shafts. The first law efficiency of the Brayton cycle is dependent on pressure ratio only and, for improved efficiency, a high pressure ratio is desired. High specific work performance is also important, and this is dependent on temperature ratio. As a result, engine performance has been significantly improved by increasing the maximum pressure and temperature of the aero-thermodynamic cycle. Engine combustors play an important role in this regard. Minimization of any losses in the



high pressure air delivered to the combustor by the compressor, and minimization of the non-uniformity of the hot gases delivered to the turbine, as well as achieving a low level of pollutant emissions are all important combustor design criteria essential for good engine performance.

Although in the history of gas turbine engines several combustor types have been used, e.g. annular and can-annular types, modern engines predominantly prefer the more lightweight and smaller size annular combustion chamber designs which uses a fully annular flame tube (or liner) contained within annular casings and fueled via evenly spaced fuel injection nozzles, Figure 1.3. One disadvantage of this flow arrangement is the difficulty in obtaining an even air-fuel distribution and thus an even outlet temperature distribution, and much research and development has been invested into efficient methods for controlling the air distribution over the several entry routes into the combustor (fuel injector, primary and dilution ports and liner cooling).

The major geometric features of annular combustion chambers include the liner, fuel nozzles (which can include several (up to 3) swirl passages), cooling slots and holes, as well as primary and secondary dilution holes to create radially penetrating and impinging jets. One major consideration in the combustor design is therefore the division of the inlet mass flow into separate flow paths. Figure 1.4 shows a typical mass flow distribution within an annular gas turbine combustor. A large portion of the combustor inlet flow is used for cooling the metal casing and diluting the combustion products to achieve an exit temperature that is optimum for the performance and life of the downstream turbine inlet guide vane. The interaction of all of these combustor components results in a very complex flow field within the combustor, Figure 1.5, and entering the downstream turbine section.

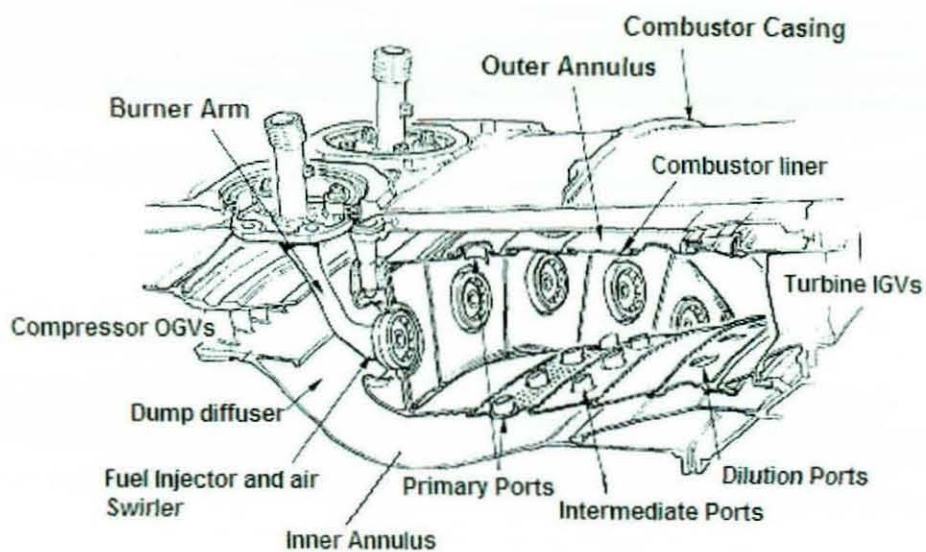


Figure 1.3 Annular type combustor [30]

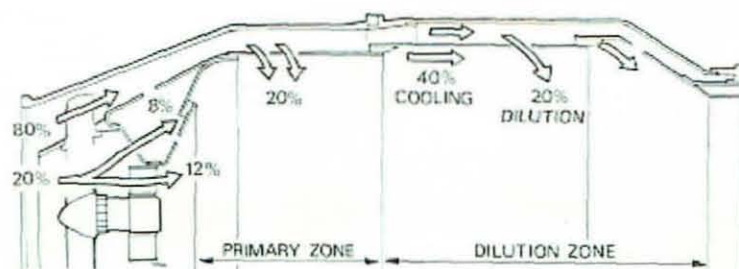


Figure 1.4 Combustor airflow distributions [30]

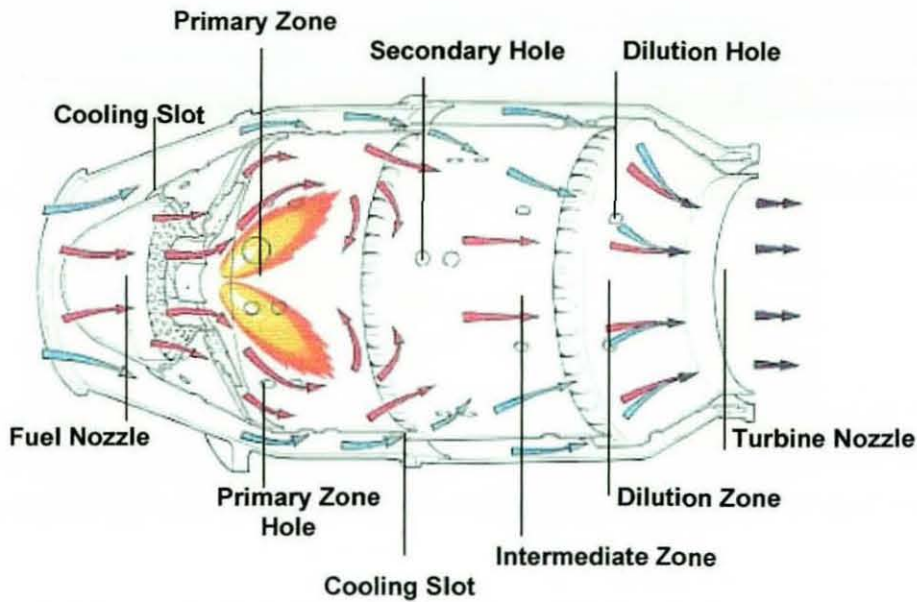


Figure 1.5 Combustor general airflow patterns [30]

From an operational point of view, the combustor must provide a flow environment that is conducive to ignition (including altitude relight) and the stability of the flame over a wide range of engine operating conditions.

It is useful at this point to indicate again some of the important flow characteristics that have influenced the development of optimum numerical techniques for combustors:

1. Low Mach number, essentially constant static pressure flow.
2. High levels of swirling air entering through the fuel injector.
3. Large recirculation regions covering a large fraction (30%) of the combustor internal volume.
4. Strong impinging jets to create large turbulence levels and rapid mixing.

5. Large fluid density changes caused by temperature/species variations rather than pressure variations.
6. High levels of mixing caused by turbulent fluctuations.

Clearly, much previous work has studied these aspects both computationally and experimentally and this is now briefly reviewed.

### 1.3 Previous Experimental and Numerical Studies

Many experimental and numerical studies have been performed to model and analyse combustor flows. Most of these studies have been focused on the combustor internal flow whilst some have examined the coupling between internal and external flows. In this section, a few important studies conducted during the last two decades which have provided major contributions will be reviewed. The literature review in this section will predominantly cover combustor cold flow (non-reacting), further literature review of some numerical and aerothermodynamic issues related to reacting combustor flow will be included in later chapters.

In 1988, Shyy et al. [33] computationally modeled one sector of a combustor with opposing dilution jets, film cooling slots and a swirl cup. Two different dilution jet configurations were modeled, the first with both a primary and a secondary row of ports whilst the second had only a primary row. The impingement of the opposing jets resulted in a complex spatially varying structure of hot gas in the centre of the combustor with sharp temperature gradients due to the film-cooling and dilution jet fluid. The flow pattern in the secondary port region showed strong vortical motions due to the interaction of the dilution fluid with the mainstream flow. The removal of the secondary row of holes reduced the extent of mixing, giving a more symmetrical flow pattern. The same authors [34] investigated the effects of dilution jets on the exit profile by performing a similar computational study, this time with a

single row of jets, varying the location of the jets with respect to the swirl cup centres. The extra dilution jets produced additional vortices and hot spots. This clearly demonstrated the complexity of the combustor exit profile, and the sensitivity of this to the geometry and fluid mechanics of the dilution jet and cooling flows in the combustor. In both studies the standard  $k-\epsilon$  turbulence model with wall functions was used. It was concluded that the computationally predicted patterns generally showed a larger degree of spatial variation than those indicated by experimental measurements, resulting from an under-prediction of the mixing process. It is the inadequate ability of RANS statistical turbulence models to predict these gross mixing effects sufficiently accurately that has led to recent interest in LES methods [21].

In 1989, a water flow study of a can-type combustor as shown in Figure 1.6 was conducted by Koutmos and McGuirk [35]. The model consisted of a swirl-driven primary zone to induce a primary zone recirculation, annular fed primary and dilution jets, and an exit contraction nozzle. The percentage of the flow passing through the swirler, the first row of primary holes, and the second row of dilution

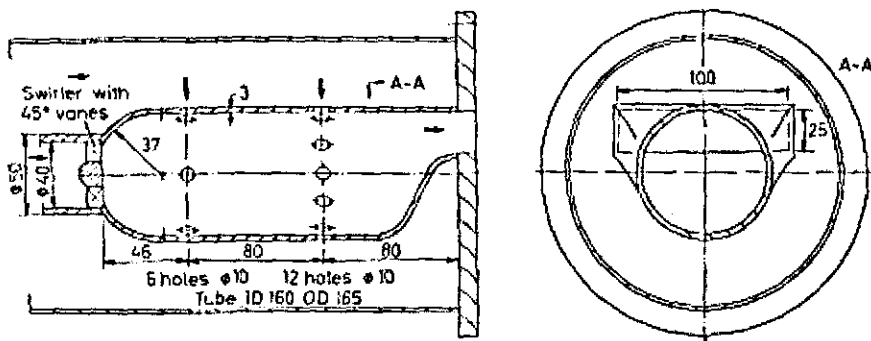


Figure 1.6 Koutmos and McGuirk experimental combustor geometry [35]



holes was 15%, 33% and 52% of the inlet mass flow respectively. This study found that increasing the swirler exit flow resulted in a reduction in strength of the recirculation and turbulence generation associated with the primary zone due to the first row of primary jets experiencing weak penetration into the mainstream. It also found that the flow mixed rapidly and efficiently throughout the first and second impinging jets zones, which led to a reduction in the velocity and turbulence non-uniformities at the combustor exit. A 50 % reduction of turbulence level was noted between the dilution region and the combustor exit. The same authors numerically simulated the internal flow of the above combustor using the finite volume pressure-based SIMPLE algorithm with standard  $k-\epsilon$  turbulence model and log-law functions for near wall nodes [36]. The combustor geometry was split into two zones as shown in Figure 1.7. Zone A comprised swirler, head, and two rows of holes, the cylindrical can geometry was artificially extended, and zero normal gradients were assigned at the flow exit. Zone B included the exit nozzle and part of the upstream cylindrical barrel including the dilution holes. The flow in the nozzle was calculated with inlet conditions taken from zone A. Grids of  $45 \times 18 \times 15$  nodes for zone A and  $12 \times 10 \times 9$  nodes for zone B were used to perform the calculations, grid refinement was limited by the available computer resources. Predicted velocity distributions showed favourable agreement with measurements in the primary and intermediate zones although discrepancies increased in the dilution region. Predicted levels of turbulence energy were too low in regions of high anisotropy. In 2003, the same combustor geometry has been numerically investigated by Bazdidi et al. [37] again using the SIMPLE pressure-correction algorithm in the Fluent commercial code with both  $k-\epsilon$  and a Reynolds Stress Turbulent Model (RSTM) and different unstructured hexahedral grids. As shown in Figure 1.8, the primary (coarse) grid had 22000 hexahedral cells and was refined up to 470000 cells to obtain a grid independent solution with local refinement in high gradient regions to capture the combustor flow features. One can notice the increase by a factor of 20 in the number of fine grid cells compared to the total size of zone A and B in the original structured grid study. This work concluded that in the reverse flow region

both turbulence models predicted the maximum reverse velocity well, but the RSTM model demonstrated a higher level of jet penetration showing better agreement with experimental results, although both models failed to predict the turbulent kinetic energy and tangential velocity distributions adequately (once again underlining the motivation to move to LES). However, both turbulence models predicted the global flow characteristics reasonably well. Using an unstructured mesh allowed the calculations to be performed using a single grid which was able to represent the whole combustor geometric complexity with no approximations; this was not possible a decade ago with a structured grid approach. It also provided the capabilities to refine the grid in regions of high gradients like ports and impinging jet regions.

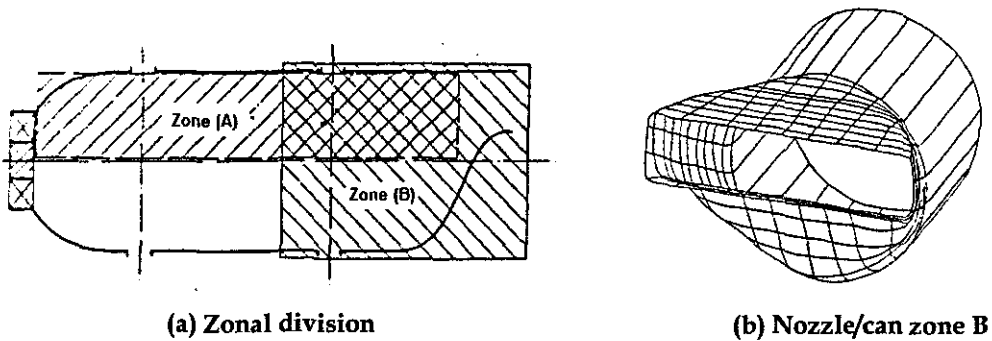


Figure 1.7 Combustor split computational zones [36]

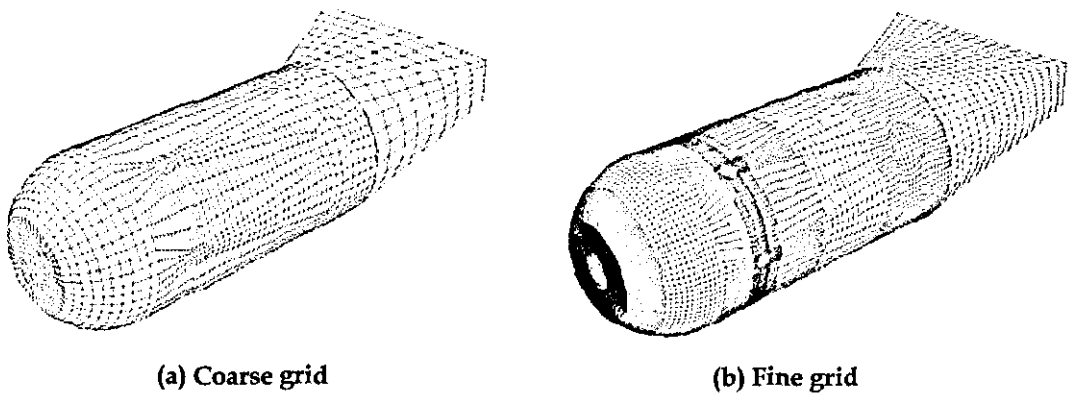


Figure 1.8 Unstructured Hexahedral Computational grids [37]

In 1990, Stevens and Carrotte [38] experimentally investigated the combustor dilution zone and jet development by focusing on the downstream thermal field in a non-reacting, annular combustor simulator. The experimental geometry contained a row of 16 slightly heated jets that were injected normally into a confined annular crossflow at a momentum flux ratio of 4. The jet flow was heated to identify the trajectory and the dispersal of the jet fluid. A complex flow field downstream of each dilution jet was observed as it exited into the crossflow. This flow field was found to vary slightly in a random manner from one jet to another. The complexity of the flow field was highly dependent on the direction of the approach flow in the feed annulus of the dilution jets and the jets deflection as they flowed through the dilution holes. The temperature distribution was found to be distorted about each hole centre plane; the temperature distributions taken two hole diameters downstream of the jet entry revealed that although each jet exhibited the same characteristic kidney-shaped profile, a lack of repeatability of the distributions between different dilution jets was apparent. The authors also concluded that since this complex flow field varied from one dilution hole to the next, each jet had its own mixing characteristics which in turn led to an overall non-uniform temperature distribution downstream.

Holdeman [39] also simulated the dilution zone of a gas turbine combustion chamber by conducting computations and experiments on the mixing of single, double, and opposed rows of dilution jets with an isothermal or variable temperature mainstream in a confined subsonic crossflow. The focus was again on the three-dimensional flow features in the dilution zone. The main finding from this investigation was that the momentum flux ratio of the jets dictated the overall combustor exit velocity and temperature profiles. The exit temperature distributions for single-sided injection were found to be very similar for both single and double row jet injection cases, indicating only slightly better mixing for the double row case. The results from the cases involving opposed-rows of jets revealed that for in-line jets the two streams mixed very rapidly and that the effective mixing



height was half the duct height for equal momentum flux ratios on both sides. For opposed-rows of staggered jets it was found that the optimum ratio of orifice spacing to duct height was double the value for single-sided injection at the same momentum flux ratio. The computational study, using the standard k- $\epsilon$  turbulence model, did not accurately predict the mixing of the dilution jets for the case with the opposed jet centres in-line but predicted the jet penetration very well by showing good agreement with the data. Similar conclusions were reached by Gulati, et al. [40]. These studies once more show the importance of rapid mixing processes in combustor flows and the current inability of RANS turbulence models to predict this sufficiently adequately.

Recent studies have shown that the formation of NO<sub>x</sub> is mainly a function of flame temperature in the combustion region [41]. Therefore, NO<sub>x</sub> production will be reduced if efficient combustion at lower temperatures can be achieved. Based on this principle, the RQL (Rich-burn, Quick-quench, Lean-burn) combustor design has been proposed, which uses a staged combustion technique to lower the flame temperature. The three stages of the combustor are: fuel rich combustion above an equivalence ratio 1.6, *quick-mixing of air accounting for 70% of the total reactant air*, and finally fuel lean combustion used to oxidize the excess fuel from the fuel rich stage. These combustors attracted the attention of many researchers. Anacleto et al. [41] studied the flow patterns typical of RQL combustors by taking detailed velocity measurements of the flow in a water model of a can-type combustor. The study consisted of a basic flow configuration with a series of geometrical modifications to determine the influence of several parameters on the overall performance of the combustor. These parameters included the swirl level in the rich zone, the geometry of the quench holes, and the momentum of the inflowing jets. One of the major findings from this study was that the impingement of the opposed jets in the center of the combustor greatly enhanced turbulent production giving rise to large velocity fluctuations. It is also found that an optimum momentum flux ratio for all geometries studied resulted in a homogeneous temperature distribution

downstream of the injection plane. These findings are in agreement with the results of similar experimental investigations of an RQL combustor reported by Doerr et al. [42] and Blomeyer et al. [43].

The effects of a swirl driven inlet flow are very important in establishing the flow pattern in the fuel injection region and have been studied by Ahmed [44], who used Laser Doppler Velocimetry (LDV) to measure the flow field and turbulence characteristics of a non-reacting, isothermal, swirling flow in an axisymmetric sudden expansion research combustor. One of the major findings of this study was that swirl enhanced the production and distribution of turbulence energy and resulted in thorough flow mixing. These results differ from those presented earlier by Koutmos and McGuirk [36] because the combustor geometry used in the experiments included the use of an inlet swirl flow coupled with strongly impinging downstream primary jets whereas the experiments performed by Ahmed did not include the use of downstream jets. A swirl driven inlet flow by itself enhances mixing of the entire flow field and leads to increased turbulence levels. Impinging jets are sometimes used in combustor design to counteract the effects of a purely swirl driven inlet flow which lead to high turbulence and rapid mixing, but also a very large elongated recirculation zone. The use of primary impinging jets can control the size of the central recirculation zone generated by the swirling motion.

In 1999, Tsao and Lin [45] numerically investigated the effect of inlet swirl level on the interaction between the primary and dilution air jets and the swirling cross flow in the interior flow field inside the can type gas turbine combustor model, Figure 1.9, as studied experimentally in [35]. Similar to the work reported in [37], they concluded that by using an RSTM model the flow features such as the decay of the axial jets after the impingement of the radial primary jets and the gradual return to solid body rotation motion of the swirl profiles were all well captured. Due to difficulties associated with structured grid capabilities, the round injection holes

were approximated by equal-area square orifices assuming results differ marginally with those adopting round shaped holes and the 'swan-neck' exit section was not included in the calculations.

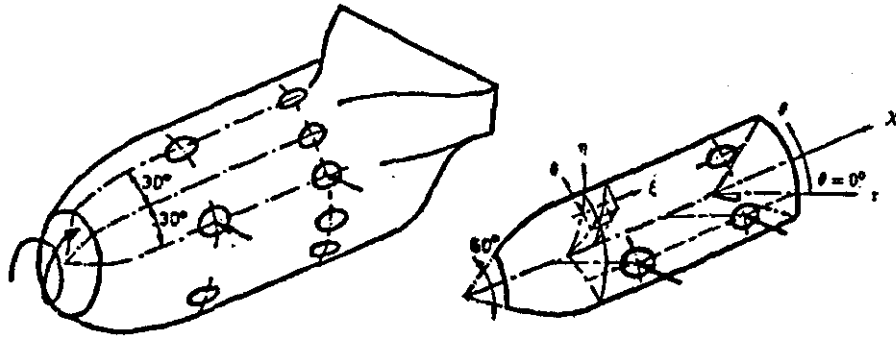


Figure 1.9 Geometry of Tsao and Lin gas turbine combustor model [45]

The calculations reported in both [37] and [45] had only been applied to predicting the internal combustor flow field, using experimentally measured (or approximated) boundary conditions at the primary and dilution jet entry holes. To assess the significance of this simplification and the importance of retaining a strong coupling between external annulus and internal combustor flow fields, Spencer [46] and McQuirk and Spencer [47] used an isothermal flow rig, as shown in Figure 1.10, designed to create generic annulus and core flow circuits, connected through a single row of ports to create radially inflowing jets. They carried out extensive experimental and computational work to study the coupling issue. Data obtained using LDA indicated a strong effect of the annulus flow details on the velocity profiles, turbulence levels and jet angle at the port exit. CFD predictions were carried out using a 3D finite volume method based on a structured grid, a pressure correction method and a high Reynolds number  $k-\epsilon$  turbulent model. Comparisons of fully coupled and internal only predictions showed notable differences in terms of predicted jet penetration and upstream recirculation. They strongly recommended that fully coupled calculations of internal and external flow should be carried out.

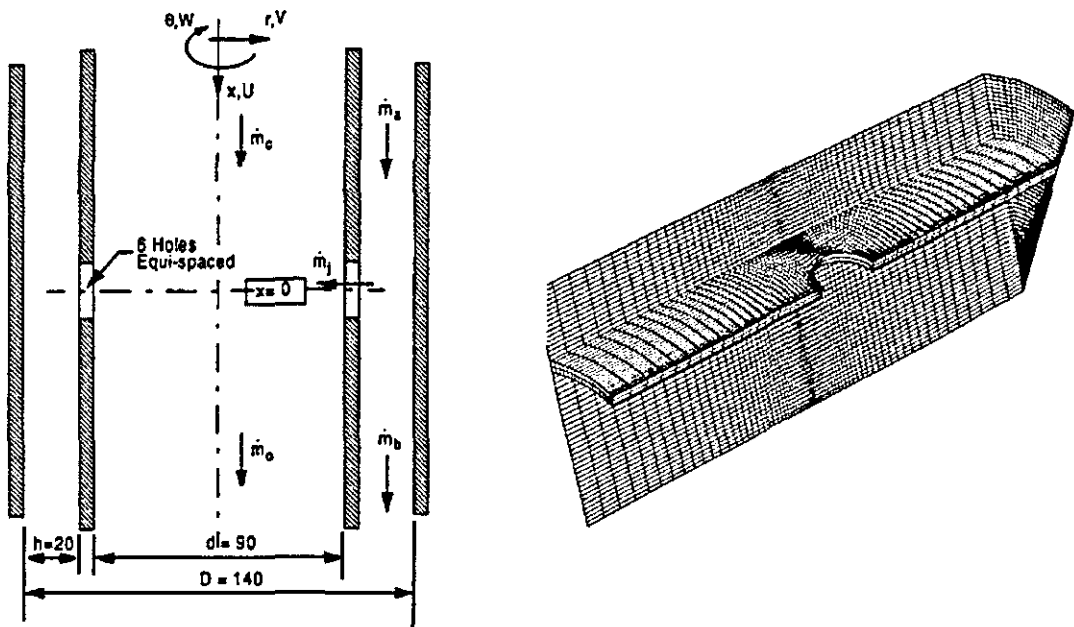


Figure 1.10 Experimental test section and numerical grid of Spencer's model [46]

Hughes [48] studied a generic multi-stream fuel injector, Figure 1.11, using three axial-swirlers experimentally and computationally using both  $k-\epsilon$  and RSTM turbulence models and a structured single block mesh. She concluded that the  $k-\epsilon$  model showed poor agreement in predicting the circumferential velocity component while the RSTM model produced better results. This is in agreement with the findings of Xia et al. [49] from their numerical and experimental study of swirling flow in a model combustor. Due to the time consuming meshing process for geometries as complex as multi-stream swirler fuel injectors, Hughes recommended unstructured grids should be investigated.

The above discussion has underlined the important role that swirling flows and impinging jet flows play in creating appropriate internal combustor flow patterns.

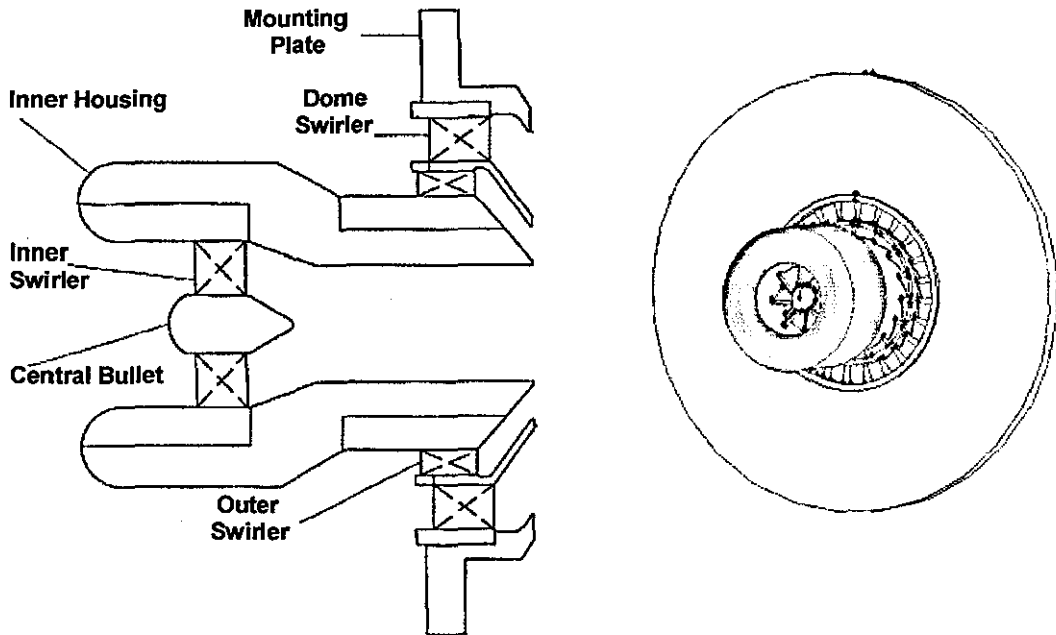


Figure 1.11 Multi-stream swirler geometry

It is clear therefore that such sub-elements of combustor flows should form important test cases if a CFD method is to be assessed for its suitability in predicting combustor flows. Accordingly, the computations and experiments of Spencer [46] and Hughes [48] are important comparison studies for the present project. Further discussions on these flow cases will therefore be provided in later chapters.

Most of the numerical calculations discussed above were focused on the use of structured grids, semi-implicit pressure-correction algorithms and segregated (uncoupled) solution methods. Despite the important contribution made by these methods, the major restrictions imposed by structured grids and their weakness in efficiently capturing the complex geometry of combustors cannot be ignored. The recent significant developments in computer hardware, mathematical models and solution algorithms allow much more reliable simulations. Unstructured methods which are able to capture complex geometry with more rapid grid generation

methods, high-resolution discretisation schemes which permit accurate and bounded solutions, and implicit coupled solution of the conservation equations to improve robustness and faster convergence (e.g. using multigrid methods) of the equation set have received much attention in the last decade, prompted by their success and publicity in external aerodynamics and turbomachinery applications. To indicate the status of this modeling approach to simulation of gas turbine combustors, the National Combustion Code NCC and its applications will be used as an example.

In 2001, the first version of NCC was released by NASA Glen Research Centre as the fruits of a joint effort with leading CFD developers and aero-engine companies [50]. The RANS unstructured baseline solver of the code solves steady or unsteady 3-D, compressible Navier-Stokes equations. The discretisation begins by dividing the computational domain into a large number of elements, which can be of mixed type. A central difference finite volume scheme with added numerical dissipation is used to generate the discretised equations, which are then advanced temporally by an explicit 4-stage Runge-Kutta scheme, which is very suitable for parallelization. For low Mach number compressible flow, a preconditioning is applied to the governing equations and the solution is advanced temporally by a "dual time step" approach, in which the Runge-Kutta scheme is used for the inner iteration. The turbulence model is based on the high Reynolds number  $k-\epsilon$  model with wall functions. The characteristics of the NCC baseline solver are very similar to those of the Hydra solver which is enhanced with multigrid acceleration scheme as an advantage over the NCC approach.

In 2002, modelling of the full combustor was a key part of the GE 90 high-bypass ratio turbofan engine numerical simulation project [51]. The aerodynamics and the turbulent combusting flow and chemistry were modelled with NCC. The 3D model of the combustor is a 24 degree sector representation of the full annulus that is

spatially periodic and includes the compressor exit diffuser, flow swirlers, cooling and dilution holes, inner and outer casings and four fuel nozzles.

A tetrahedral grid with 1.1 million cells was used for the simulation with local refinement in regions of high gradient such as holes and jet regions as shown in Figure 1.12. Mass averaged radial profiles from the compressor were used as inlet boundary conditions whilst mass averaged radial profile boundary conditions were transferred from combustor to turbine. The simulation of the complete engine was achieved by utilizing two interface planes to exchange boundary condition data at the combustor inlet and exit. At the two planes of data exchange, the radial profile exit boundary conditions were transferred to the downstream components as inlet boundary conditions. The compressor and turbine were modelled with the APNASA flow code [51]. Although the 3-D flow was successfully simulated in all of the major components of the turbofan engine, no comparisons with experimental data were presented.

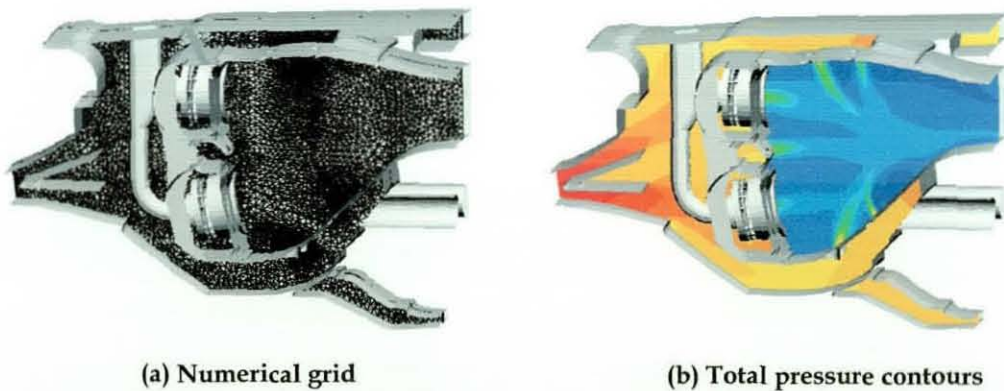


Figure 1.12 Gas turbine combustor of GE 90 turbofan engine [51]

To demonstrate the modelling capabilities of NCC, Davoudzadeh and Liu [52] numerically modelled an experimental combustor exhibiting typical flow features associated with gas turbine combustors. The overall combustor assembly consists of three distinct sections: fuel delivery, main combustion chamber, and a tailpipe as



shown in Figure 1.13. Flow is delivered through two separate co-annular concentric pipes. The low velocity methane fuel is delivered through the inner pipe, whereas the higher velocity air is delivered through the annulus of the two pipes. Both fuel and airflows pass through 45° helical swirlers and become highly swirling flows as they enter the main combustion chamber. Both fuel and airflows pass through 45° helical swirlers and become highly swirling flows as they enter the main combustion chamber.

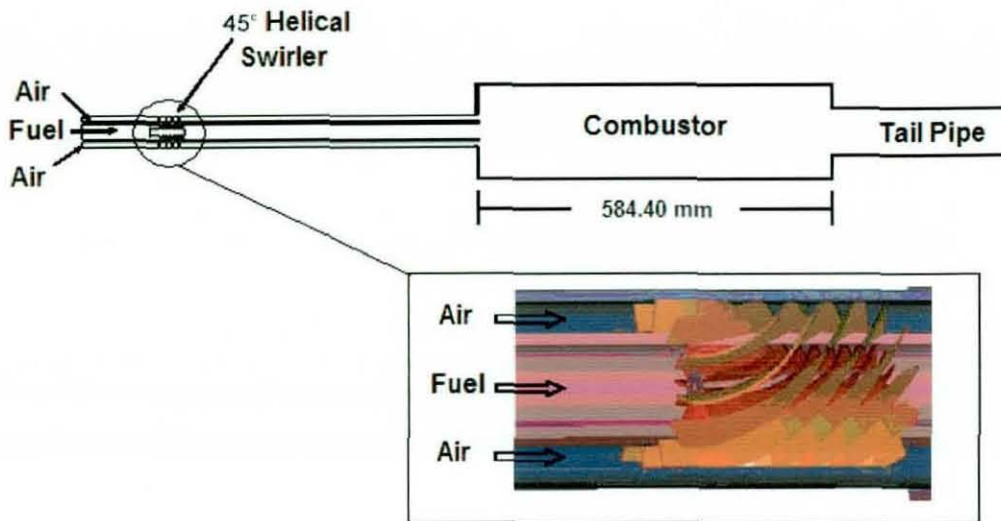


Figure 1.13 Davoudzadeh et al. experimental gas turbine combustor model [52]

Despite the periodicity of the model which would allow considering only a 45° sector, simulation was conducted for the full 360° geometry by using a hexahedral mesh with about 2.5 million cells. No justification has been brought by the authors but it might be due to the fact that meshing the whole complex geometry is considered much easier than meshing a single sector which needs a time consuming effort but will end up with less simulation time. Results of the simulation demonstrated that the code can predict the essential features of the gas turbine combustors such as the compact recirculation zone near the tip of the fuel nozzle and corner recirculation zones. In addition, comparisons of the computed velocity components with the experimental data showed good agreement.



#### 1.4 Summary of Current Literature

The literature review covered in the previous section has exposed the level of understanding that currently exists on gas turbine combustor flows. Furthermore, the latest developments in simulating these flows using some modern numerical methodologies have been covered. The survey was mainly limited to non-reacting (cold) flow simulation which reveals the overall structure of the flow field and shows the level of mixing inside the combustor and the uniformity of the flow at the exit which is the main target for the combustor designer. The literature indicates the importance of cold-flow solutions to perform parametric studies of the various combustor components and their influence on the overall flow pattern and their role in providing initial values of velocity, turbulent kinetic energy and turbulent dissipation for the reacting (hot) flow simulation.

The survey indicated that the most significant combustor components that contribute to the exiting non-uniform thermal and pressure fields are swirlers, film-cooling slots, primary holes, and dilution holes. The numerical predictions performed on different combustor components showed that flow features can be quantitatively predicted. However, they also revealed the importance of coupling the combustor components, defining an appropriate meshing strategy and using a suitable turbulence model.

Most of the reviewed computational predictions were carried out in uncoupled mode considering only the internal flow of the combustor. Experimental data reveal the strength of the interaction between annulus, swirler and core flows, which ultimately determines the jet characteristics at the hole exit. These data illustrate the improvement in the prediction of exit jet characteristics which is obtained by adopting fully coupled calculations compared to the internal-flow-only approach. The difficulty of creating computational grids which can adequately represent the complex geometries of actual combustors was found to be the main reason behind

uncoupling the combustor CFD predictions. Structured grids, which have been widely used, turned out to be time consuming to generate and sometimes produced poor quality meshes which at the end alter the solution accuracy. Unstructured grids appeared to be more attractive due to their capabilities to handle the complex geometry of the combustor and their flexibility to control the quality of the grid in certain zones of the domain without affecting other zones. The literature shows the advantages of using unstructured grids which enable to simulate, in a coupled mode, not only the combustor components but the whole aircraft engine [51]. It also shows that the use of unstructured methods and parallel computing minimizes the overall time needed to achieve a numerical solution. On the other hand, the use of unstructured grid methods with turbulence dominated flows is considered as an area that has only recently received much attention. Therefore, it is difficult to conclude the suitability of these methods for use to simulate combustor flows. The uncertainty that lies within this approach is in connection with the solution quality that is obtained through the use of tetrahedral grids with free shear and recirculating flows. It is believed that extensive assessment of such methods is necessary, since not much attention has been given to it in the literature so far. This approach, if verified, may provide to aircraft engine manufacturers the capability to assess engine performance numerically, including the effects of component interactions, prior to building and testing the engine.

The survey shows the importance of experimental data to validate the numerical predictions and to provide suitable boundary conditions at the combustor inlet and exit. Obviously, numerical solvers must include the capability to deal with fixed velocity inlet boundary conditions and/or mass flow boundary conditions.

### 1.5 Objectives of the Present Study

Given the goal stated in section 1.1 and the summary in the previous section, the following main objectives were set for the present project:

- To assess the compatibility of a typical, modern, RANS based CFD algorithm formulated for turbomachinery-type flows and using a density-based, coupled solver approach, for application to gas-turbine combustor-type predictions, under both isothermal and reacting flow conditions. (The Rolls-Royce Hydra code [53] will be used for this).
  
- To assess and, if necessary, modify the CFD algorithm in areas where this is needed to make it suitable for combustor relevant flow problems, for example:
  - The need for fixed velocity and periodic boundary condition.
  - The need for numerically and physically accurate predictions of scalar mixing (i.e. low numerical diffusion and prediction of both mean and variance of a conserved scalar property).
  - The need for a model of turbulent diffusion flame combustion (a basic model will suffice involving a flamelet description and an assumed shape probability density function (pdf) for turbulence-chemistry interaction).
  
- To quantify performance from a series of test cases selected for relevance to gas-turbine combustor flows:
  - Impinging jet aerodynamics (isothermal)
  - Fuel injector swirling flow aerodynamics (isothermal).
  - Fuel (gaseous)-air mixing (isothermal) and reaction under turbulent diffusion flame condition.

Three different test cases will therefore be used to validate and improve the numerical simulation capabilities of the Hydra solver in predicting non-reacting and reacting flows typical of gas turbine combustors. The first test case is the jet in confined cross flow (JICCF) associated with combustor liner-port-core flow and strongly impinging jets, which has been intensively investigated by Spencer and

McGuirk [46, 47] experimentally and numerically as discussed in section 1.3. The second test case is the highly swirling flow through a generic multi-stream swirler studied experimentally and numerically by Hughes [48] as discussed in the literature review. These two cases represent the main flow features associated with the complex primary zone of combustors such as recirculation zones due to swirling motion and jet impingement and interaction with core cross flow. The current study will also assess the influence of the various types of unstructured grids on the solution accuracy and their suitability to simulate combustor flows. The advantages of the local refinement capabilities associated with unstructured methods in capturing flow details should be tested and evaluated. Hydra as a density-based unstructured code will also be compared to a pressure-correction unstructured solver by simulating the above two cases with the Fluent commercial code. Hydra capabilities will be extended towards dealing with velocity inlet and periodic flow boundary conditions which are essential in gas turbine combustor simulations. The amount of the undesirable numerical diffusion associated with the unstructured discretisation of the convection terms of scalar variable equations will be investigated and methods to preserve solution boundedness and control the inherited error will be developed. Finally, a turbulent combustion model based on the conserved scalar approach will be incorporated into the Hydra numerical algorithm to simulate the non-premixed reacting flows typical of gas turbine combustor, the test case selected here is the one of Owen [54] which has been used before for assessment of both RANS and LES models of combustion flows [55, 56].

## 1.6 Outline of the Thesis

*The rest of the thesis consists of six chapters. In chapter two, the governing flow equations are presented in their differential and integral forms as well as the turbulence model equations. Boundary conditions are briefly discussed and finally the finite volume form of the equations, numerical discretisation and solution algorithm as used in the Hydra code are developed. In chapter three the*

modifications to the basic Hydra code which would allow application to combustor-relevant aerodynamic problems are presented. These modifications include the fixed velocity and the centreline boundary conditions and the transport equations and a combustion sub-model that would allow variable density turbulent reacting flows to be predicted. Jets in confined cross flow as an effective way of mixing in combustors is investigated in chapter four. The flow characteristics are described and previous experimental and numerical studies reviewed. The results of the numerical simulations of the selected configuration are presented. In chapter five, a generic multi stream swirler is investigated. Numerical predictions and the difficulties associated with modelling such a complex geometry and flow are discussed. Chapter six describes a method which has been developed for implementing a non-premixed turbulent combustion model in the Hydra code. Hydra predictions of simple diffusion flames are compared with previous experimental data and numerical predictions. The thesis ends in chapter seven with conclusions of the present work and recommendations for future work.

# Chapter 2

## Mathematical Methodology and Numerical Techniques of the Basic Hydra Code

### 2.1 Introduction

The main objective of fluid mechanics is to understand the physical events that occur in a flow within designated geometry and boundaries. These events are related to the interaction of aero-thermodynamic and chemical phenomena such as dissipation, diffusion, convection, turbulence and chemical reactions. Generally speaking, most of these phenomena are governed by the compressible Navier-Stokes equations. Many important aspects of these relations are non linear and, consequently, have no analytical solution. This motivates the use of numerical solution techniques for the partial differential equations governing the physics of fluid flow. To accomplish the numerical solution, the first step involves the specification of the problem, including the geometry and flow conditions. Once the problem has been specified, an appropriate set of governing equations and boundary conditions must be selected. The phenomena of importance in the field of continuum fluid dynamics are governed by the conservation of mass, momentum, and energy, resulting in the Navier-Stokes partial differential equations. In most cases, physical models must be chosen for processes which cannot be simulated within the constraints used in the derivation or solution of the governing equations. Turbulence and chemical reactions are rarely simulated in a practical context, and are thus often modelled. The success of a simulation depends

greatly on the methodology involved in selecting the governing equations and physical models, and on the numerical techniques implemented in solving these governing equations with specific boundary conditions.

In this chapter the methodology followed to develop Hydra [53, 57-59], the nonlinear flow solver used in this research, will be explained in detail. The schematic of the flow solver and its interaction with the preprocessing and post-processing software as well as the sequence of the solution will be illustrated. The Navier-Stokes equations which are the mathematical expressions of the conservation of mass, momentum, and energy for a continuum, Newtonian fluid will be presented in instantaneous and time-averaged form. The modifications introduced to the governing equations based on Favre averaging concept to include the effects of the turbulence in the flow field will be explained. The finite volume form of the equations, used in the numerical discretisation of Hydra, will be developed, and the boundary conditions necessary to complete the flow model will be discussed. The numerical integration scheme, preconditioning, and multigrid techniques used by the solver will be illustrated.

## 2.2 Equations of Fluid Motion

The Navier-Stokes equations in Cartesian coordinates can be written in the following differential form:

$$\frac{\partial Q}{\partial t} + \frac{\partial F_x}{\partial x} + \frac{\partial F_y}{\partial y} + \frac{\partial F_z}{\partial z} = S \tag{2.1}$$

where  $Q$  is the conservative variables vector:

$$Q = \begin{pmatrix} \rho \\ \rho u \\ \rho v \\ \rho w \\ \rho E \end{pmatrix} \tag{2.2}$$

and  $S$  is the source term matrix, which is in absence of Coriolis and centrifugal forces given as follows:

$$S = \begin{pmatrix} 0 \\ 0 \\ 0 \\ 0 \\ 0 \end{pmatrix} \quad (2.3)$$

The flux vectors in the  $x$ ,  $y$  and  $z$  directions are  $F_x$ ,  $F_y$  and  $F_z$ , which are given as follows:

$$F_x = \begin{pmatrix} \rho u \\ \rho u^2 + p - \tau_{xx} \\ \rho uv - \tau_{yx} \\ \rho uw - \tau_{zx} \\ (\rho E + p)u - u\tau_{xx} - v\tau_{yx} - w\tau_{zx} + q_x \end{pmatrix} \quad (2.4)$$

$$F_y = \begin{pmatrix} \rho v \\ \rho uv - \tau_{xy} \\ \rho v^2 + p - \tau_{yy} \\ \rho vw - \tau_{zy} \\ (\rho E + p)v - u\tau_{xy} - v\tau_{yy} - w\tau_{zy} + q_y \end{pmatrix} \quad (2.5)$$

$$F_z = \begin{pmatrix} \rho w \\ \rho uw - \tau_{xz} \\ \rho vw - \tau_{yz} \\ \rho w^2 + p - \tau_{zz} \\ (\rho E + p)w - u\tau_{xz} - v\tau_{yz} - w\tau_{zz} + q_z \end{pmatrix} \quad (2.6)$$

In the above equations,  $t$  is time,  $\rho$  is fluid density,  $u$ ,  $v$  and  $w$  are the Cartesian velocity components in the  $x$ ,  $y$  and  $z$  directions respectively,  $p$  is the static pressure and  $E$  is the total internal energy. The equation of state relates the flow conservative variables by



$$p = \rho RT = (\gamma - 1)\rho \left( E - \frac{1}{2}(u^2 + v^2 + w^2) \right) \quad (2.7)$$

where  $R$  is the gas constant,  $T$  is the temperature and  $\gamma$  is the specific heat ratio.

The heat fluxes in the  $x, y$  and  $z$  directions are given as follows

$$q_x = -k \frac{\partial T}{\partial x} \quad (2.8)$$

$$q_y = -k \frac{\partial T}{\partial y} \quad (2.9)$$

and

$$q_z = -k \frac{\partial T}{\partial z} \quad (2.10)$$

where  $k$  is the thermal conductivity given by

$$k = \frac{\mu C_p}{Pr} \quad (2.11)$$

In the above equation,  $Pr$  is the Prandtl number and  $\mu$  is the molecular dynamic viscosity modeled by Sutherland's law as follows

$$\mu = \frac{S1 T^{3/2}}{T + S2} \quad (2.12)$$

where  $S1 = 1.461 \times 10^{-6} \frac{kg}{m.s.\sqrt{K}}$  and  $S2 = 110.3K$

In the flux vectors the shear stress terms and heat flux terms constitute the so called viscous or diffusive fluxes and the other terms constitute the inviscid or convective fluxes.

The viscous stresses for a Newtonian fluid are given as follows:

$$\tau_{xx} = 2\mu \frac{\partial u}{\partial x} - \frac{2}{3}\mu \left( \frac{\partial u}{\partial x} + \frac{\partial v}{\partial y} + \frac{\partial w}{\partial z} \right) \quad (2.13)$$

$$\tau_{yy} = 2\mu \frac{\partial v}{\partial y} - \frac{2}{3}\mu \left( \frac{\partial u}{\partial x} + \frac{\partial v}{\partial y} + \frac{\partial w}{\partial z} \right) \tag{2.14}$$

$$\tau_{zz} = 2\mu \frac{\partial w}{\partial z} - \frac{2}{3}\mu \left( \frac{\partial u}{\partial x} + \frac{\partial v}{\partial y} + \frac{\partial w}{\partial z} \right) \tag{2.15}$$

$$\tau_{xy} = \tau_{yx} = \mu \left( \frac{\partial u}{\partial y} + \frac{\partial v}{\partial x} \right) \tag{2.16}$$

$$\tau_{xz} = \tau_{zx} = \mu \left( \frac{\partial u}{\partial z} + \frac{\partial w}{\partial x} \right) \tag{2.17}$$

$$\tau_{yz} = \tau_{zy} = \mu \left( \frac{\partial v}{\partial z} + \frac{\partial w}{\partial y} \right) \tag{2.18}$$

In the above equations, normalisation is now used for the flow variables in order to obtain equations where solutions are bounded and to provide conditions upon which dynamic and energetic similarity can be obtained. In this study the normalisation is used in which the reference length scale  $L_{ref} = 1\text{ m}$  and the reference density  $\rho_{ref}$ , pressure  $p_{ref}$  and temperature  $T_{ref}$  correspond to standard sea level density, pressure and temperature. The reference velocity  $U_{ref}$  is therefore defined as

$$U_{ref} \equiv \sqrt{\frac{p_{ref}}{\rho_{ref}}} \tag{2.19}$$

Accordingly, normalised quantities are defined as follows

$$\begin{aligned} x^* &= \frac{x}{L_{ref}}, \quad y^* = \frac{y}{L_{ref}}, \quad z^* = \frac{z}{L_{ref}}, \quad u^* = \frac{u}{U_{ref}}, \quad v^* = \frac{v}{U_{ref}}, \quad w^* = \frac{w}{U_{ref}}, \quad t^* = \frac{t U_{ref}}{L_{ref}}, \\ \rho^* &= \frac{\rho}{\rho_{ref}}, \quad p^* = \frac{p}{p_{ref}}, \quad T^* = \frac{T}{T_{ref}}, \quad \mu^* = \frac{\mu}{\rho_{ref} U_{ref} L_{ref}} \end{aligned} \tag{2.20}$$

For convenience, the superscript “\*” will be dropped in the rest of the study. All variables will be considered to be in normalised form unless otherwise specified.

### 2.3 Turbulence Modeling

Although the above equations apply to both laminar and turbulent flows, the large range of length and time scales observed in turbulent flows at high Reynolds number renders the exact Navier-Stokes equations computationally extremely expensive to solve. This direct numerical simulation (DNS) approach is not yet practically possible for industrial flow problems. The usual alternative approach is to modify the equations of motion by adopting a statistical approach. In compressible flows, the instantaneous point values of density, and all other flow variables, are decomposed into a time average part  $\bar{\rho}$  and a fluctuating part  $\rho'$

$$\rho = \bar{\rho} + \rho' \tag{2.21}$$

where

$$\bar{\rho} = \lim_{\Delta t \rightarrow \infty} \left( \frac{1}{\Delta t} \int_{t_0}^{t_0 + \Delta t} \rho \, dt \right) \tag{2.22}$$

These two quantities are represented graphically in Figure 2.1. The time interval of integration must be larger than the longest period associated with fluctuations caused by turbulence but smaller than any time-scale associated with boundary condition unsteadiness (e.g. blade rotational speed). Thus the time interval is problem dependant and depends on the geometry and physics of the flow field to be investigated. Using the above defined standard concept of Reynolds averaging, the continuity equation may be transformed into the following time-averaged tensor form

$$\frac{\partial \bar{\rho}}{\partial t} + \frac{\partial}{\partial x_i} (\bar{\rho} u_i + \overline{\rho' u_i'}) = 0 \tag{2.23}$$

Thus, an additional unknown term correlating the fluctuating components of velocity and density appear in the continuity equation and similar unknown triple correlations appear in the momentum and energy equations. Favre [4] suggested a

density weighted averaging procedure which simplifies the equations and avoids the difficulty of modeling extra correlations.

The mass-averaged or Favre-averaged velocity  $\tilde{u}_i$ , is defined by

$$\tilde{u}_i = \frac{1}{\bar{\rho}} \lim_{\Delta t \rightarrow \infty} \left( \frac{1}{\Delta t} \int_t^{t+\Delta t} \rho(x,t) u_i(x,t) dt \right) \quad (2.24)$$

Expansion of the right hand side of the above equation gives the following expression relating the Favre-averaged velocity and the standard Reynolds averaged velocity

$$\bar{\rho} \tilde{u}_i = \bar{\rho} \bar{u}_i + \overline{\rho' u_i'} \quad (2.25)$$

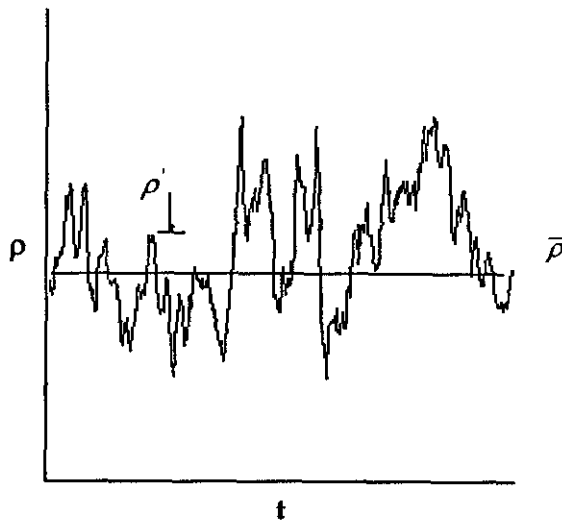


Figure 2.1 Average and fluctuating quantities for turbulent flow

Using equations (2.24) and (2.25), the mass conservation equation may be derived as follows:

$$\frac{\partial \bar{\rho}}{\partial t} + \frac{\partial}{\partial x_i} (\bar{\rho} \tilde{u}_i) = 0 \quad (2.26)$$

This approach underlines the point that the most appropriate time-averaged dependent variable in a compressible flow is the momentum per unit volume ( $\bar{\rho} \tilde{u}_i$ )

rather than the primitive variable ( $u$ ). This definition has physical justification since what is conserved in a flow is the momentum per unit volume rather than the velocity. According to Favre averaging, for any fluctuating fluid property  $\phi$ :

$$\phi_i = \tilde{\phi} + \phi_i'' \tag{2.27}$$

and

$$\overline{\rho\phi_i} = \tilde{\rho}\tilde{\phi}_i + \overline{\rho\phi_i''} \tag{2.28}$$

where  $\tilde{\phi}_i$  is the Favre-averaged component and  $\phi_i''$  is the fluctuating component of  $\phi_i$ .

The Favre-averaged conservation equations may be written in tensor form as follows:

Continuity equation:

$$\frac{\partial \tilde{\rho}}{\partial t} + \frac{\partial}{\partial x_i} (\tilde{\rho}\tilde{u}_i) = 0 \tag{2.29}$$

Momentum equations (along  $x_i$  direction):

$$\frac{\partial}{\partial t} (\tilde{\rho}\tilde{u}_i) + \frac{\partial}{\partial x_j} (\tilde{\rho}\tilde{u}_j\tilde{u}_i) = -\frac{\partial \tilde{P}}{\partial x_i} + \frac{\partial}{\partial x_j} [\tilde{\tau}_{ji} + \tilde{\tau}_{ji,RS}] \tag{2.30}$$

where  $\tilde{\tau}_{ij}$  and  $\tilde{\tau}_{ij,RS}$  are the viscous stress and the Reynolds stress tensors respectively given as

$$\tilde{\tau}_{ij} = \mu \left( \frac{\partial \tilde{u}_i}{\partial x_j} + \frac{\partial \tilde{u}_j}{\partial x_i} \right) - \frac{2}{3} \mu \frac{\partial \tilde{u}_k}{\partial x_k} \delta_{ij} \tag{2.31}$$

assuming  $\mu$  as a constant

$$\tilde{\tau}_{ij,RS} = -\overline{\rho u_i'' u_j''} \tag{2.32}$$

The total enthalpy equation:

$$\frac{\partial}{\partial t}(\bar{\rho}H) + \frac{\partial}{\partial x_i}(\bar{\rho}\tilde{u}_i H) = \frac{\partial}{\partial x_j} \left[ -q'_j - q'_j + \overline{v_{ij}u_i''} - \rho u_j'' \frac{1}{2} u_i'' u_i'' \right] + \frac{\partial \bar{P}}{\partial t} + \frac{\partial}{\partial x_j} [\tilde{u}_i (\bar{v}_{ij} + \tau_{ij})] \quad (2.33)$$

and the equation of state

$$\bar{P} = \bar{\rho}R\bar{T} \quad (2.34)$$

Where  $H$  is the total enthalpy including the mean kinetic energy and also the turbulent kinetic energy, expressed as

$$H = \tilde{h} + \frac{1}{2} \tilde{u}_i \tilde{u}_i + k \quad (2.35)$$

where  $\tilde{h}$  is the static enthalpy and  $k$  is the turbulent kinetic energy where,  $\bar{\rho}k = 0.5 \overline{\rho u_i'' u_i''}$ .  $q'_j$  and  $q'_j$  are the laminar and turbulent heat flux vectors respectively given as follows

$$q'_j = -\frac{\mu}{Pr} \frac{\partial \tilde{h}}{\partial x_j} \quad (2.36)$$

$$q'_j = -\frac{\mu_t}{Pr_t} \frac{\partial \tilde{h}}{\partial x_j} \quad (2.37)$$

Favre averaging leaves an unclosed term  $\overline{\rho u_i'' u_j''}$  which has to be modeled with a turbulence model. Turbulence models are commonly based on Boussinesq eddy viscosity assumption, where the Reynolds stress tensor is expressed in terms of mean strain rate as follows:

$$\tau_{ij} = -\overline{\rho u_i'' u_j''} = \mu_t \left( \frac{\partial \tilde{u}_i}{\partial x_j} + \frac{\partial \tilde{u}_j}{\partial x_i} - \frac{2}{3} \frac{\partial \tilde{u}_k}{\partial x_k} \right) - \frac{2}{3} \bar{\rho} k \delta_{ij} \quad (2.38)$$

A commonly used turbulence model for RANS flow solvers is the  $k-\varepsilon$  model where two additional transport equations are solved in order to determine the eddy viscosity [60]. The two partial differential equations are derived for the turbulence kinetic energy  $k$  and the turbulence dissipation  $\varepsilon$  as follows:

$$\frac{\partial}{\partial t}(\bar{\rho}k) + \frac{\partial}{\partial x_j}(\bar{\rho}\tilde{u}_j k) = \frac{\partial}{\partial x_j} \left\{ \left( \mu + \frac{\mu_t}{\sigma_k} \right) \frac{\partial k}{\partial x_j} \right\} + P_k - \bar{\rho}\varepsilon \quad (2.39)$$

$$\frac{\partial}{\partial t}(\bar{\rho}\varepsilon) + \frac{\partial}{\partial x_j}(\bar{\rho}\tilde{u}_j \varepsilon) = \frac{\partial}{\partial x_j} \left\{ \left( \mu + \frac{\mu_t}{\sigma_\varepsilon} \right) \frac{\partial \varepsilon}{\partial x_j} \right\} + C_1 \frac{\varepsilon}{k} P_k - C_2 \bar{\rho} \frac{\varepsilon^2}{k} \quad (2.40)$$

where the turbulence dissipation is:

$$\bar{\rho}\varepsilon = \nu_\mu \overline{\frac{\partial u_i''}{\partial x_j}} \quad (2.41)$$

and the production term  $P_k$  is:

$$P_k = \left[ \mu_t \left( \frac{\partial \tilde{u}_i}{\partial x_j} + \frac{\partial \tilde{u}_j}{\partial x_i} - \frac{2}{3} \frac{\partial \tilde{u}_k}{\partial x_k} \delta_{ij} \right) - \frac{2}{3} \bar{\rho} k \delta_{ij} \right] \frac{\partial \tilde{u}_i}{\partial x_j} \quad (2.42)$$

The model constants are:

$$C_\mu = 0.09, C_1 = 1.44, C_2 = 1.92, \sigma_k = 1.0, \sigma_\varepsilon = 1.3 \quad (2.43)$$

And the turbulent viscosity  $\mu_t$  is related to  $\varepsilon$  by

$$\mu_t = \rho C_\mu \frac{k^2}{\varepsilon} \quad (2.44)$$

Similar to the fluid flow equations, the turbulence equations for  $k - \varepsilon$  model can be expressed in vector form as follows:

$$\frac{\partial Q_i}{\partial t} + \frac{\partial [(F_i^C)_x - (F_i^D)_x]}{\partial x} + \frac{\partial [(F_i^C)_y - (F_i^D)_y]}{\partial y} + \frac{\partial [(F_i^C)_z - (F_i^D)_z]}{\partial z} = S_i \quad (2.45)$$

where  $Q_i$  is the turbulence variables vector and  $S_i$  is the source term vector given as follows:

$$Q_i = \begin{pmatrix} \bar{\rho}k \\ \bar{\rho}\varepsilon \end{pmatrix} \text{ and } S_i = \begin{pmatrix} P_k - \bar{\rho}\varepsilon \\ C_1 P_k \frac{\varepsilon}{k} - C_2 \bar{\rho} \frac{\varepsilon^2}{k} \end{pmatrix} \quad (2.46)$$

and the convective and diffusive flux vectors in the x, y and z directions are given by

$$\begin{aligned}
 (F_i^c)_x &= \begin{pmatrix} \widetilde{\rho}uk \\ \widetilde{\rho}u\varepsilon \end{pmatrix}, \quad (F_i^c)_y = \begin{pmatrix} \widetilde{\rho}vk \\ \widetilde{\rho}v\varepsilon \end{pmatrix}, \quad (F_i^c)_z = \begin{pmatrix} \widetilde{\rho}wk \\ \widetilde{\rho}w\varepsilon \end{pmatrix}, \\
 (F_i^D)_x &= \begin{pmatrix} \left( \mu + \frac{\mu_t}{\sigma_k} \right) \frac{\partial k}{\partial x} \\ \left( \mu + \frac{\mu_t}{\sigma_\varepsilon} \right) \frac{\partial \varepsilon}{\partial x} \end{pmatrix}, \quad (F_i^D)_y = \begin{pmatrix} \left( \mu + \frac{\mu_t}{\sigma_k} \right) \frac{\partial k}{\partial y} \\ \left( \mu + \frac{\mu_t}{\sigma_\varepsilon} \right) \frac{\partial \varepsilon}{\partial y} \end{pmatrix}, \quad (F_i^D)_z = \begin{pmatrix} \left( \mu + \frac{\mu_t}{\sigma_k} \right) \frac{\partial k}{\partial z} \\ \left( \mu + \frac{\mu_t}{\sigma_\varepsilon} \right) \frac{\partial \varepsilon}{\partial z} \end{pmatrix} \quad (2.47)
 \end{aligned}$$

## 2.4 Finite Volume and Spatial Discretisation

### 2.4.1 Control volume definition

Finite volume techniques differ from each other initially by the control volume definition they adopt. The best direct way to define the control volume is to use the cells provided by the primary mesh itself i.e. a mesh which fills the solution domain volume and fits the boundaries of the solution domain. The unknowns are related to a particular point in the cell, which is usually chosen as the cell centroid. Such methods are called cell-centred as shown in Figure 2.2 (a) [61]. The second class of methods, called vertex centered, locates the unknowns at the vertices and defines the control volumes around each vertex as in Figure 2.2 (b). The control volume can be constructed by joining directly the centroids of the surrounding cells (centroid dual control volume) or indirectly by connecting the middle of each edge to the centroid (median dual control volume). A third method is a mixture of the two previous techniques. The unknowns are located at the vertices of the mesh as in Figure 2.2 (c), but the control volume is as in the cell-centered method [12, 62] (cell-vertex method).



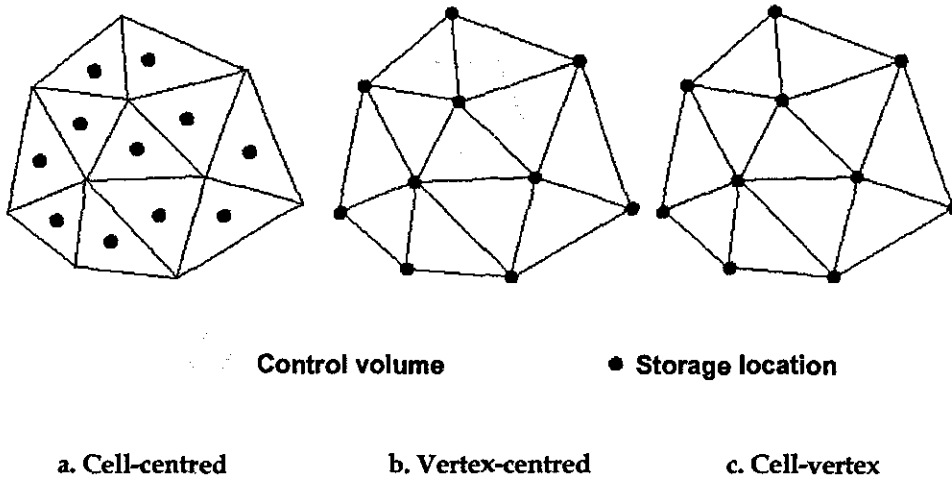


Figure 2.2 Control volume types

The first two methods, cell-centred and vertex-centred, are widely used in CFD finite volume discretization techniques. The advantages of these two methods have been under discussion for a long time by many authors [63-67]. The discussions usually focus on the accuracy of the numerical evaluation of the flux across a given control volume surface on a given grid. On a simplicial grid in two or three dimensions, there are approximately twice (in 2D) or six to seven times (in 3D) as many cells as vertices. Therefore, for the same simplicial grid, the vertex-centred methods require significantly less storage than the cell-centred methods. However, the storage is approximately the same on quadrilateral and hexahedral grids.

Barth [63] has concluded that for a given tetrahedral grid, the vertex-centred method requires a smaller number of operations than the cell-centred method in order to evaluate the flux although for a hexahedral grid the number of operations is approximately the same. Mavriplis [64] found that the solution variables are more strongly coupled to neighbouring solution variables in vertex-centred methods, which may contribute to higher accuracy. Venkatakrishnan [65] suggested that the cell-centred method might be more accurate because of the

larger number of cells than vertices in a given simplicial grid. On quadrilateral and hexahedral grids, the above arguments are irrelevant since the number of cells and vertices are approximately the same.

In the unstructured finite volume discretisation employed in Hydra, a median dual vertex-centred control volume approach has been selected. It is important at this stage to present some definitions and geometrical relations associated with this type of control volume before proceeding with derivation of the spatial discretisation. Considering the 2D triangular grid shown in Figure 2.3, the median dual control volume  $V$  (abcde) surrounding node ( $j$ ) is related to the large cell  $\Omega$  (12345), which is constructed from the original grid elements which contain node ( $j$ ), according to the following relations

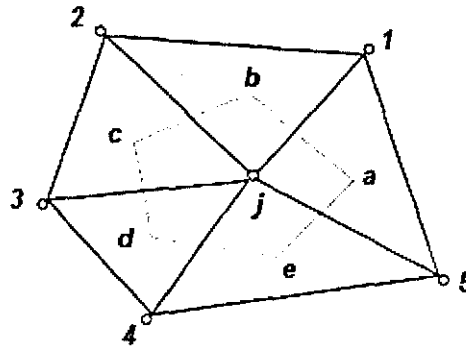


Figure 2.3 Median dual control volume in triangular mesh

$$\Omega = 3 \times V$$

$$L = 3 \times S$$

$$L = n_{12} + n_{23} + n_{34} + n_{45} + n_{51}$$

$$S = n_{ab} + n_{bc} + n_{cd} + n_{de} + n_{ea}$$

$$n_{ab} = (n_{51} + n_{12}) / 3$$

$$n_{bc} = (n_{12} + n_{23}) / 3$$

$$n_{ab} = (n_{23} + n_{34}) / 3$$

$$n_{ab} = (n_{34} + n_{45}) / 3$$

$$n_{ab} = (n_{45} + n_{51}) / 3$$

where  $\Omega$  is the volume of cell (12345),  $L$  is the surface area of cell (12345),  $V$  is the volume of cell (abcde),  $S$  is the surface area of volume (abcde),  $n_{ab}$  is the edge weight (i.e. in this 2D instance the length of ab) of edge  $j1$ ,  $n_{bc}$  is the edge weight of edge  $j2$ , etc. In the rest of this chapter the edge weight  $n$  will be referred to as  $\Delta s$  (e.g.  $n_{ab} = \Delta s_{ij}$ ) so that the symbol  $n_{ij}$  may be used for the unit normal between node  $i$  and  $j$  (where  $i = 1-5$  in Figure 2.3)

The 3-D compressible RANS equations can be expressed as follows:

$$\frac{\partial Q}{\partial t} + \nabla \cdot F(Q, \nabla Q) = S(Q, \nabla Q) \tag{2.48}$$

The above equation can be written in semi-discrete form as

$$\frac{\partial Q}{\partial t} + R_j = 0 \tag{2.49}$$

where the residual  $R_j$  is the summation of the flux and source term vectors at each grid node  $j$

$$R_j = \nabla \cdot F(Q, \nabla Q) - S(Q, \nabla Q) \tag{2.50}$$

It is required to have the residual  $R_j = 0$  for steady state solution all over the domain. First, apply the divergence theorem to integrate the above equation over the median dual control volume  $V_j$  constructed around each node in the numerical domain.

$$R_j = \frac{1}{V_j} \left[ \oint_{\partial V_j} F(n, Q, \nabla Q) ds - \oint_{V_j} S(Q, \nabla Q) dv \right] = 0 \tag{2.51}$$

Where each edge of the control volume has area  $\Delta s_{ij}$  and unit normal  $n_{ij}$ . The integration over the control volume surfaces can be replaced by a sum over adjacent edges since each of them corresponds to a face of the control volume.  $E_j$  is defined to be the set of nodes connected to node  $j$  by an edge and  $F_{ij}$  is the flux across the face. To distinguish the internal nodes from the boundary nodes,  $B_j$  is the set of the boundary faces associated with the node  $j$ ,  $\Delta s_{ik}$  is the area of the boundary face and  $F_{ik}$  is the flux across the boundary face. Therefore, the integral in equation (2.47) can be approximated by:

$$R_j = \frac{1}{V_j} \left[ \sum_{i \in E_j} F_{ij} \Delta s_{ij} + \sum_{k \in B_j} F_{ik} \Delta s_{ik} - S_j V_j \right] \tag{2.52}$$

The flux term in the above equation is divided into a convective (inviscid) flux term  $F^I$  and a diffusive (viscous) flux term  $F^V$  as follows

$$F = F^I + F^V \tag{2.53}$$

Each of the two terms will be evaluated separately for each face of the control volume faces.

**2.4.2 Convective flux**

The convective term discretization described here is motivated by the MUSCL approach in which a functional representation of  $Q$  is used within each control volume to arrive at a Riemann problem at the interface between control volumes. The flux at the interface is based on Roe upwind differencing [68] which combines the central differencing of the nonlinear inviscid flux with a smoothing flux based on a one dimensional characteristics variable. The method will be described first for a 1D case then extended to 3D.

Consider the one dimensional inviscid flow equation which has the form

$$\frac{\partial Q}{\partial t} + \frac{\partial F}{\partial x} = 0 \quad (2.54)$$

The above equation can be linearized as

$$\frac{\partial Q}{\partial t} + A \frac{\partial Q}{\partial x} = 0 \quad (2.55)$$

where  $A$  is the linearisation Jacobian matrix

$$A = \frac{\partial F}{\partial Q} \quad (2.56)$$

The discrete form of this equation using an upwind scheme (velocity in  $j$  direction) is:

$$\frac{Q_j^{n+1} - Q_j^n}{\Delta t} = -A \frac{Q_j^n - Q_{j-1}^n}{\Delta x} \quad (2.57)$$

According to upwind differencing, the above equation is unstable if  $A < 0$  and stability can be accomplished by upwinding in the correct direction according to the characteristics of the equation. Define  $A^+$  and  $A^-$  for the opposite upwinding directions

$$A^+ = \max(A, 0) = \frac{1}{2}(A + |A|) \quad (2.58)$$

$$A^- = \min(A, 0) = \frac{1}{2}(A - |A|) \quad (2.59)$$

Substitute equation (2.58) and (2.59) into (2.57) to obtain

$$\frac{Q_j^{n+1} - Q_j^n}{\Delta t} = -\frac{1}{\Delta x} [A^+(Q_j^n - Q_{j-1}^n) + A^-(Q_{j+1}^n - Q_j^n)] \quad (2.60)$$

Rearrange these terms:

$$Q_j^{n+1} - Q_j^n = -\frac{A\Delta t}{2\Delta x} (Q_{j+1}^n - Q_{j-1}^n) + \frac{|A|\Delta t}{2\Delta x} (Q_{j+1}^n - 2Q_j^n + Q_{j-1}^n) \quad (2.61)$$

The above equation shows that the upwind scheme is equivalent to a central difference scheme plus an additional 2<sup>nd</sup> difference numerical dissipation term.

Define the numerical flux  $F_{j+1/2}^n$  as:

$$F_{j+1/2}^n = \frac{A}{2}(Q_{j+1}^n - Q_j^n) - \frac{|A|}{2}(Q_{j+1}^n - Q_j^n) \tag{2.62}$$

Substitute the above equation into (2.61)

$$\frac{Q_j^{n+1} - Q_j^n}{\Delta t} = -\frac{1}{\Delta x} [F_{j+1/2}^n - F_{j-1/2}^n] \tag{2.63}$$

Where for the nonlinear system, equation (2.62) can be referred to as:

$$F_{j+1/2}^n = \frac{1}{2}(F(Q_{j+1}^n) - F(Q_j^n)) - \frac{|A|}{2}(Q_{j+1}^n - Q_j^n) \tag{2.64}$$

Equations from (2.54) to (2.64) show an example of the 1D case, following the direction from node  $(j-1)$  to  $(j)$  to node  $(j+1)$ .  $(j-1/2)$  is the interface between  $(j-1)$  and  $(j)$ ;  $(j+1/2)$  is the interface between  $(j)$  and  $(j+1)$ .

The 3D case can be derived in a similar manner, treating each edge connecting  $(i)$  and  $(j)$  in the 3D case as the 1D case treats the edge connecting nodes  $(j)$  and  $(j+1)$ , the convective flux term then can be expressed as follows:

$$F_{ij}^i = \frac{1}{2}(F_{ij}^i(Q_i) - F_{ij}^i(Q_j)) - |A_{ij}|(Q^+ - Q^-) \tag{2.65}$$

The central differencing part of the above equation is based on the nodal variables which make it computationally cheap to evaluate, while the reconstruction of  $Q^+$  and  $Q^-$  in the dissipation part is an expensive process and needs to be simplified. Considering the reconstruction stencil shown in Figure 2.4,  $Q^+$  and  $Q^-$  can be evaluated as follows

$$Q^+ = \frac{1}{2}Q_{j+} - Q_j + \frac{1}{2}Q_i \text{ and } Q^- = \frac{1}{2}Q_j - Q_i + \frac{1}{2}Q_{i-} \tag{2.66}$$

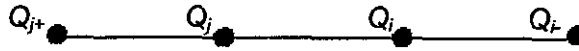


Figure 2.4 One dimensional reconstruction stencil

The above two quantities are equivalent to  $Q^+ = L_j(Q)$  and  $Q^- = L_i(Q)$ , where  $L_j(Q)$  and  $L_i(Q)$  are two undivided pseudo-Laplacian with unit central coefficients. For an unstructured mesh  $L_j(Q)$  is defined as

$$L_j(Q) = \frac{1}{N(E_j)} \sum_{i \in E_j} (Q_i - Q_j) \tag{2.67}$$

$N(E_j)$  represents the number of elements in set  $E_j$ . Therefore, smoothing term in (2.4.5) can be expressed as follows

$$|A_v|(Q^+ - Q^-) = \frac{1}{2}(1 - \kappa)|A_v|(L_j(Q) - L_i(Q)) \tag{2.68}$$

$\kappa \in [0,1]$  represents a one parameter family of second order schemes for a one-dimensional uniform mesh.

Crumpton et al. [57] noticed that using the above pseudo-Laplacian definition will give poor results on general grids. Therefore, it is modified to be linear preserving

$$L_j^p(Q) = L_j(Q) - \nabla Q_j \cdot L_j(x) \tag{2.69}$$

The gradient  $\nabla Q_j$  can be approximated by the following relation

$$\nabla Q_j = \sum_{i \in E_j} \frac{1}{2} (Q_i + Q_j) \tag{2.70}$$

To avoid numerical instability on highly stretched grids, Crumpton et al. introduced anisotropic scaling

$$\hat{L}_j(Q) = \left( \sum_{i \in E_j} \frac{1}{|x_i - x_j|} \right)^{-1} \sum_{i \in E_j} \frac{(Q_i - Q_j)}{|x_i - x_j|} \quad (2.71)$$

This shows extra smoothness in the solution and therefore more stability. The disadvantage of this approach is that the operator  $\hat{L}_j^p$  is anisotropic only on highly stretched grids therefore will only damp error modes which are of high frequency in the direction of highest grid resolution.

A limiter  $\Psi$  has been introduced in the dissipation term in the flux equation to obtain a monotonic resolution of regions with high gradient like shear layers and shock waves while maintaining the accuracy in regions where flow is smooth. The modified flux equation will as follows

$$F_y^I = \frac{1}{2} \left[ (F_y^I(Q_i) + F_y^I(Q_j)) - |A_y| \left( -\frac{1}{3} (1 - \Psi)(L_i^p - L_j^p) + \Psi(Q_i - Q_j) \right) \right] \quad (2.72)$$

where

$$\Psi = \min \left[ \varepsilon^{(2)} \left( \frac{|L_i^p(p)|}{|L_i^p(p)| + 2p_i} + \frac{|L_j^p(p)|}{|L_j^p(p)| + 2p_j} \right), 1 \right] \quad (2.73)$$

In the above limiter function,  $\varepsilon^{(2)}$  is a user defined constant taken to be 8 and  $p$  is the pressure at the node.

The Jacobian  $A_y = \frac{\partial F^I}{\partial Q}$  in equation (2.68) is defined as

$$A_y = (T \Lambda T^{-1})_y \quad (2.74)$$

where  $T$  is the eigenvector matrix given as

$$T = (r1 | r2 | r3 | r4 | r5) \quad (2.75)$$

The five columns in the above definition are the eigenvectors given in Appendix A with their inverse. The Jacobian  $A_y$  will be evaluated at the control volume faces by averaging the quantities at nodal values  $i$  and  $j$ .



2.4.3 Diffusive flux

In order to calculate the shear stresses and heat fluxes which form the diffusive flux matrix, the gradient on the control volume faces  $\nabla Q_{ij}$  must be calculated. The diffusive flux discretization has been performed using various methods by several researchers [58,67,69,70]. Formulations based on Galerkin approximations are widely used in the density based approach [70]. However, the nonlinearity associated within the edge-based data structure makes the application of these methods difficult and numerically expensive as they require huge storage of viscous edge weights [58]. The approach used in the current study is to approximate the viscous flux half-way along each edge and then use Gauss theorem to integrate the fluxes around each control volume. This approach requires an approximation of  $\nabla Q$  at the midpoint of each edge. The flow variables gradients can be approximated at the nodes using the existing edge weights.

Using the two dimensional control volume of Figure 2.3, the gradient  $\nabla Q$  can be evaluated as follows:

$$\nabla Q = \frac{1}{\Omega} \left( \iiint_{\Omega} \nabla Q \, d\Omega - \iint_{\Omega} \nabla Q_j \, d\Omega \right) \tag{2.76}$$

$Q_j$  is constant and therefore,  $\nabla Q_j = 0$

Applying Green's theorem to the volume integral yields

$$\begin{aligned} \nabla Q &= \frac{1}{\Omega} \left( \oint Q \, dL - \oint Q_j \, dL \right) \tag{2.77} \\ &= \frac{1}{\Omega} \left( \begin{aligned} &\left( \frac{1}{2}(Q_1 + Q_2)n_{12} + \frac{1}{2}(Q_2 + Q_3)n_{23} + \frac{1}{2}(Q_3 + Q_4)n_{34} + \frac{1}{2}(Q_4 + Q_5)n_{45} + \frac{1}{2}(Q_5 + Q_1)n_{51} \right) \\ &\left( -Q_j(n_{12} + n_{23} + n_{34} + n_{45} + n_{51}) \right) \end{aligned} \right) \\ &= \frac{1}{\Omega} \left( \begin{aligned} &\left( \frac{1}{2}(Q_1 - Q_j)n_{12} + \frac{1}{2}(Q_2 - Q_j)n_{12} + \frac{1}{2}(Q_2 - Q_j)n_{23} + \frac{1}{2}(Q_3 - Q_j)n_{23} + \frac{1}{2}(Q_3 - Q_j)n_{34} \right) \\ &\left( + \frac{1}{2}(Q_4 - Q_j)n_{34} + \frac{1}{2}(Q_4 - Q_j)n_{45} + \frac{1}{2}(Q_5 - Q_j)n_{45} + \frac{1}{2}(Q_5 - Q_j)n_{51} + \frac{1}{2}(Q_1 - Q_j)n_{51} \right) \end{aligned} \right) \end{aligned}$$

$$\begin{aligned}
 &= \frac{1}{\Omega} \left( \frac{1}{2}(\varrho_1 - \varrho_j)(n_{12} + n_{51}) + \frac{1}{2}(\varrho_2 - \varrho_j)(n_{12} + n_{23}) + \frac{1}{2}(\varrho_3 - \varrho_j)(n_{23} + n_{34}) \right. \\
 &\quad \left. + \frac{1}{2}(\varrho_4 - \varrho_j)(n_{34} + n_{45}) + \frac{1}{2}(\varrho_5 - \varrho_j)(n_{45} + n_{51}) \right) \\
 &= \frac{1}{\Omega} \left( \frac{1}{2}(\varrho_1 - \varrho_j)(3 \times n_{ab}) + \frac{1}{2}(\varrho_2 - \varrho_j)(3 \times n_{bc}) + \frac{1}{2}(\varrho_3 - \varrho_j)(3 \times n_{cd}) \right. \\
 &\quad \left. + \frac{1}{2}(\varrho_4 - \varrho_j)(3 \times n_{de}) + \frac{1}{2}(\varrho_5 - \varrho_j)(3 \times n_{ea}) \right) \\
 &= \frac{1}{\Omega} \times 3 \times \frac{1}{2} \sum_{j=1}^5 (\varrho_i - \varrho_j) n \, dS \\
 &= \frac{1}{V} \times \frac{1}{2} \sum_{i=1}^5 (\varrho_i - \varrho_j) n \, dS
 \end{aligned}$$

Therefore, an approximation at the midpoint of the edge can be obtained as follows:

$$\overline{\nabla Q_y} = \frac{1}{2}(\nabla Q_i + \nabla Q_j) \tag{2.78}$$

It has been found that the two central differences in the above averaging relation will not damp high frequency modes and the dissipation in the inviscid flux is not sufficient to damp these especially in the boundary layer where the viscous effect is dominant. To overcome this, the face gradient is replaced with a simple difference along the edge [58]. Therefore, the face flux is given as follows

$$\nabla Q_y = \overline{\nabla Q_y} - \left( \overline{\nabla Q_y} \cdot \delta y - \frac{(\varrho_i - \varrho_j)}{|x_i - x_j|} \right) \delta y \tag{2.79}$$

where

$$\delta y = \frac{x_i - x_j}{|x_i - x_j|} \tag{2.80}$$

#### 2.4.4 Discretisation of turbulence model equations

The implementation of  $k-\varepsilon$  model into unstructured density-based algorithms gained popularity in the past decade after the success in solving the turbulence transport equations as a separate system from the mean flow equations. This

procedure has been reported by many researchers such as Kunz and Lakshminarayana [71], Stolics and Johnston [72] and Mavriplis and Martinelli [73]. In their studies, they found that despite the separation between the two systems, coupling can be retained through the eddy viscosity which is updated at each iteration of the solution. This procedure has been adopted into the Hydra solver since it has an advantage of providing code modularity for a range of turbulence models.

The discretisation of the turbulence transport equations is performed on the same control volumes used for the mean flow equations and the turbulence state vector is stored at the same locations as the mean flow state vector. The convective part of the flux vector for the system of turbulence model equations  $F_i^C$  is formulated in a similar manner to the mean flow equations; thus the discrete flux vector can be written as follows:

$$(F_i^C)_y = \frac{1}{2} \left[ \begin{array}{l} ((F_i^C)_y(Q_i)_i + (F_i^C)_y(Q_i)_j) \\ -|A_i|_y \left( -\frac{1}{3}(1-\Psi)(L_i^p(Q_i) - L_j^p(Q_i)) + \Psi((Q_i)_i - (Q_i)_j) \right) \end{array} \right] \quad (2.81)$$

where  $A_i = \frac{\partial F_i^C}{\partial Q_i}$  and which satisfies the relation

$$A_i = R|\Lambda|R^{-1} \quad (2.82)$$

$|\Lambda|$  and  $R$  are the eigenvalue and eigenvector matrices and are given as follows:

$$|\Lambda| = \begin{pmatrix} v.n & 0 \\ 0 & v.n \end{pmatrix}, R = \begin{pmatrix} \rho & 0 \\ 0 & \rho \end{pmatrix} \quad (2.83)$$

A linear-preserving pseudo-Laplacian is used to construct the fourth order dissipation term and is blended in with a second order dissipation term through the limiter  $\Psi$ . The limiter is based on the primitive form of the dependent flow variable  $\phi$  for each respective transport equation and is given by

$$\Psi = \min \left[ \varepsilon^{(2)} \left( \frac{|L_i^p(\phi)|}{|L_i^p(\phi)| + 2\phi_i} + \frac{|L_j^p(\phi)|}{|L_j^p(\phi)| + 2\phi_j} \right), 1 \right] \quad (2.84)$$

In the discretisation of the diffusive flux  $F_i^D$ , the cell face gradients for the turbulent quantities are evaluated using an analogous interpolation of the cell centre gradients to that given by Equation (2.79) for the mean flow variables. At the cell centres, gradients are evaluated in a similar manner to Equation (2.70) providing a consistent discretisation with the mean flow equations. Following the evaluation of the turbulence gradients at control volume faces, the discrete diffusive flux vector can then be computed from

$$F_i^D = \left( \mu + \frac{\mu_t}{\sigma_\phi} \right)_{ij} (\nabla Q_t)_{ij} n_{ij} \quad (2.85)$$

Where  $\sigma_\phi$  takes the appropriate value defined in equation (2.43) for the two transport equations  $k$  and  $\varepsilon$ . The eddy viscosity  $\mu_t$  is a function of  $k$  and  $\varepsilon$ . It is typical procedure to treat the eddy viscosity  $\mu_t$  as a constant quantity within each iteration (in fact it is function of  $k$  and  $\varepsilon$ ) in order to linearize the turbulent diffusive fluxes. The value of  $\mu_t$  is then evaluated before both transport equations are solved using the last computed values of  $k$  and  $\varepsilon$ .

In contrast with the mean flow equations, the turbulence transport equations contain source terms  $S_i$  that require an appropriate discretisation. The source terms are usually divided into two parts, a production (positive) term and a destruction (negative) term. Physically, these terms are responsible for the generation and destruction of turbulence in a given flow. The source terms are defined in Equation (2.46). The production term constitutes a product between different components of the Reynolds stress tensor and the velocity gradient. For  $k-\varepsilon$  model, the source term vector  $S_i = (S_k \ S_\varepsilon)^T$  can be written explicitly in the form

$$S_k = P_k - \rho \varepsilon \tag{2.86}$$

$$S_s = C_1 \frac{\varepsilon}{k} P_k - C_2 \rho \frac{\varepsilon^2}{k} \tag{2.87}$$

The cell centre gradients are available following the evaluation of the viscous fluxes. The required components are then used to evaluate  $P_k$  and hence the source terms. Consistent with the procedure adopted for the diffusive fluxes, the eddy viscosity is treated as a constant during the computation of the source terms which are calculated before either equation is solved.

## 2.5 Integration Scheme

### 2.5.1 Mean flow equations

The discretization of the Navier-Stokes equations described in the last subsection results in a set of coupled ordinary differential equations. A time integration scheme must be introduced to march the solution to a steady state. The Runge-Kutta time integration techniques can provide a high order of accuracy for nonlinear equations, and have proved very effective in practice. A detailed examination of these methods can be found in Hirsch [74], Gear [75], and Lambert [76]. Hirsch describes the Runge-Kutta method as a technique that evaluates the convective and dissipative flux gradients at several values of the state vector in the interval between  $n\Delta t$  and  $(n+1)\Delta t$  and then combines these in order to obtain a high-order approximation of the state vector at the  $(n+1)$  iteration. In this work, the explicit 5-stage Runge-Kutta iterative scheme introduced by Martinelli [77] has been employed. This scheme can be written as

$$\begin{aligned} Q_j^{(0)} &= Q_j^n \\ Q_j^{(k)} &= Q_j^n - \alpha_k \Delta t_j R_j^{(k-1)}, \quad k = 1, 2, 3, 4, 5 \\ Q_j^{n+1} &= Q_j^5 \end{aligned} \tag{2.88}$$

where

$$R_j^{(k-1)} = C_j(Q^{(k-1)}) - B_j^{(k-1)}$$

$$B_j^{(k-1)} = \beta_k D_j(Q^{(k-1)}) + (1 - \beta_k) B_j^{(k-2)} \quad (2.89)$$

$C_j(Q^{(k-1)})$  and  $D_j(Q^{(k-1)})$  are the inviscid and viscous contributions to  $R_j$ . The coefficients  $\alpha_k$  and  $\beta_k$  are

$$\alpha_1 = \frac{1}{4}, \alpha_2 = \frac{1}{6}, \alpha_3 = \frac{3}{8}, \alpha_4 = \frac{1}{2}, \alpha_5 = 1$$

$$\beta_1 = 1, \beta_2 = 0, \beta_3 = \frac{14}{25}, \beta_4 = 0 \text{ and } \beta_5 = \frac{11}{25} \quad (2.90)$$

The stability of the Runge-Kutta technique has been extensively studied by many researchers [78-80]. For hyperbolic problems, the maximum stability limit on the CFL number is  $(M-1)$  along the imaginary axis for an  $M$  stage scheme. Solutions of the Navier-Stokes equations exhibit a combination of hyperbolic behaviour in the main domain of the flow with parabolic behaviour in regions close to the surface boundary where the viscous terms are dominant. Thus in addition to stability along the imaginary axis which is needed for a hyperbolic problem, stability along the real axis is also needed. This scheme extends the stability region along the real axis by treating the convective and dissipative fluxes separately. It also has low computational cost since  $\beta_2$  and  $\beta_4$  are zero and therefore the inviscid and viscous contribution will not be computed in the second and fourth stages.

Increasing the time step would naturally accelerate the convergence of the time integration scheme but it is subjected to a limit defined by the stability region. The basic approach in Hydra to accelerate the convergence is to use a variable time step, where the state vector in each cell is advanced using a local time step  $\Delta t_j$  satisfying the stability limit for that cell. The limit can be calculated by taking the ratio of the cell volume to the sum of the spectral radii of the flux Jacobian matrices. For this purpose we need to determine the eigenvalues and spectral radii

$(\rho(A), \rho(B))$  of the inviscid and viscous Jacobians  $(\partial F^I / \partial Q, \partial F^V / \partial Q)$ . Therefore, the inviscid and viscous time steps can be calculated as follows

$$\Delta t_j^I = \frac{\sum_{i \in E_j} \rho(A_{ij}) \Delta s_{ij} + \sum_{k \in B_j} \rho(A_k) \Delta s_k}{V_j} \quad (2.91)$$

$$\Delta t_j^V = \frac{\sum_{i \in E_j} \rho(B_{ij}) \left[ \frac{1}{|x_i - x_j|} \right] \Delta s_{ij}}{V_j} \quad (2.92)$$

and the local time step is

$$\Delta t_j = \frac{CFL}{\max \left( \frac{1}{\Delta t_j^I}, \frac{\varepsilon^V}{\Delta t_j^V} \right)} \quad (2.93)$$

where  $CFL$  is the inviscid  $CFL$  number and  $\varepsilon^V = 0.5$  [58]

For very stiff problems with large variations in their eigenvalues such as reacting flows and high Reynolds number flows, explicit methods require a large number of iterations to converge. Although the cost per iteration is relatively small compared to other methods, the *CPU* time can still be excessive because so many iterations are required. This is a result of the relatively small time steps imposed by stability limits. However when incorporated as the driving scheme within a multigrid method explicit methods can be very effective [70]. Another class of methods which has proven to be very effective in dealing with stiff systems is to use a matrix time step or preconditioner which can improve the convergence rate without affecting the steady state solution. Both methods are employed in the Hydra solver and will be discussed in the following subsections.

### 2.5.2 Turbulence model equations

The turbulence transport equations are solved using the same integration procedure presented for the mean flow equations. The main difference between the

two systems of equations is due to the additional source terms in the turbulent system which needs special treatment within integration procedure. During solving the turbulence equations boundedness should be maintained such that negative turbulence quantities are not allowed since they lead to immediate solution failure. It has been found that the explicit treatment of the source terms may lead to negative updates during the solution particularly in regions where the source terms are dominant and the dissipation is larger than production. Therefore, special treatment should be given to the source terms by using an implicit treatment rather than the explicit. To illustrate the procedure a single stage explicit scheme is used as a starting point

$$\Delta Q_i^n = -\Delta t . R_i(Q_i)^n \tag{2.94}$$

with

$$R_i(Q_i) = \sum_{j \in E_i} (F_i^C - F_i^D)_{ij} \Delta S_{ij} - S_j \Omega_j \tag{2.95}$$

The source terms are local in nature since they do not provide spatial coupling as the fluxes. Any implicit treatment of the source terms therefore results in a point implicit discretisation. A point implicit method, such as the block-Jacobi preconditioner is applicable to explicit schemes [25]. Therefore, the use of such a method in the source terms treatment does not introduce any further complications for the turbulence equations; equation (2.94) is then modified to be as follows:

$$\left[ I - \Delta t \left( \frac{\partial S_i}{\partial Q_i} \right) \right] \Delta(Q_i)^n = -\Delta t . R_i(Q_i)^n \tag{2.96}$$

which can be written in terms of  $Q_i^{n+1}$ :

$$\left[ I - \Delta t \left( \frac{\partial S_i}{\partial Q_i} \right) \right] \Delta(Q_i)^{n+1} = \left[ I - \Delta t \left( F_i^C - F_i^D - \left( S_i - \frac{\partial S_i}{\partial Q_i} \right) \right) \right] Q_i^n \tag{2.97}$$



To ensure positivity for a scheme such as the above one, the left hand side matrix operator on the vector  $(Q_i)^{n+1}$  must be an M-type matrix which is defined as one that is diagonally dominant with positive diagonal elements and negative or zero off diagonal elements [81]. In addition, a positive matrix operator is required on the vector  $Q_i^n$  on the right hand side.

The source Jacobians can now be chosen to ensure that the source term contributions to the matrix operators satisfy the conditions required to yield an M-type matrix. No guarantee can be provided however as to the positivity of the complete matrix operator on the right hand side as additional flux contributions are not accounted for by any implicit treatment. To compensate for the explicit treatment of the fluxes, the source Jacobians are multiplied by a scaling matrix  $\Gamma$ . A detail of how this is chosen depends on the form of the Jacobian and is given later. In the current implementation, a diagonal Jacobian is chosen as shown in Equation (2.98). This choice decouples the two turbulent equations thus simplifying the positivity analysis as each turbulent transport equation can be considered separately.

$$\frac{\partial S_k}{\partial Q_p} = \begin{pmatrix} \frac{\partial S_k}{\partial k} & \frac{\partial S_k}{\partial \epsilon} \\ \frac{\partial S_\epsilon}{\partial k} & \frac{\partial S_\epsilon}{\partial \epsilon} \end{pmatrix} = \begin{pmatrix} \frac{\partial S_k}{\partial k} & 0 \\ 0 & \frac{\partial S_\epsilon}{\partial \epsilon} \end{pmatrix} \tag{2.98}$$

To evaluate the terms  $(\partial S_k / \partial k)$  and  $(\partial S_\epsilon / \partial \epsilon)$  in the above equation, the dissipation term in the turbulent kinetic energy equation is expressed in terms of  $k$  through the eddy viscosity relation (2.44). The resulting expression for the negative part of the source terms in the turbulent kinetic energy equation is

$$S_k^- = -C_\mu \frac{\rho k^2}{\mu_t} - \max \left[ 0, 0, \left( \frac{2}{3} (\nabla \cdot v) \rho k \right) \right] \tag{2.99}$$

Treating  $\mu_t$  as a constant,

$$\begin{aligned} \frac{\partial S_k}{\partial(\rho k)} &= -2C_\mu \frac{k}{\mu_t} - \max\left[0.0, \left(\frac{2}{3}(\nabla \cdot v)\right)\right] \\ &= -\frac{2\varepsilon}{\rho k} - \max\left[0.0, \left(\frac{2}{3}(\nabla \cdot v)\right)\right] \end{aligned} \tag{2.100}$$

Similarly,

$$S_\varepsilon^- = -C_2 \frac{\rho \varepsilon^2}{k} - C_1 \frac{\varepsilon}{k} \max\left[0.0, \left(\frac{2}{3}(\nabla \cdot v)\rho k\right)\right] \tag{2.101}$$

$$\frac{\partial S_\varepsilon}{\partial(\rho \varepsilon)} = -2C_2 \frac{\varepsilon}{k} - C_1 \max\left[0.0, \left(\frac{2}{3}(\nabla \cdot v)\right)\right] \tag{2.102}$$

The scaling matrix  $\Gamma$  can now be chosen to guarantee the update  $\Delta Q_i$  does not produce negative values of  $k$  and  $\varepsilon$ . Numerical problems regarding positivity of the turbulence variables will generally arise only when

$$R_i(\phi) > \frac{\partial S_\phi}{\partial \phi} \tag{2.103}$$

where  $\phi$  represents either  $k$  or  $\varepsilon$ . The source Jacobians must therefore be multiplied by the scaling factors when this condition arises. If the condition given by Equation (2.103) does not arise, the scaling factors are set to unity to prevent a degrading in convergence rate. It is possible to trigger the use of the scaling factors under these circumstances through

$$\Gamma = \begin{pmatrix} \max\left(1.0, \varepsilon^{(4)} \frac{-R(\rho k)^n}{\left(\frac{\partial S_k}{\partial(\rho k)}\right)^n}\right) & 0 \\ 0 & \max\left(1.0, \varepsilon^{(4)} \frac{-R(\rho \varepsilon)^n}{\left(\frac{\partial S_\varepsilon}{\partial(\rho \varepsilon)}\right)^n}\right) \end{pmatrix} \tag{2.104}$$

$\varepsilon^{(4)}$  is a user defined value that is  $> 1$  to provide updates that satisfy the strict inequality

$$|\Delta Q_i^n| < |Q_i^n| \tag{2.105}$$

A value of 1.5 is used in the current work. The above arguments are valid for a single stage scheme. For a multi-stage Runge-Kutta scheme, the resulting time integration can be written as

$$\begin{aligned} Q_i^{(0)} &= Q_i^n \\ \left[ I - \alpha_k \Delta t (\Gamma^k \frac{\partial S_i}{\partial Q_i}) \right] Q_i^{(k)} &= Q_i^n - \alpha_k \Delta t \left[ F_i^C - F_i^D - (S_i - \Gamma^k \frac{\partial S_i}{\partial Q_i}) \right] Q_i^{(k)} \\ Q_i^{n+1} &= Q_i^{(5)} \end{aligned} \tag{2.106}$$

Rearranging the second step yields

$$\left[ I - \alpha_k \Delta t (\Gamma^k \frac{\partial S_i}{\partial Q_i}) \right] Q_i^{(k)} = \left[ I - \alpha_k \Delta t (F_i^C - F_i^D - (S_i - \Gamma^k \frac{\partial S_i}{\partial Q_i})) \right] Q_i^n \tag{2.107}$$

Where

$$Q_r = \begin{pmatrix} \frac{(\rho k)^{(k)}}{(\rho k)^n} & 0 \\ 0 & \frac{(\rho \varepsilon)^{(k)}}{(\rho \varepsilon)^n} \end{pmatrix} \tag{2.108}$$

This form is similar to that found in the single stage scheme. To guarantee positivity with the multi-stage scheme, the following modification to the Jacobian matrix is required

$$\frac{\partial S_i}{\partial Q_i} = \begin{pmatrix} -\frac{2\varepsilon}{\rho k} - \max \left[ 0.0, \left( \frac{2}{3} \nabla \cdot v \right) \right] & 0 \\ 0 & -2C_2 \frac{\varepsilon}{\rho k} - C_1 \max \left[ 0.0, \left( \frac{2}{3} \nabla \cdot v \right) \right] \end{pmatrix} Q_r \tag{2.109}$$

### 2.7 Preconditioning

The disadvantage of the local time step approach is that the different speeds of characteristics waves will cause the CFL condition to restrict the evolution of the slower waves in order to satisfy the stability requirement for the faster waves. To accelerate the solution convergence in Hydra, a block-Jacobi local preconditioner has been implemented [58]. This numerical preconditioner constructs a matrix which has the effect of clustering the eigenvalues of the residual spatial operator in a region of the complex plane where the iterative method has good damping properties. To illustrate the preconditioner, consider the characteristics time step (matrix time step)

$$P = \begin{pmatrix} \Delta t_k & 0 & 0 & 0 & 0 \\ 0 & \Delta t_k & 0 & 0 & 0 \\ 0 & 0 & \Delta t_k & 0 & 0 \\ 0 & 0 & 0 & \Delta t_k & 0 \\ 0 & 0 & 0 & 0 & \Delta t_k \end{pmatrix} \quad (2.110)$$

where  $\Delta t_k \leq \frac{\Delta s}{|\lambda_k|}$  and  $\lambda_k$  is the  $k$ th eigenvalue of Jacobian matrix  $A$

By using this time step, the stiffness in characteristics speeds is overcome by advancing each of the characteristic waves separately using a CFL condition based on the corresponding characteristics speed.

The preconditioner  $P^{-1}$  can be introduced into equation (2.49) as follows

$$P^{-1} \frac{\partial Q}{\partial t} + R = 0 \quad (2.111)$$

which can be presented as

$$\frac{\partial Q}{\partial t} + PR = 0 \quad (2.112)$$

If we decompose equation (2.112) into characteristic fields using the eigenvector matrices  $T^{-1}$  and  $T$  of the flux Jacobian we get

$$T^{-1} \frac{\partial Q}{\partial t} + T^{-1} R = 0 \tag{2.113}$$

Let  $T^{-1} \partial Q = \partial \Omega$ , the residual  $R$  is split into contributions of the characteristics components of  $\Omega$ . Therefore,  $\Omega_k$  can be updated indivisually using separate CFL conditions based on the corresponding  $\lambda_k$ . Therefore

$$(\Omega_k^{n+1} - \Omega_k^n) = -\Delta t_k T^{-1} R \tag{2.114}$$

To obtain the overall updating procedure of the system, the above equation is multiplied by  $T$  to transfer back from  $T$  to  $Q$

$$\begin{aligned} T \frac{\partial \Omega}{\partial t} &= \frac{\partial Q}{\partial \Omega} \frac{\partial \Omega}{\partial t} = \frac{\partial Q}{\partial t} \\ (Q^{n+1} - Q^n) &= -T [\Delta t]_{char} T^{-1} R \\ (Q^{n+1} - Q^n) &= -T \left[ \frac{\Delta s}{|\Lambda|} \right] T^{-1} R \\ (Q^{n+1} - Q^n) &= -T |\Lambda|^{-1} T^{-1} \Delta s R \\ (Q^{n+1} - Q^n) &= -|A|^{-1} \Delta s R \end{aligned} \tag{2.115}$$

In the above equation,  $|A|^{-1}$  is the inviscid contribution for the preconditioner,  $P^i$ , or  $(P^i)^{-1} = |A|$ . Similarly, the viscous contribution is derived as in the above procedure by replacing the matrix  $A$  for inviscid part by matrix  $B$  for viscous part and using the corresponding eigenvectors and eigenvalues matrices of the viscous part. The matrix preconditioner has a contribution form the inviscid and viscous fluxes at each node locally.

$$P_j^{-1} = (P_j^i)^{-1} + (P_j^v)^{-1} \tag{2.116}$$

the inviscid and the viscous contributions are

$$(P_j^i)^{-1} = \frac{1}{2V_j} \left( \sum_{i \in E_j} |A_i| \Delta s_i + \sum_{k \in B_i} |A_k| \Delta s_k \right) \tag{2.117}$$

$$(P_j^v)^{-1} = \frac{1}{V_j} \sum_{i \in E_j} B_i M^{-1} \frac{1}{|x_j - x_i|} \Delta s_i \tag{2.118}$$

where the matrices  $B$  and  $M$  are given in Appendix  $A$

The block-Jacobi preconditioner matrix is computed and inverted for each cell before the first stage of each time step. The residual vector  $R$  is then multiplied by  $P$  at each stage of Runge-Kutta scheme. This procedure has been modified by Moinier and Giles [82] to deal with low Mach numbers as it has been found that the disparity between the acoustic and convective wave speeds cannot be adequately handled by the current approach and convergence slowdown is observed. Further details about low Mach preconditioner can be found in Moinier thesis [58].

### 2.8 Multigrid Method

Multigrid methods are another class of schemes which are effective in solving stiff systems of equations by using a sequence of coarser grids to accelerate the convergence of the solution on the fine grid. The concept of the multigrid method is based on the observation that point explicit solvers such as the multi-stage Runge-Kutta scheme are very effective at eliminating the high frequency errors in the solution on any given mesh [83]. They are much less effective at eliminating the low frequency errors on that mesh. The multigrid method accelerates the reduction of the low frequency errors by using a sequence of progressively coarser meshes. Low frequency error modes on the fine mesh become higher frequency modes on the coarser meshes and so are more effectively reduced by the point explicit solver

or smoother in multigrid terminology. The cycle begins by taking a time step on the fine grid and then interpolating the solution and the residual to the next coarser grid. Usually a simple explicit method is used for the time advancement on the various grids. On the coarse grid, a slightly modified version of the problem involving a forcing function derived from the fine grid residuals is then advanced one time step. This process is repeated recursively until the coarsest grid in the sequence is reached. At that point, the solution corrections from the coarse grids are interpolated back to the fine grid where the solution is updated. As the grids in the sequence become progressively coarser, the allowable time step becomes larger because the element size increases. At the same time the amount of work decreases because there are fewer grid points. These two features combine to produce a very efficient computational method.

On a structured grid, the construction of the coarse grids is straightforward; they are formed by simply removing every other mesh line in each direction. This has the advantage that the interpolation operators between the grids can be easily constructed. On an unstructured grid, the construction of the coarse grids is not as straightforward. Methods have been developed which use a set of independently generated, non-nested grids [73]. Because it is not always easy to generate really coarse grids, particularly for complex three dimensional geometries, a better alternative is to create the coarse grid cells by agglomerating cells from the fine grid [84]. The agglomeration procedure has been shown to provide multigrid convergence rates comparable to those obtained using independent non-nested coarse grids. Recently, this approach has been extended to handle mixed-element meshes [85]. The agglomeration method has been selected for use in Hydra, which also, as part of the grid collapse procedure, adopts an automatic point removal algorithm to generate coarse grids from the initial fine grid [58, 86]. The resulting grid sequence can be used by any grid based algorithm, including those which use an edge-based data structure.

## 2.9 Boundary Conditions

The solution of the Navier-Stokes equations is driven by the initial and boundary conditions. The discretised flow model must therefore be completed by suitable boundary conditions. Various boundary conditions have been developed for Hydra solver to suit a wide range of compressible fluid dynamics applications, and the options available in the Hydra solver at the start of the present project are briefly described here.

### 2.9.1 Free stream boundary condition

The free stream boundary condition is appropriate where a supersonic free stream flows enter the domain. However, it can be applied to subsonic flows in some cases where the subsonic boundary is far enough from any flow disturbances such as solid surfaces. Implementing the free stream boundary condition in Hydra involves defining the state vector  $Q_\infty$  by specifying the free-stream density, static pressure, Mach number and flow direction angles [53]. Therefore, the boundary conditions are imposed in a weak form through the inviscid flux term given by equation (2.65). The boundary flux  $F_k$  is evaluated by solving the Riemann problem

$$F_k = \frac{1}{2} (F_k^l(Q_k) - F_k^l(Q_\infty) - |A_k|(Q_k - Q_\infty)) \quad (2.119)$$

### 2.9.2 Solid walls and symmetry boundary conditions

Viscous effects imply that the flow velocity at the wall must be equal to zero (no-slip condition) for a stationary wall ( $V_{wall} = 0$ ). For a slip wall and planes of symmetry, a vanishing normal velocity component is enforced  $(V.n)_{wall} = 0$ . Furthermore, an adiabatic wall assumption implies that the heat flux through the wall also equals zero. Therefore, the following boundary conditions are applied at a wall



$$(q.n)_{wall} = 0 \tag{2.120}$$

where  $n$  is the unit vector normal to the wall.

Inside a boundary layer growing on a solid wall, the local Reynolds number in the viscous sub-layer region adjacent to the wall is low. Therefore, the high Reynolds number  $k - \varepsilon$  model used in Hydra cannot be integrated down to this region. To overcome this limitation standard wall functions based on the well-known "law of the wall" approach are used [87]. With wall functions the viscous sub-layer is bridged by employing empirical formulae to provide near-wall boundary conditions for the mean-flow and turbulence transport equations. These formulae therefore connect the wall conditions to the dependent variables at the near-wall grid node [25, 88]. This first grid node is presumed to be located outside the viscous sub-layer in fully turbulent fluid. The wall shear stress, production of turbulent kinetic energy and the dissipation at near wall grid nodes are set as follows

$$\tau_w = \frac{\rho u C_\mu^{1/4} k^{1/2}}{\frac{1}{\kappa} \ln(Ey^+)} \tag{2.121}$$

$$P = \frac{\rho u C_\mu^{1/2} k}{y \ln(Ey^+)} \tag{2.122}$$

$$\varepsilon = \frac{C_\mu^{3/4} k^{3/2}}{\kappa y} \tag{2.123}$$

where  $y^+$  is non-dimensional distance to the wall given as

$$y^+ = \frac{y C_\mu^{1/4} k^{1/2}}{\nu} \tag{2.124}$$

and  $E=8.8$  is the wall function constant,  $\kappa = 0.41$  is the von-Karman constant.

In addition, the value of turbulence kinetic energy at the wall itself is set to zero so that

$$k_{wall} = 0 \quad (2.125)$$

Wall functions approach is valid when the flow near the wall is predominantly parallel to the wall and the effects of body forces are small and the boundary layer is close to equilibrium. If this is fulfilled then the shear stress and the heat flux are very nearly constant and equal to the corresponding values of these quantities at the wall. It becomes less appropriate when there is significant departure from local one-dimensionality in the near-wall region. Such a case can be found near points of separation, reattachment, and stagnation, and in other situations involving strong acceleration or body forces.

In cases where the viscous effects vanish and the boundary layer is not presented, the above assumptions are not applicable and the wall may be considered as an inviscid wall (slip condition). In this case, the boundary flux given by  $F_k$  in equation (2.119) is set to zero. In addition, the normal momentum component is set to zero and its contribution to the residual is explicitly removed. Thus any updates on the state vector will not change the normal velocity component on this boundary. These assumptions are also valid for symmetry plane which can be considered as an inviscid wall.

### **2.9.3 Subsonic inflow/outflow boundary condition**

The subsonic inflow boundary condition is specified via fixed values of inlet total pressure, total temperature and flow angles [53]. The basic methodology used in implementing this boundary condition is then similar to the free-stream boundary condition. Rather than using the Riemann problem approach given above, an alternative state vector is used which is evaluated from user-specified inlet properties. The procedure starts by extrapolating static pressure from the interior

cell and then using the isentropic relationship to calculate the boundary temperature. Once static temperature and pressure are determined, the density can be calculated by using the equation of state. The flow velocity is then determined by calculating the Mach number, and the specified flow angle is maintained to determine the individual velocity components. At a subsonic outflow boundary, the boundary static pressure is specified and held constant at the domain exit, corresponding to the single incoming characteristic. The other flow variables are set equal to those of the first interior cell. The implementation is essentially the same as that used for the inlet conditions.

#### **2.9.4 Periodic boundary condition**

In cases of periodicity (e.g. where one blade passage only is considered), it is sufficient to consider only one repeating sector of the domain which is advantageous to mesh size and simulation time. The periodic planes must be identically meshed. Hydra treats the flow at a periodic boundary as if the opposing periodic plane were a direct neighbour to the cells adjacent to the first periodic boundary. Thus, when calculating the flow through the periodic boundary adjacent to a fluid cell, the flow conditions at the fluid cell adjacent to the opposite periodic plane are used

#### **2.10 Flow Solver Overview**

Hydra, a three-dimensional RANS compressible flow solver, is a key element in the HYDRA user suite which is designed within Rolls-Royce to perform CFD simulation and optimisation for various external and internal flow systems [28, 29]. In addition to the flow solver, the main elements of the user suite are: (a) JM52, a primary preprocessing tool for the HYDRA suite; (b) JM54, an unstructured multigrid level generator [89]; (c) JM56, which is used for multi-passage and multi-stage turbomachinery applications including casing treatment; and (d) Spy and JL09, post-processor tools based on Visual 3 [90]. The schematic diagram in Figure 2.5 illustrates the interaction between the above codes based on the solution

sequence adopted in this study. JM52 is used to translate meshes generated using a number of in-house and commercial software packages from the initial natural mesh format used by these packages into a standard Hydra format for subsequent use in JM54 and the Hydra flow solver; it also performs diagnostics checks for negative cell volumes, mesh periodicity, cell connectivity and for point redundancy. JM52 is also used to initialise the flow data and define boundary condition as well as solution control parameters such as number of iterations, convergence criterion, CFL number, number of multigrid levels (generated within JM54) and number of multigrid cycles; input for these parameters comes from user supplied files. JM54 is used to create a multigrid sequence of grids for the flow solver. It is also used to compute the edge connectivity and weights (i.e. face areas) for each mesh in the multigrid sequence and so is needed even when the code is being run on a single grid level. The Hydra flow solver is now ready to perform the simulation in sequential or parallel mode according to the flowchart shown in Figure 2.6. Solution starts by reading in mesh, initial and boundary conditions, followed by the solution control parameters prepared by JM52 and JM54. After this, a time-marching procedure starts to compute the flow field variables by first updating the boundary conditions and then computing the residual vector by calculating and summing the convective and diffusive fluxes. A 5x5 block-Jacobi preconditioner is then computed and inverted for each node before the start of each time step. The residual vector is then multiplied by the preconditioner at each stage of the 5-stage Runge-Kutta integration scheme. The solution is considered converged when the residual values fall below the convergence criterion or it will stop when the maximum number of steps specified by the user is reached. The flow solver has an option for a low Mach number preconditioner to improve the convergence of cases with very low speed. The multigrid technique is another option to accelerate the solution convergence. For post-processing, there are two post-processors available for Hydra. Both are based on the Visual 3 graphics library developed at MIT. The first is Spy which is linked directly with the core routines of Hydra and so gives access to some of the internal parameters used by

Hydra. The second is JL09 which is a stand-alone package which reads a range of solution formats, including Hydra. Spy is maintained because it has a number of capabilities that are not available in JL09 such as accessing number of data arrays (e.g. y+) that are not currently available within JL09.

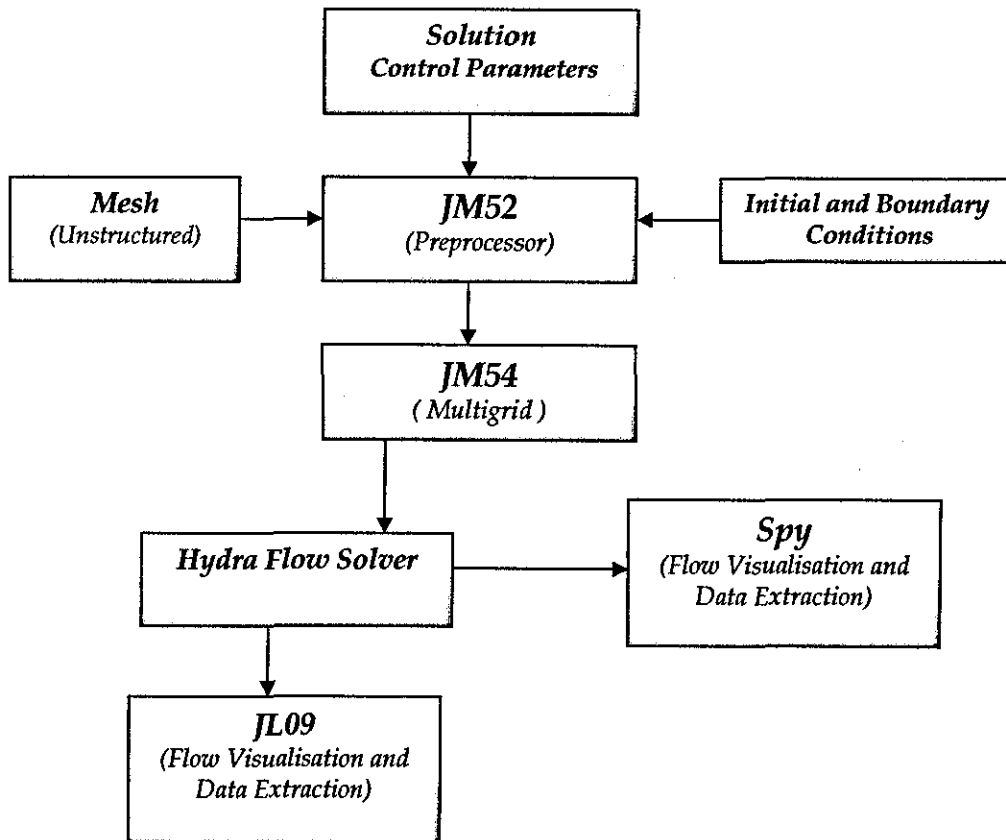


Figure 2.5 Schematic representation of Hydra user suit

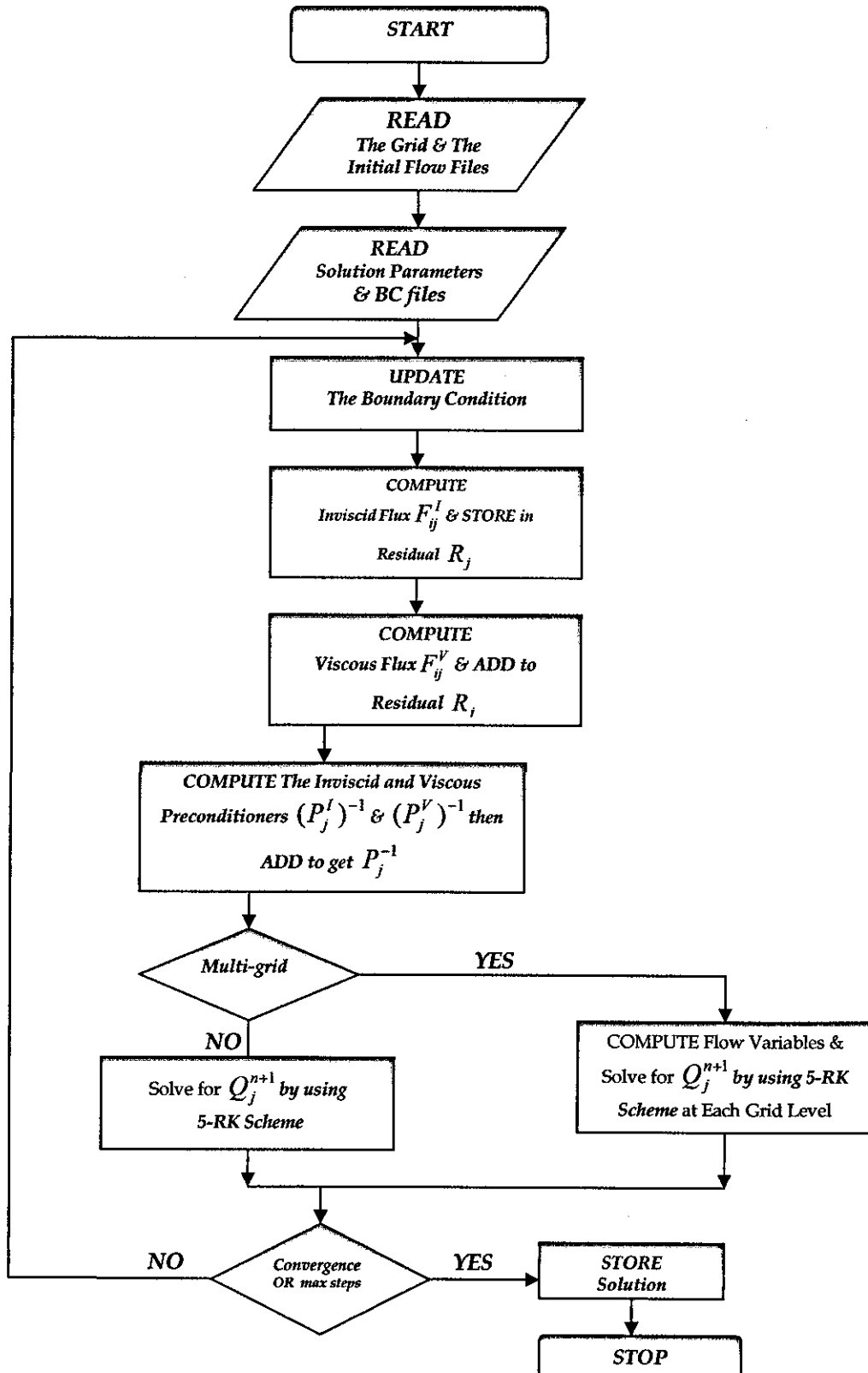


Figure 2.6 Flowchart of Hydra nonlinear solver

# Chapter 3

## Modifications to the Basic Hydra Code

### 3.1 Introduction

In a real gas-turbine combustor, flows are three-dimensional, multi-phase, turbulent, chemically reacting and radiating. To model such flows numerically, a computer code must in principle deal with all of these effects simultaneously which is an extremely costly task. It is difficult but not impossible to separate these effects to assess individual physical model performance. The most reasonable approach to model validation is to divide the real flow into a number of well controlled component flows that include only one or two of the above physical processes at the same time. The complete code may be assessed by verification of the individual flow elements of which the overall analysis is composed. A commonly used approach is to divide the modeling of combustor flow into two main areas, non-reacting (cold) flow modeling and reacting (hot) flow modeling. The main target of the cold flow investigation is to get insight into the main aerodynamic features responsible for the efficient mixing processes inside the combustor whilst in the reacting flow the investigation is extended to the combustion process itself and its interaction with the aero-thermodynamics of the flow.

To validate the physical modeling, experiments are needed in the areas of combustion reactions and kinetics, thermal radiation, liquid fuel sprays, fluid

mechanics, and soot radiation. The combustion models can only be evaluated after the accuracies of the turbulent isothermal models have been established. Through the use of experiments it has been demonstrated in the literature that the calculated flow fields can be significantly changed by different sets of assumed inlet boundary conditions. This point is of significance in the context of the current work is that the typical inlet/outlet conditions used in turbomachinery codes such as Hydra (fixed total pressure at inlet, fixed static pressure at outlet) are not really suitable for combustor flow applications where fixed velocity at the various inlets to the combustor is more typical in order to fix the flow split. The inlet boundary conditions have been noted to be of great importance in determining the quantitative accuracy of the calculations [91].

Furthermore, the type of periodic boundary condition coded into Hydra is again restricted on its applications to turbomachinery flow cases. In particular it does not allow for the presence of a centreline because in turbomachinery (especially in axial compressors, fans and turbines) flows are limited to an annulus between two cylindrical bodies extending from blade root to the outer casing as shown in Figure 3.1. Therefore, periodic boundary plane pairs never intersect each other, and this has been hard coded as the way the Hydra solver treats periodic boundary conditions. In combustor flows the situation is different, a centreline boundary condition is essential because the geometry often contains a boundary plane pair which coincides at a centreline. Therefore, to extend Hydra capabilities towards modelling gas turbine combustor flow a vital first step was to introduce suitable velocity inlet and centreline boundary conditions. This would then allow application of Hydra to combustor-relevant aerodynamic problems, but is not sufficient to allow application to combustion flow. To enable this, the necessary second step was to include transport equations and a combustion sub-model that would allow variable density turbulent reacting flows to be predicted. The contributions and code modifications in these areas are described in the following sections.



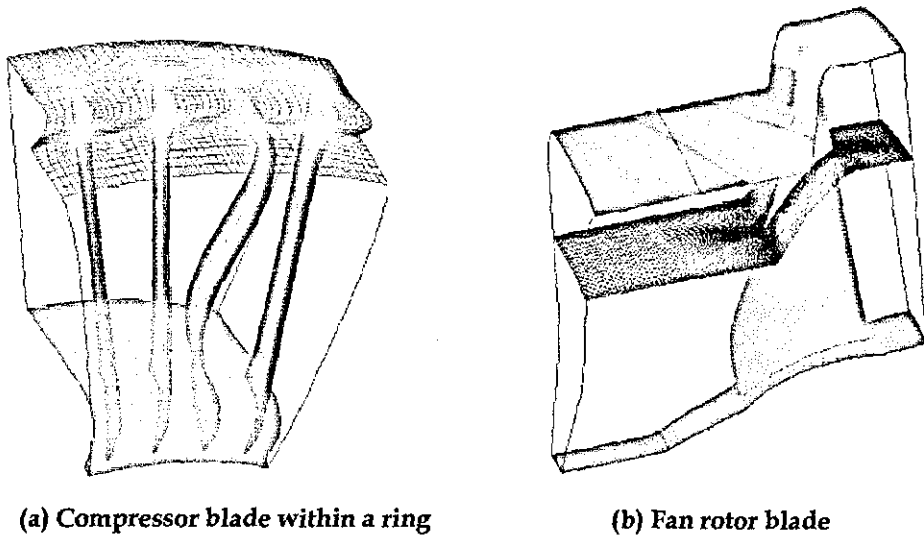


Figure 3.1 Periodicity in turbomachinery [26]

### 3.2 Fixed Velocity Inlet Boundary Condition

A robust and flexible numerical methodology for the implementation of boundary conditions is required to formulate a well-posed problem at the inlet. A boundary condition should be if possible non-reflecting to avoid spurious perturbations that can induce unsteadiness or instabilities. In the case of compressible flows, it is therefore natural to formulate boundary condition treatments in terms of characteristic variables. Whenever a perturbation approaches a boundary and is not in agreement with the imposed boundary conditions, it generates noise which propagates in principle both externally and into the interior. This transmission reflection process is governed by the coupling of the boundary condition treatment with the incoming signal, and the use of characteristic variables ensures this is treated in the best possible way, predicting the smallest possible spurious disturbances.

In aerodynamics applications, inlet flow can be either supersonic or subsonic. For a supersonic inlet, any propagating information should not be able to reach the inlet boundary (all characteristics point into the solution domain, all eigenvalues are

positive) and all of the flow variables must be prescribed. The total temperature, the total pressure (or the entropy), and the inlet Mach number are usually assigned. In the case of subsonic flows (eigenvalues of mixed signs) there are three different approaches to deal with a subsonic inlet boundary. The first approach (total condition approach) is the specification of total pressure, total temperature and the flow direction angle at the inlet with the extrapolation of the static pressure at the inlet from the value predicted just inside the domain. This approach is commonly used in turbomachinery applications and nozzle flows [92]. In the second approach here called (RINV), Riemann invariants are used to calculate the velocity at the inlet boundary. Constant entropy is assumed from its value upstream of the inlet boundary, and this is used to determine the inflow temperature, pressure and density. This approach has gained popularity in internal flow applications where velocity profiles need to be fixed [91]. The final approach here called (VIN) is to set only velocity and temperature at the inflow and is fairly common in low speed viscous flow applications [58,92]. The last two approaches have been implemented into Hydra for application to combustor flow inlet boundary treatment where velocity profiles (e.g. extracted from experimental work) need to be fixed.

The reflectiveness of various boundary conditions and the mechanism of reflection of an incident perturbation have been subject of research for a long time [92-97]. Dramofal et al. [92] tested the above three subsonic boundary condition approaches at different subsonic Mach numbers with and without different preconditioning techniques. They noticed different behaviour in the reflectiveness and convergence rate between the different approaches. They concluded that boundary conditions based on Riemann invariants are found to be reflective in conjunction with preconditioning at low Mach numbers while they were nonreflective without preconditioning. The total condition boundary treatment was found to be nonreflective both with and without preconditioning. Dramofal et al. also concluded that a reflective inflow condition may significantly slow

convergence compared to non-reflecting boundary conditions. Motivated by well-posedness requirements of inverse design methodologies, Ferlauto et al. [94] investigated the mechanism of reflection of an incident perturbation through an analysis of the characteristic wave system in the proximity of the flow field boundary. They defined a parameter, the ratio of the incident and reflected signal strengths, to measure the reflectiveness of various boundary conditions. They tested both total condition and RINV boundary conditions in turbine blade and fan stage design. Their numerical experiments suggested that inverse problems using the conventional total condition boundary condition were solved faster than when using the RINV. This conclusion is in contrast with the conclusion of Dramofal et al. Conversely, RINV boundary conditions enhanced the robustness and required a lower computational effort. It seems from previous work that the RINV type of boundary condition may be more generally applicable and more computationally efficient, hence this was the first inlet condition treatment considered.

### 3.2.1 Riemann invariant boundary condition (RINV)

From one dimensional characteristic theory, Riemann invariants are known to be constant along both forward and the backward moving characteristics. A plus sign is here used to denote the forward moving wave whilst a minus sign denotes the backward moving wave, the corresponding Riemann invariants are:

$$R^{\pm} = u \pm \frac{2a}{\gamma - 1} \quad (3.1)$$

As it can be seen from Figure 3.2, the forward moving wave originates in the inlet stream (IN) and the backward moving wave from the interior (2). This will give the following two equations to determine the boundary velocity,  $u_1$ , and the speed of sound  $a_1$ ,

$$R_{IN}^{+} = u_{IN} + \frac{2a_{IN}}{\gamma - 1} = u_1 + \frac{2a_1}{\gamma - 1} \quad (3.2)$$

$$R_2^- = u_2 - \frac{2a_2}{\gamma - 1} = u_1 - \frac{2a_1}{\gamma - 1} \quad (3.3)$$

Solve the above two equations to obtain

$$u_1 = \frac{R_{IN}^+ + R_2^-}{2} \quad (3.4)$$

$$a_1 = \frac{\gamma - 1}{4} (R_{IN}^+ - R_2^-) \quad (3.5)$$

To solve for other flow variables at the boundary, the entropy at the inlet boundary can be set to be equal to the entropy in the inlet stream:

$$s_1 = \frac{P_{IN}}{\rho_1^\gamma} \quad (3.6)$$

The density at the boundary,  $\rho_1$ , can then be determined as follows:

$$\rho_1 = \left( \frac{a_1^2}{\gamma s_1} \right)^{\frac{1}{\gamma - 1}} \quad (3.7)$$

From the density and speed of sound the pressure at the boundary can be determined as follows:

$$p_1 = \frac{a_1^2 \cdot \rho_1}{\gamma} \quad (3.8)$$

Initially, we need to set the inlet velocity,  $u_{IN}$ , temperature  $T_{IN}$  and pressure  $p_{IN}$ . In each iteration the above procedure will be implemented to update the primitive variables at the boundary.

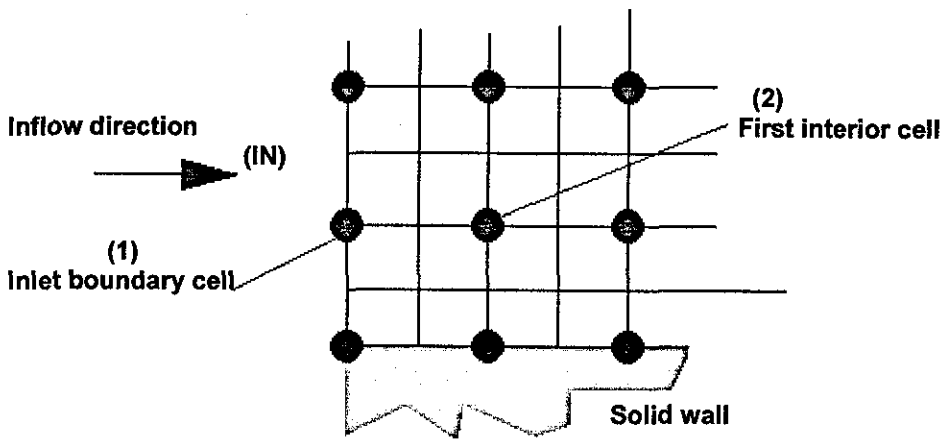


Figure 3.2 Nomenclature used with the velocity inlet boundary condition

### 3.2.2 Velocity and temperature boundary condition (VIN)

This type of boundary condition is used mainly for subsonic flow with low Mach number [92]. Only the velocity,  $u_{IN}$ , and temperature,  $T_{IN}$ , are prescribed at the inlet. Therefore, the speed of sound, Mach number and total temperature can be calculated as follows:

$$a_{IN} = \sqrt{\gamma \cdot R \cdot T_{IN}} \quad (3.9)$$

$$M_{IN} = \frac{u_{IN}}{a_{IN}} \quad (3.10)$$

$$T_0 = T_{IN} \left( 1 + \frac{(\gamma - 1)}{2} M_{IN}^2 \right) \quad (3.11)$$

Extrapolate the density from the interior and then calculate the total density and total pressure as follows:

$$\rho_0 = \rho_1 \left( 1 + \frac{(\gamma - 1)}{2} M_{IN}^2 \right)^{\frac{1}{(\gamma - 1)}} \quad (3.12)$$

$$P_0 = \rho_0 \cdot R \cdot T_0 \quad (3.13)$$

The static pressure at the boundary now can be calculated,

$$p_1 = P_0 / \left(1 + \frac{(\gamma - 1)}{2} M_{IN}^2\right)^{\frac{\gamma}{\gamma - 1}} \quad (3.14)$$

This procedure will enable to determine the primitive variables at the boundary and update them during the solution.

### 3.2.3 Validation test case

The above two methods have been tested on a convergent-divergent nozzle test case with subsonic inlet and outlet flow. The nozzle length is  $L = 200$  mm and the inlet and outlet diameters are  $\phi_{IN} = 40$  and  $\phi_{OUT} = 50$  mm respectively, while the throat diameter is  $\phi_T = 38.1$  mm and located 30 mm downstream of the inlet. The rate of area variation along the nozzle is relatively low in order to keep the flow as close as possible to 1-D flow and therefore make the comparisons with the isentropic 1-D exact solution reasonable. The numerical grid is a tetrahedral type with prismatic layers on the wall to resolve the boundary layer as shown in Figure 3.3.

The Riemann invariant boundary condition RINV has been tested at two different inlet velocities. In both cases the inflow air pressure and temperature were 100000 Pa and 300 K respectively. The inlet velocities were 40 m/s in the first case and 100 m/s in the second. The flow was turbulent with Reynolds number of approximately 100,000 and 250,000 for the above two cases respectively. The velocity and temperature inlet boundary condition VIN was also tested with the same two inlet velocities and temperature. At the exit, the corresponding static pressure, based on isentropic flow relations solution, was prescribed. In all cases the solutions were initialized with the inlet conditions in order to test the ability of the boundary condition to deal with severe initial conditions. Figure 3.4 shows the Mach number contours for the solution obtained using RINV boundary condition, while Figure 3.5 shows the solutions obtained using VIN boundary condition. The

velocity and Mach number distributions along the nozzle axis are compared with the 1-D exact solution in Figures 3.6 to 3.9. The continuous and smooth variation of the velocity near the boundary should be noted. Predictions are close to the exact solution with slight differences in the region with slight curvature which may be explained via small boundary layer effects. Significantly, the RINV solutions took much less convergence time compared to the VIN approach (8 to 10 times less) as can be seen in Figure 3.10. This is because the RINV approach is based on a characteristic method which is matching the nature of the compressible flow solver and therefore provides smooth boundary update. The RINV approach will therefore be used in the rest of this study.

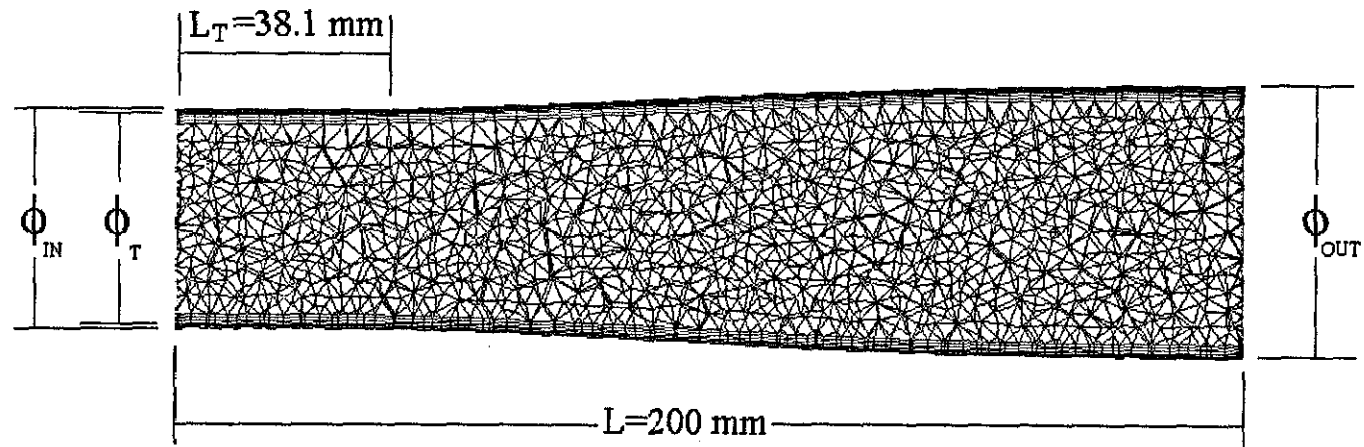
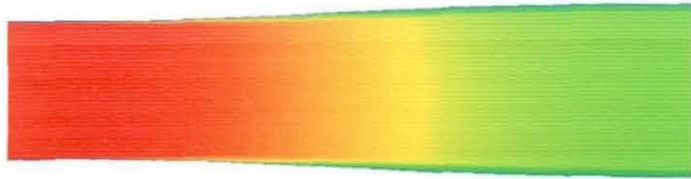
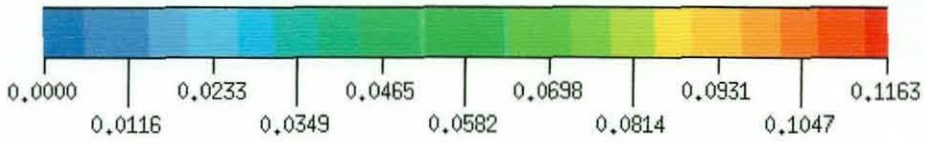
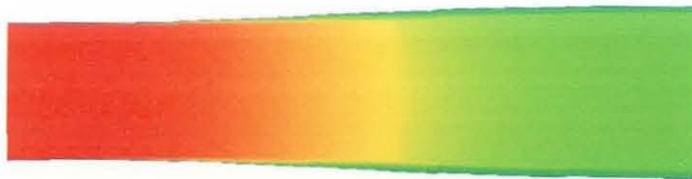
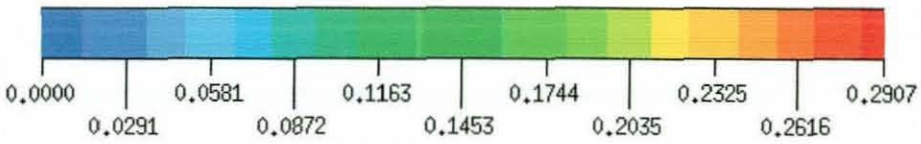


Figure 3.3 Nozzle geometry and computational mesh



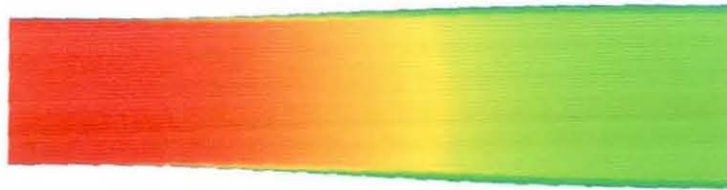
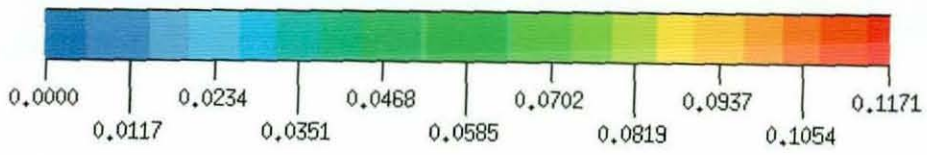


(a)  $U_{IN} = 40$  m/s

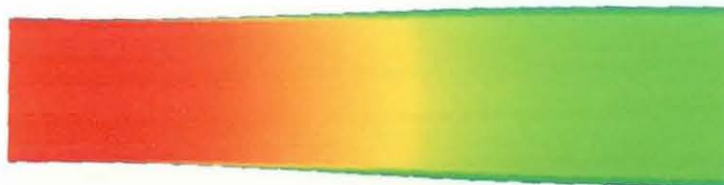
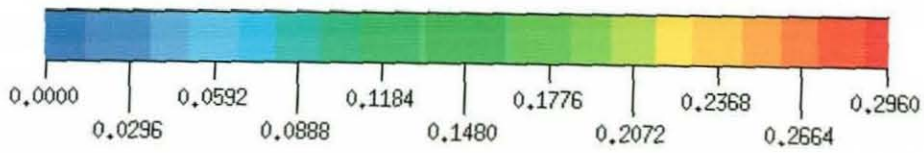


(b)  $U_{IN} = 100$  m/s

Figure 3.4 Mach number contours (RINV)



(a)  $U_{IN} = 40$  m/s



(b)  $U_{IN} = 100$  m/s

Figure 3.5 Mach number contours ( $V_{IN}$ )

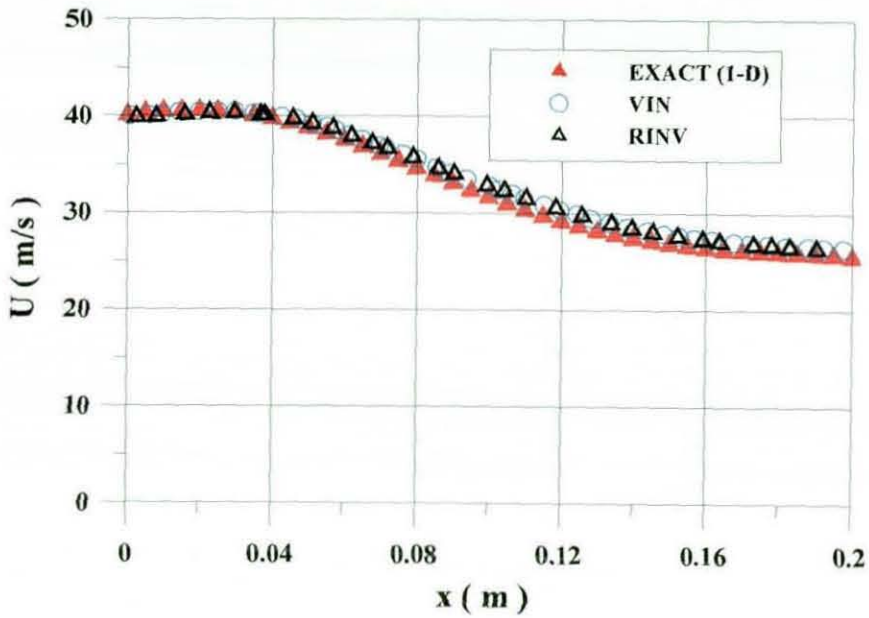


Figure 3.6 Velocity distribution along the axis,  $U_{IN} = 40$  m/s

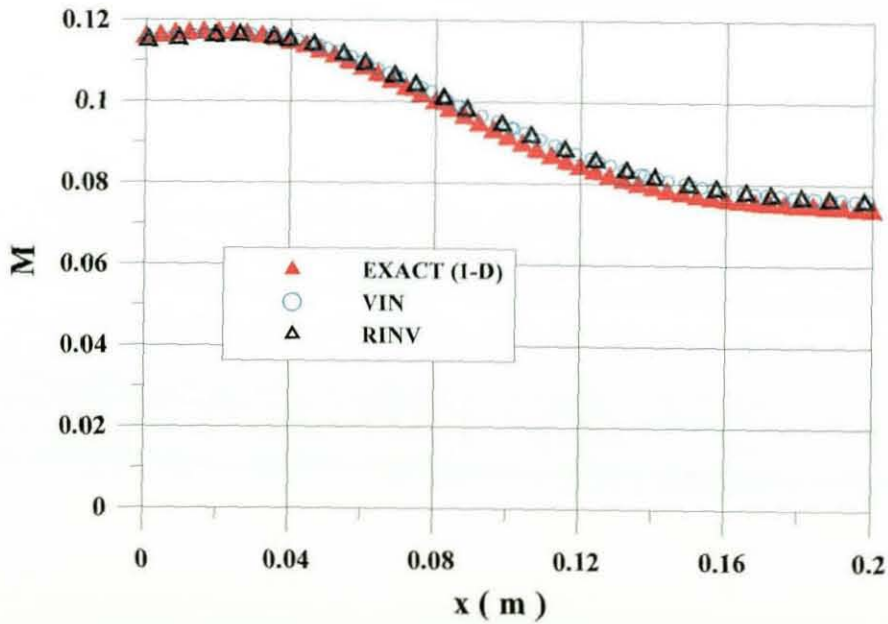


Figure 3.7 Mach number distribution along the axis,  $U_{IN} = 40$  m/s

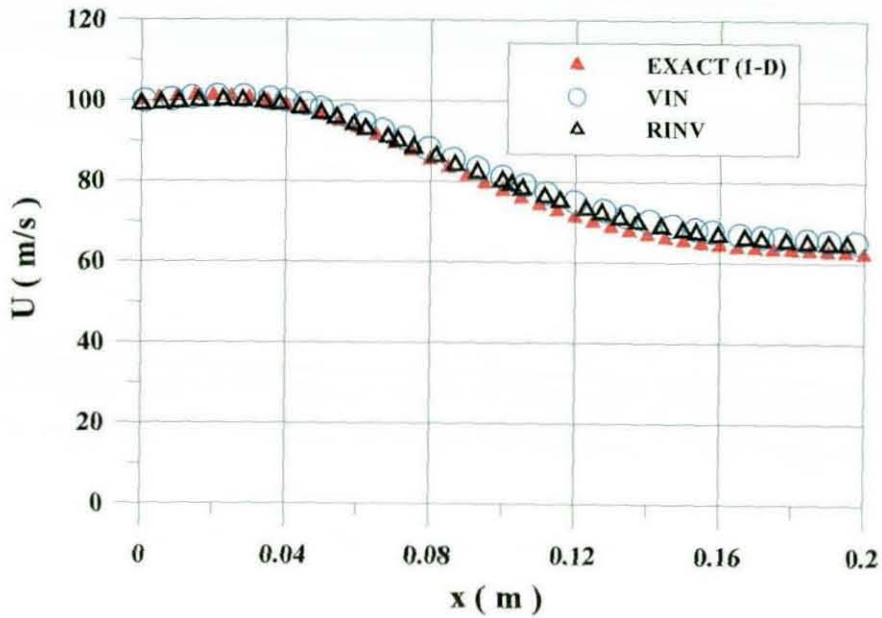


Figure 3.8 Velocity distribution along the axis,  $U_{IN} = 100$  m/s

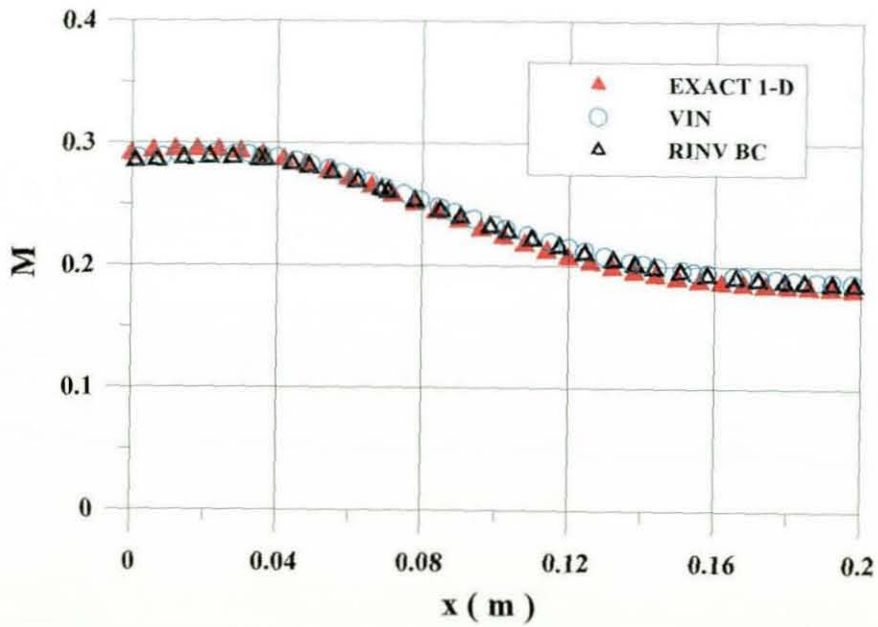
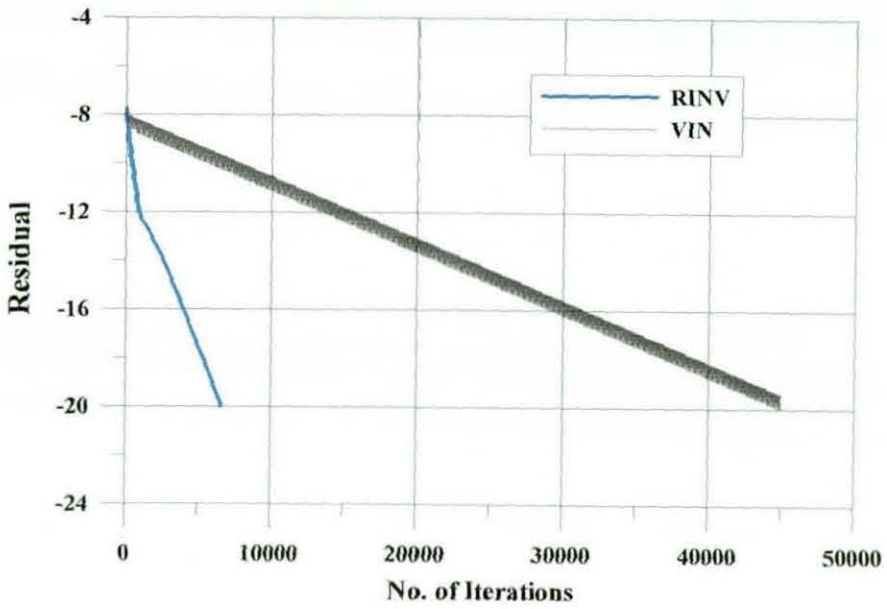
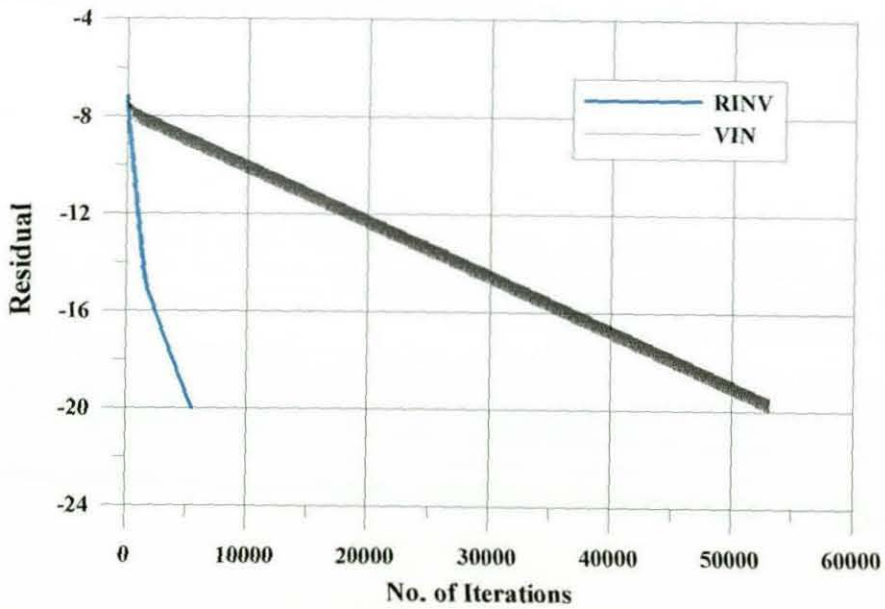


Figure 3.9 Mach number distribution along the axis,  $U_{IN} = 100$  m/s



(a)  $U_{IN} = 40$  m/s



(b)  $U_{IN} = 100$  m/s

Figure 3.10 Convergence history



### 3.3 Periodicity and Centreline Boundary Condition

Periodic boundary conditions are used when the flows across two opposite planes in the computational domain are identical. Periodicity can be between opposed planes which are either translated or rotated relative to each other. In combusting flows, the use of swirl velocities within the fuel injector via angled injection ports leads to periodically repeating flow very often. Figure 3.11 illustrates a typical application of a rotational periodic boundary condition. In this example the flow entering the computational model through one periodic plane (e.g. the plane  $y=0$ ) is identical to the flow exiting the domain through the opposite periodic plane (the plane  $z=0$ ). Periodic planes are always used in pairs as illustrated in this example.

In Hydra preprocessing, periodicity is set up by declaring pairs of labels (*hip\_per\_inlet*) and (*hip\_per\_outlet*) on the respective surfaces. Once periodicity is declared, the hip (*jm54*) pre-processor establishes a list of periodic vertex pairs (*npe(1,ip)* and *npe(2,ip)*) and tests for geometric matching. After the proper coordinate transformation is applied (rotational periodicity is only allowed around the  $x$ -axis), the matching vertices must have the same local surface coordinate to a precision of *epsOverlap* [89]. If this is not the case, hip will move the vertex in the outlet surface to a position of nearest match in the inlet surface. Grid generators such as Gambit and ICEM-CFD provide robust procedures to ensure proper matching for the periodic pairs before transfer to the flow solver; this is usually obtained through linking the periodic pairs and meshing them identically. This task is time consuming especially in complex geometries when a large number of periodic pairs are required. In the hip adf format output files, which are used as input for the Hydra solver, hip generates a list of periodic nodes that contains a "periodic edge" for each periodic connectivity between vertices. In a case of single periodicity, where each node has only one sibling, there is one edge per pair. In the case of multiple periodicity, e.g. a box channel where top and bottom as well as left and right are periodic, the points on the edges of the box have double periodicity.

In this case, four edges are listed that establish all possible connections. A list of symmetry vertices is also appended to the list of periodic edges. These edges are recognisable as symmetry ones by the fact that both ends point to the same vertex ( $npe(1,ip) = npe(2,ip)$ ). In the convention of the adf files, they would be interpreted as symmetry nodes, being periodic with themselves.

In the Hydra solver, the treatment of the rotational periodic boundary condition is performed by copying the solution on the inlet edge to the corresponding outlet edge, taking into consideration the need to rotate the velocity and gradient vectors by using the periodic rotation matrix which is constructed according to the periodicity angle.

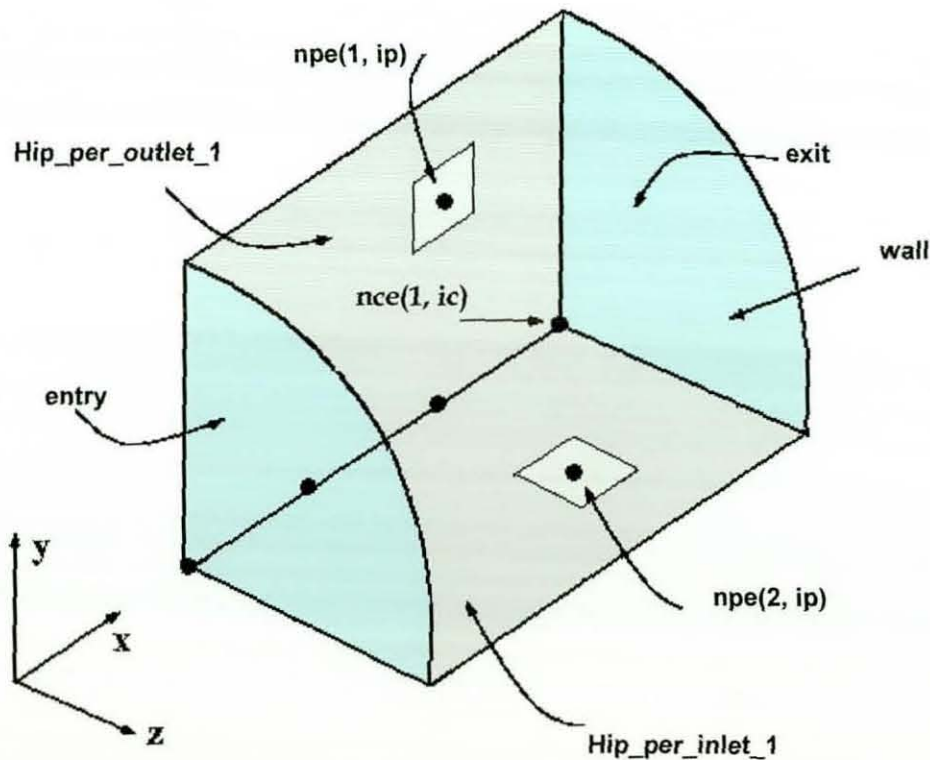


Figure 3.11 Periodic setup for 90° sector of cylindrical domain

In an axisymmetric case the centreline nodes ( $ncc(1,ic)$ ) are recognised by  $y$  and  $z$  coordinates below  $epsOverlap$  nodes but which are not listed as periodic pairs. To avoid a centreline it is common to introduce a cylindrical tube along the centreline with a very small radius to split the periodic pairs and make Hydra calculations possible. However, this approximate procedure implies that the basic grid generated with centreline tube cannot be used by other solvers than Hydra; it also introduces further complexity with geometries which contain centre bodies and a centreline at the same time. Hence, a modification has been implemented to overcome this drawback by introducing special treatment for the centreline nodes. Momentum fluxes in the  $y$  and  $z$  directions are enforced to be zero along the centreline [98]. This procedure has been successfully tested on a  $30^\circ$  sector of a cylindrical duct. The convergence history and the axial velocity distributions obtained before and after the modifications are shown in Figures 3.12 and 3.13 respectively. It can be seen from the two figures that an unrealistic solution with no convergence was obtained before the current modifications which provide a realistic and converged solution.

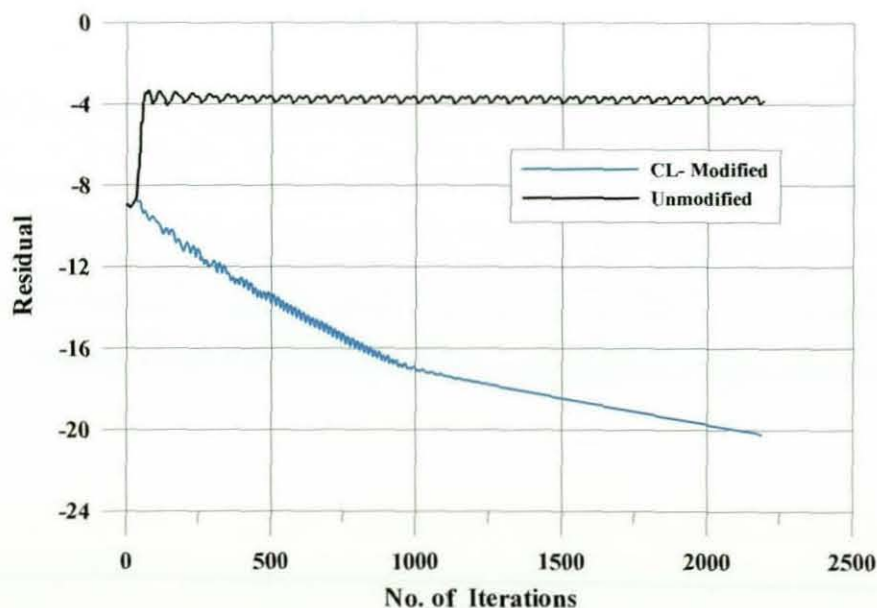
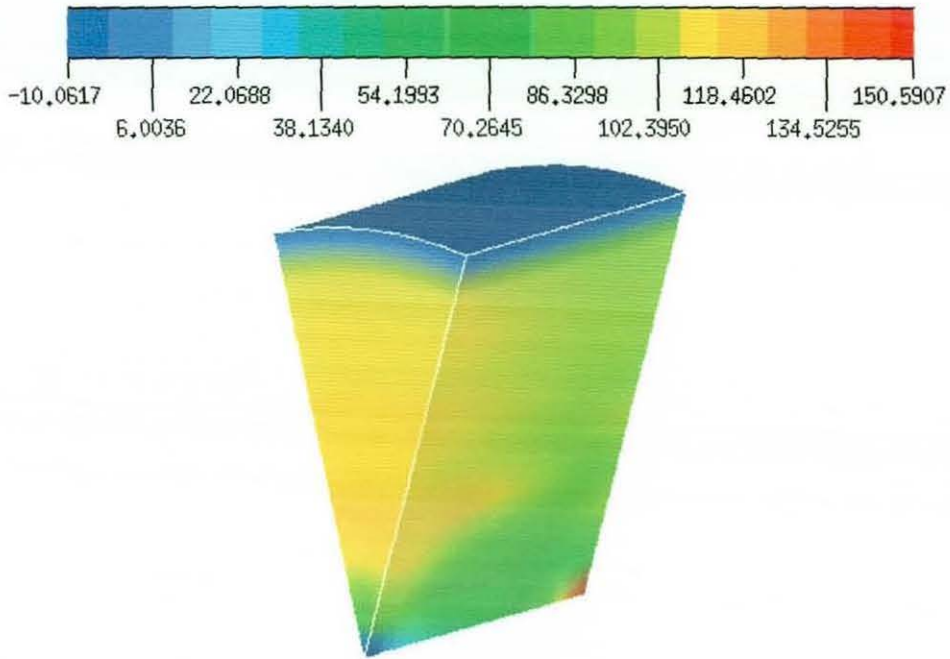
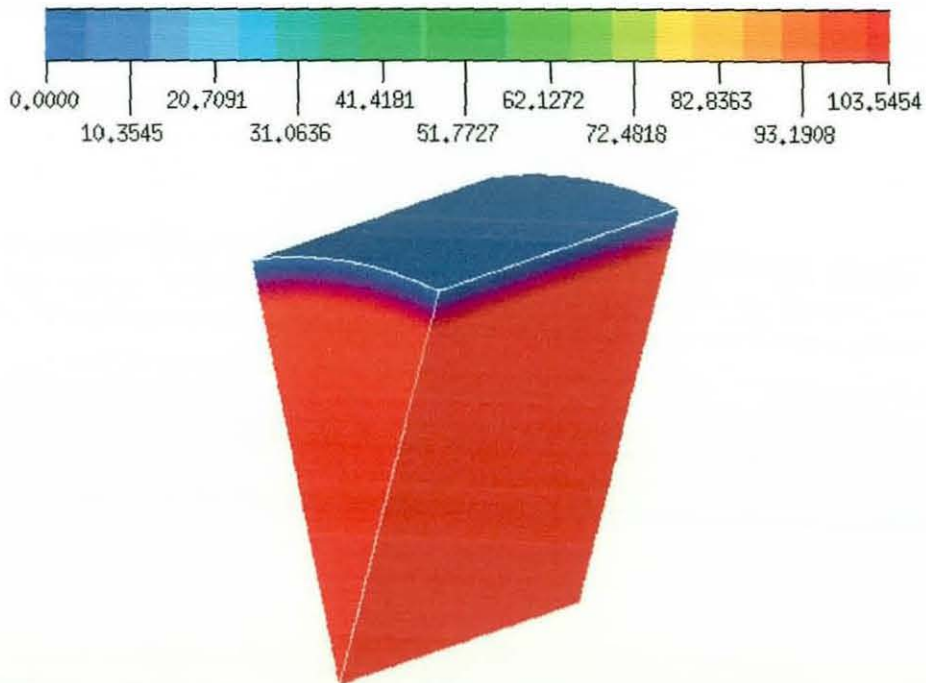


Figure 3.12 Convergence history





(a) Before centreline boundary condition modifications



(b) After centreline boundary condition modifications

Figure 3.13 Axial velocity distribution

### 3.4 Reacting Flow Modelling

The mathematical and numerical models of Hydra presented in the previous chapter are based on assumptions which are valid for isothermal non-reacting flows. The fluid, usually air, is assumed to be a calorically perfect gas where only translational and rotational modes of energy contribute to the total internal energy. For this perfect gas, the enthalpy,  $h$ , and internal energy,  $e$ , both hold linear relationship with the temperature such that,

$$h = C_p T \quad (3.15)$$

$$e = C_v T \quad (3.16)$$

Where the specific heats  $C_p$  and  $C_v$  and their ratio ( $\gamma = C_p / C_v$ ) are constant.

In reacting flow with influence of chemical reactions and high temperatures, a mixture with a wide range of chemical species is produced. Therefore, the influence of each specie on the mixture has to be considered [99]. The total mixture pressure is the summation of the species ( $N$  species with  $k = 1, \dots, N$ ) partial pressures and given as

$$p = \sum_{k=1}^N p_k = \sum_{k=1}^N \rho_k R_k T = \rho \tilde{R} T \quad (3.17)$$

where the mixture gas constant  $\tilde{R}$  and the mixture density  $\rho$  have been introduced and are defined as

$$\tilde{R} = \sum_{k=1}^N \frac{\rho_k}{\rho} R_k \quad (3.18)$$

and

$$\rho = \sum_{k=1}^N \rho_k \quad (3.19)$$

where  $R_k$  is the species gas constant determined as

$$R_k = \frac{\bar{R}}{M_k} \quad (3.20)$$

$\bar{R}$  is the universal gas constant and  $M_k$  is the species molecular weight.

The mass fraction of each specie  $k$  is defined as the ratio of mass of the specie to the whole mass of the mixture

$$Y_k = \frac{m_k}{m} \quad (3.21)$$

To numerically simulate the reacting flow, it requires solving  $N$  equations for the conservation of species in addition to the RANS equations presented in section 2.4.

The conservation of species equations are given as follows

$$\frac{\partial \rho Y_k}{\partial t} + \frac{\partial \rho u_i Y_k}{\partial x_i} = -\frac{\partial J_j^k}{\partial x_j} + \dot{\omega}_k \quad (3.22)$$

where  $J_j^k$  is the molecular diffusive flux of the specie  $k$  and  $\dot{\omega}_k$  is the mass reaction rate per unit volume of the same specie.

The enthalpy equation is modified to be

$$\frac{\partial \rho H}{\partial t} + \frac{\partial \rho u_i H}{\partial x_i} = \frac{\partial p}{\partial t} + \frac{\partial}{\partial x_j} (J_j^k + u_i \tau_{ij}) \quad (3.23)$$

The number of species, which could be very large, and the associated conservation equations means that the total computational effort required for the simulation of reacting flow can be very time consuming. Therefore, instead of solving the mass fraction equations a combustion model to simplify the flow calculations approach is required. Various combustion models can be found in the literature each based on certain assumptions according to the combustion category and modeling approach as summarized in Figure 3.14. In this study, the conserved scalar approach is selected to simulate the gas-turbine combustor non-premixed turbulent combustion flow because it is simple and widely used in engineering

applications. Scalar variables such as mixture fraction and species concentrations are essential in the conserved scalar models. Therefore, it is of great importance to assess the accuracy and the boundedness of the calculations of the scalar variables within the flow solver before proceeding with incorporating any combustion model into the solver. In the following section, the numerical diffusion associated with the discretisation of the convective term in the Hydra code will be tested on a simple scalar transport test problem. Finally in the last section of this chapter, the conserved scalar transport equations will be incorporated into the Hydra solver and validated against experimental and numerical solutions to predict the conserved scalar field. The implementation of a non-premixed turbulent combustion model into Hydra will be presented in chapter six.

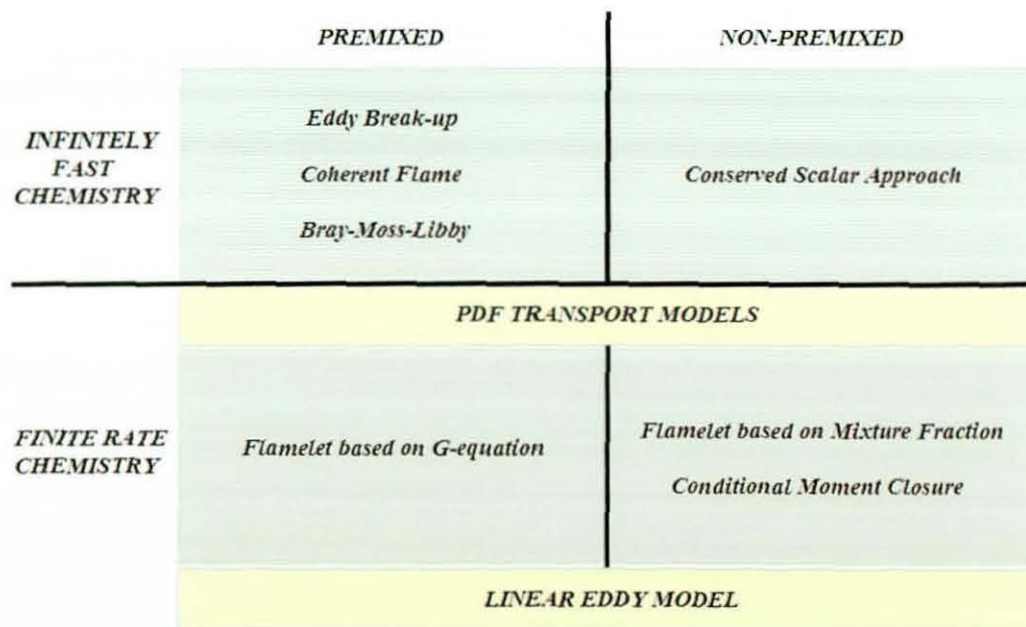


Figure 3.14 Combustion modeling approaches



### 3.5 Convective Error Analysis and Estimation

Numerical diffusion (ND), sometimes referred to as numerical dissipation, can be a serious source of error in the simulation of multidimensional fluid flow problems. It is also known as false diffusion because the diffusion introduced is not physical, but its influence on the flow calculation is similar to that of increasing the real diffusion coefficient. The main source of numerical diffusion is the truncation error associated with the discretisation of the convective fluxes. Depending on the details of the discretisation, its magnitude will depend on grid size but also it can increase when the flow is oblique to the grid lines.

ND is least noticeable when real diffusion is large and the flow is not convective dominated i.e. at all low Reynolds/Peclet numbers [13]. However, most fluid flows encountered in nature and industry are characterized by high Reynolds number, implying the dominance of convective effects over diffusive effects. Therefore, important consideration in CFD must be given to the discretisation of the convection terms since the accuracy, numerical stability and the boundedness of the solution depends on the numerical scheme used for these terms.

Second order centered differencing (CD) would be a consistent discretisation scheme for the convective term in particular because, since its leading truncation error depends on a third (rather than a second) derivative, on a high quality meshes no numerical diffusion introduced. However, it is found to be unstable and produces non-physical oscillations in the solution (numerical dispersion), severely reducing its preference. Consequently, it may also produce values of the dependent variable that are outside of their physically meaningful bounds. If one considers the transport of scalar properties commonly used in combusting flow problems, such as mixture fraction, turbulent kinetic energy and species concentration, the importance of boundedness becomes clear. As an example, a negative value of turbulence properties results in a negative viscosity which

implies serious effects on the solution algorithm. Equally, a negative value of a scalar property (e.g. mixture fraction) from which fluid density is being calculated would lead to a negative density, which couples through the momentum equations and often leads to solution divergence. It is therefore essential to obtain bounded numerical solutions when solving transport equations for bounded properties.

A first order upwind differencing (UD) has been found to be the only convection differencing scheme that is guaranteed to preserve boundedness, since the coefficients in the system of algebraic equations will be positive even in the absence of physical diffusion [99]. This is effectively achieved, however, by introducing an excessive amount of numerical diffusion which changes the nature of the problem. It is also noted in [95] that in cases of flow misalignment with the grid, degradation of accuracy becomes unacceptable.

Peric [100] proposed a blending approach, using a certain amount of upwinding combined with second order CD until boundedness was achieved. This approach potentially improves the accuracy of the solution. Disregard the amount of upwinding needed, Peric proposes a constant blending factor for the whole mesh. Local grid refinement and grid adaptation techniques may be used to remedy the problem of numerical diffusion especially in schemes with unstructured discretisation. On the other hand the structured mesh approach allows development of discretisation schemes with high order truncation error in an attempt to improve the solution accuracy.

In this section, the numerical diffusion associated with the discretisation of the convective term in the Hydra code will be investigated. The problem will be isolated by studying the influence of mesh type and discretisation practices on a single scalar variable convection test case. The test problem suggested by Smith and Hutton [101] has often been used as a valuable benchmark for assessment of numerical diffusion and hence it is used for this purpose here.



3.5.1 Scalar transport test problem

Considering the scalar convection part of transport equation as solved by the Hydra code, one obtains the following form (expressed here for simplicity in non-conservative form)

$$\frac{\partial \phi}{\partial t} + u \frac{\partial \phi}{\partial x} + v \frac{\partial \phi}{\partial y} + w \frac{\partial \phi}{\partial z} = 0 \tag{3.24}$$

The above equation when discretised by the finite volume method and numerically integrated over the median dual control volumes results in:

$$\sum_{j \in E_i} \frac{1}{2} \left[ \underbrace{\rho(u_j \cdot n_{ij})(\phi_j + \phi_i)}_{\text{convective flux term}} - \underbrace{|u_j \cdot n_{ij}|}_{\text{4th order term}} \left( (1 - \Psi) \cdot \rho(L_j^p - L_i^p) + \Psi \cdot \rho(\phi_j - \phi_i) \right) \right] \Delta s_{ij} \tag{3.25}$$

2<sup>nd</sup> order term

numerical dissipation term

As discussed in chapter two, the convective flux term above represents a second order central difference approximation stabilized by the addition of a numerical dissipation term consisting of fourth order and second order smoothing terms which may be scaled by the switch  $\Psi$ .

Equation (3.24) may be solved for the test case shown in Figure 3.15 and may be used to test the influence of grid type, grid density and the effect of the smoothing terms on the solution quality. A rectangular domain in Figure 3.15 is initialized with a zero scalar value  $\phi = 0$  and with a fixed velocity field given as follows:

$$u = 2y(1 - x^2) \tag{3.26}$$

$$v = -2x(1 - y^2) \tag{3.27}$$

$$w = 0 \tag{3.28}$$

This gives rise to the streamline pattern shown in Figure 3.15 for the rectangular region defined by  $-1.0 \leq x \leq 1.0$  and  $0 \leq y \leq 1.0$ . A scalar inlet boundary condition on the lower left side of the domain inlet is specified as follows:

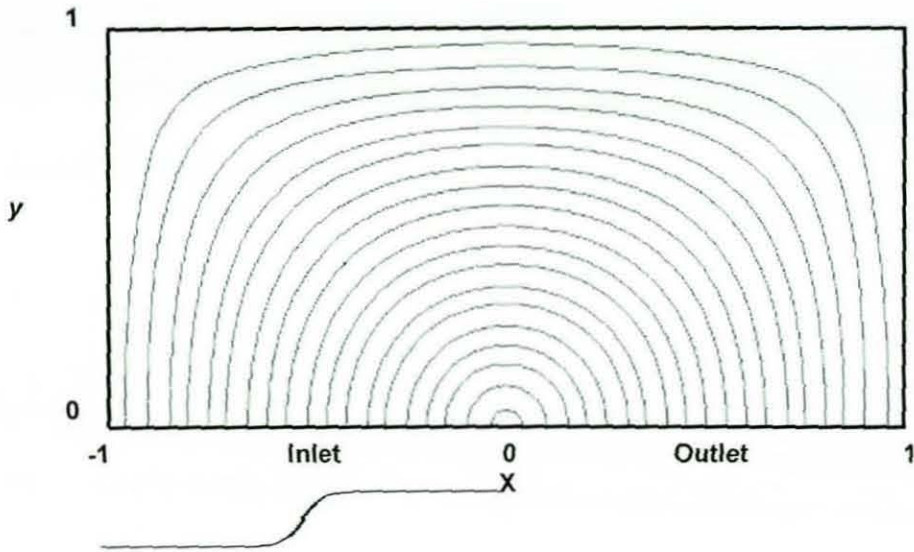
$$\phi(x,0) = 0.5 + 0.5 \tanh[10(2x+1)] \quad -1 \leq x \leq 0 \quad (3.29)$$

Ideally (if the solution method contains no numerical diffusion), the steep gradient scalar profile at the inlet should be convected unchanged around the streamlines since equation 3.24 contains no physical diffusion. Numerical solution accuracy can be estimated by comparing any numerical solution with the exact solution. Departure from the exact solution will depend on the numerical diffusion and dispersion characteristics of the applied numerical scheme. The global error can be evaluated and expressed as the sum of all local errors in each cell normalized by the sum of the exact solution as follows:

$$Error = \frac{\sum |\phi^{numerical} - \phi^{exact}|}{\sum \phi^{exact}} \quad (3.30)$$

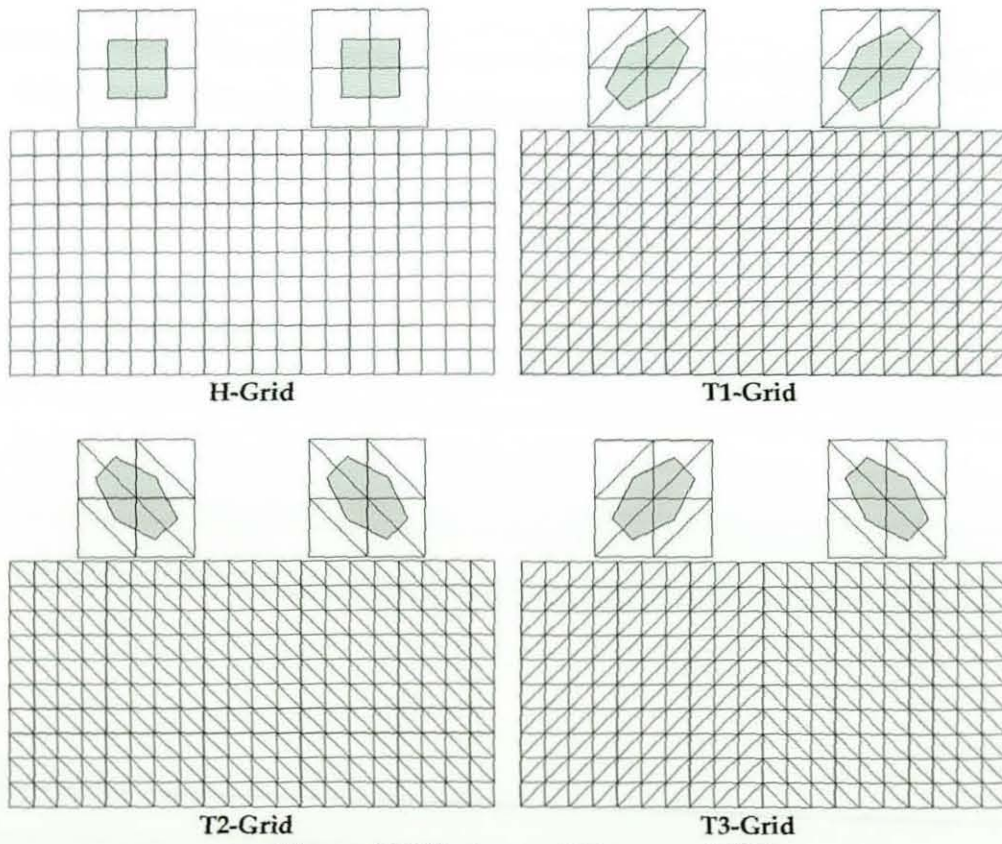
Four types of grids have been generated to investigate this problem each of them with four different sizes. The first grid is a purely hexahedral grid (H-grid) which was then triangulated in different ways to generate three grids (T1, T2, and T3) each with different orientations of the median dual control volumes on the left hand side and right hand side of the domain as shown in Figure 3.16. This allows a variety of orientations between the velocity vector field and median dual finite volume edges to be considered. The coarsest hexahedral grid is generated with 21X11 grid spacings in the  $x$  and  $y$  directions respectively. This resolution is successively doubled to obtain three finer grids (41X21, 81X41, and 161X81).





Scalar profile

Figure 3.15 Streamlines of the fixed velocity flow field



H-Grid

T1-Grid

T2-Grid

T3-Grid

Figure 3.16 Various grid types and CVs

Typical solutions of the scalar field on the coarsest grid using the central differencing scheme CDS (where the dissipation term in equation (3.25) is set to zero) and the upwind differencing scheme UDS (where the switch  $\Psi$  is set to be unity i.e. CDS and second order dissipation term only) are shown in Figures 3.17 and 3.18. The first figure clearly illustrates the presence of the steep gradient region in the scalar field, which is convected around the mesh. Results using UDS, Figure 3.18, show strong evidence of numerical diffusion; this is particularly visible via the increasing width of the scalar mixing layer. Better results are expected on the same grid if CDS is used and Figure 3.17 shows much smaller spreading of the scalar gradient region. However wiggles can be noticed in the solution contours which are due to the lack of smoothing in CDS. Among the four grids, the hexahedral grid shows a better performance in terms of accuracy compared with the triangulated grids, where the extent of increase in numerical error is highly dependant on the median dual control volume type. The overall global error estimates as shown in Figure 3.19 always indicates the error decreasing in the order T2/T1/T3/H for all grid densities. The grid with T2 type element always gives the worst performance with both central and upwind differencing methodologies. Using CDS the left hand side of the domain captures more wiggles and spreading than the right hand side. The T3 element shows better performance as the solutions using both CDS and UDS appear to be close to the hexahedral grid solution. The T1 grid, which has a triangulation orientation opposite to the T2 grid in both sides of the domain, shows better performance in the right hand side of the domain rather than the left hand side which is opposite to the performance of the T1 grid. Grid refinement improves the solution quality significantly but the superiority of the H and T3 grids over the other two grid types can be seen from the global error versus grid size curves in Figure 3.19. The observation that particular triangulations influence the results has been observed before by many researchers. Roe [102] showed that for UDS, the coefficient of numerical viscosity is lowered by a factor of four when the diagonals are aligned with the flow as compared to being nearly orthogonal to the flow direction. These observations confirmed by Haselbacher [57]



who also found the influence of the orientation of the diagonals to be more important than that of grid distortion. For the current test case, in the left hand side of domain, the flow is broadly upwards and to the right, whilst in the right hand side it is broadly downward and to the right; using Roe's observation this would suggest that T3 grid is the best triangulation for the flow problem, and this is indeed shown to be the case for CDS as well. Since the flow is left-right symmetric it might be expected that T1 and T2 triangulations would give similar results, however, the history effect of error being produced by the poor diagonal alignment of the left hand side of T2 increases the total error in the domain as compared to T1. Jiang et al. [103] investigated this test case and observed similar behavior using structured and unstructured methodologies. They found that by triangulating the quadrilateral mesh in different ways, there is a significant influence in error, but this is likely to be very problem dependent.

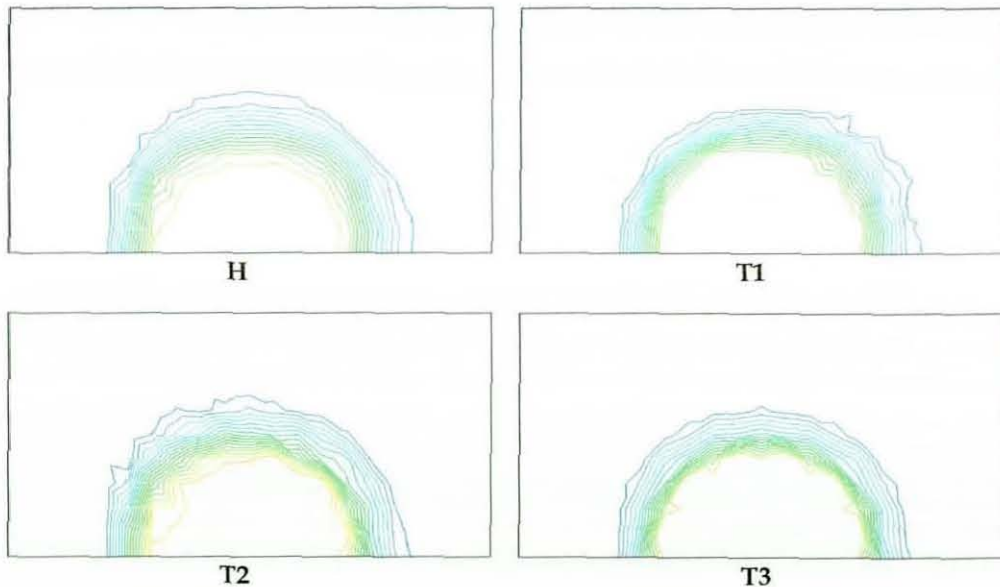


Figure 3.17 Scalar field contours  
(central differencing scheme and 21x11 coarse grid)

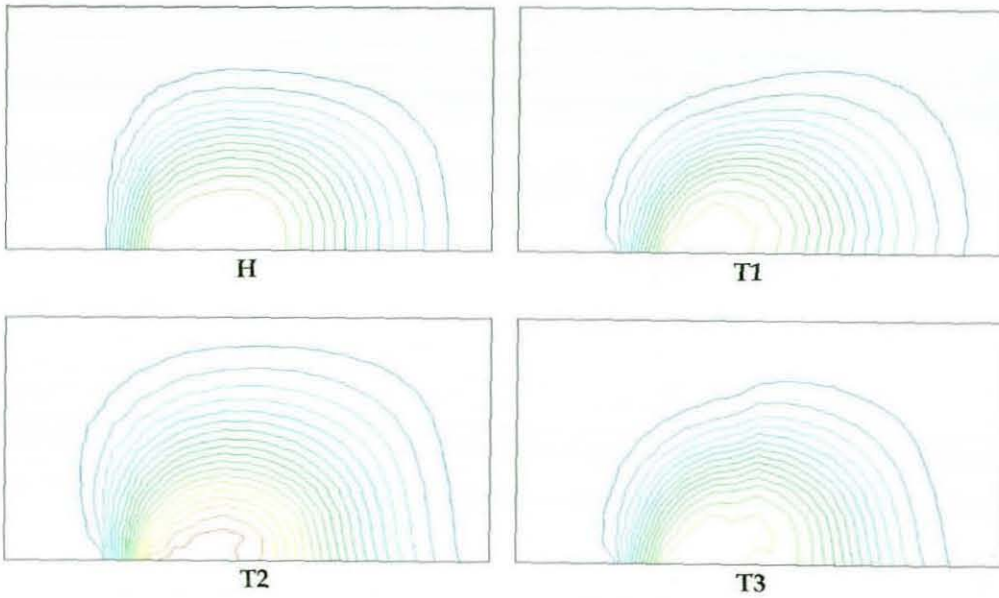
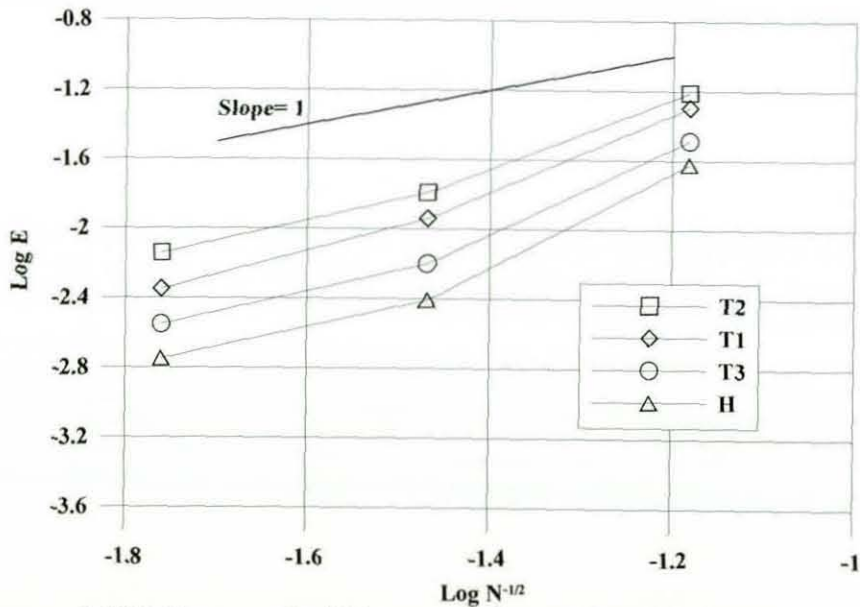


Figure 3.18 Scalar field contours  
(upwind differencing scheme and 21x11 coarse grid)



3.19 Influence of grid type and size on the global error

In order to simplify the comparisons and give a quantitative insight on the solutions, profiles of the scalar along a horizontal line across the domain at  $y = 0.2$

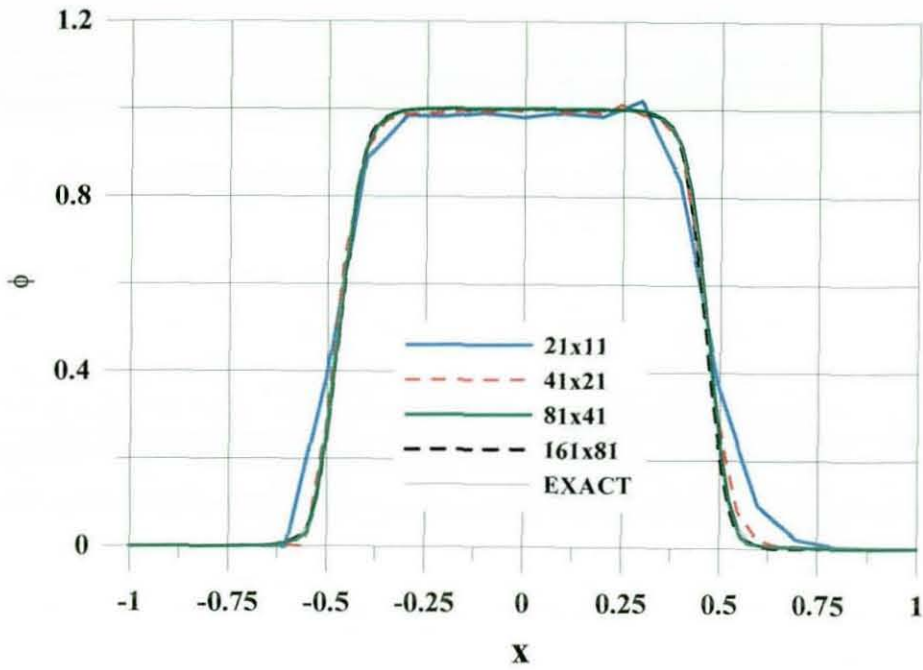
are plotted, as shown in Figure 3.20, for the exact solution and the hexahedral grids solutions for both CDS and UDS. The flow angle along the same line is plotted in Figure 3.21 to indicate the amount of misalignment of the flow with the various median dual elements. The centred difference solutions show rapid improvement with the grid refinement compared to upwind differencing solutions as it can also be seen from the contours in Figure 3.22 and 3.23. However, a serious overshooting ( $\phi > 1$ ) appears in the CDS solutions with the two coarsest grids (21X11 and 41X21) which also can be seen from the wiggles associated with the scalar contours in Figure 3.24. This overshooting puts the boundedness of the solution under question as the values of the scalar exceeded unity. This phenomenon, as discussed early in this section, is common with centred differencing schemes; grid refinement is a probable solution to remedy unboundedness problem as it can be seen with the fine grids (81X41 and 161X81). In contrast to the centred differencing, upwind differencing scheme preserves boundedness at the cost of accuracy which also shows slow improvement with grid refinement. An alternative is to use the fourth order dissipation term in order to obtain bounded solutions to such a convection dominated problems. Fourth order dissipation was originally proposed, as an alternative to upwinding, by Jameson in a Runge-Kutta scheme for the compressible Euler equations [104]. Unfortunately, the fourth order derivative may be very large when used with other flow variables due to physical phenomena such as shocks or other discontinuous phenomena. In such situations, the fourth order dissipation must be switched off and, to retain boundedness, substituted by the second order term. For the current case, solutions with fourth order dissipation term, i.e.  $\Psi = 0$  in equation (3.25), show better performance than the second order term solutions as it can be seen in Figure 3.25 where the spread regions are smaller and the influence of grid refinement is more effective. However, in coarse grids wiggles can be noticed in the solution contours. Using a switch to balance a blend of both second order and fourth order smoothing terms can be a better solution to combine the advantages of



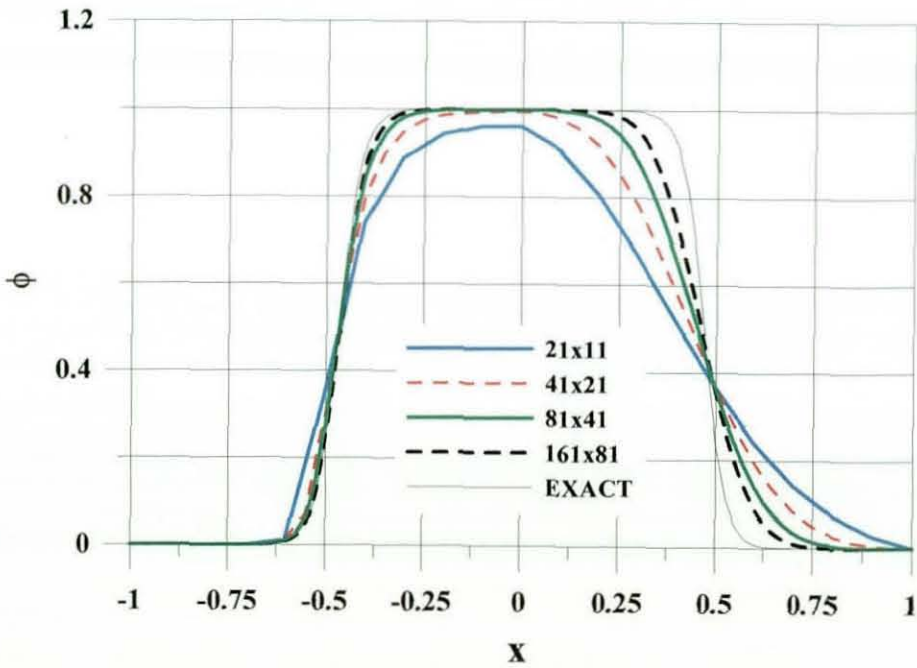
high accuracy of CDS and boundedness preserving ability of the smoothing terms. The switch is similar to the pressure limiter introduced in the dissipation term of the inviscid flux equation to obtain a monotonic resolution and can be written for scalar variable as follows

$$\Psi = \min \left[ \varepsilon^{(2)} \left( \frac{|L_i^p(\phi)|}{|L_i^p(\phi)| + 2\phi_i} + \frac{|L_j^p(\phi)|}{|L_j^p(\phi)| + 2\phi_j} \right), 1 \right] \quad (3.31)$$

where  $\varepsilon^{(2)}$  is a user defined constant taken to be 8 and  $\phi$  is the scalar magnitude at the node. Solutions with  $\varepsilon^{(2)} = 0.5$  are shown in Figure 3.26 and provide reasonable predictions in terms of accuracy and boundedness. This version of the limiter was used in all conserved scalar calculations presented in this thesis.



(a) Central differencing



(b) Upwind differencing

Figure 3.20 Scalar distribution along  $y=0.2$  horizontal line

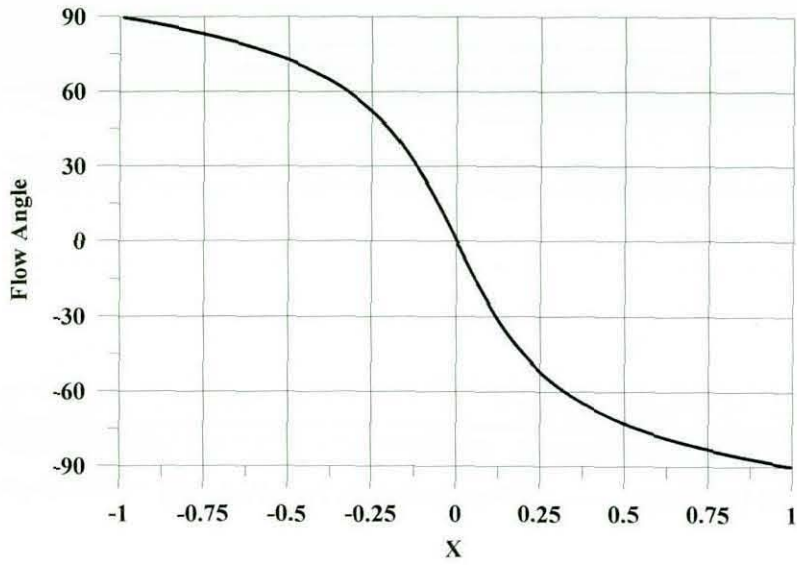


Figure 3.21 Flow angle along  $y=0.2$  horizontal line

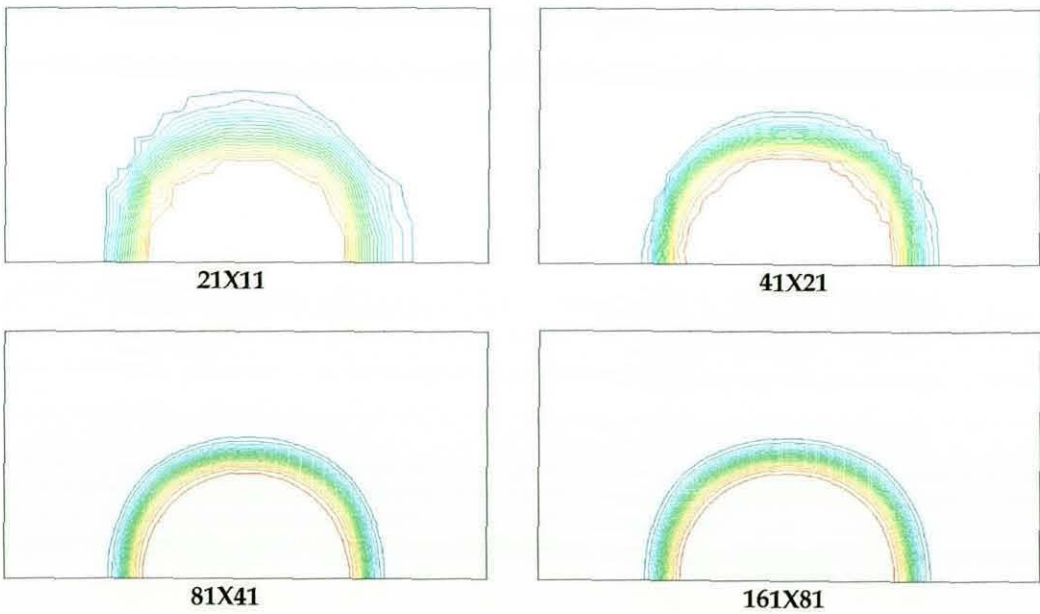


Figure 3.22 Centred (no smoothing terms)



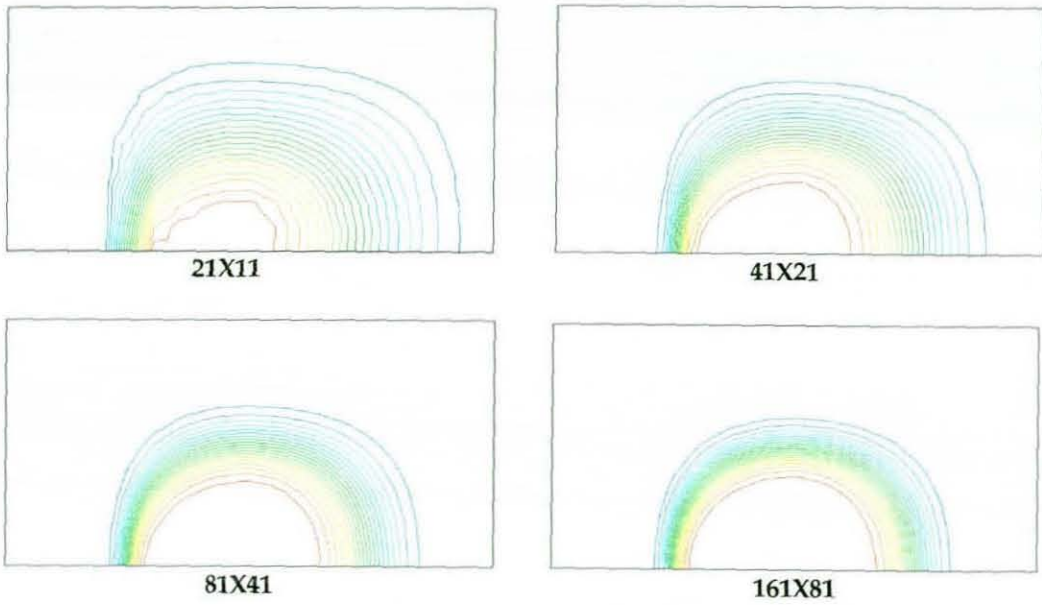


Figure 3.23 Upwind (second difference term only)

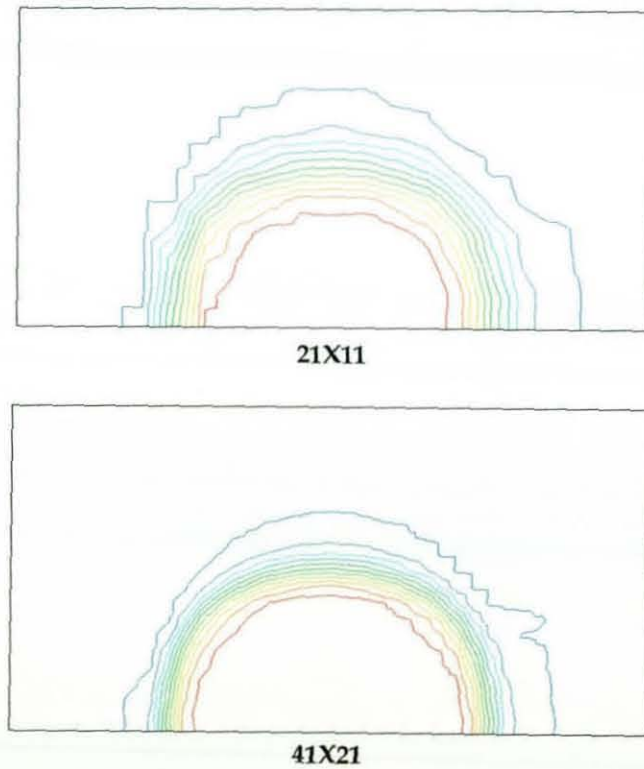
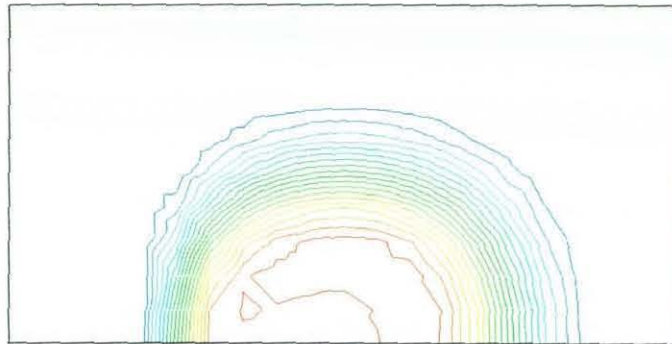
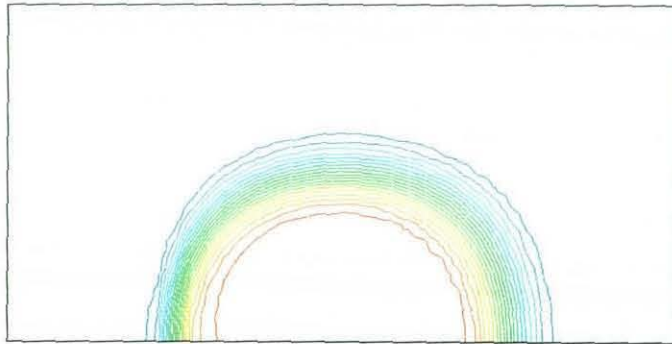


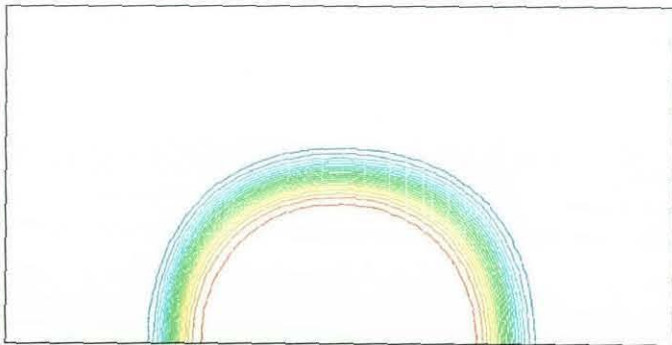
Figure 3.24 Wiggles associated with scalar contours on CDS and coarse grids



21X11

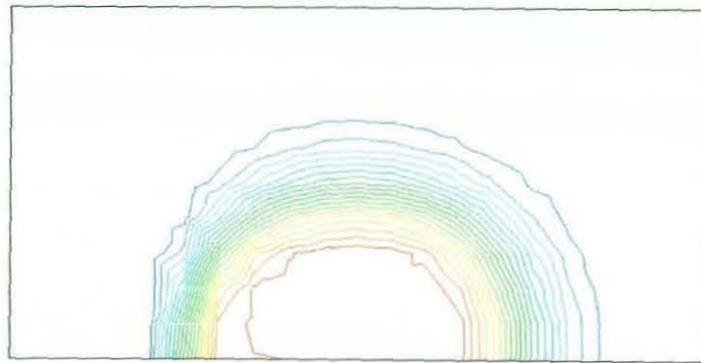


41X21

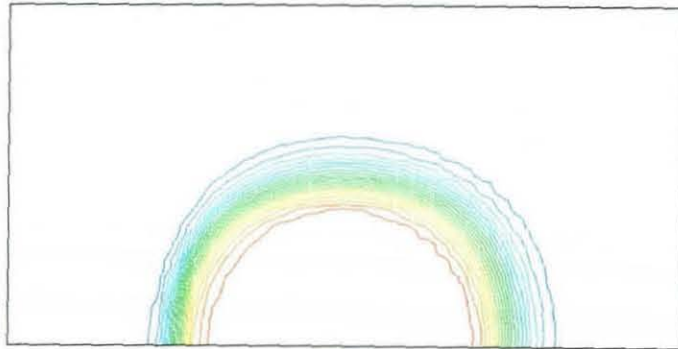


81X41

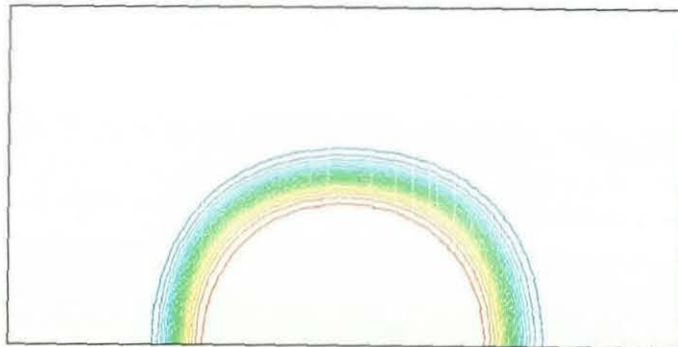
Figure 3.25 Fourth difference term only



21X11



41X21



81X41

Figure 3.26 Blend of second and fourth difference ( $\epsilon^{(2)} = 0.5$ )

### 3.6 Conserved Scalar Implementation and Validation

The conserved scalar can be interpreted as any scalar property that is conserved throughout the flow field. For example, absolute enthalpy is conserved at every point in the flow when there is no source of thermal energy. Mass fraction of any inert specie is also a conserved scalar since it is neither created nor destroyed by chemical reactions [105, 106]. Burke and Schumann introduced the concept of mixture fraction for the representation of non-premixed combustion [107,108]. They defined the mixture fraction as a conserved scalar describing the fuel-air mixing state with values ranging between zero (pure air) and one (pure fuel)

$$f \equiv \frac{\text{Mass of Fuel}}{\text{Mass of Mixture}} \quad (3.32)$$

One of the simplest approaches for relating chemical states to mixture fraction is to assume equilibrium chemistry. When the chemical kinetics are infinitely fast relative to other processes in the flow, the mixture is always completely reacted, or in a state of chemical equilibrium. A similar assumption, called fast chemistry, is equilibrium chemistry combined with a one-step global reaction assumption. The opposite extreme of fast chemistry is the case of pure mixing (frozen chemistry), which is the limit in which the rates of chemical reactions are negligible. With each of these assumptions the chemical composition is a unique function of mixture stoichiometry, total enthalpy, and pressure.

Considering a system with single inlet stream of fuel (mass flux  $\dot{m}_1$ ) and single inlet stream of oxidizer (mass flux  $\dot{m}_2$ ) as shown in Figure 3.27, for homogeneous mixture of two streams, equation (3.32) can be expressed as follows:

$$f = \frac{\dot{m}_1}{\dot{m}_1 + \dot{m}_2} \quad (3.33)$$

The mass fraction of the fuel  $Y_{Fuel}$  in the mixture is proportional to the mass fraction in the original fuel stream  $Y_{Fuel,1}$  and the mixture fraction

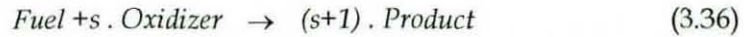


$$Y_{Fuel} = Y_{Fuel,1} \cdot f \tag{3.34}$$

Similarly, the mass fraction of the oxidizer  $Y_{Oxidizer}$  in the mixture can be defined as a function of the mass fraction of the oxidizer in its original stream

$$Y_{Oxidizer} = Y_{Oxidizer,2} \cdot (1 - f) \tag{3.35}$$

Therefore for reacting flow with one step chemical reaction



The mixture fraction can be defined as follows

$$f = \frac{(s \cdot Y_{fuel} - Y_{oxidizer}) + Y_{oxidizer,2}}{s \cdot Y_{fuel,1} + Y_{oxidizer,2}} \tag{3.37}$$

In the above normalized equation,  $s$  is the reaction stoichiometric coefficient and the mixture fraction varies between  $f=1$  in fuel stream inlet and  $f=0$  in the oxidizer stream inlet.

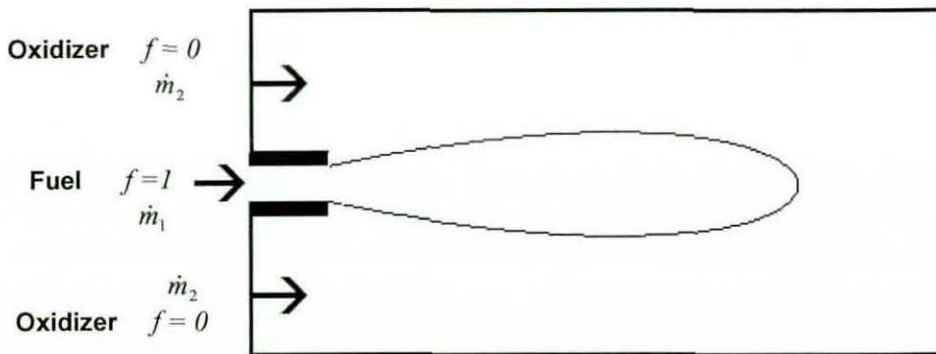


Figure 3.27 System with single inlet stream of fuel and oxidizer

The mean value of the mixture fraction  $\tilde{f}$  gives an indication of the local fuel/oxidizer in turbulent flows. In addition, the structure and properties of the flame depend on the mixture fraction variance  $\tilde{f}''^2$  which measures the degree of

mixing between reactants [105]. Under the above assumptions, the thermochemical compositions are functions of mixture fraction  $f$  only. This approach minimizes the numerical cost by avoiding the solution of additional equations for conservation of species and chemical reaction. In addition to RANS equations and the  $k-\varepsilon$  turbulence model equations, two transport equations for the mixture fraction mean  $\tilde{f}$  and variance  $\tilde{f}^{n2}$  need to be solved and are given as follows:

$$\frac{\partial \rho \tilde{f}}{\partial t} + \frac{\partial}{\partial x_j} (\rho u_j \tilde{f}) = \frac{\partial}{\partial x_j} \left[ \left( \frac{\mu_t}{\sigma_k} \right) \frac{\partial \tilde{f}}{\partial x_j} \right] \quad (3.38)$$

$$\frac{\partial \rho \tilde{f}^{n2}}{\partial t} + \frac{\partial}{\partial x_j} (\rho u_j \tilde{f}^{n2}) = \frac{\partial}{\partial x_j} \left[ \left( \frac{\mu_t}{\sigma_g} \right) \frac{\partial \tilde{f}^{n2}}{\partial x_j} \right] + C_{g1} \mu_t \left( \frac{\partial \tilde{f}}{\partial x_j} \right)^2 - C_{g2} \mu_t \rho \frac{\varepsilon}{k} \tilde{f}^{n2} \quad (3.39)$$

In the two above equations the first term in the RHS is the transport term, in equation (3.39) the second term is the production of the fluctuations by the mean gradients and the third term is the scalar dissipation rate while  $C_{g1}$  and  $C_{g2}$  are model constants with the values of 2.0 and 2.8 respectively.

The above two transport equations look similar to the transport equations of turbulent kinetic energy and energy dissipation rate in the  $k-\varepsilon$  model discussed in the previous chapter. This similarity makes the process of implementation of the mean and variance equations into the code easier. The solution procedure described in section (2.6.2) for the  $k-\varepsilon$  model transport equations will be adopted here with slight modification to the boundary condition implementation. Inlet boundary conditions were modified to account for the values of new variables  $\tilde{f}$  and  $\tilde{f}^{n2}$  while at the solid walls normal gradients of both variables are assumed to be zero. Before proceeding to the combustion modeling, the ability of the solver to predict scalar field will be tested. The experimental and numerical work presented by Spalding et al. [109] to investigate the concentration fluctuations in

isothermal turbulent coaxial jets will be used to validate the solver with conserved scalar modifications in the following section.

### 3.6.1 Validation test case

Unmixedness phenomenon of fuel and air associated with the turbulent non-premixed flames has attracted the attention of many researchers [109-112]. The presence of fuel and air at different times at a given point does not allow the reaction to proceed rapidly and it has been found that this is directly related to the fluctuations of concentration i.e. mean  $\tilde{f}$  and variance  $\tilde{f}''^2$  of the scalar variable (mixture fraction). The turbulent mixing system of confined axial jets shown in Figure 3.28 has been intensively investigated numerically and experimentally by Spalding et al. [109], Elgobashi et al. [110], Becker et al. [111] and Torrest et al. [112] over a wide range of Craya-Curtet numbers. These studies considered two steady coaxial jets of equal density issuing into a circular concentric duct. At the central jet, the mean scalar variable is set to be unity,  $\tilde{f} = 1$ , while at the outer stream is set to be zero,  $\tilde{f} = 0$ . The flow pattern in this geometry is governed by many parameters together represented by the Craya-Curtet number defined as follows:

$$C_t = \frac{U_0}{\sqrt{(U_1^2 - U_2^2) \frac{A_j}{A_0} + 0.5(U_2^2 - U_0^2)}} \quad (3.40)$$

Where

$$U_0 = (U_1 - U_2) \frac{A_j}{A_0} + U_2 \quad (3.41)$$

The subscripts 1 and 2 denote the central jet and the outer jet inlets respectively, while  $A_j$  is the central jet area and  $A_0$  is the whole inlet area. When the velocity ratio of the central jet to the outer jet increases progressively, a point beyond which the rate of entrainment into the central jet will exceed the supply from the outer jet



will be reached. Consequently, a recirculation zone will be created downstream the inlet plane.

To validate the solution procedure of the conserved scalar equations introduced into the Hydra solver and to test its ability to predict the scalar field, the above case will be simulated over different Craya-Curtet numbers. For simplicity only a  $30^\circ$  sector has been considered and the velocity ratio selected to match with experimental data. At the inlet boundary, the mean and variance are set to be 1 and 0 respectively for the central jet; while both are set to zero for the outer jet since no scalar is injected.

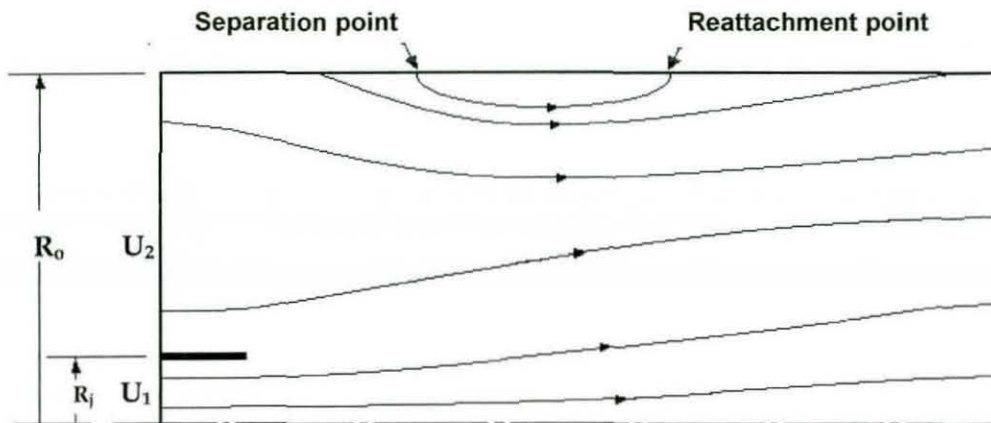
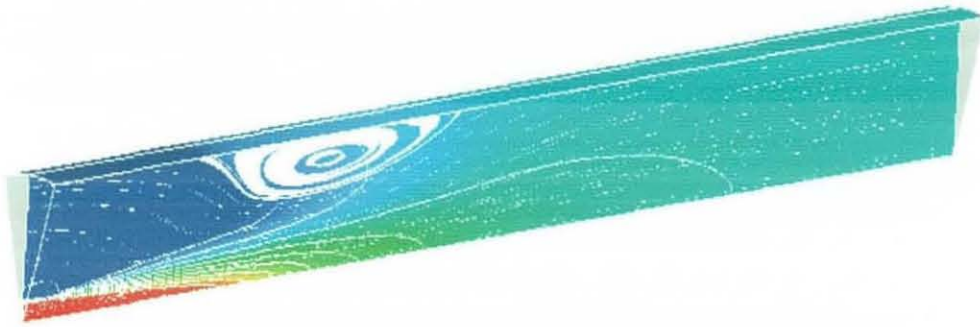
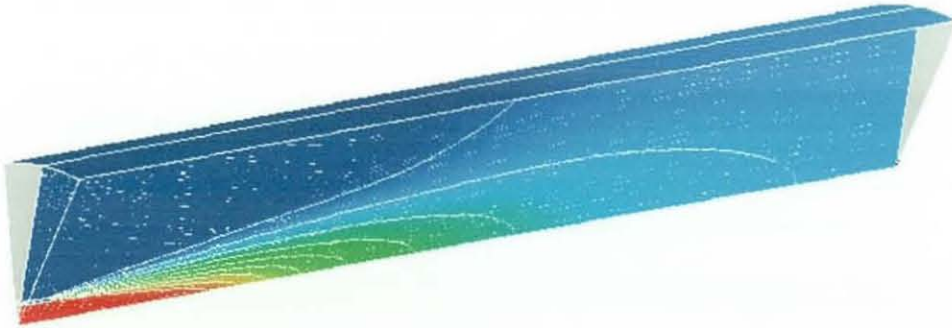


Figure 3.28 The system of coaxial (fuel-air) jets

In Figure 3.29 the particle tracks and conserved scalar contours are shown for two different cases with Craya-Curtet numbers of 0.51 and 0.837 respectively. The separation and reattachment points in the first case are in good agreement with those measured by Becker et al [111]. The second case, where no recirculation occurs, is also in agreement with the experimental results which indicated no recirculation zone was observed with Craya-Curtet numbers above 0.72. In Figure 3.30 the decay of the scalar mean along the centreline is presented for a  $C_c$  value of 0.875 and compared to the experimental data measured by Torrest et al. [112] and the numerical prediction of Elghobashi et al. [110] with very good agreement. The



radial variation of the normalized square root of  $\tilde{f}^{*2}$  at two axial locations for  $C_t$  value of 0.673 are shown in Figure 3.31 and Figure 3.32 and compared with Becker et al measurements and Elghobashi et al. predictions. Hydra calculations are close to the experimental data specially in predicting the peak values and their corresponding locations.

(a)  $C_t = 0.51$ (b)  $C_t = 0.837$ **Figure 3.29** Scalar variable contours and particle tracks

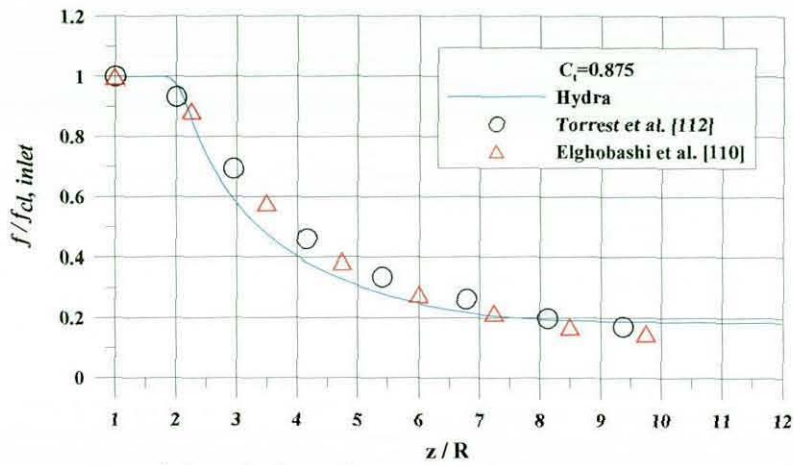


Figure 3.30 Axial variation of concentration mean along centreline

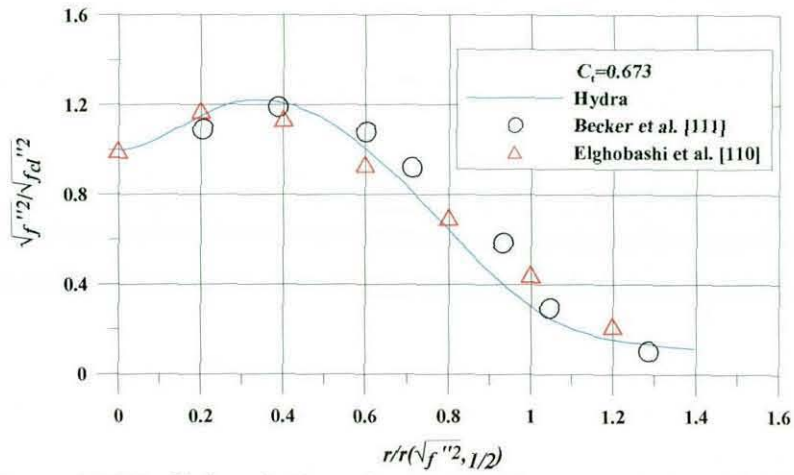


Figure 3.31 Radial variation of concentration variance at  $z/R_j \approx 28$

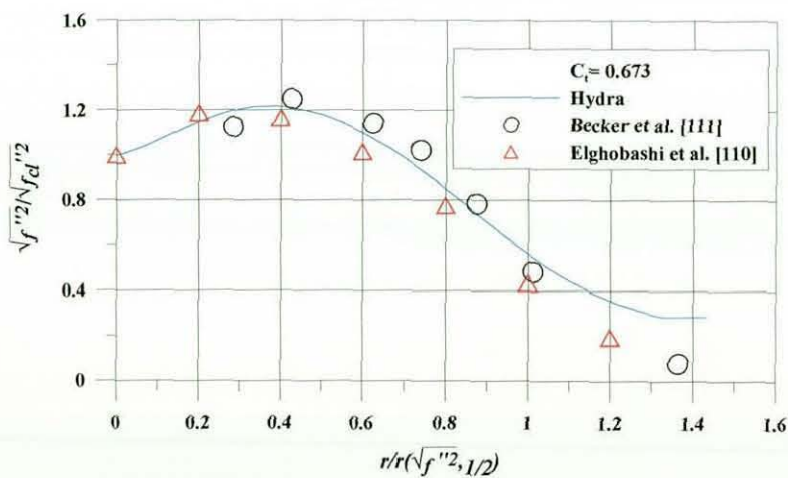


Figure 3.32 Radial variation of concentration variance at  $z/R_j \approx 40$

# Chapter 4

## Jet in Confined Cross Flow (JICCF)

### 4.1 Background Review

The mixing of jets with a cross flow is encountered in many engineering applications in both confined and unconfined environments. Internal cooling of turbine blades, dilution air jets in combustion chambers and jets from VSTOL aircraft in transition flight into ground effect are some examples of jets issuing into a confined cross flow JICCF. Jets issuing into essentially unconfined cross flow (JICF) can be found in many other applications such as film cooling of turbine blades, chimney discharges into the atmosphere and discharge of waste into open waters. Many features of the general structure of jets in confined and unconfined flows are found to be almost the same. Figure 4.1 illustrates the various structures associated with a single jet injected into an unbounded cross flow [113]. The counter rotating cross flow vortex pair is the most dominant vortex system. The jet shear layer vortices, the wake vortices and the horseshoe vortex are often called secondary vortices, as they play a minor role in the far field development of the jet.

The importance of research on JICCF has been recognized as having a significant impact on a variety of practical applications. The interest in research has mostly focused on the gas turbine combustor application, motivated by the strict pollutant reduction regulations which are forcing designers to enhance and develop better methods of the fuel-air mixing. JICCF also plays an important role in the dilution



zone of the combustor where the combustion products are mixed with air to produce an acceptable temperature profile at the turbine inlet. The importance of this flow type to combustion systems means that previous work directing on this problem will now be reviewed briefly.

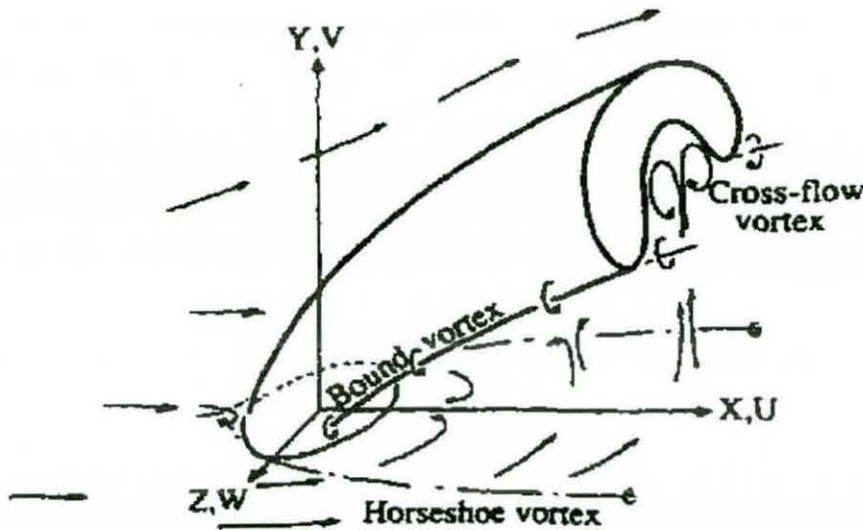


Figure 4.1 JICF various structures [113]

Most previous research studies have focused on investigating the characteristics of the jet-cross flow interaction and its influence on mixing performance in both cylindrical and rectangular confinement geometries with both single and multiple jet injection. The majority of studies involved cold jets of air injected normally into a hot mainstream flow (cross flow) of air [114-123]. The temperature differences were rather small, so that temperature was considered as a conserved scalar field (adiabatic flow) to describe the mixing characteristics of different flow configurations through the following normalised relation

$$\theta = \frac{T_c - T}{T_c - T_j} \tag{4.1}$$

Thus,  $\theta = 1$  represents jet fluid and  $\theta = 0$  represents the cross flow fluid.

Detailed studies involving both velocity and temperature measurements of JICCF reveal interesting structures with the jet as it progresses downstream [113-119]. The jet creates a blockage in the cross flow, and as a consequence, the flow upstream of the jet decelerates causing an increase in pressure. This and the shearing effect of the cross flow deflected around the jet edges causes the deformation of the jet and the bend over of the jet plume trajectory. Turbulent shear layers develop around the periphery of the jet due to high mixing between the cross flow and jet fluid. The lower momentum fluid in the shear layer at the sides of the jet will follow a more curved trajectory than that of the higher velocity fluid in the core. This will form the characteristic kidney-shaped jet profile as shown in Figure 4.1. Downstream of the injection plane, the flow field is dominated by three vortex systems that control the entrainment of the cross flow by the jet (see Figure 4.1); the horseshoe vortex system is formed in the same way as in the flow around a cylinder mounted on a flat surface. These studies also reveal that the key parameters affecting the fluid mixing are:

1. The momentum flux ratio.
2. The number of jet ports.
3. The port shape.

The momentum flux ratio is the ratio of the momentum flux of the jet to that of the cross flow defined as:

$$J = \frac{\rho_j \cdot V_j^2}{\rho_c \cdot V_c^2} \quad (4.2)$$

In the above equation the subscript  $j$  denotes the jet and the subscript  $c$  denotes the cross flow. In cases where the jet and the cross flow have the same species and temperature the above expression can be simplified as:

$$J = \frac{V_j^2}{V_c^2} \quad (4.3)$$

i.e.  $J$  represents the square of the jet to crossflow velocity ratio.

Different flow regimes, described by jet penetration, can be determined within different ranges of momentum flux ratios. The three possible regimes are:

1. Under-penetration.
2. Optimum penetration.
3. Over-penetration.

Under-penetration occurs at low  $J$  values in which the jets are located close to the wall. The cross flow or core fluid is minimally affected by the entraining jets and forms a relatively unmixed core that continues downstream. At optimum penetration the jets interact with the cross flow and better mixing is observed. As the optimum  $J$  value is exceeded, a recirculation region starts to form upstream of the strongly impinging jets. This results in over-penetration with undesirable upstream mixing and large blockage effects. The increased jet penetration towards the centre directs a larger portion of the jet flow toward the duct's core, hence decreasing the circumferential mixing along the walls. Figure 4.2 illustrates the three behaviour patterns of jet penetration as a function of  $J$ . The second contributing factor to jet penetration and mixing is the number of ports used in the configuration. It has been found that by increasing the number of ports in a cylindrical duct, while keeping the overall (total) mass flow ratio constant, jet penetration is reduced [116]. By studying the effect of momentum flux ratio on the mass-weighted standard deviation of temperature from the fully mixed value for different numbers of ports, it has been found [116] that the optimal configuration changes with the number of ports. In addition, at a constant  $J$  value, mixing performance is improved with an increased number of ports.

The third factor is the port shape which has been investigated extensively. Experiments for a fixed number of orifices with round hole, straight slot and slanted slot shape were conducted to investigate the effects on the mixing process [116, 118, 123]. The findings indicate that initial mixing is better for the round holes, but slot ports improve mixing downstream. Round ports with chutes were found to improve the jet penetration and enhance the mixing [116, 118]. By



investigating ports with square, elongated slots and equilateral angles shapes, it was found that larger slanted slot angles and aspect ratios provide generally the best mixing configurations at higher  $J$  values. However, at the lower  $J$  values analysed, square and triangular ports yielded better mixing. Therefore, the design of an optimum mixing section strongly depends on the operating conditions. From these conditions, it is possible to select the appropriate port configuration.

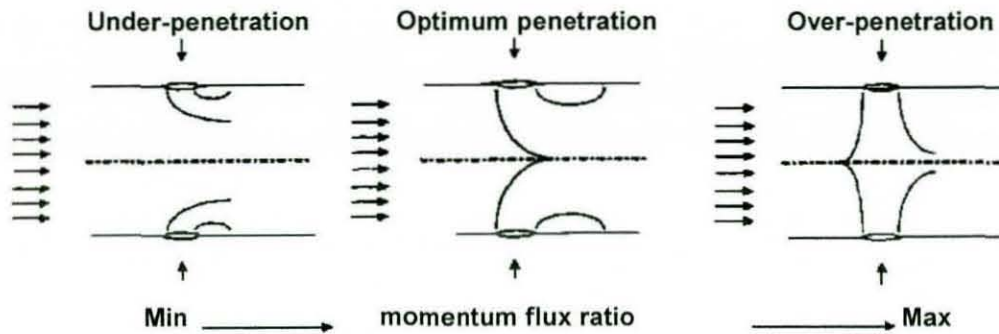


Figure 4.2 Jet penetration as a function of ( $J$ ) [116]

As indicated above, experimental studies have contributed significantly to establish a better understanding of many of the issues related to jet-cross flow interaction. However, test rigs capable of running full scale experiments are expensive to build and operate. Therefore, faster and cheaper approaches are needed. Empirical correlation-based models were used widely during the past two decades [121, 122]. These are useful for estimates of global properties such as jet trajectory, temperature and velocity decay rates but numerical models (CFD) will clearly offer a wider range of applicability. Although many qualitative and quantitative features of jets in cross flow have been predicted with numerical models, many issues affecting accuracy such as grid resolution and turbulence model are not completely resolved. Therefore, in the following section the development in numerical modeling of JICCF during the last two decades will be reviewed.

## 4.2 Numerical Investigations Review

One of first numerical investigation of JICF has been made by Sykes et al. [124]. This early work simplified the calculations by using a slip wall as the cross flow wall. Hence, the cross flow boundary layer was neglected and the horseshoe vortex and wake vortices could not be calculated. In spite of this, the obtained results agreed qualitatively with the measurements of Andreopoulos [117, 119].

The majority of early RANS simulations for jets in cross flow have employed the  $k$ - $\epsilon$  model to obtain the eddy viscosity [125-129]. Patankar et al. [127] used this model to perform a detailed investigation of a jet in cross flow, and even with a very coarse (15x15x10) grid, obtained reasonable agreement with experimental data for the jet trajectory. Jones and McGuirk [128] used still a coarse (20x15x15) grid but obtained only qualitative agreement with measured velocity profile data due to the low grid resolution although trajectory predictions were again good. Demuren [129] investigated the grid resolution requirements in his numerical calculations for a row of jets in cross flow. Results on (37x70x14) grid were shown to capture the experimental trends reasonably well. By using a 5-level multigrid method (with a fine grid of about 2.4 million cells) and  $k$ - $\epsilon$  model, Claus and Vanka [130] were however still not able to capture the horseshoe vortex system and achieve complete grid independence of the computed velocity and turbulence fields.

The question of the adequacy of the grid resolution cannot of course be separated from that of the order of accuracy of the numerical scheme. Most studies from this time period (early 1990's) used the hybrid upwind-central difference scheme to approximate convection terms, which is known to be highly diffusive. Studies in which higher-order schemes such as the QUICK scheme were utilized showed that similar results as obtained with lower-order schemes could be obtained on coarser grids [131, 132]. However, higher-order schemes tend to suffer from lack of boundedness in regions with high gradients. The inadequacy of the turbulence



model was also questioned in these early calculations which used reasonably fine grids or higher order schemes (or both) due to the lack of agreement between computed results and experimental data particularly of turbulence kinetic energy.

In 1992, Demuren [133] studied turbulence model effects by applying a multigrid procedure with both the  $k-\epsilon$  model and the Reynolds stress model. The results were compared to experimental data of Atkinson et al. [115] for opposed jets in cross flow, see Figure 4.3. For the mean flow, there was little to choose between both model predictions, but the Reynolds stress model clearly gave better predictions of Reynolds stress profiles.

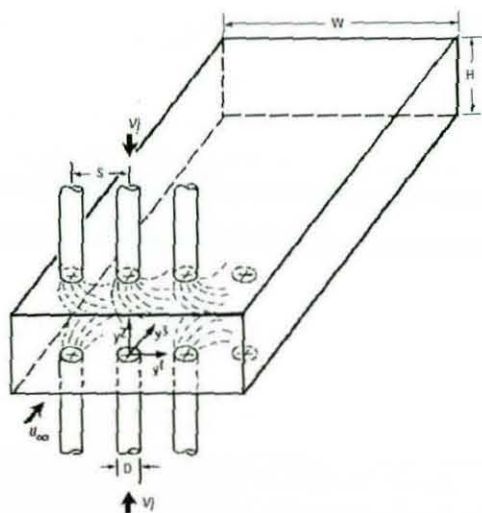


Figure 4.3 Opposed jets in confined cross flow in a rectangular duct [133]

Pathak et al. [134] have recently (2006) referred to this question of turbulence model importance in JICF and carried out a detailed computational investigation of the 3D mean flow field resulting due to the interaction of a rectangular heated jet issuing into a cross flow in a narrow channel. They used the SIMPLE algorithm within the commercial Fluent code (segregated solver) to predict the mean flow and temperature fields for a jet to cross flow velocity ratio of 6 using the standard  $k-\epsilon$  and the RSTM turbulence models. They adopted a series of hexahedral grids of

increasing node density in their solution. The finest grid, as shown in Figure 4.4, contained about 729,000 cells. Important flow features such as the formation of different vortical structures and their effects on the flow field were described to be predicted well by both turbulence models. The predicted mean and turbulent flow properties from both models were shown to be in good agreement with the experimental data. The performance of the RSTM approach was, however, found to be better than that of the standard  $k-\epsilon$  model especially in predicting the shear stresses in regions with highly nonlinear flows in support of the findings of Demuren [133]. The authors mentioned the long time it took for the solution to converge (13 days of CPU time on Pentium 4 machine). The mesh implemented had equal cell size over all the domain; further reduction in calculation time would be possible if the mesh were optimized by performing local refinement of the grid in high gradient regions and grid coarsening in low gradients regions. The multigrid technique may also enable the additional cost to be minimized by ensuring grid-independent convergence rate. This work provided some useful information but is also a good example of the high computational cost imposed by a non-optimised numerical grid.

From the above two studies, it may be concluded that if highest priority lies in predicting the mean flow, the use of an advanced turbulence model beyond the  $k-\epsilon$  turbulence model is not necessary.

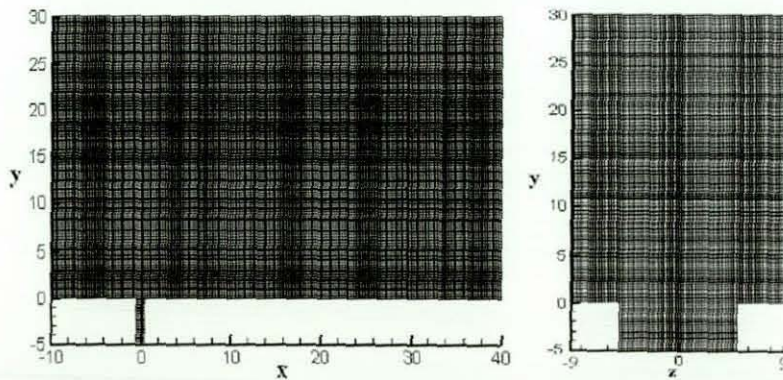


Figure 4.4 Numerical hexahedral grid at x-y and y-z plane [134]



Most of JICCF experimental and numerical investigations have been performed assuming uniform velocity and turbulence profiles at the entry into the solution domain of both the cross flow and the jets. There are two reasons for this. Firstly, uniform profiles can be implemented easily in numerical calculations. Secondly, a uniform profile jet assumption simplifies the computational grid to be used as the port geometry and any geometry of the supply plenum feeding the ports need not be considered. However, the accuracy of the numerical results may be influenced by the acceptability of these choices and may adversely affect comparison with experimental data. In 1990, Carrotte and Stevens performed measurements in a fully annular test facility, downstream of a row of heated jets injected into a confined cross flow at a momentum flux ratio of 4 [113]. They concluded that the use of a uniform velocity profile over the jet geometric inlet area may result in a flow with jet over-penetration and mixing characteristics which are not representative of the actual flow. In order to capture the jet and cross flow coupling, they suggested to model an effective port flow area corresponding to the geometric port area multiplied by a designated discharge coefficient ( $C_D$ ), where the  $C_D$  value was chosen to correct for the effects on the flow through the port of the jet/cross flow interaction in the main flow area. A much better solution would be to simulate directly in the numerical calculation a flow entering the port from a plenum feed volume. An attempt to address this problem was reported by Kim and Benson [135], who included a pipe feeding the jet port in the calculation domain.

In 1993, Baker and McGuirk presented one of the early numerical studies which attempted to take the supply annulus/port flow configuration effects into account [136]. Using the QUICK discretisation scheme, 3D numerical calculations with the  $k-\epsilon$  turbulent model demonstrated good qualitative agreement with the experimental data but displayed several features at variance with the data. The size of the backflow generated at impingement was over-predicted by about 40 percent

and the hole discharge coefficient was in error probably due to using the castellated mesh approximation of the hole shape.

In 1996, Bain et al. [137] using the CFD-ACE RANS code with the standard  $k-\epsilon$  turbulent model and a multi-block grid with about 60,000 hexahedral cells to perform 3-D numerical calculations on a port flow geometry with and without the addition of plenum to feed the jet as shown in Figure 4.5. This geometry was selected as representative of the plenum-fed quick-mix section of a Rich Burn/Quick Mix/Lean Burn combustor. The calculations showed that the jet velocity entering the combustor was very non-uniform, with a low through port velocity at the leading edge of the port and a high velocity at the trailing edge. A no-plenum case with specified uniform inlet jet profile was analysed but it did not match with plenum-fed calculations. This indicates a strong coupling between the jet flow and the mainstream flow which can not easily be captured by specifying uniform jet velocity boundary conditions over the port surface itself. The authors concluded that the only way to predict accurately the jet-in-cross flow is to include both the interior and the exterior (plenum) in the CFD analysis. This coupling approach also allowed the CFD analysis to capture the effect of liner thickness on jet penetration and mixing. The authors found that the velocity profiles at the port exit for thick-walled and thin-walled liner cases exhibited similar characteristics, although one significant difference seen was that the velocity profiles for the thin-walled case penetrated farther into the mainstream flow which means more jet penetration into the quick-mix zone than for the thin-walled case.



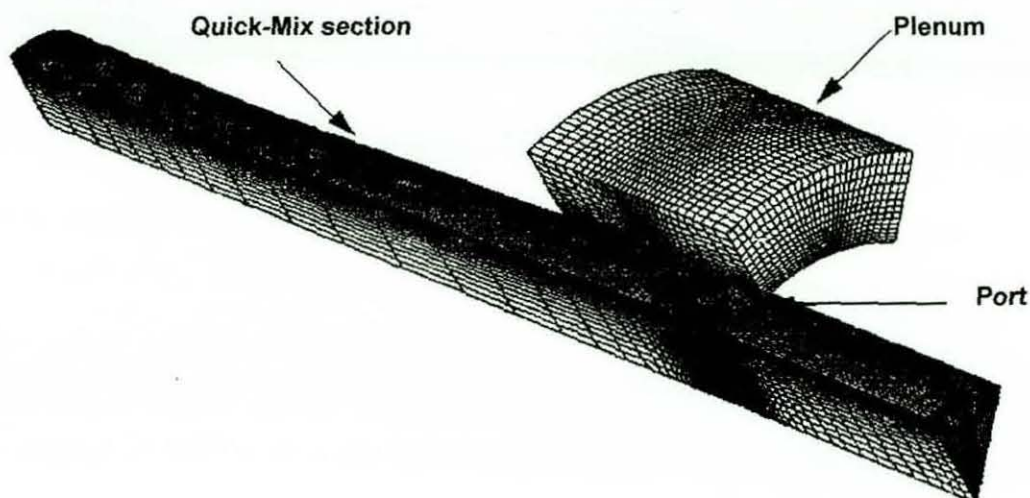


Figure 4.5 Computational mesh of coupled combustor geometry [137]

Spencer in a detailed experimental and numerical investigation solved RANS equations with the  $k-\epsilon$  model to predict the coupling of annulus/liner, port/core flows [46]. He reported good agreement with experimental data for jet exit angles and velocity fields while turbulence levels were under-predicted within the core area. The most probable reason was the low resolution of the numerical grid. The computations and experiments of Spencer form an important test case for the present research. Hence, further discussions of the details of this flow problem are provided in the following section.

It can be concluded from the above review that numerical models offer a practical choice as predictive tools of jets in cross flow over a wide range of applications. The three dimensional complex jet-cross flow interactions under different conditions and with different configurations can be analysed with acceptable accuracy. However, some questions still need further investigation these include the effects of grid resolution, turbulence model and boundary conditions on the overall accuracy of computed results. For many reasons, as discussed in chapter one, it is of interest to examine the performance of unstructured grid methods

when applied to this test case. In the following sections the capability and the accuracy of the Hydra unstructured CFD code will be compared to experimental data and other unstructured and structured numerical predictions. The influence of the grid resolution, grid type and boundary conditions on the solution accuracy will be tested and improvements to the solver proposed.

### **4.3 Previous Experimental and Numerical Work on the Selected Test Case**

The particular JICCF configuration which has been selected in this study to validate the numerical methodology of Hydra is the one studied experimentally using the LDA technique by Spencer [46] and recently using the PIV technique by Hollis [138]. Spencer used the experimental data to assess the three-dimensional, structured, incompressible RANS solution. The computational work focused mainly on improving the port representation within CFD models. Further numerical investigations were carried out by McGuirk and Spencer [47] to study the importance of annulus-port-core coupled and uncoupled calculations on the primary zone flow patterns.

A water model of a simplified generic geometry which represents a generic combustor annulus-port-core system was used to investigate the strength of the interaction between annulus and core flows and the influence of the port shape on the jet characteristics at port exit. A schematic of the experimental setup [47] is shown in Figure 4.6. It consists of two circular pipes 600 mm long; the inner was held concentric with the outer at each end through a set of NACA 0015 struts. The water flows vertically downwards from a constant head tank through the inner core pipe and the outer annular duct. The inlet mass flow split between the annulus and core was controlled by a valve mechanism. To facilitate laser measurements, a strut and worm gear were used to rotate the inner pipe relative to the laser optical axis which therefore presented a differential azimuthal plane to the measurement plane. The test section, as shown in Figure 4.7, consisted of two



concentric cylinders with a single row of six equally spaced circular ports. The length of the test section was 180 mm while the radii of the inner and outer cylinders were 45 mm and 70 mm respectively with a 5 mm wall thickness. The ports were 20 mm in diameter with their centres located 90 mm from the inlet. With different port shapes, a wide range of bleeding ratios  $B$ , ( $B = Q_b / Q_a$ ) and core-jet velocity ratios  $R$ , ( $R = V_j / U_c$ ) were investigated. The case with  $B=50\%$ ,  $R=5$ ,  $Re_j > 2.4 \times 10^4$  and circular shape port was selected here as measured and predicted in previous work [46]. This case will be used as a test case for unstructured calculations because with these ratios all the flow features such as jet penetration, core vortex and annulus separation and reattachment are present strongly within the flow field.

The RANS code employed by Spencer was based on a pressure-correction methodology and a cell-centred finite volume discretisation scheme. The standard high Reynolds number two-equation  $k-\epsilon$  turbulence model was used with the standard wall function approach adopted for solid wall treatment. The diffusive fluxes were evaluated using central differencing, whereas the convective fluxes were evaluated using the HYBRID differencing scheme. The numerical solution was considered as grid independent with a computational grid of around 60,000 cells as shown in Figure 1.10. A large number of iterations ( $\sim 15,000$ ) were required for the solution to converge due to slow convergence of the centreline, where the cell aspect ratios were unavoidably high.

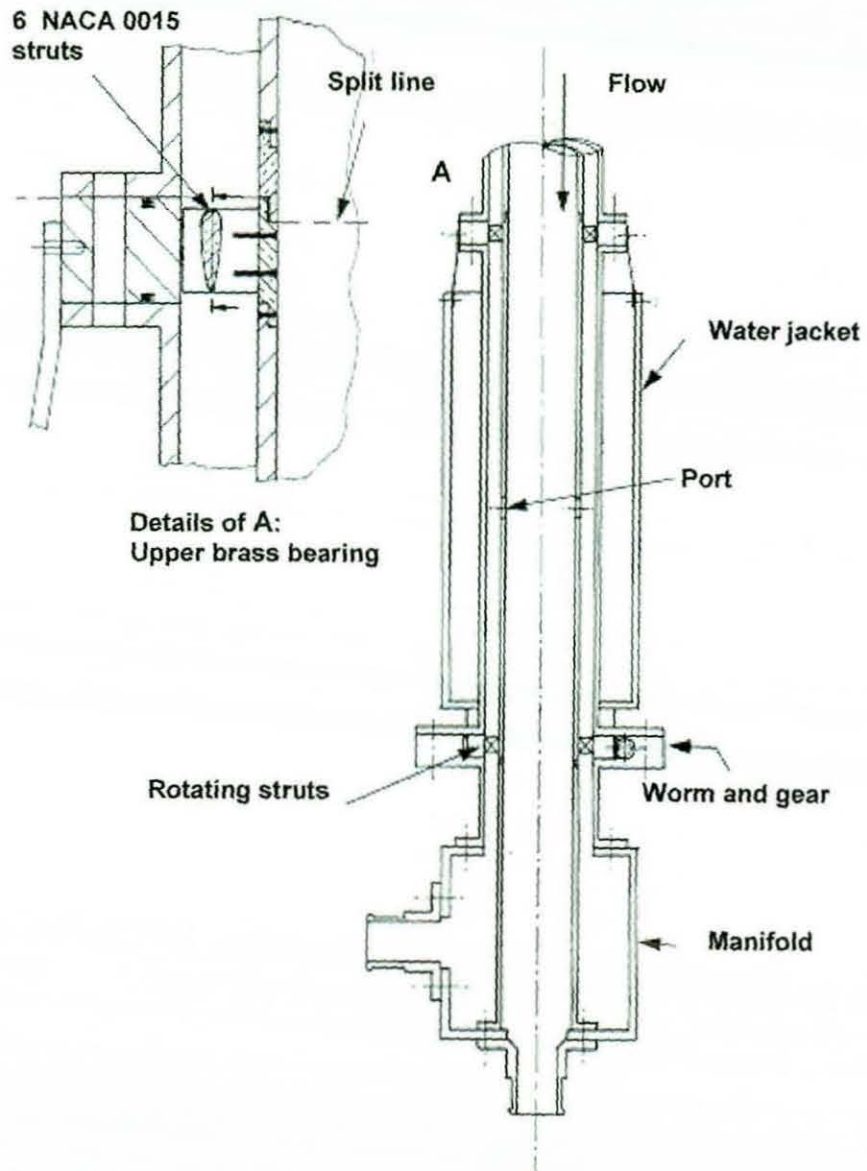


Figure 4.6 Schematic of the experimental setup [46]



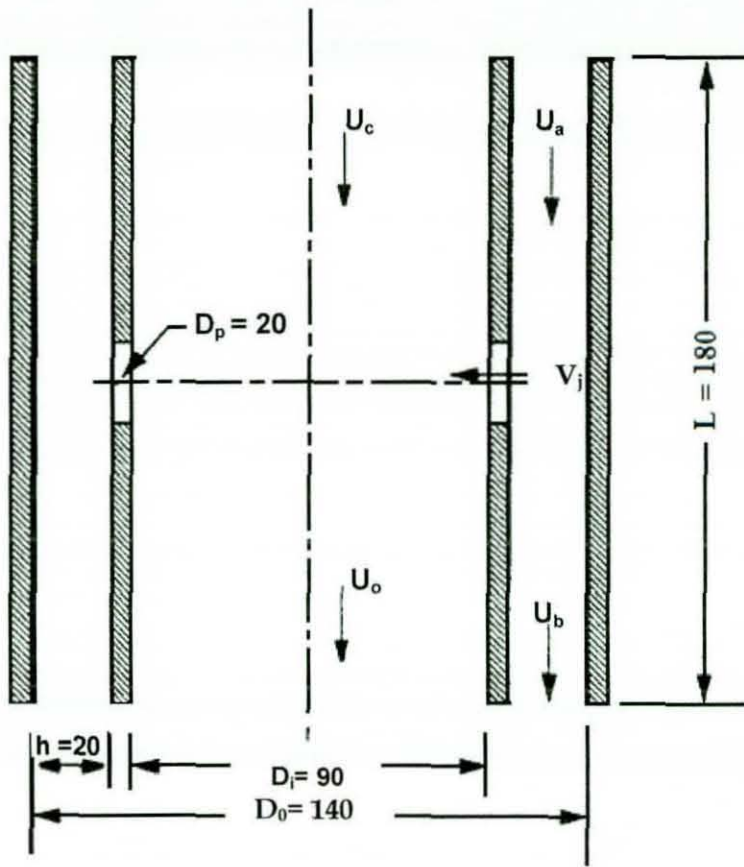
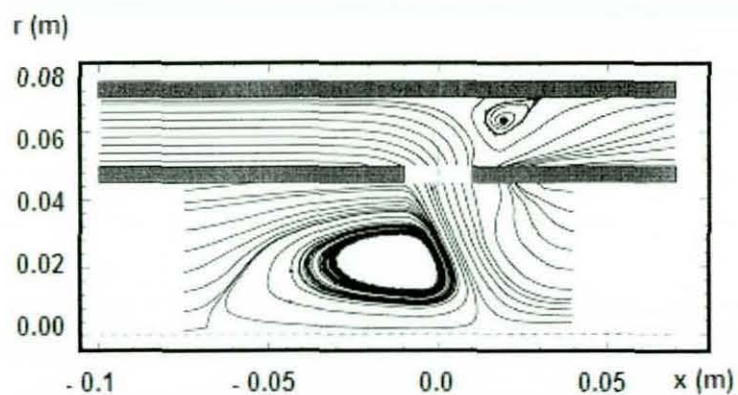


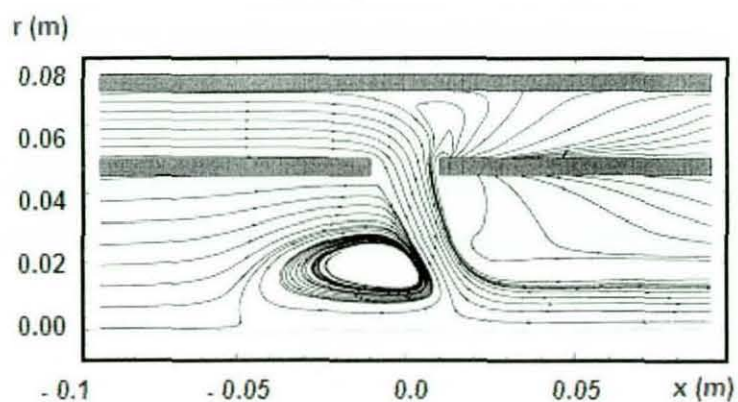
Figure 4.7 Test section dimensions and nomenclature

To highlight the main features of the flow field and provide a convenient qualitative comparison between previous predictions and measurements, the particle tracks shown in Figure 4.8 on the plane of symmetry through the port were presented in [46]. In the core region, the predicted upstream vortex appeared weaker and was spread over a shorter distance in both axial and radial directions compared to measurements. In the annulus region, the vortex associated with separation in the vicinity of the upper wall downstream of the port was not captured by the numerical solution. Figure 4.9 provides quantitative comparisons between data taken using both experimental techniques and the numerical

predictions of [46]. Axial and radial velocity profiles are shown on the plane of symmetry at two axial locations ( $x = -5$  mm and 5 mm). These two lines are selected to pass through the main flow features like the upstream vortex in the core, jet shear layers, the port region, and the annulus separation region. Starting with the core zone, LDA data taken at  $x = -5$  mm indicated a negative axial velocity at the core centreline ( $r = 0$ ) 20% higher than the PIV measurement. This difference decreases radially until it vanishes at  $r = 0.02$  m. Quite good agreement between the two measurement techniques can be seen in the  $x = 5$  mm profile. Near the port exit ( $r = 0.045$  m), a further discrepancy between the predictions and measurements is observed in the maximum radial velocity value. LDA shows a 20% and 40% increase in the radial velocity near port exit compared with PIV at  $x = -5$  and 5 mm locations respectively. This may be due to a slight difference in the momentum flux ratio ( $R = 5$ ) [138] between the two experimental setups. Numerically, the core centreline axial velocity was badly under-predicted (up to 50% smaller, compared to the experimental data). In the annulus region, it can be noticed that the predicted radial velocity agreed with experimental data reasonably in both locations while the axial velocity appears to be under-predicted as the profiles approach the separation zone in the vicinity of the upper wall. Figures 4.10 and 4.11 provide comparisons between the experimental data taken at the port exit and the numerical predictions of the axial and radial velocity components and turbulence levels respectively. The port was experimentally seen to have a region of reverse flow at the front of the port indicated by the negative radial velocity over  $x/r_{port}$  of -1.0 to around -0.7 (see Figure 4.10). The reverse flow region has been smeared by the predictions, indicating that the flow has not been fully resolved in this region. In Figure 4.11, the turbulent kinetic energy levels are reasonably well predicted over the rear three-quarters of the port, whereas it is underpredicted in the reverse flow region.



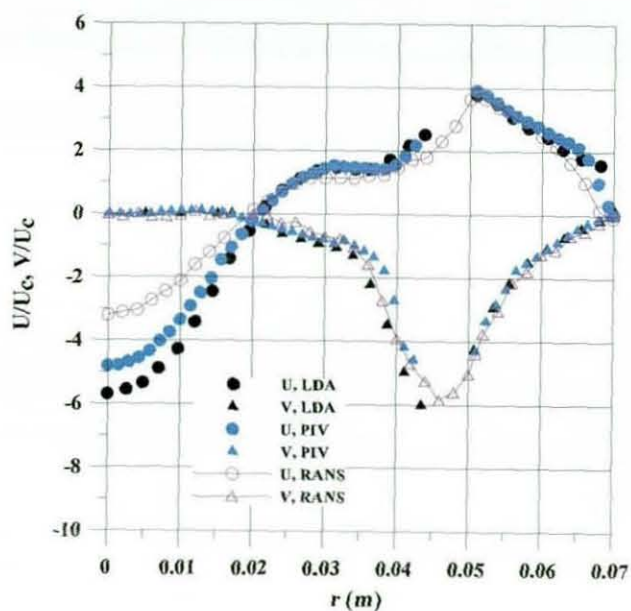
(a) Experimental



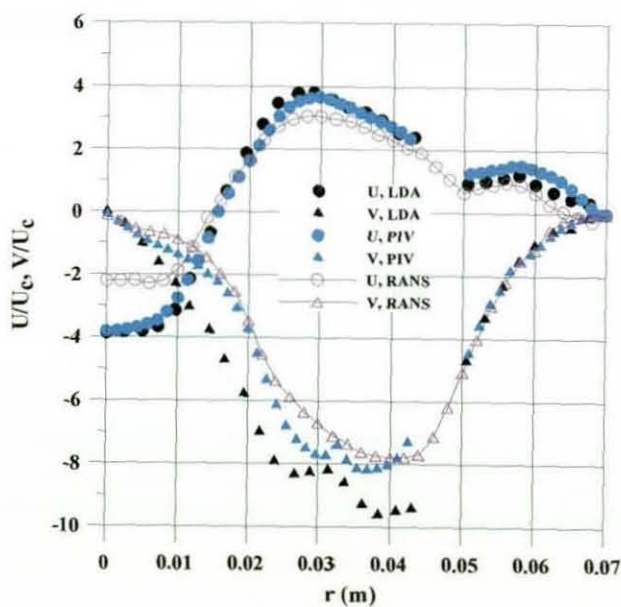
(b) Numerical

Figure 4.8 Particle tracks on symmetry plane [46]





(a)  $x = -5 \text{ mm}$



(b)  $x = 5 \text{ mm}$

Figure 4.9 Numerical and experimental velocity profiles on the axial plane of symmetry [46, 138]

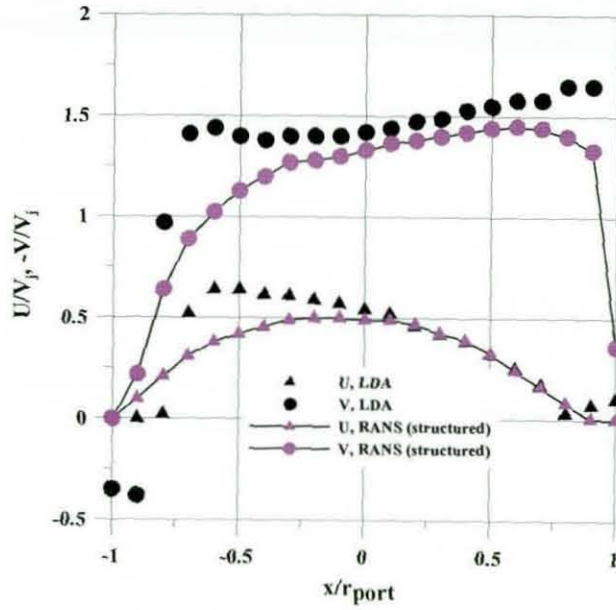


Figure 4.10 Velocity profiles at port exit  
(Experimental and structured predictions vs. RANS structured) [46, 138]

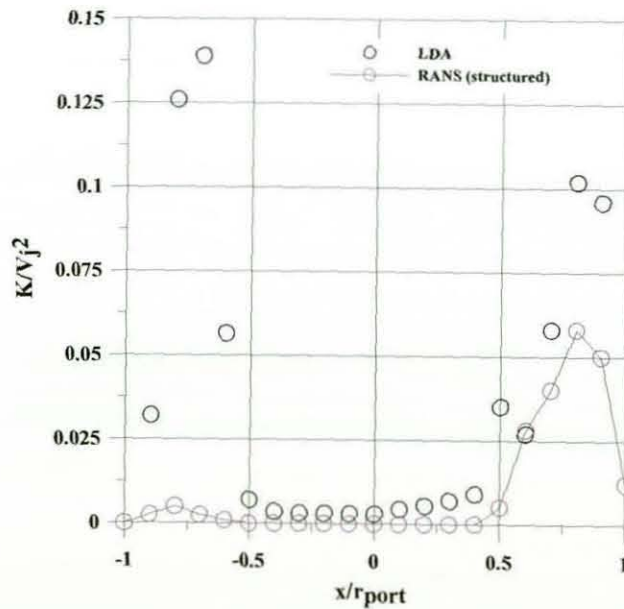


Figure 4.11 Turbulent kinetic energy at port exit  
(Experimental measurements vs. RANS structured predictions) [46, 138]

#### 4.4 Present Unstructured Mesh Numerical Predictions

In this section the JICCF case described above will be simulated using both Fluent and Hydra as two different unstructured codes. The Fluent segregated solver, which is based on pressure-correction methodology, was selected because it represents the standard methodology for prediction of low speed incompressible flows and is therefore a useful benchmark comparison for the Hydra code which is adopting a density-based compressible flow approach.

Apart from the solution methodology (density-based for Hydra and pressure-based for Fluent) a further important difference between the two codes lies in the selection of the control volume. Fluent uses a cell-centred approach treating each primary grid cell as a finite volume, while Hydra (as discussed in the previous chapter) uses a vertex centred approach constructing a dual mesh to build the finite volumes around vertices. Since the number of cells in a typical 3D unstructured tetrahedral grid is around 6 times greater than the number of vertices, the cell centred approach stores approximately 6 times more variables than the vertex centred approach. It is clear that for the same primary grid the cell-centred method consumes more memory more than the vertex centred approach but may deliver more accurate results since there are more control volumes. For the hexahedral grids, the above arguments do not apply as the number of cells and vertices are approximately identical. In what follows, is important to compare solutions across different grid types that consist of the same number of cells.

In CFD simulations, the grid should be fine enough to capture the flow gradients and to minimise the numerical errors. This is usually achieved by meshing with different numbers of grid cells and observing the change in a certain quantity of interest until the solution becomes grid independent. To investigate the influence of grid type and grid density on the JICCF case solutions with different sizes of hexahedral and tetrahedral grids have been employed. Three grids with sizes of 100,000 cells (grid A), 560,000 cells (grid B) and 1,100,000 cells (grid C) were



generated using Gambit the standard grid generator of Fluent [139]. Due to symmetry and to reduce the numerical cost, only a  $60^\circ$  sector of the geometry, as shown in Figure 4.12, has been considered (contains just one port). The tetrahedral grid shown in Figure 4.13(a) is the finest grid employed in the calculations (*grid C*) with about 1,100,000 cells and 200,000 nodes. The nodes are distributed as follows: 140 nodes distributed equally along the centre line, 50 nodes in the radial direction (35 nodes in the core pipe and 15 nodes in the annulus pipe) and 50 nodes on the outer circumferential wall. The port is meshed using 50 nodes on the circumferential periphery and 6 nodes in the radial direction of the wall port as shown in Figure 4.13(b). The hexahedral grid mesh (*grid B*) in Figure 4.14(a) is meshed with about 560,000 nodes and almost the same number of cells. 180 nodes were distributed along the centreline, 60 nodes in the radial direction and 85 nodes on the outer boundary. The port has 100 nodes on its circumference and 6 nodes in the liner wall as shown in Figure 4.14(b). Meshing the tetrahedral grid was straight forward and accomplished with a single volume. While the main volume was divided into 24 sub-volumes in order to produce the hexahedral grid. This task is time-consuming but it provides more flexibility in grid local refinement process in certain regions since each sub-volume can have a different grid resolution.

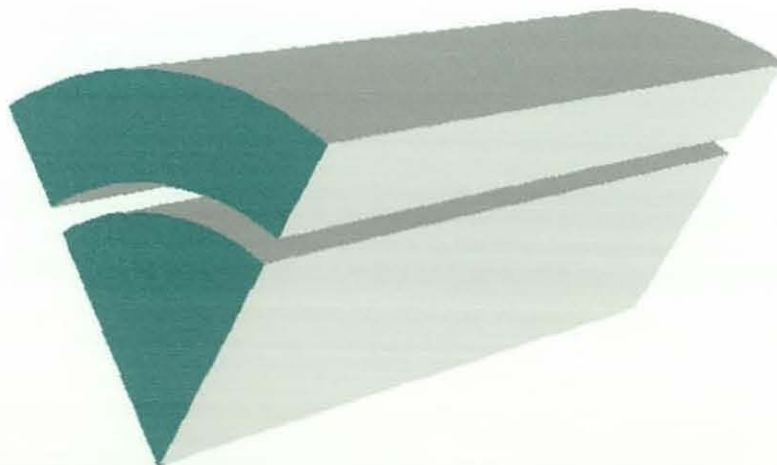
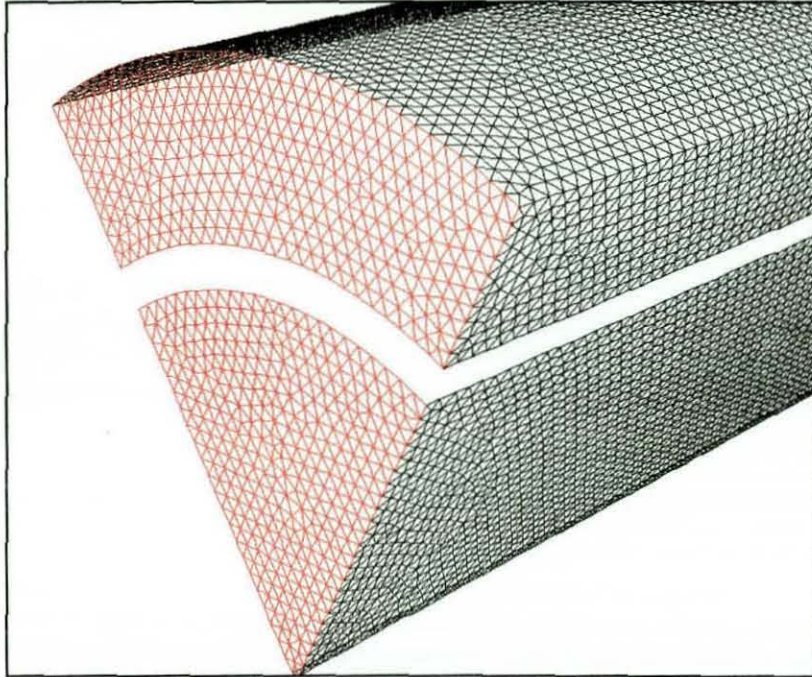
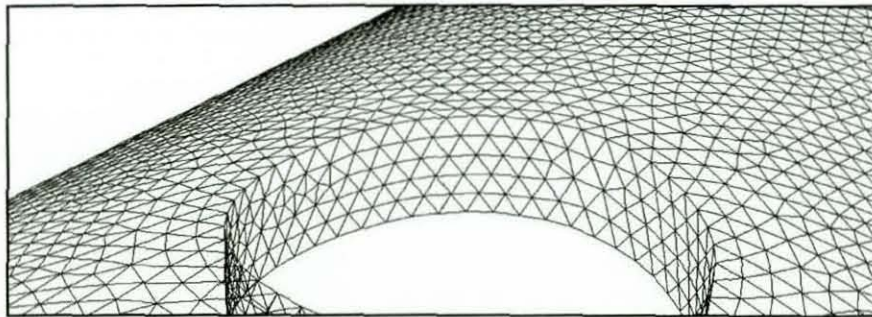


Figure 4.12 Computational domain ( $60^\circ$  sector with single port)



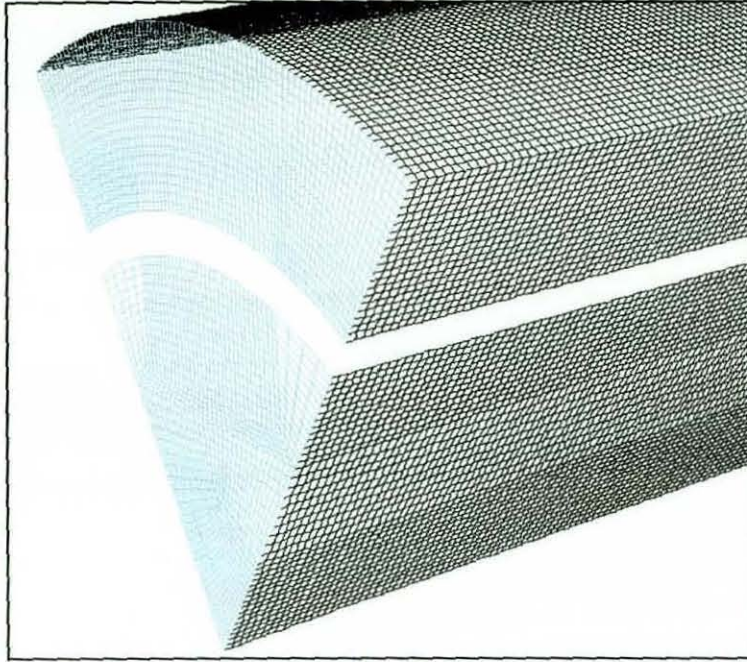


(a) Outer boundary grid

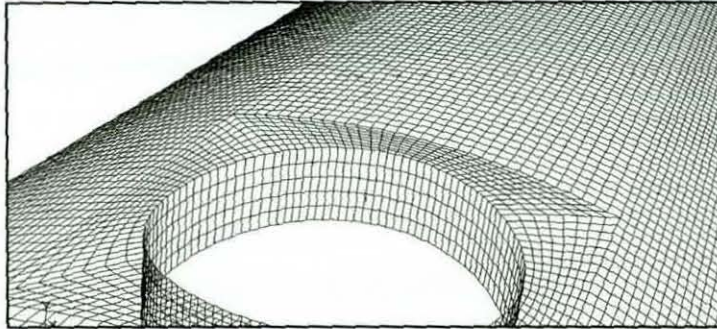


(b) Port region grid

Figure 4.13 Tetrahedral computational grid



(a) Outer boundary grid



(b) Port region grid

**Figure 4.14 Hexahedral computational grid**

At the start of the work presented in this chapter, the inlet boundary conditions in Hydra were still limited to the two standard types, a far field boundary condition, where free stream Mach number could be specified, and a total pressure-total temperature boundary condition. Both types are not suitable for the case under investigation. The total pressure-total temperature boundary condition represents a possible boundary condition for use in Hydra calculations, but this is made problematic since the available experimental data were of velocity and turbulence

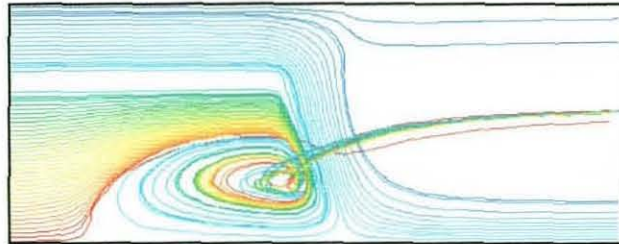


quantities and total pressure was not measured. To overcome this problem initially a Fluent calculation was carried out using experimental data at the inlet boundaries. From this calculations total pressure and total temperature as predicted by Fluent at the inlet boundary were extracted from the converged solution and used as inlet condition. This illustrates the need to develop the fixed velocity condition as described in the previous chapter.

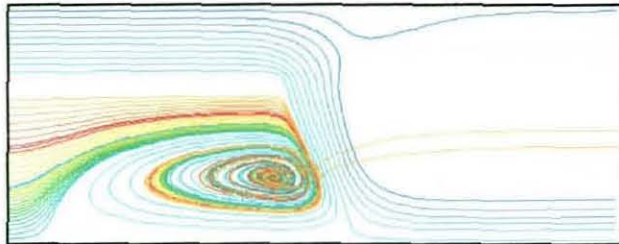
Since the experimental data were obtained using water as the working fluid while the CFD codes used air as the working fluid, the corresponding flow quantities for air at the inlet boundary were obtained by equating the Reynolds number of the flow. The bleed ratio ( $B= 50\%$ ), the jet Reynolds number ( $Re_j \approx 2.4 \times 10^4$ ) and the core-jet velocity ratio ( $R= 5$ ) were achieved by performing repeating runs with Fluent to adjust the pressure at the core and annulus exit until the correct flow split was obtained. These static pressures were then used in the Hydra calculations also at the core and annulus outlets. A series of Fluent calculations were carried out to obtain grid independent solution using the above mentioned various grids types. In these calculations, the SIMPLE scheme was adopted for the pressure correction equation, with first order upwind scheme for both momentum and turbulence equations.

Qualitatively, grid independency can be checked by monitoring the particle tracks created by injecting particles on a radial line at the inlet of the domain on the plane through the port centreline. Figures 4.15 and 4.16 represent these particle tracks for the different sizes and types of grids. They reveal discrepancies in different zones. Firstly, the separation and reattachment of the flow close to the annulus outer wall shows different behaviour with different grid sizes. Coarse grids (e.g. grid A) were not able to capture the vortex associated with the separation; finer grids did capture this (grid C) but the flow reattachment point moved downstream as the grid became finer. Secondly, the upstream core vortex size was predicted to be larger with finer grids (compare A and C); this behaviour was similar on both

hexahedral and tetrahedral grids, although the coarse grid tetrahedral solutions were farther from the fine grid solutions than for hexahedral meshes.

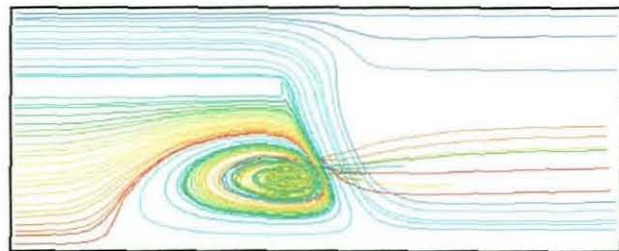


Grid A

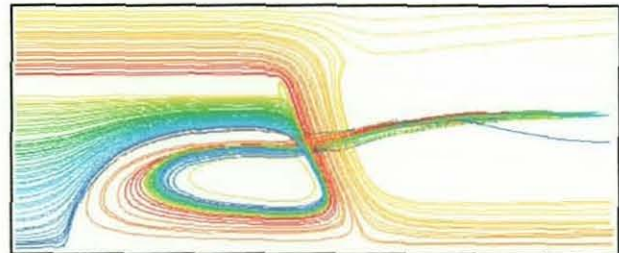


Grid C

Figure 4.15 Flow particle tracks using Fluent with hexahedral grids



Grid A



Grid C

Figure 4.16 Flow particle tracks using Fluent with tetrahedral grids

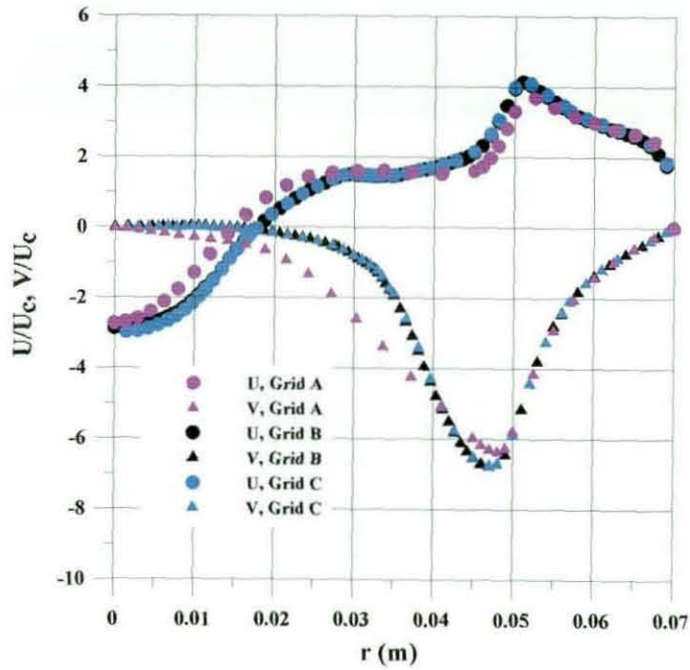


Hexahedral and tetrahedral coarse grids underpredicted the size of the upstream core vortex by 30% compared to the experimental data. This was reduced to 15% and 10% with the fine hexahedral and tetrahedral grids respectively. Quantitatively, Figures 4.17 and 4.18 show the axial and radial velocity profiles at the two axial locations in the plane of symmetry discussed in the previous section,  $x = -5$  mm and  $x = 5$  mm. For the hexahedral grids (Figure 4.17), the solutions are almost identical in the annulus region with a slight difference in the boundary layer region while in the port and the core, where high gradient flows exist, differences can be noticed (especially in the centreline axial velocity which has a significant influence in determining the size of the upstream vortex) between grids A and B, but little change between grid B and C. For hexahedral grids, B and C seem to represent a grid independent solution. In case of tetrahedral grids, the differences are limited to high gradient zones. Only the fine grid was able to predict well the annulus, the boundary layer region, and the centreline axial velocity. Further refinement did not show any more improvement except for port local refinement. Therefore, the fine grid solution will be considered as the accurate solution and will only be used in the rest of the chapter.

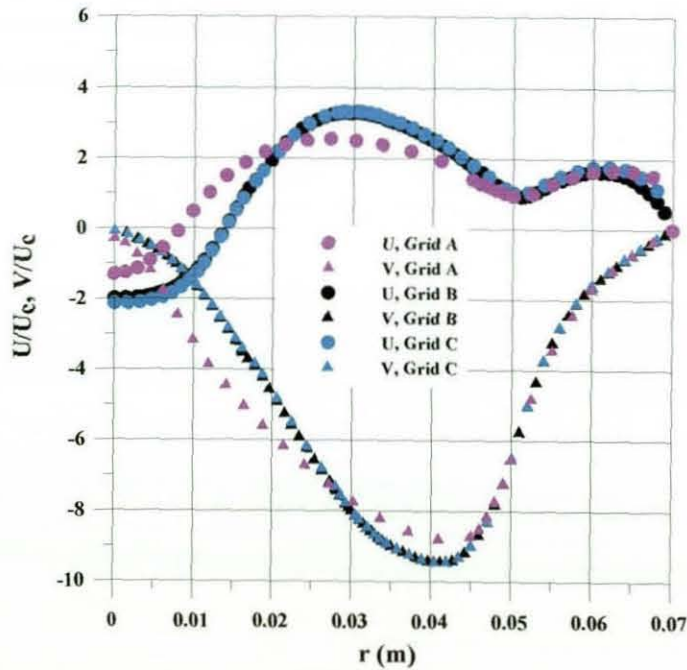
Figures 4.19 and 4.20 represent some comparisons between the numerical predictions and the LDA and PIV experimental data. For the hexahedral solution, in figure 4.19 the centreline axial velocity has been badly under predicted to be around 50% of the experimental value at  $x = -5$  mm and  $x = 5$  mm. Tetrahedral solution, as can be noticed in Figure 4.20, predicted the centre line axial velocity to be identical to the experimental results at  $x = 5$  and while it is 20-30% less at  $x = -5$ . At the port exit which determines the strength of the jet penetration, the hexahedral solution was in good agreement with LDA data while the tetrahedral solution was much closer to the PIV data. Figure 4.21 and 4.22 presented to compare the previous numerical solution which was produced by using a relatively coarse hexahedral structured grid with the unstructured solutions obtained with fine grids. In Figure 4.21, both the structured and the hexahedral

unstructured solutions show good agreement in predicting the axial velocity in core zone. While in the annulus it is obvious that structured solution was not able to well predict the separation where large differences in velocity values can be noticed. For the tetrahedral grid as shown in Figure 4.22, both solutions are identical in predicting the radial velocities while significant differences are obvious in the axial velocities.

The port exit velocities play a crucial role in determining the jet penetration strength and therefore the mixing process. In Figures 4.23 and 4.24 comparisons are presented to investigate the ability of numerical predictions to resolve this aspect of the complex port flow. In the experimental data, the negative velocity at the front of the port indicates that separation has occurred inside the liner wall and flow is actually directed from the core into the port over a small region. Due to low grid resolution, the structured solution was not able to capture this phenomenon while it has been well predicted by the tetrahedral grid solution and, to a lesser degree of accuracy, by the hexahedral unstructured solution when compared to the experimental data. Similar behaviour can be seen from the turbulent kinetic energy levels (Figure 4.25 and 4.26) where the tetrahedral grid showed better solution in the reverse flow region, indicating that the flow was not fully resolved by the hexahedral grid in this region. In the centre of the port, both unstructured solutions are almost identical to the experimental data while the structured solution predicted the axial velocity to be around 10-15% less and almost same axial velocity.



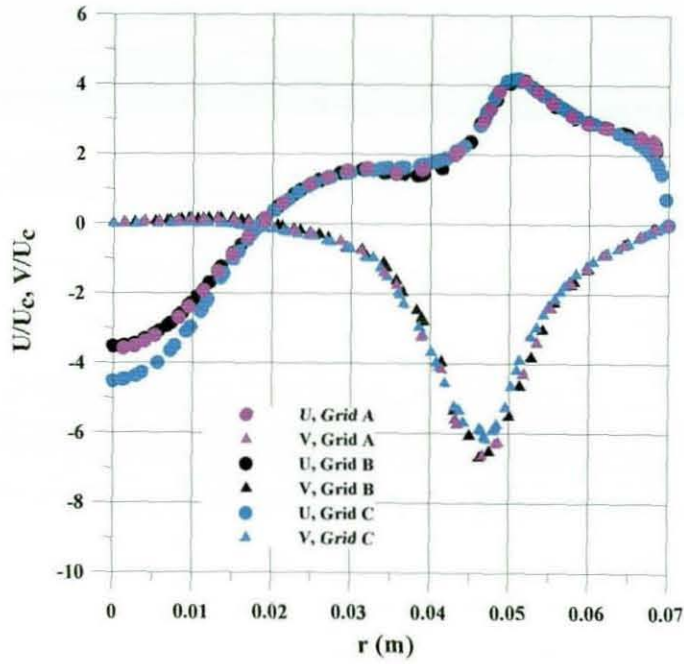
(a)  $x = -5$  mm



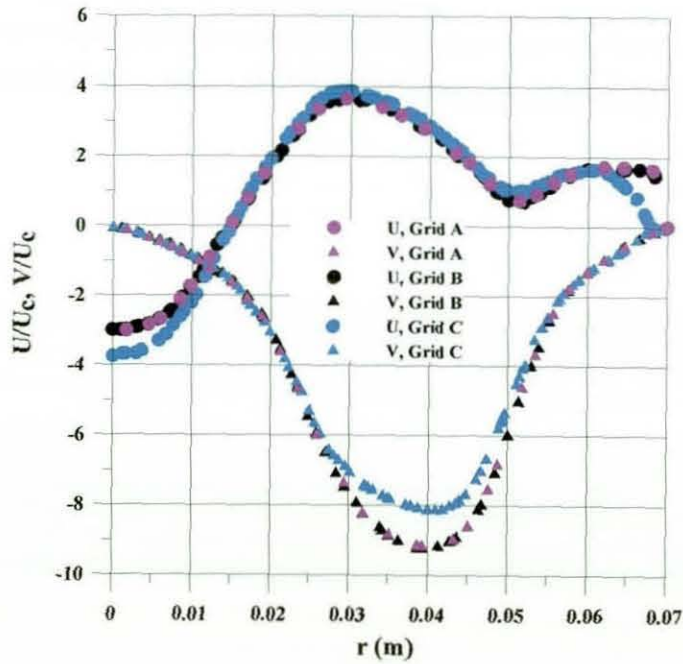
(b)  $x = 5$  mm

Figure 4.17 Velocity distribution using Fluent with hexahedral grid



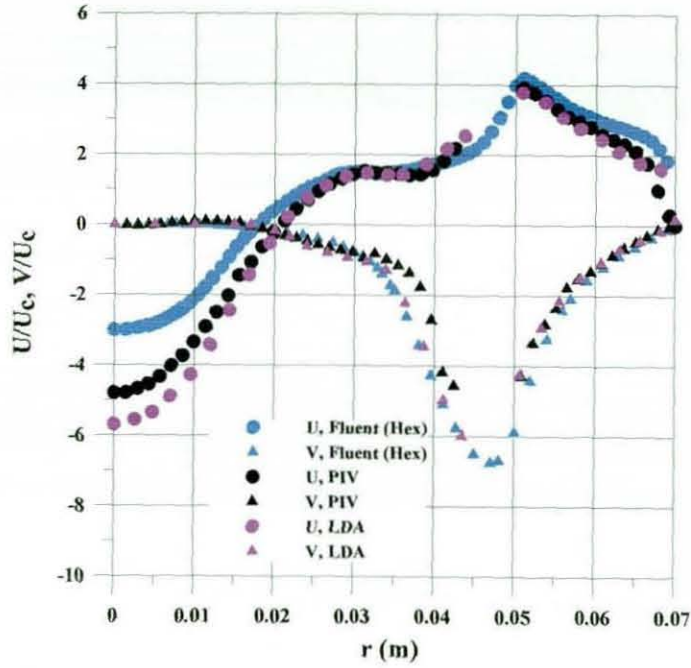


(a)  $x = -5$  mm

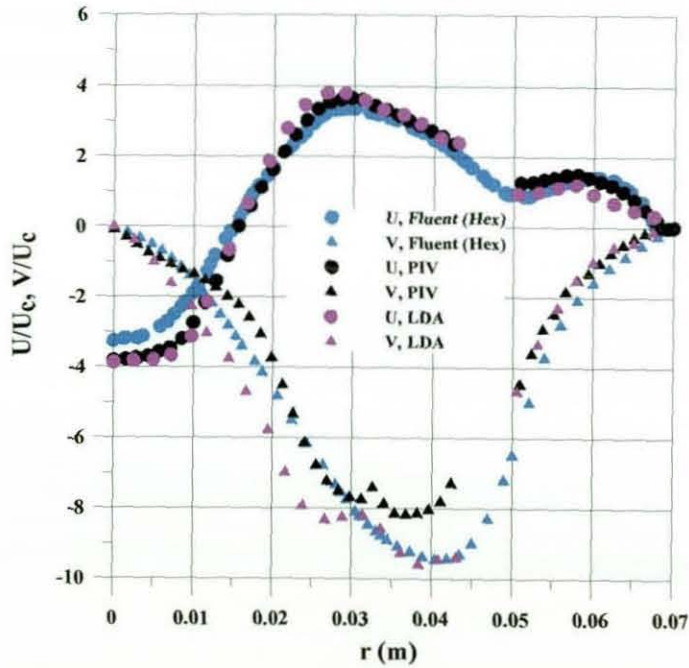


(b)  $x = 5$  mm

Figure 4.18 Velocity distribution using Fluent with tetrahedral grids

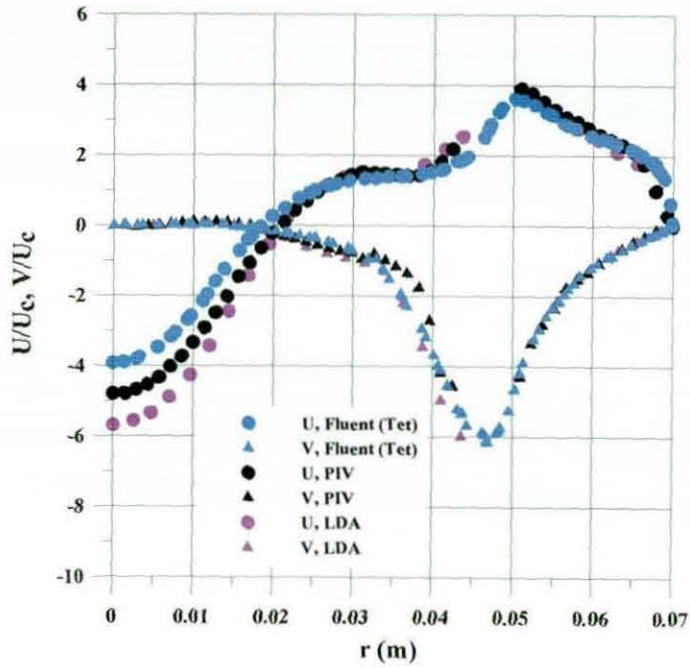


(a)  $x \approx -5 \text{ mm}$

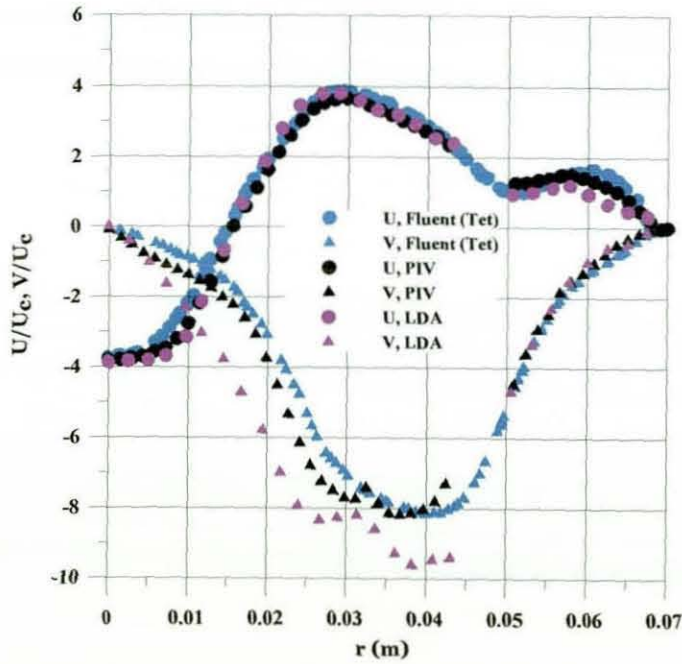


(b)  $x = 5 \text{ mm}$

Figure 4.19 Velocity radial profiles  
(Experimental measurements vs. Fluent with hexahedral grid)

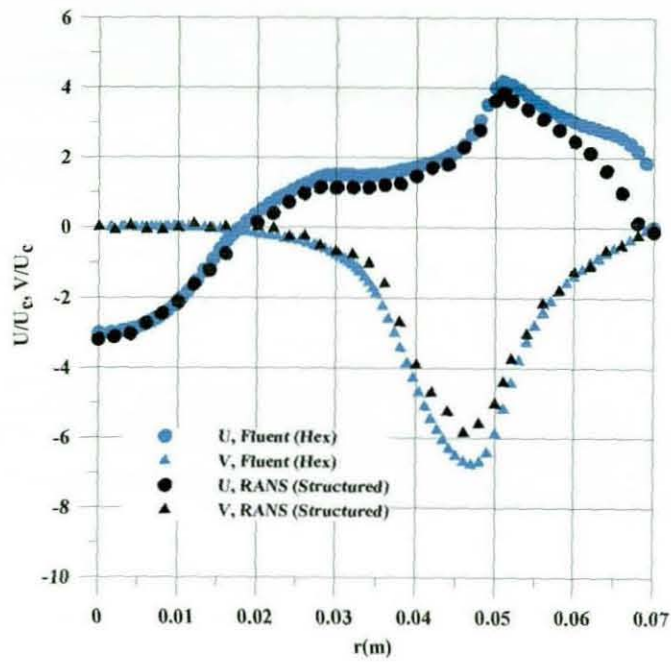


(a)  $x = -5 \text{ mm}$

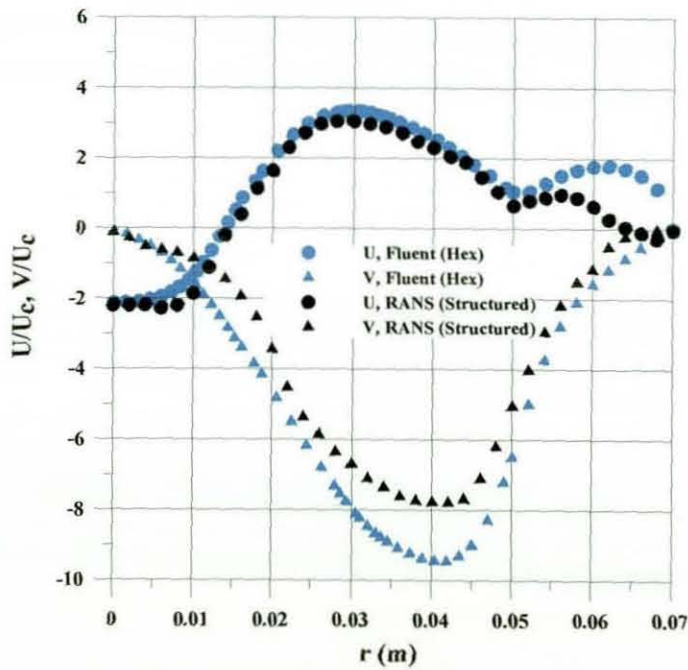


(b)  $x = 5 \text{ mm}$

Figure 4.20 Velocity radial profiles  
(Experimental measurements vs. Fluent with tetrahedral grid)

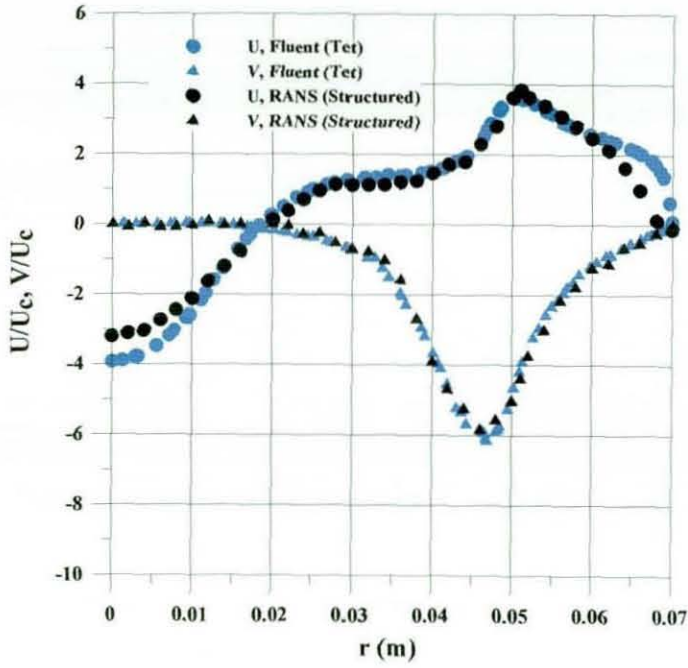


(a)  $x = -5 \text{ mm}$

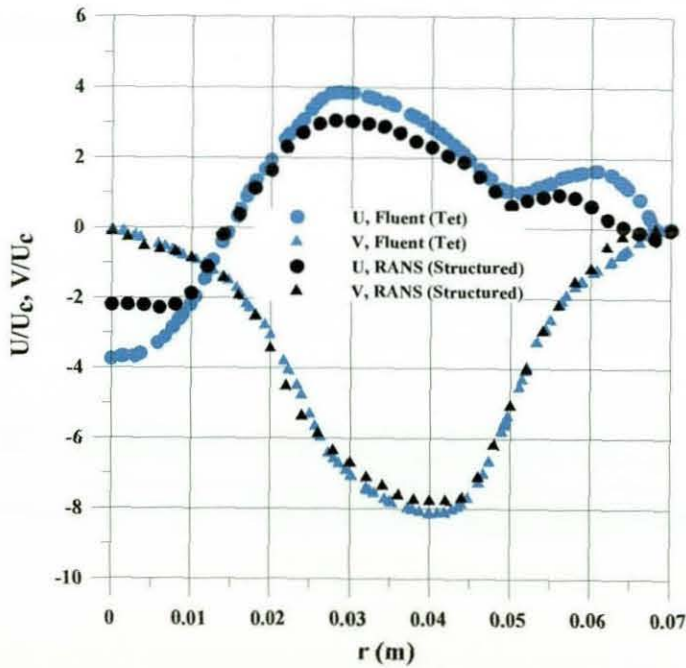


(b)  $x = 5 \text{ mm}$

Figure 4.21 Velocity radial profiles  
(RANS structured predictions vs. Fluent with hexahedral grid)



(a)  $x = -5 \text{ mm}$



(b)  $x = 5 \text{ mm}$

Figure 4.22 Velocity radial profiles  
(RANS structured predictions vs. Fluent with tetrahedral grid)



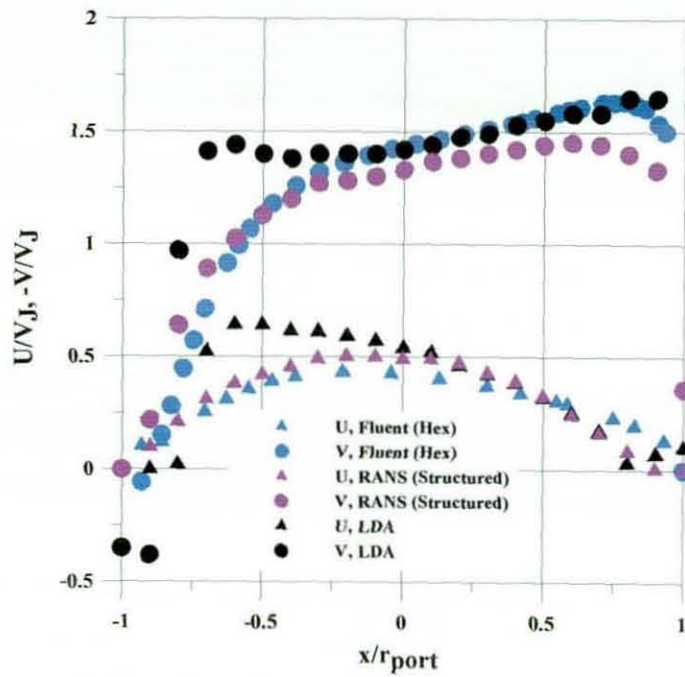


Figure 4.23 Velocity profiles at port exit  
(Experimental and structured predictions vs. Fluent with hexahedral grid)

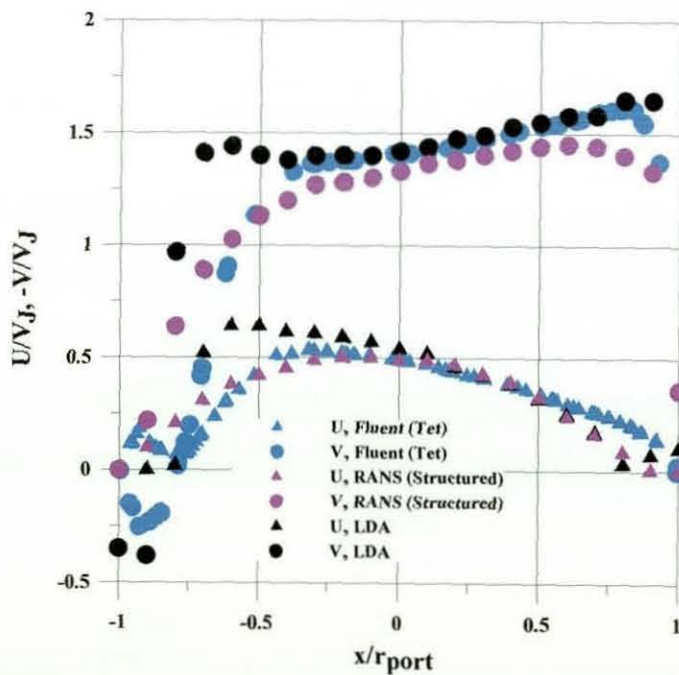


Figure 4.24 Velocity profiles at port exit  
(Experimental and structured predictions vs. Fluent with tetrahedral grid)

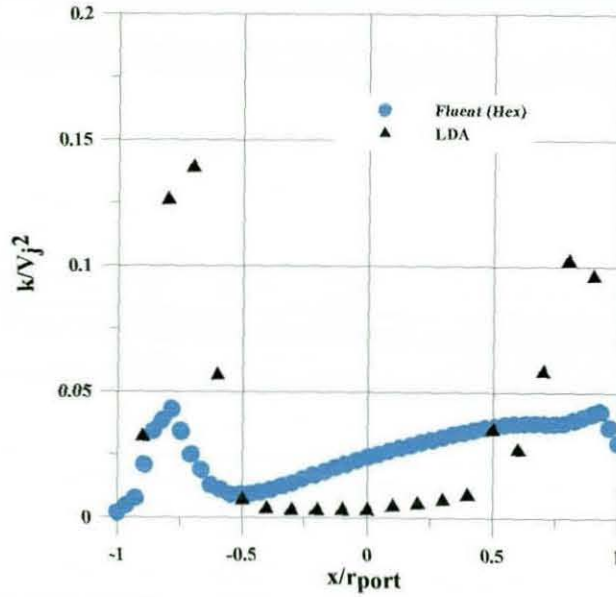


Figure 4.25 Turbulent kinetic energy at port exit (Experimental measurements vs. Fluent with hexahedral grid)

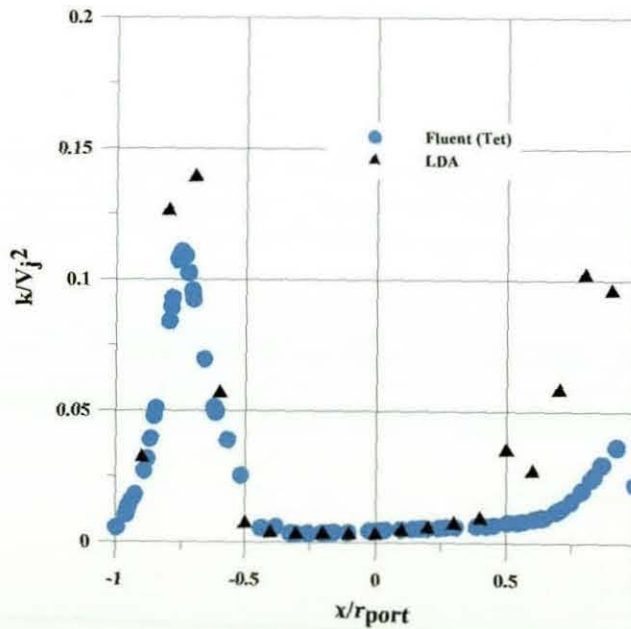


Figure 4.26 Turbulent kinetic energy at port exit (Experimental measurements vs. Fluent with tetrahedral grid)



From these Fluent calculations the sizes of the tetrahedral and hexahedral unstructured grids which provide accurate solutions have been established. In addition, the total pressure and total temperature profiles of the core and the annulus inlets have been predicted in order to be used as Hydra inlet boundary conditions. Figure 4.27 shows the solution obtained from the Hydra code by using a purely tetrahedral grid where an abnormal growth of the boundary layer near the wall and significant increase in the velocity within the annulus region can be noticed. This phenomenon is common with many unstructured codes when boundary layer flows are computed using tetrahedral control volumes [12]. In the basic discretisation used in Hydra, the numerical smoothing operator is anisotropic on highly stretched grids and so will only damp error modes in the direction of the highest grid resolution. In the boundary layer where the gradient normal to the wall is high, the errors will not be damped unless highly stretched cells with high resolution in the normal direction are implemented. The tetrahedral becomes too flat and the severe distortion creates large numerical errors. To avoid this problem use of a layer of prisms along the walls and tetrahedral cells in the rest of the domain is recommended by many researchers [12, 140, 141]. Most grid generators (e.g. TGrid, Gambit, ICEM PRISM) offer prism layer creation tools which provide greater mesh flexibility, particularly in the case of complicated shapes. To examine what effect of this approach would have in the Hydra calculations, a tetrahedral grid with prismatic layers on the walls as shown in Figure 4.28 has been created with the same density as the purely tetrahedral grid. Figure 4.29 shows the Hydra solution obtained with this grid. It can be noticed that the problem of the large boundary layer growth seen in Figure 4.27 with the purely tetrahedral grid has been eliminated and Hydra predicted a flow solution closer to the Fluent prediction. Axial velocity profiles at three different locations in the annulus upstream the port hole ( $x = -22.5, -45$  and  $-67.5$  mm) are presented in Figure 4.30 to compare the tetrahedral grid predictions of Hydra with and without prismatic layers. It is clear from the profiles that the amount of error induced was significant and was not confined only to the boundary layer region but also propagated to the

interior. This gives clear evidence that the pure tetrahedral grids are not suitable for Hydra calculations when viscous flows are involved.

As can be seen in Figure 4.31, the total pressure-total temperature boundary condition used in Hydra and deduced from the Fluent calculations did not predict the same inlet velocities as those used in Fluent. Compared to the actual velocity, the drop is highest at the centreline at around 25% less and 10 % less at the annulus inlet. This is because fixed velocity inlet boundary conditions do not prescribe the inlet static pressure; this emerges as part of the solution as a higher level than the exit static pressure, to provide the pressure drop required to drive the flow. The pressure difference that is predicted does however depend on the pressure losses that are predicted in the converged solution. Thus, the total properties of the flow at inlet are not fixed and will converge on whatever value is necessary to provide the prescribed flow distribution. Further discussions about the treatment of the velocity inlet boundary condition in Fluent solver can be found in the code user's guide [142]. The inlet static pressure is predicted to rise more in the centre of the core flow than towards the walls in order to overcome the greater losses due to impingement and recirculation near the core pipe. This leads to a smaller axial velocity at inlet near the centreline. This change in the inlet velocities will definitely result in an undesirable change in both core-jet velocity ratio and bleeding ratio. This example emphasizes the inappropriateness of specified total pressure inlet conditions for combustion flow problems. Thus, the fixed velocity boundary condition based on Riemann invariants developed in the previous chapter will be used through the rest of this work instead of the total pressure-total temperature boundary condition.

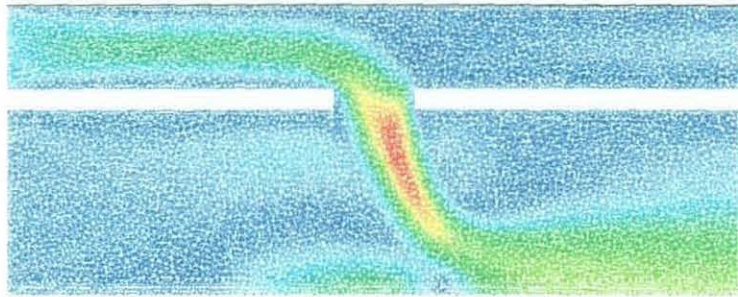
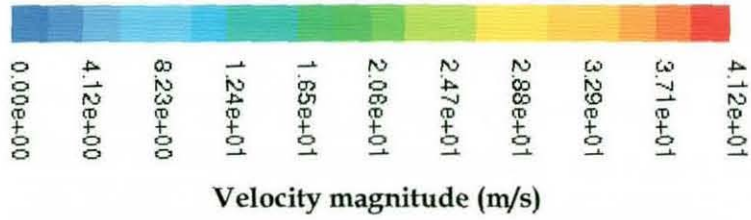
To investigate the accuracy of the Hydra solution with different types of grids, tetrahedral-prismatic and hexahedral grids have been used with almost the same number of nodes as those implemented in Fluent calculations. Figure 4.32 shows the velocity magnitude contours and particle tracks of the tetrahedral-prismatic



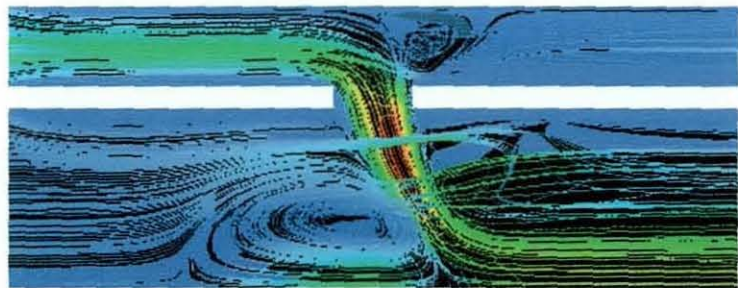
and hexahedral grid solutions. Both solutions were able to capture the flow main features but discrepancies appeared in some areas. For the tetrahedral-prismatic solution, the size of the upstream vortex is 5% less than the experimental data while the hexahedral grid predicted a vortex which is 30% larger than the experimental one. A similar case was reported by McGuirk and Baker [64] where the size of the vortex was 40% overpredicted by using the QUICK scheme compared to that observed experimentally. Tetrahedral-prismatic grid solution predicted a weaker jet penetration compared to the hexahedral grid solution. Similar behavior has been noticed with the Fluent tetrahedral grid solutions. Velocity profiles of the tetrahedral solution in Figure 4.33 show better agreement with the experimental data except the significant deceleration in the annulus axial velocity downstream of the port. This has been changed by using the hexahedral grid as shown in Figure 4.34 which on the other hand overpredicted the centreline axial velocity. In the front edge of the port hexahedral solution overpredicted the size of the separation zone compared to the tetrahedral solution and experimental data which can be noticed from the radial velocity at the port exit in Figure 4.35 and 4.36. Turbulent kinetic energy levels for both solutions have good agreement with experimental data in the port centre zone as shown in Figure 4.37 and 4.38. Both solutions under-predicted the kinetic energy levels in the front edge while the tetrahedral-prismatic has better predictions in the rear edge.

One of the important advantages of the unstructured methodologies is providing local grid refinement capability in certain regions of the flow field. In the port region, successive grid refinements have been carried out to investigate the influence on the solution. Figure 4.39 shows the radial velocity contours predicted by three different sizes of hexahedral grids (Grid 1 refined by doubling the number of cells two times to obtain Grids 2 and 3) where the recirculation and separation region in the port front edge appeared with more obvious details as the grid became finer. This also can be concluded from the axial and radial velocity profiles

in Figure 4.40 and the turbulence levels which improved significantly if compared with the experimental data as it can be seen in Figure 4.41.



a. Velocity field and numerical grid



b. Velocity field and particle tracks

Figure 4.27 Velocity field predictions and flow particle tracks using Hydra with purely tetrahedral grid



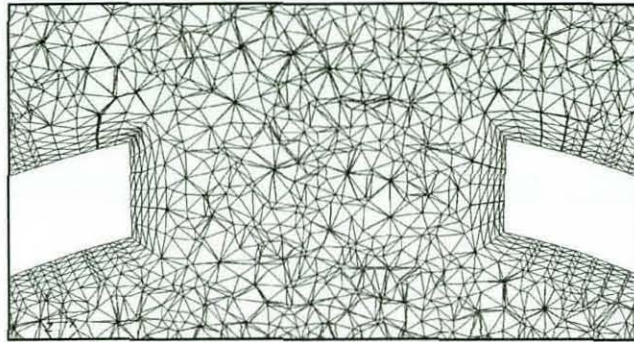
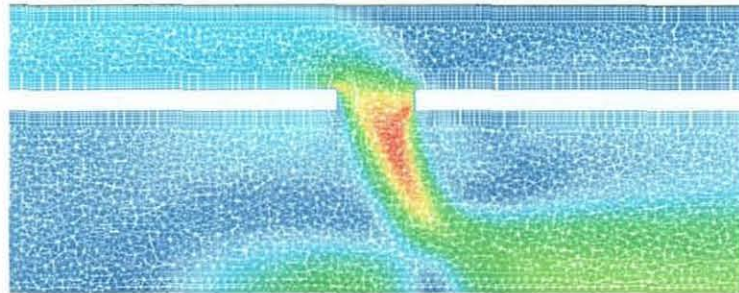
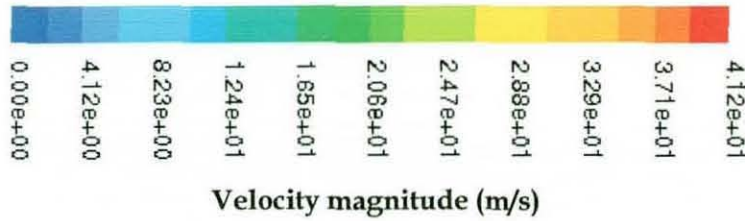
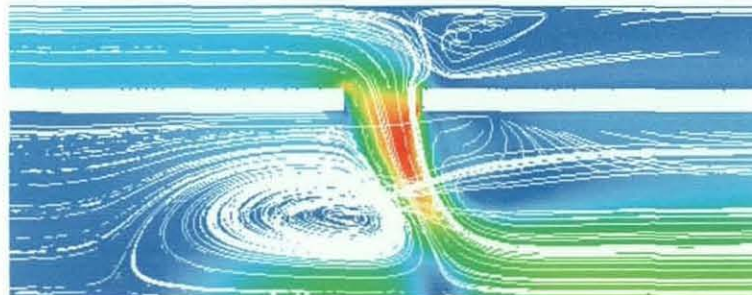


Figure 4.28 Tetrahedral-prismatic grid in the port region



(a) Velocity field and numerical grid



(b) Velocity field and particle tracks

Figure 4.29 Velocity field predictions and flow particle tracks using Hydra with tetrahedral-prismatic grid

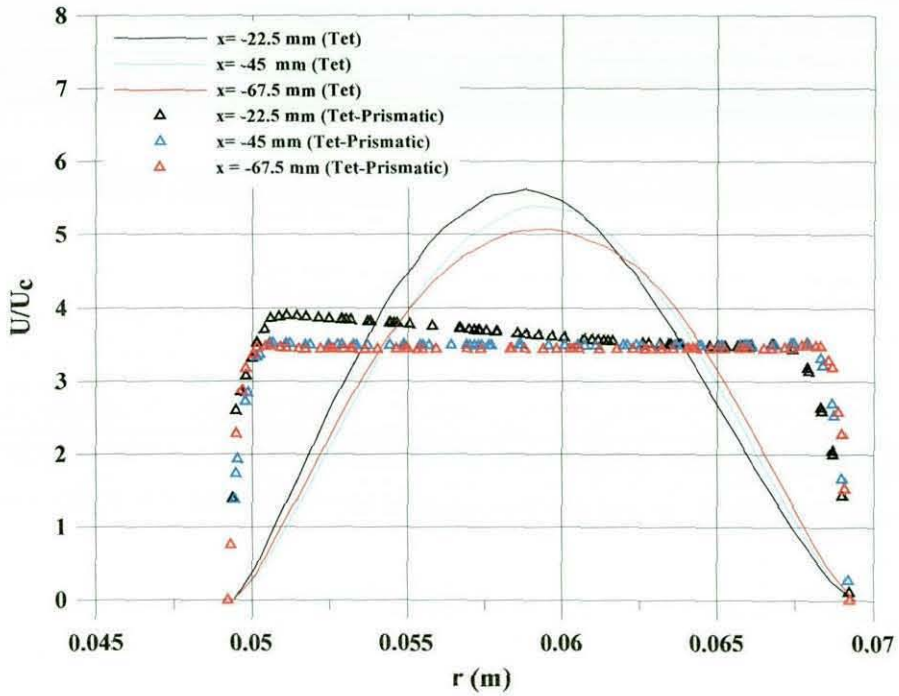


Figure 4.30 Velocity radial profiles at the annulus (Hydra purely tetrahedral vs. tetrahedral-prismatic grid)

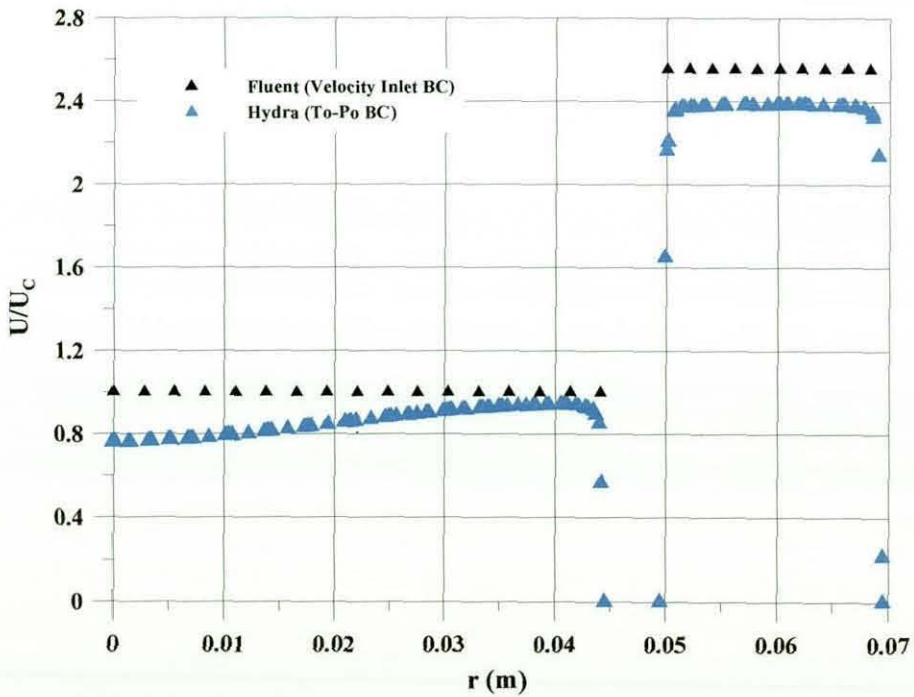
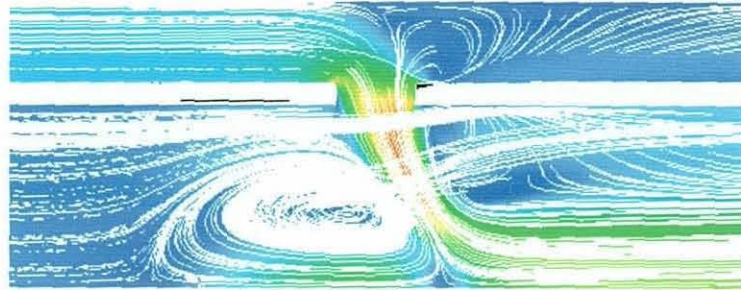
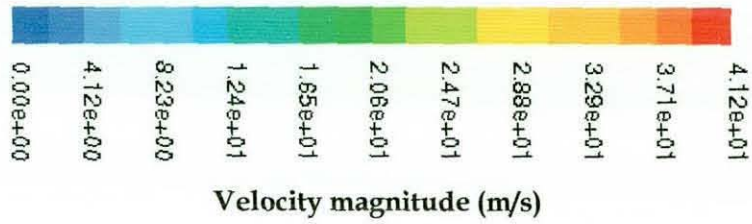
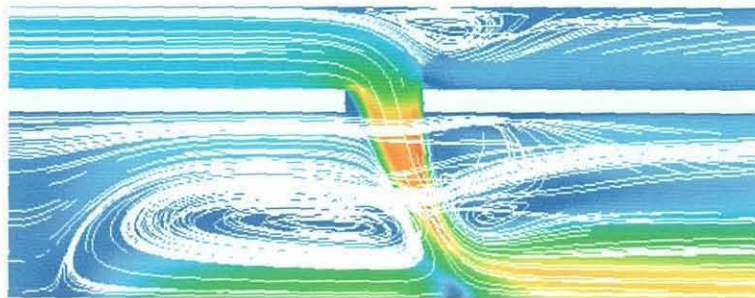


Figure 4.31 Inlet velocity profile with different boundary conditions



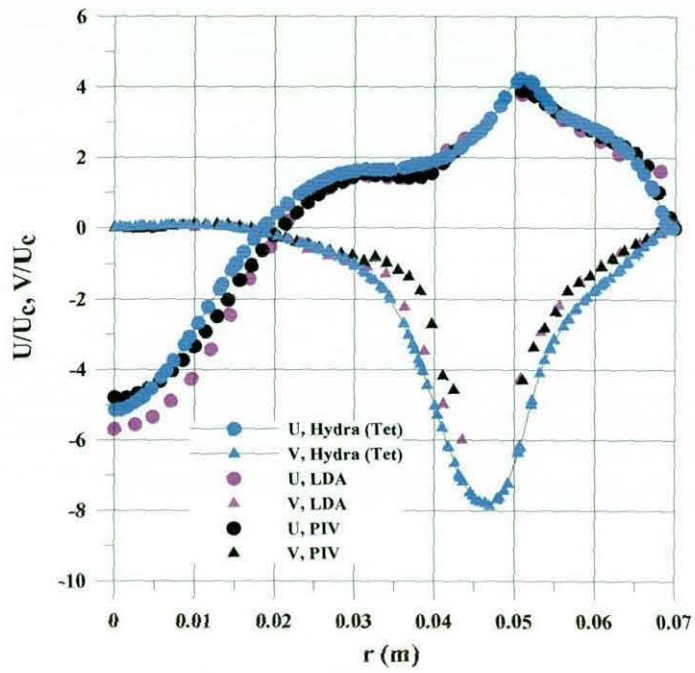


(a) Tetrahedral-prismatic grid

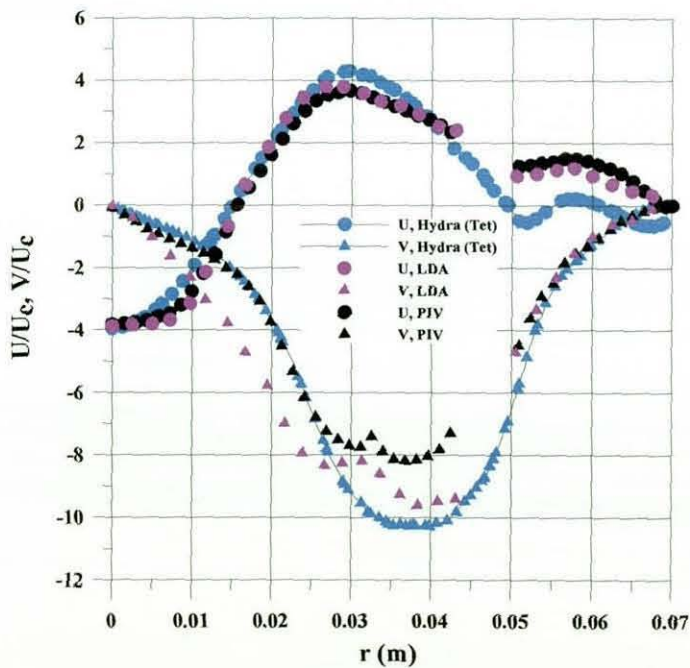


(b) Pure hexahedral grid

Figure 4.32 Velocity field prediction and particle tracks using Hydra with velocity inlet boundary condition and various types of grids

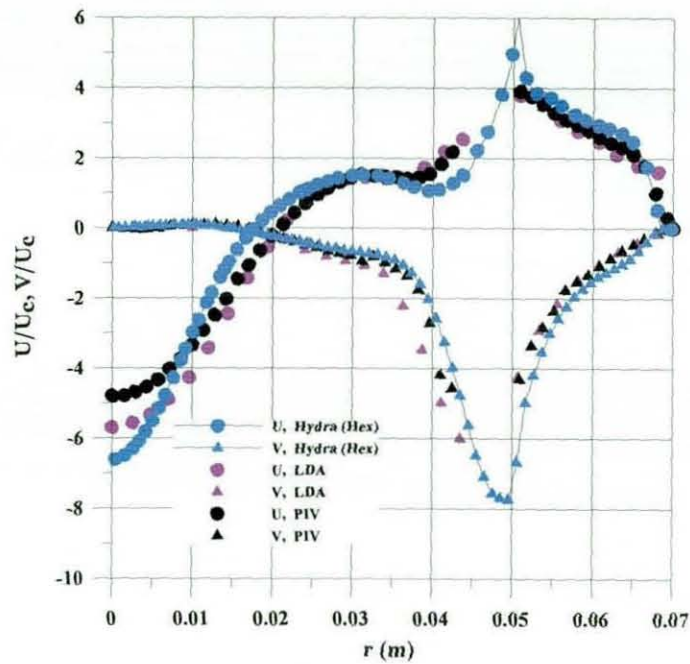


(a)  $x = -5 \text{ mm}$

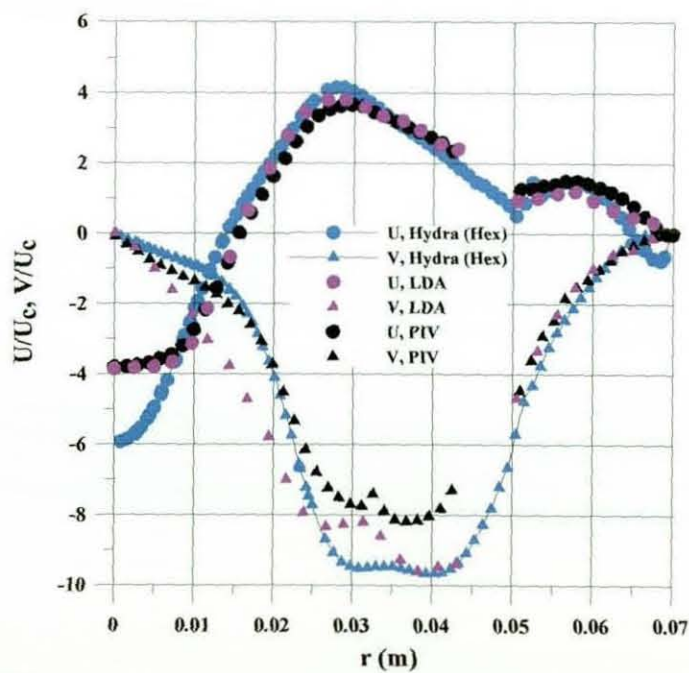


(b)  $x = 5 \text{ mm}$

Figure 4.33 Velocity radial profiles  
(Experimental measurements vs. Hydra with tetrahedral-prismatic grid)



(a)  $x = -5 \text{ mm}$



(b)  $x = 5 \text{ mm}$

Figure 4.34 Velocity radial profiles  
(Experimental data vs. Hydra with hexahedral grid)

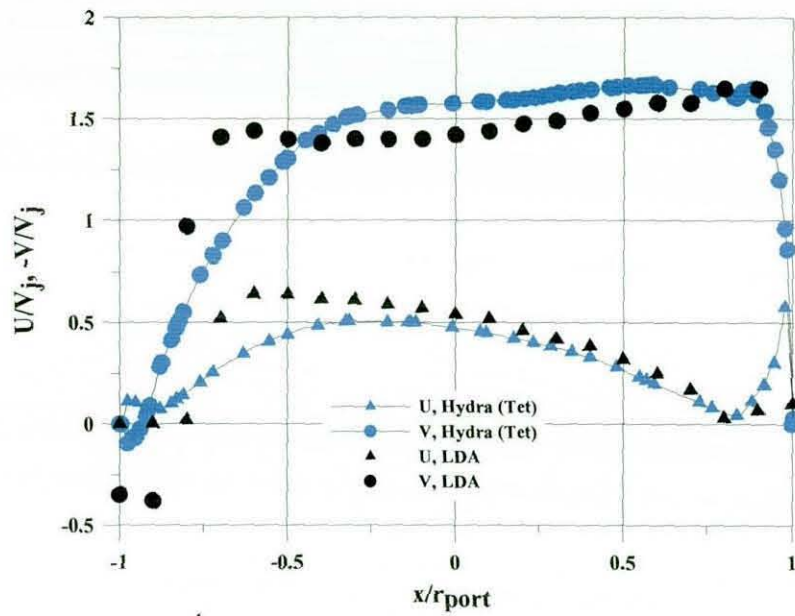


Figure 4.35 Velocity profiles at port exit  
(Experimental data vs. Hydra with tetrahedral-prismatic grid)

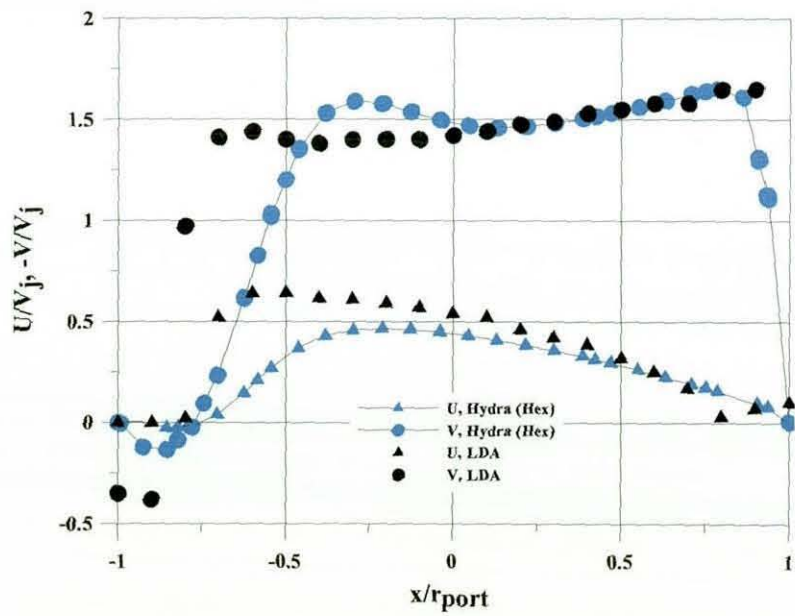


Figure 4.36 Velocity profiles at port exit  
(Experimental data vs. Hydra with hexahedral grid)



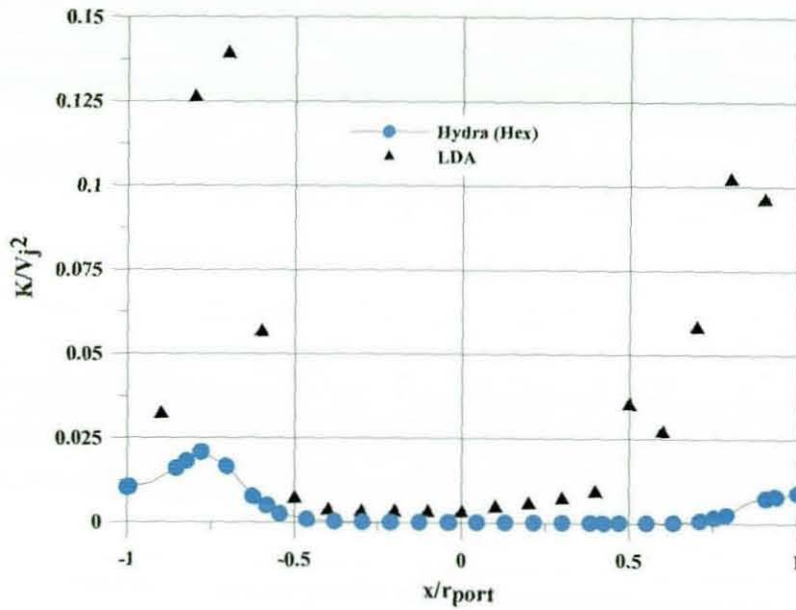


Figure 4.37 Turbulent kinetic energy at port exit (Experimental data vs. Hydra with hexahedral grid)

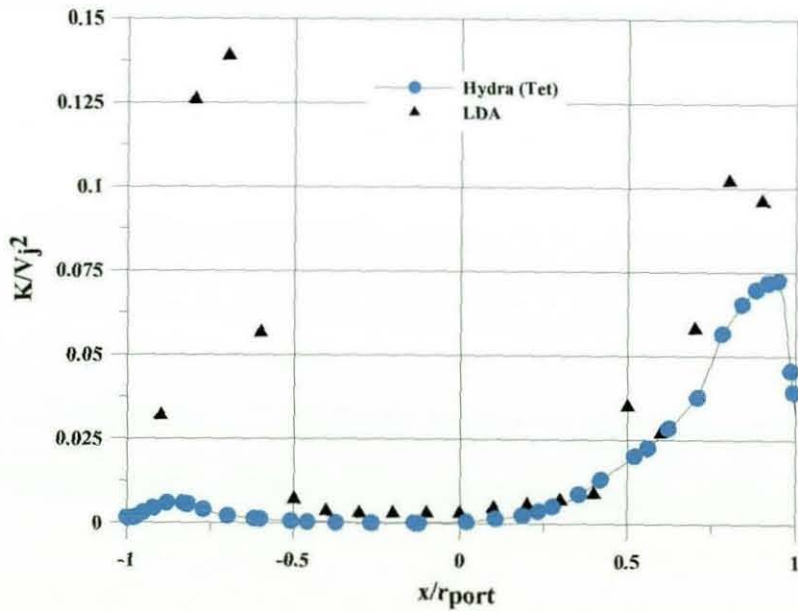
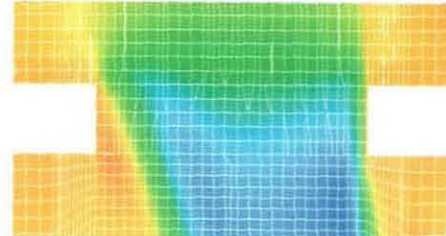
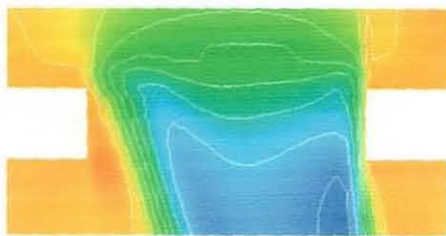
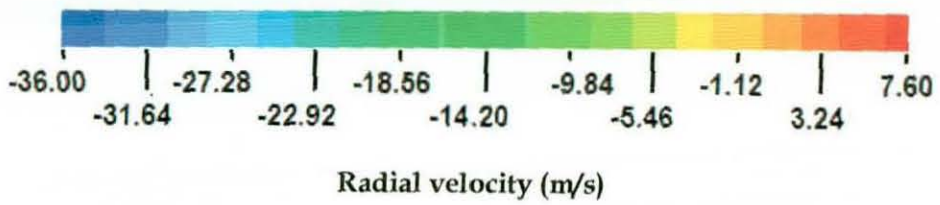
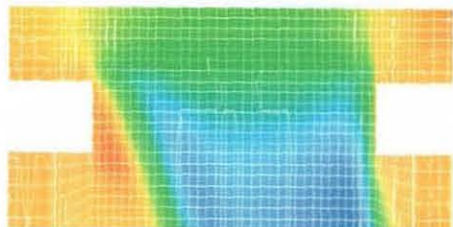
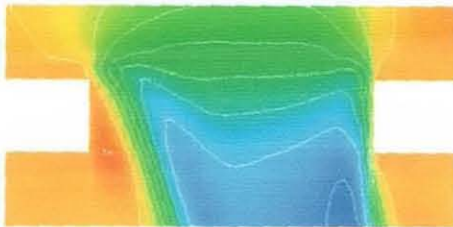


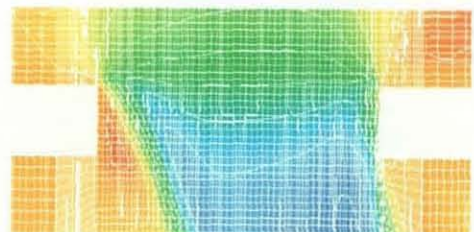
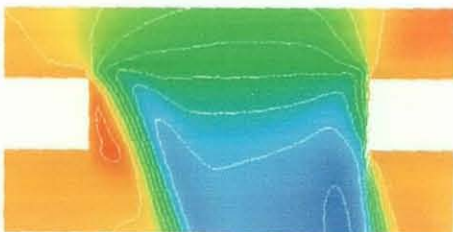
Figure 4.38 Turbulent kinetic energy at port exit (Experimental data vs. Hydra with tetrahedral-prismatic grid)



(a) Grid 1



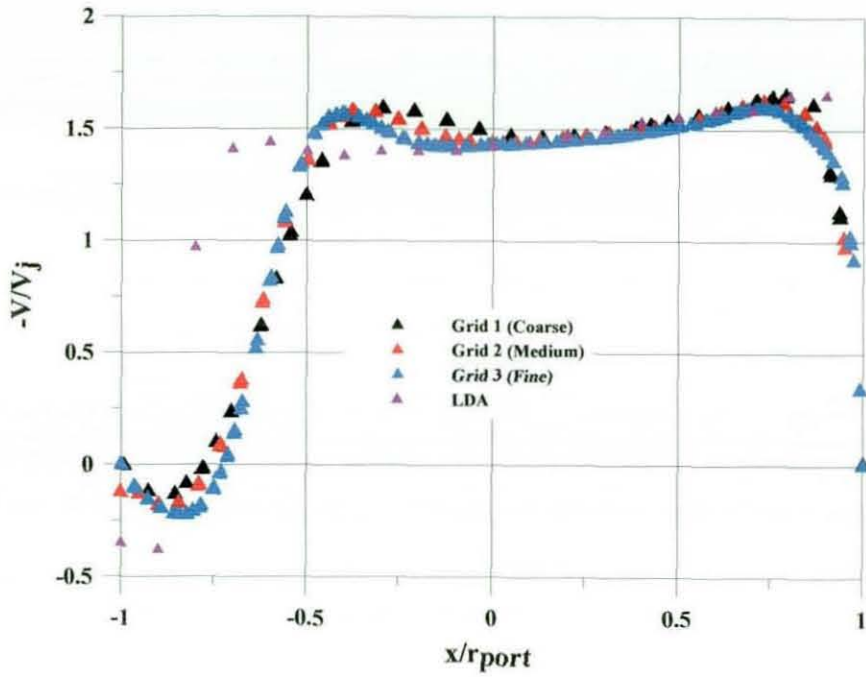
(b) Grid 2



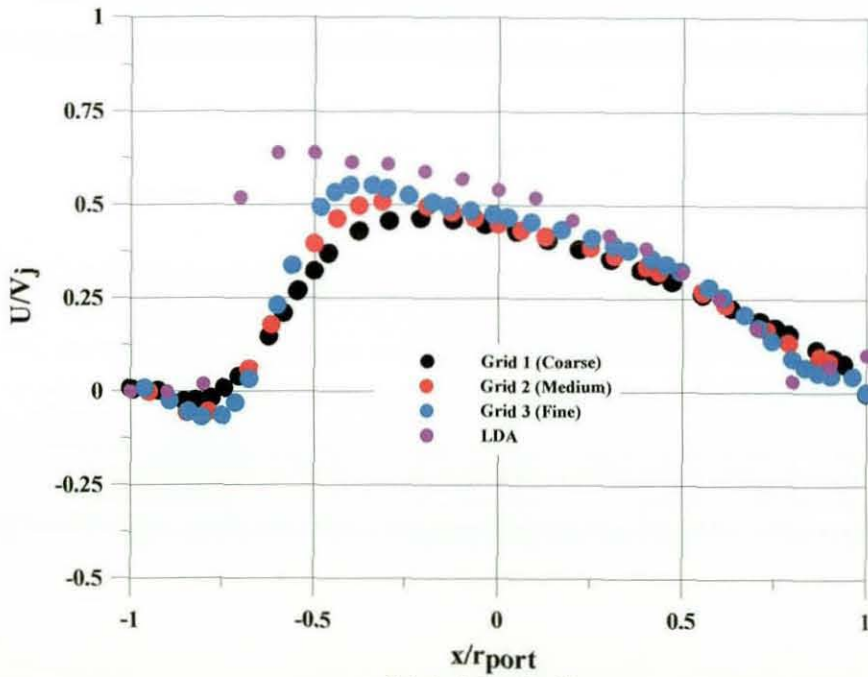
(c) Grid 3

Figure 4.39 Port radial velocity contours and locally refined grids





(a) Radial velocity



(b) Axial velocity

Figure 4.40 Port exit velocity profiles  
(Experimental vs. different sizes of locally refined hexahedral grids)

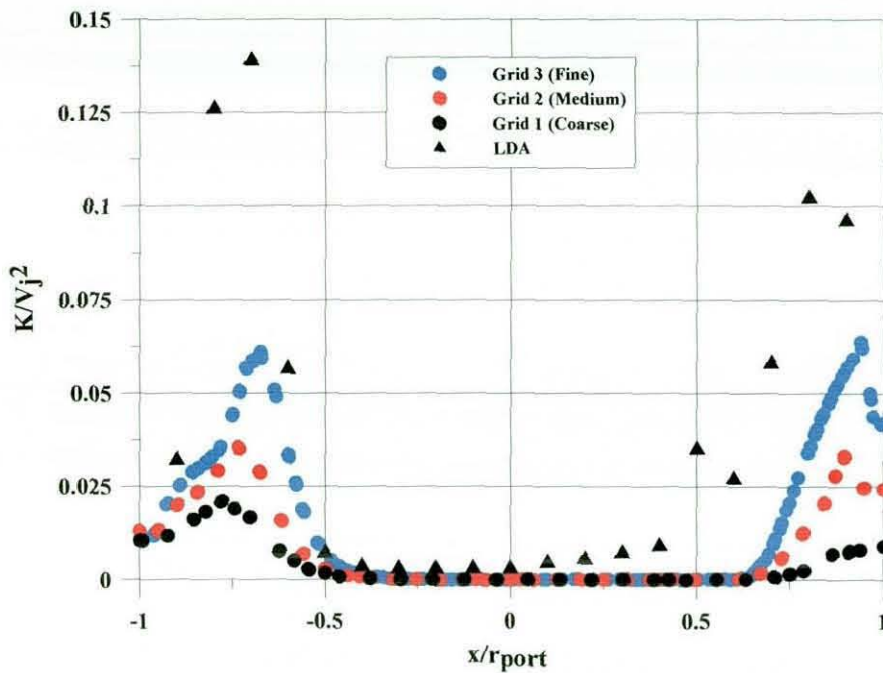


Figure 4.41 Turbulent kinetic energy at port exit (Experimental vs. different sizes of locally refined hexahedral grids)

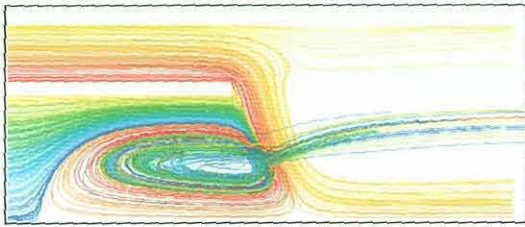
#### 4.5 Conclusions and Discussions

From the calculations presented in this chapter, a strong coupling between the jet flow and mainstream flow exists as evidenced by the large velocity profile and turbulence levels at the port exit. This coupling effect could not be easily captured by specifying the commonly used uniform jet velocity boundary conditions for core-only calculations. Therefore, the only way to accurately predict JICCF flow fields is to include both the interior (core) and exterior (annulus) flow fields in the CFD analysis.

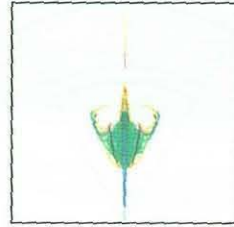
The unstructured solvers of Fluent and Hydra predicted the flow characteristics of the complex multiple jets impingement case reasonably well compared to the experimental data. With the standard  $k-\epsilon$  model all flow major structures observed experimentally were captured with different levels of accuracy. Figure 4.42 shows

different views of the predicted flow particle tracks where jet shear layers, core vortex, counter rotating vortices, and the horse shoe vortices are well presented. Using different type of grids, Fluent and Hydra predictions show different behavior especially in high gradient regions. Jet penetration appeared stronger with the hexahedral grids predictions than those of tetrahedral and tetrahedral-prismatic grids. Jet penetration has strong influence on determining the shape of the flow various structures. Strong jet penetration in the core region leads to more flow blockage upstream and therefore larger core vortex size and consequently different shapes of horse shoes and counter rotating vortices. This can be seen clearly from Hydra predictions in Figure 4.43 and 4.44. The large core vortex predicted by using hexahedral grid creates wider spreading horse shoe structure than that predicted by tetrahedral grid as appeared downstream of the core region, Figure 4.44. The reason behind these differences is mainly due to numerical diffusion which is a source of error in three dimensional calculations. Numerical (false) diffusion is noticeable mostly when the real diffusion is small, that is, when the situation is convection-dominated as in most of practical fluid flow cases. This phenomenon arises due to the one-dimensional interpolation practices being employed in multi-dimensional cases especially when the flow is oblique to the grid lines and when there is a nonzero gradient of the dependent variable in the direction normal to the flow direction. Due to flow complexity of the current case, neither tetrahedral nor hexahedral grids are able to provide best grid alignment with flow direction all over the domain and it is difficult to generate one single grid that would satisfy the grid alignment at every part of the domain. Grid refinement found to reduce the numerical diffusion and improve the solution accuracy. In addition to the grid type, the amount of numerical diffusion may vary according to the convective term discretisation. Fluent upwind discretisation provides more numerical diffusion but it possesses better stability and boundedness compared to the centred differencing discretisation of Hydra where smoothing terms are added to ensure stability.

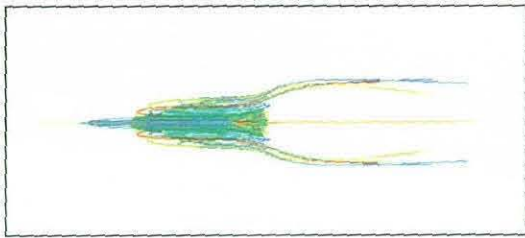




(a) Core vortex and jet shear layers

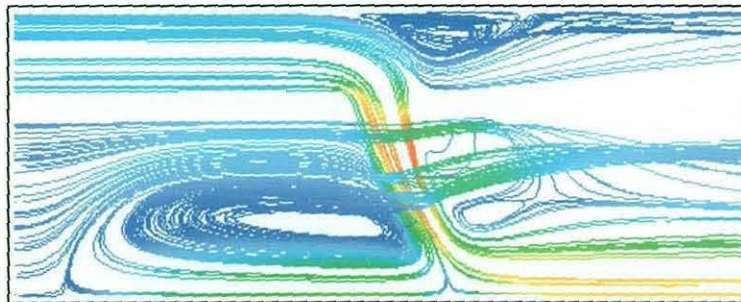


(b) Counter rotating vortices

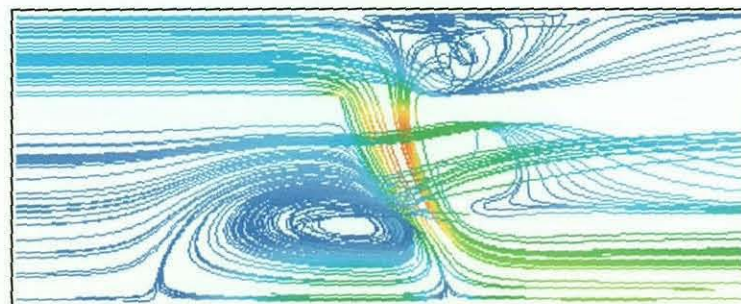


(c) Horse shoe vortex

Figure 4.42 The various structures of the predicted JICCF flow

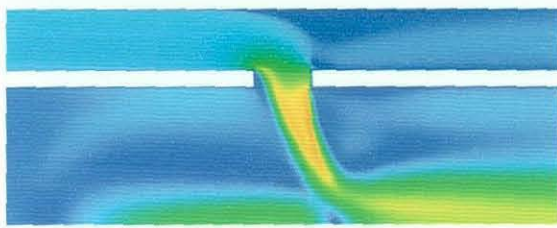


(a) Pure hexahedral



(b) Tetrahedral-prismatic

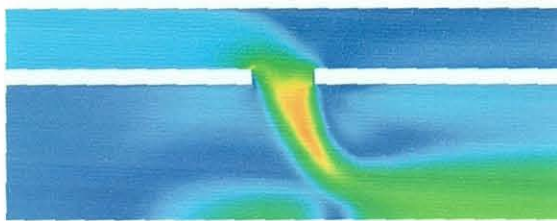
Figure 4.43 Flow particle tracks as predicted by Hydra



(a) Pure hexahedral predictions



x=30 mm



(b) Tetrahedral-prismatic predictions



x=30 mm

Figure 4.44 Velocity contours as predicted by Hydra

The new velocity inlet boundary condition of Hydra were tested and found to be essential to preserve the boundary condition extracted from the experimental data compared to the total pressure-total temperature boundary condition which failed to predict accurately the velocity inlet profiles. Compared to the segregated solver of Fluent, Hydra required a large amount of memory to setup the calculation procedure and a higher number of iterations to converge the solution. Hexahedral grid consisting of 1,100,000 nodes required 614 MB to perform the calculations using the segregated solver of Fluent. In Hydra calculations, the same grid required about 1062 MB and almost three times the number of iterations required by Fluent to converge the solution. Hydra calculations however performed on a parallel PC cluster with different number of nodes provided fast and efficient performance compared to the sequential solver of Fluent.

# Chapter 5

## Multi Stream Swirling Flow (MSSF)

### 5.1 Background Review

Swirling flow can be found in a wide range of engineering applications. Gas turbine combustors are foremost amongst these applications where swirl is utilised to ensure combustion stability and efficiency by enhancing the air-fuel mixing and anchoring the flame by creation of a primary recirculation zone where the local velocity is in regions less than the flame propagation velocity. This region also helps to fulfil many of the combustor performance requirements by reducing the flame length and enhancing the mixing of the combustion products which leads to improved engine performance, lower emissions and extended life of the combustor.

Swirling flow is a result of the application of a spiraling motion to the mean axial flow jets. This motion can be induced by different methods such as vaned swirlers, tangential entry generators and solid body rotation, as shown in Figure 5.1. Above a certain level of swirl strength, a central toroidal recirculation zone (CTRZ) located at the swirler exit will be generated. A typical structure of such a recirculation region in a swirling annular jet can be seen in Figure 5.2. Flow in this region is generally associated with high shear and hence high turbulence intensity. The swirling flow undergoes vortex breakdown, creates a large scale and often unsteady recirculation region. This is also sometimes observed to "wobble" or precess about the geometric centreline, which is referred to as a precessing vortex core (PVC). Although this kind of flow promotes the mixing of fuel and air and



extends the range of flame stability, it is sometimes not a desirable characteristic because it has a tendency to drive combustion instability, this can also occur via an acoustic feedback mechanism where the flow may couple resonantly with acoustic waves in the combustor [144].

From experiments, it has been found that a CTRZ is observed only in strongly swirling flows and its characteristics are affected by the degree of swirl imparted to the flow. Swirl strength or degree of swirl is characterized by the swirl number  $S$  which is defined as the ratio of axial flux of swirl momentum  $M_\theta$  to the axial flux of axial momentum  $M_x$  times the swirler outer radius  $R$ ,

$$S = \frac{M_\theta}{M_x R} \quad (5.1)$$

where

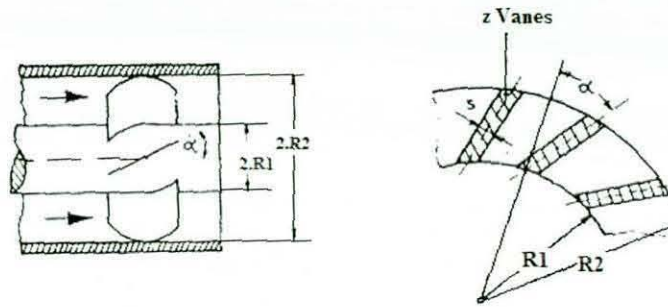
$$M_\theta = \int_0^R 2\pi(\rho\overline{uw} + \rho\overline{u'w'})r^2 dr \quad (5.2)$$

$$M_x = \int_0^R 2\pi(\rho\overline{u^2} + \rho\overline{u'^2} + (p - p_x))r dr \quad (5.3)$$

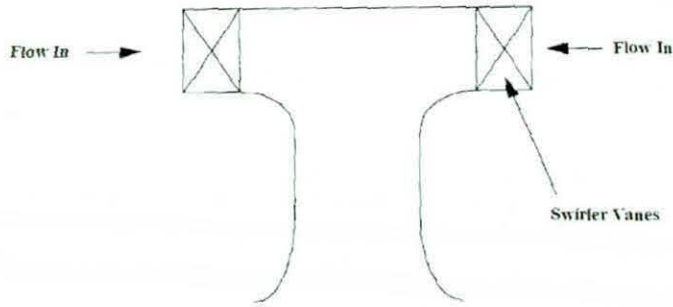
The pressure and fluctuating terms are often ignored in the above expressions. For swirling flows generated by vane type swirlers as is usually the case in gas-turbine combustors, the swirl intensity is characterized by an approximation to the swirl number given as

$$S = \frac{2}{3} \left[ \frac{1 - \left(\frac{d_i}{d_o}\right)^3}{1 - \left(\frac{d_i}{d_o}\right)^2} \right] \tan \Phi \quad (5.4)$$

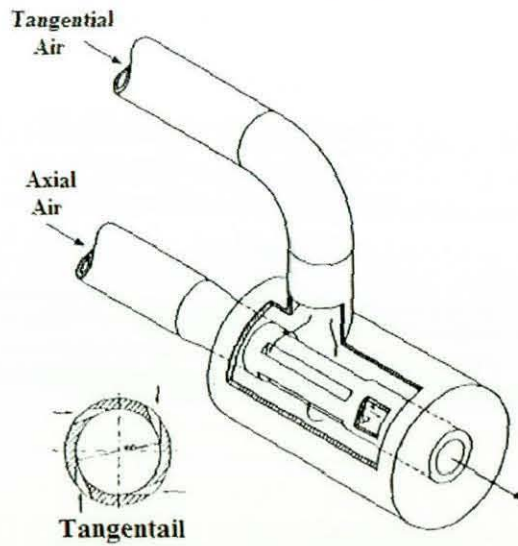
where  $\Phi$  is the vane inlet angle,  $d_i$  is the inner diameter and  $d_o$  is the outer diameter. It can be noticed from the above definition that the swirl number is only a function of the geometry.



(a) Axially vaned swirler [48]



(b) Axially and radially vaned swirler [48]



(c) Axial and tangential entry swirl generator [143]

Figure 5.1 Various types of swirl generator

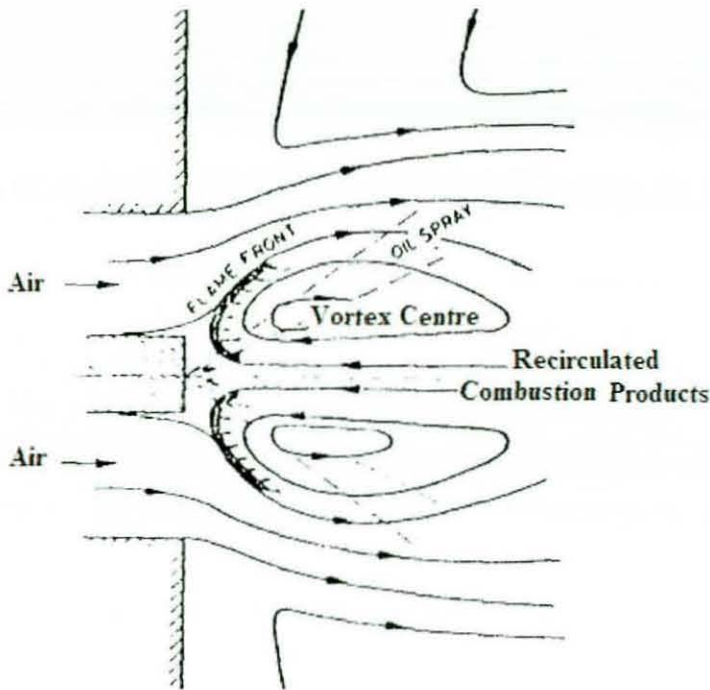


Figure 5.2 Structure of Recirculation Region in Swirling Annular Jet [143]

For low swirl number ( $S < 0.8$ ) increased jet spread, enhanced mixing with the co-flowing fluid, and increased decay rates are found. With further increase in the level of swirl ( $S \approx 1.0$ ) a critical condition is reached where the flow along the jet axis is found to oscillate between forward and backward flow. As the amount of swirl is increased beyond this critical value a definite region of backflow, defined earlier as the CTRZ, can be identified. The formation of this reverse flow region is due to the progressive development of a positive axial pressure gradient with increasing swirl. The axial pressure gradient is formed through the downstream decay of tangential velocity. Near the jet exit the swirl is at a maximum, with a large centrifugal acceleration creating a positive radial pressure gradient. Downstream, with the decay in the tangential velocity, the centrifugal acceleration is reduced allowing a higher pressure on the jet axis than at the jet exit. The axial pressure gradient is thus produced by the decay in tangential velocity and increases with increasing swirl.



The major difference between a freely swirling flow and swirling flow in a gas turbine combustor is the effect on the flow field of confinement. The high entrainment rates associated with a large amount of swirl ( $S > 1.0$ ) may cause the swirling jet to attach to the wall, mainly due to the initial part of the jet entraining and causing backflow. In general, confinement causes an increase in the recirculated mass flow, and consequently a longer recirculation zone. Motivated by the increase of combustion efficiency and reduction of NO<sub>x</sub> emissions, many experiments related to swirling flows within combustors have been conducted utilising various geometries, methods of swirl generation, and measurement techniques. Most of these studies have involved the measurement of mean velocities and turbulence characteristics, and the most relevant of these to the present interest will be briefly reviewed.

## 5.2 Review of Previous Swirling Flow Studies

Gore et al. [144] investigated the formation and characteristics of recirculation zones in swirling flows with a variable geometry apparatus. With the application of a weak amount of swirl the general jet cross section was found to be expanded. No backflow was evident but velocities on the jet centerline were reduced from the zero swirl case, indicating the existence of an axial pressure gradient. As the amount of applied swirl was gradually increased the flow near the axis was found to oscillate. This critical swirl condition was found to be dependent on geometric conditions. Beyond this critical swirl condition a backflow region was clearly evident, with both forward and rear stagnation points well defined. The authors also found the jet spread angle to be a function of the applied swirl which was also reported by Chigier et al. [145] who found the spread angle increased continuously with swirl level but approached an asymptotic value.

In 1984, So et al. [146] used a swirler with guide vanes, as shown in Figure 5.3, to impart swirl to the flow inside a tube of 125 mm in diameter. A jet, with a diameter of 8.73 mm, was situated in the centre of the swirler so that the confining tube axis

was aligned with the jet axis. Both the swirler and the jet Reynolds number could be changed if required. The experiment was carried out with gases of different densities and the jet velocities selected to give the same jet momentum flux for each gas. Mean velocity and turbulence measurements were made with one-component LDV. Results for air-air and helium-air jets showed that jets in confined flow with large area ratio were highly dissipative. As a result, both air and helium-air jet centreline velocity decays rapidly. For air jets, the jet-like behaviour in the tube centre disappeared at about 20 diameters downstream of the jet exit. This phenomenon is independent of the initial jet velocity. The turbulence field at this point also decays to that of the background swirling flow. On the other hand, a jet-like behaviour in the tube centre is noticed even at 40 diameters for helium-air jets. The subsequent flow and turbulence field depend highly on the initial jet velocity. Since the jets are fully turbulent, therefore, independent of jet Reynolds number, and the jet momentum fluxes for both air and helium/air are the same, the cause of this difference in behaviour is attributed to the combined action of swirl and density difference.

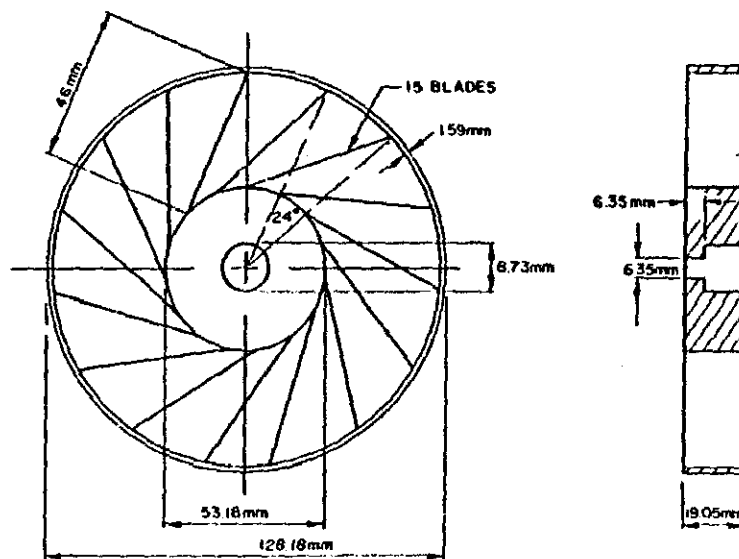


Figure 5.3 Details of So et al. swirler geometry

Further review of fundamental experimental studies on swirl jets can be found in several articles and books. The review articles by Syred and Beer [147] and Lilley [148] give an excellent overview on swirling flows in the field of combustion in general.

CFD techniques have been applied to swirling flows to give a better understanding of the various turbulent structures and phenomena associated with swirling flows. In the open literature, most of the early numerical investigations of swirling flows were limited to simple axisymmetric geometries, allowing use of 2D computational grids. Jones and Pascau [149] for example have performed 2D calculations of the single swirler geometry investigated experimentally by So et al. [146] using two different turbulence models and the first measurement plane as the inlet boundary. They concluded that the RST model performed better than the standard  $k-\epsilon$  model, especially in predicting the circumferential velocity. Although the swirl produced was not sufficiently strong to induce recirculation, the physics of the flow field was such that a converged solution could not be attained with the RST model when a simple zero gradient exit boundary condition was prescribed. They overcame this problem by fixing the axial velocity profile at the exit. Using the  $k-\epsilon$  model, Ramos [150] performed 2D calculations of the Vu and Gouldin [151] experimental measurements. He found a great deviation in prediction of the circumferential velocity and attributed this to the simple eddy viscosity turbulence model which unlike the RST model does not account for streamline curvature effects. Similar results have been found by Habeeb et al. [152] who also emphasised the great influence of the inlet boundary condition variations on the entire flow field.

In 1995, Sharif et al. [153] investigated the performance of three different turbulence models based on the comparison of the predictions against the experiments of So et al. [146]. The models evaluated were: a nonlinear  $k-\epsilon$  model, an RST Model, and the Algebraic Stress Model (AST). Comparisons of predictions with the experiments showed the superiority of the RST model and the AST model



over the nonlinear  $k-\epsilon$  model. The RST and AST models provided good agreement with measured mean velocity profiles. They also found for a typical case, that the RST model takes about 1.5 times more CPU time than the AST model. Despite the larger CPU time and memory requirements, the improvement in the RST model predictions over the AST model predictions is marginal for most cases. The authors concluded that satisfactory prediction of the complex swirling flows is strongly depending on the specified inlet mean velocities and turbulence quantities; thus benchmark data containing detailed measurements of the mean velocities and turbulence quantities are necessary for turbulence-model validation.

Crocker et al. [154], performed a 3D simulation of the internal and external flow in a sector of a can type combustor. The injector inlet plane was taken as the outlet plane of swirl vanes plane. They suggested including the vanes of fuel injectors in the computational domain to enable the non uniform feed pressure at the inlet of the combustor. They added 100,000 cells to account for vanes inclusion ending up with 5,000,000 cells for the whole calculations. Although this does not seem excessive, they also raise the problem of creating a structured grid which would pass through the fuel injector and into the combustion can. The authors suggested that an unstructured grid approach would be the best solution to the problem.

In 2000, Widmann et al. [155] used the Fluent code with the RNG  $k-\epsilon$  turbulence model and an unstructured grid with about 277000 cells to simulate the air flow through a  $30^\circ$  sector of a 12 vane cascade swirl generator as shown in Figure 5.5. They conducted a parametric study in which the effect of vane angles from  $30^\circ$  to  $60^\circ$ , and Reynolds number from 5000 to 30000 was investigated. They found that the effect of the vane angle on the shape of the predicted velocity profiles and recirculation zone was more significant than the effect of Reynolds number. Compared to experimental results they also found the RNG  $k-\epsilon$  model has superior performance relative to the standard  $k-\epsilon$  model.

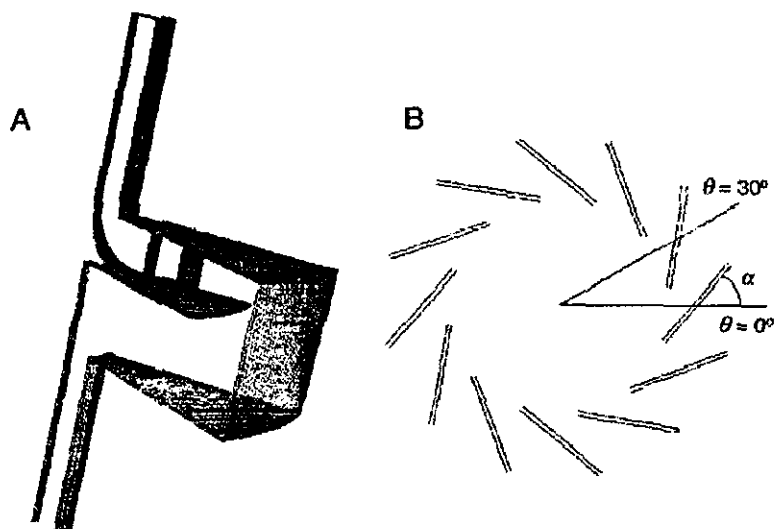
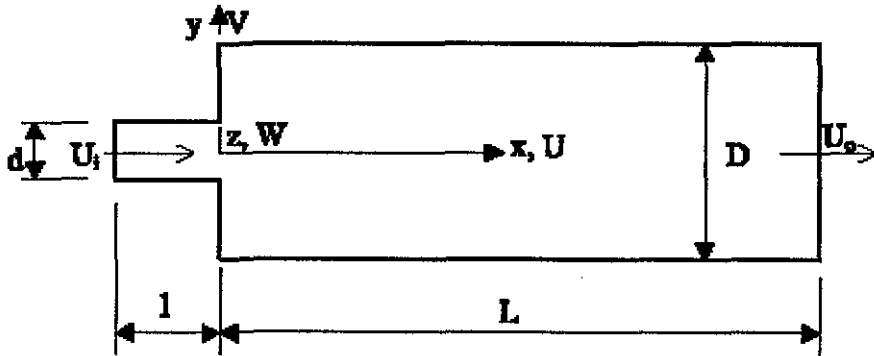
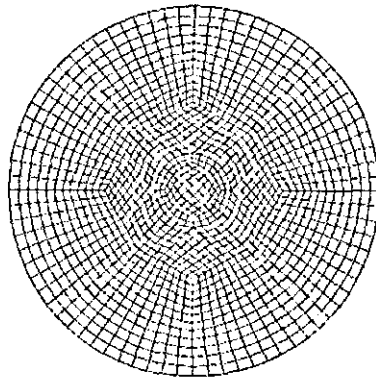


Figure 5.5 Computational domain of Widmann et al. swirl generator [155]

In 2002, Guo et al. [156] employed the finite volume CFD code CFX-4 with multi-block approach and the standard  $k-\epsilon$  model to simulate the axisymmetric swirl flow in a sudden expansion chamber as shown in Figure 5.6 with expansion ratio of 5.0. Calculations carried out on three different sizes of grids (148000, 152000, and 218000 cells) over a swirl number range between 0.0 and 0.48. Despite periodicity and geometry simplicity, the full geometry was considered in the calculations, as shown in Figure 5.6, which leads to unnecessary large number of cells. Since the swirling vanes were not modeled, a uniform axial velocity profile was set and a swirl velocity imparted to the flow at the inlet. At the outlet, the axial velocity gradient was assumed to be zero. They observed several modes of vortex core oscillation and they limited this phenomenon to low swirl numbers. They also reported that the increase in swirl intensity leads to reduction in precession amplitude of the PVC. Unfortunately, no comparisons with experimental results were given in this work.



(a) Sudden expansion chamber



(b) Cross section of the computational grid

Figure 5.6 A schematic of the geometry and grid used by Guo et al. [156]

In 2003, Fudihara et al. [157] used the CFX-4 code to carry out a 3D numerical simulation to study the main characteristics of the flow through the movable block swirl burner shown in Figure 5.7 and investigated experimentally by Beér and Chigier [158]. Calculations were performed using the standard  $k-\epsilon$  and RNG  $k-\epsilon$  turbulence models assuming incompressible and isothermal flow. Five different structured grids were used each represents certain location of the movable blocks with sizes in the range of 52800 to 90700 cells. Both models predicted a reverse flow in the burner expansion core region, but only the RNG  $k-\epsilon$  model predicted a reverse flow extending back into the annular duct of the burner. The predicted swirl numbers were lower than the available experimental data as well as the

approximate analytical correlation provided for this geometry by Beér and Chigier [21]. The use of a second-order numerical interpolation scheme produced higher swirl numbers, which were closer to the experimental data than the first-order interpolation scheme.

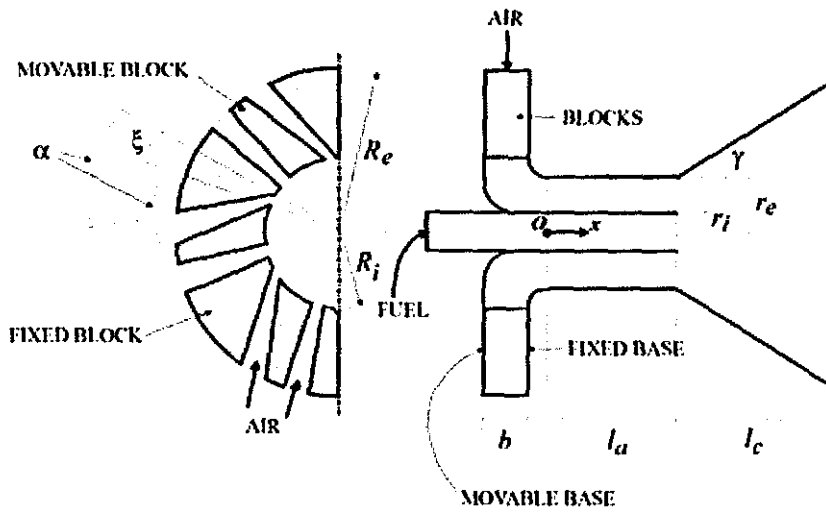


Figure 5.7 Schematic layout of the movable block burner

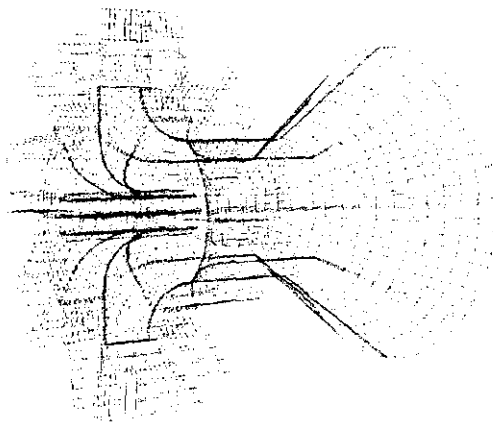


Figure 5.8 Computational grid for location number 3 of the burner

The above numerical studies beside those reviewed in section 1.3 [50-51] have emphasised several issues raised in chapter one and chapter four regarding the prediction accuracy of gas turbine combustor flows. The high sensitivity of the swirling flow to inlet boundary condition implementation and the importance of *coupling the swirler with the combustor to provide accurate numerical simulation*. The limitations imposed by structured grids capabilities to handle complex geometries, mostly limited to simple geometries unless simplifications are imposed to complex ones. The adequacy of the turbulence models to accurately predict the complex swirling flows was also one of the important raised issues. Although, the above issues were commonly reported in many of the open literature, it was obvious from the previous chapter that the standard k- $\epsilon$  model is capable to predict the complex JICCF flow fields with acceptable accuracy when a coupled calculations approach and an unstructured methodology is used. In this chapter, the investigation of Hydra capabilities will continue on the second selected test case. The selected case is the generic multi stream swirl geometry studied numerically and experimentally by Hughes [48] and discussed briefly in chapter one. In addition to testing the accuracy of Hydra on this type of flow, the current investigation will also focus on pre-processing issues (solid geometry modelling and grid generation) as these are found to be very important (and often time-consuming) aspects of simulation of such flows.

### **5.3 Previous Experimental and Numerical Work on the Selected Test Case**

*The swirler under investigation consists of three axially fed vane passages creating co-rotating streams as shown in Figure 5.9. In the inner swirler there are eight uniformly distributed curved vanes attached radially to a central bullet. The vanes leading and trailing edge angles are 60° to the axial direction and the surface curvature is to ensure the flow leaves the vane at the same angle as at the leading edge with less pressure drop due to flow turning. The inlet duct of the inner swirler is aerodynamically designed to provide clean and uniform flow at the*

swirler inlet. The outer and the dome swirlers consist of 16 and 24 helical slots respectively with a  $45^\circ$  helix angle. The swirler numbers and locations in the three streams are aligned to create a  $45^\circ$  periodicity which then allows reduced solution domain size to be used.

The experimental rig used to have measurements of this swirler is shown in Figure 5.10 and was used by Hughes [48] to investigate the swirling flow field using an LDA technique. The swirler module was attached to a circular mounting plate and mounted concentrically within the 260 mm outer diameter cylindrical rig casing. A solid cylinder of 200 mm diameter was located 750 mm downstream of the swirl module exit. The laser equipment was attached to a precise traverse mechanism to allow accurate measurements. The LDA technique was used to measure the velocity components and turbulence levels at different axial locations downstream of the swirler exit plane at  $(x/D= 0.0)$  where  $x$  is the axial distance starting from swirl exit and  $D$  is the swirl exit diameter used as a reference diameter ( $D= 100$  mm). Due to limitations imposed by the travel of the traverse mechanism the measurements were taken only downstream as far as  $(x/D= 4.2)$  whereas the top of the downstream cylinder was located at  $(x/D= 7.5)$ . This has an impact on determining the size of the CTRZ since it was reported [48] that the CTRZ was not closed before the final measurement plane. The measurements showed that, although the flow through the swirler was highly three dimensional due to the wake of the swirler vanes, this three dimensionality disappeared very rapidly downstream of the swirler exit plane and the flow was axisymmetric due to the rapid mix out of the vane wakes. Therefore, initial 2D calculations were performed to investigate the ability of the RST and  $k-\epsilon$  turbulence models to predict the axisymmetric flow downstream of the geometry in isolation from the need to resolve the complex geometry of the swirler module. Experimental measurements at the  $x/D= 0.05$  plane were utilised as inlet boundary conditions. The three mean velocity components and all Reynolds stresses were available at this plane, such that only the value of the turbulence dissipation needs to be approximated. The



final measurement plane ( $x/D= 4.2$ ) was chosen as the exit boundary condition where the axial velocity component was prescribed from experimental measurements. Hughes found that the above 2D calculations and assumptions required for the prescription of turbulence dissipation at the inlet were not ideal for such case. Therefore, calculations of the full swirler geometry were performed which required a complex grid. A  $45^\circ$  sector of the physical domain has been simulated numerically in the thesis of Hughes [48] by using a pressure correction RANS solver with a single block structured grid and the standard  $k-\epsilon$  turbulence model.

In Figure 5.11 the predicted streamlines offered by Hughes [48] are plotted downstream of the swirler exit for both the experimental and the 3D numerical predictions. Although the main flow features were captured, obvious differences in spreading angle and recirculation zone structure can be noticed. Quantitatively, the axial and circumferential velocity components and turbulence levels at ( $x/D= 0.05$ ) are compared with experimental data in Figure 5.12. They show reasonably good agreement with the general shape of the three curves being captured. The calculated axial velocity is close to the experimental data, despite a recirculation which is predicted at ( $r= 0.03m$ ) which is not present in the experimental data and is attributed to flow separation on the outer shroud surface. The double peaks of the circumferential velocity distribution are predicted less well compared to the experimental values; and same can be noticed at the centreline where the turbulence energy level also shows poor agreement. The large differences close to the centreline are described by Hughes [48] as being due to flow unsteadiness (e.g. a precessing vortex core) which is noticed experimentally but cannot be predicted by steady state RANS CFD predictions. The Boussinesq eddy-viscosity approximation assumes that the principal axes of the Reynolds stress tensor are coincident with those of the mean strain rate tensor at all points in a turbulent flow. These assumptions make the  $k-\epsilon$  model potentially in error when predicting flows with strong streamline curvature and flows with boundary layer separation.

Another issue which might worsen the calculations is the location of the exit boundary condition which is in a non uniform flow region i.e. no zero gradient exit plane. Hughes reported a time consuming complicated structured grid generation and suggested a tetrahedral unstructured grid to be used to enable full geometry calculations and improve the boundary condition implementation.

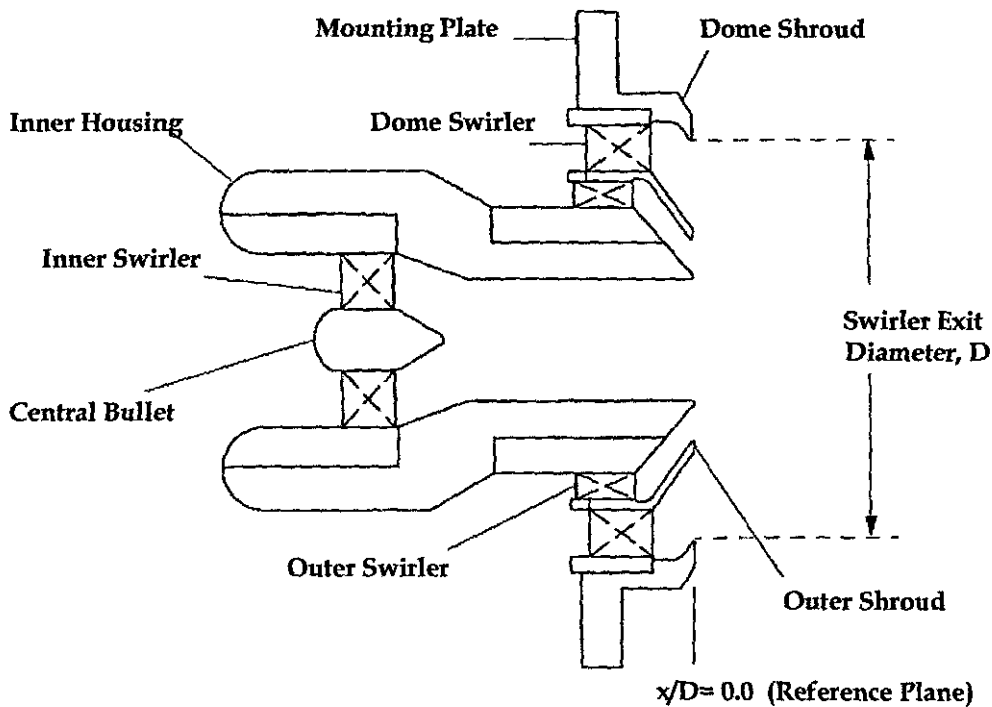


Figure 5.9 Swirler model components

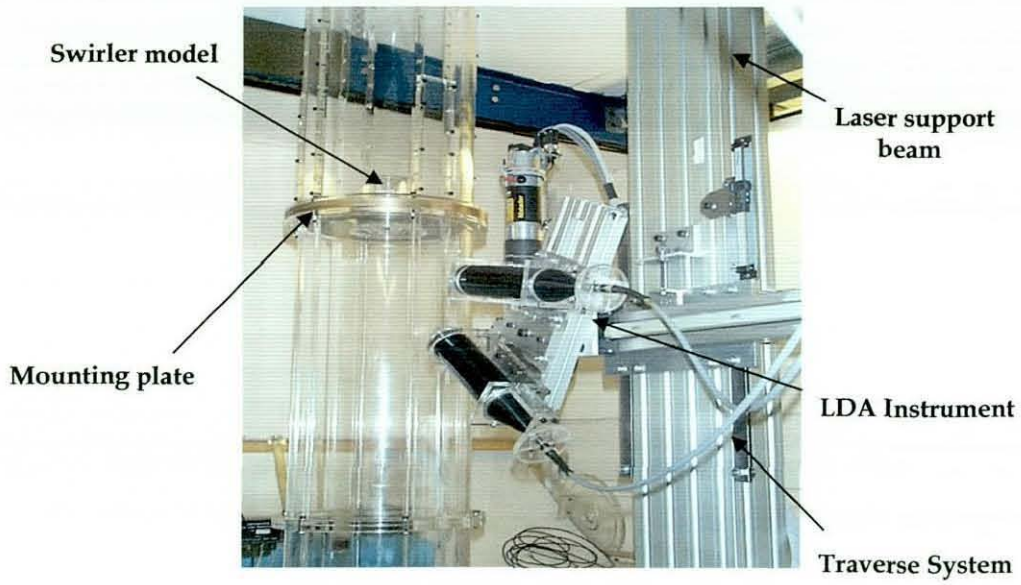


Figure 5.10 Experimental testing setup

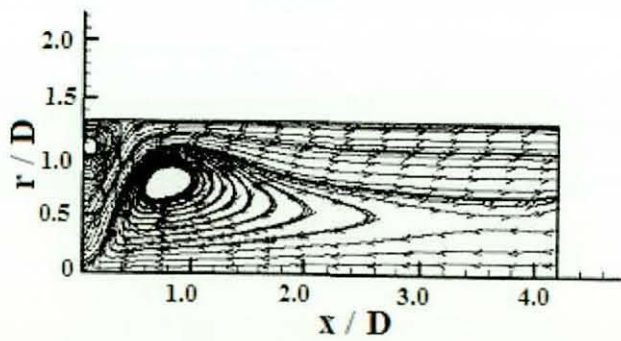
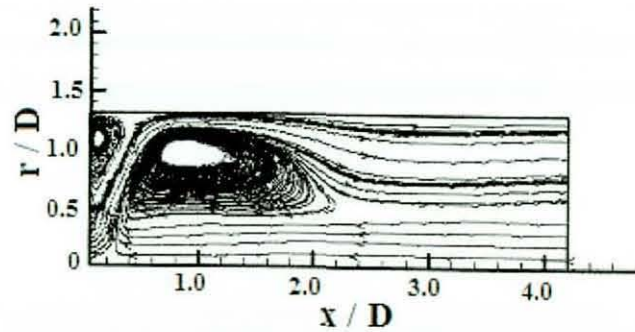
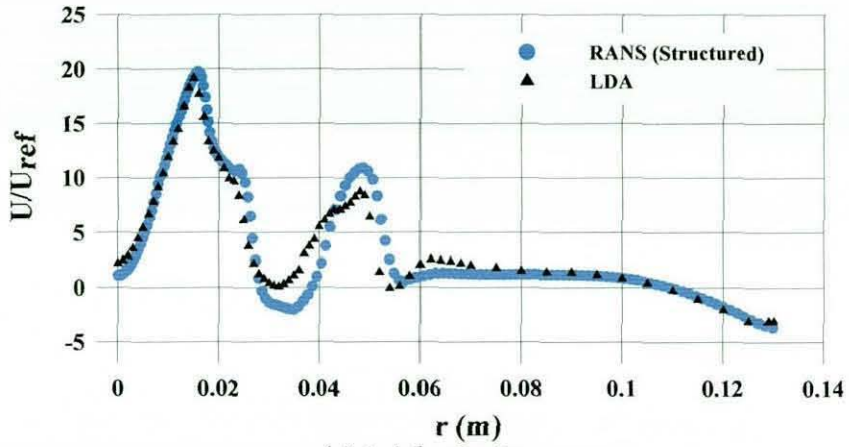
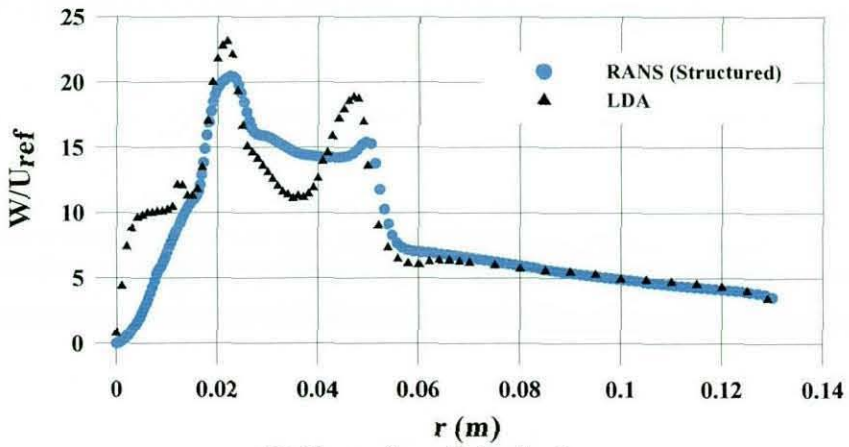


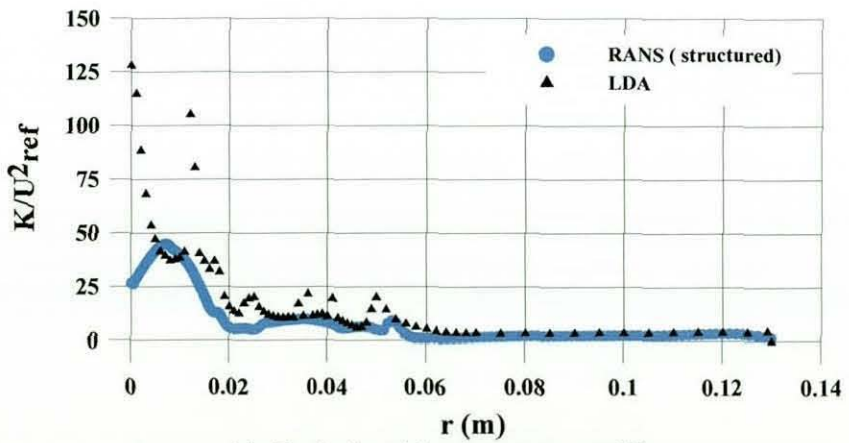
Figure 5.11 Streamline contours of the flow downstream the swirler exit [48]



(a) Axial velocity



(b) Circumferential velocity



(c) Turbulent kinetic energy profile

Figure 5.12 Experimental data vs. structured grid predictions at ( $x/D=0.05$ ) [48]

#### 5.4 Solid Geometry Modeling and Grid Generation

Geometry modeling and grid generation are the most time-intensive aspects of CFD analysis when complex geometries are involved. In the previous section, it was noted that Hughes [48] has pointed out that besides the limitations imposed on the accuracy of the numerical simulation by the employment of a single structured grid, a complex and time-consuming solid modeling and grid generation procedures were necessary to complete the multi-stream swirl prediction. A tetrahedral unstructured grid approach was suggested in order to improve prediction accuracy by allowing fully coupled calculations of the flow upstream, through the swirler, and downstream in the mixing region, more flexible grid refinement, and facilitating accurate implementation of the boundary conditions. Although tetrahedral grids are much easier to generate, they have been found to produce incorrect solutions especially in regions where mixing effects are important and flow/mesh misalignment is large. This was clearly evident in the previous chapter from the unrealistic growth of the boundary layer in the calculations carried out for the JICCF case using a purely tetrahedral grid. Thus, the best approach for unstructured mesh calculations was found to be to use a tetrahedral-prismatic and/or a purely hexahedral grid. In this section, the procedure employed to create the solid model of the multi-stream swirler and to generate appropriate numerical grids will be discussed. The constraints imposed by the geometric complexity and flow solver requirements on this procedure will be highlighted.

A priori knowledge of the flow field provides important insight to facilitate the grid generation procedure by allowing the grid density to be adjusted in order to capture adequately known flow field features. From the previous chapter, tetrahedral and tetrahedral-prismatic grids were found easy to generate compared to hexahedral grids, where large numbers of sub-volumes were needed to capture the geometry accurately. For the MSSF case therefore, Fluent calculations were



initially carried out on a tetrahedral grid as a quick and easy way to indicate important flow features before proceeding with generating other types of grids.

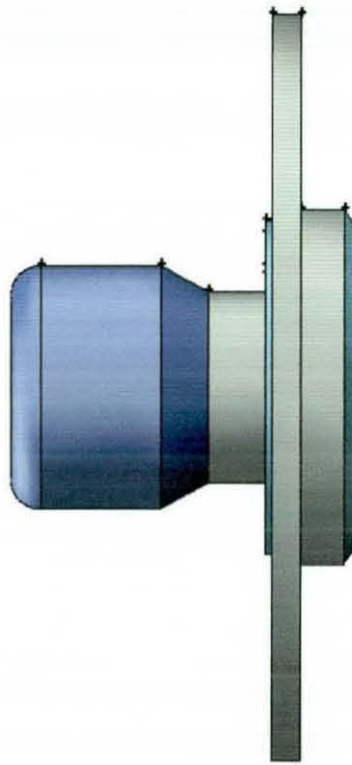
Defining the solid geometry is the first step in any complex geometry grid generation procedure. To avoid the cleaning up process associated with importing solid geometry into the grid generator from an external CAD system, the MSSF solid model has been created within the Gambit grid generation package provided by the Fluent software suite. Gambit provides flexibility in creating complex solid models by sub-dividing the geometry into simpler parts which can be easily created and assembled together to form the final geometry. The MSSF solid model was created according to the manufacturing drawings provided in Hughes [48] as follows:

1. Create a 2D cross-section of the outer parts of the MSSF mounting plate, dome swirler shroud, outer swirler shroud and inner housing and then revolve this  $360^\circ$  around the z-axis to create a 3D solid geometry as shown in Figure 5.13 (a).
2. Similarly, draw the central bullet 2D cross-section and revolve this. It is highly recommended here to create a number of circumferential edges (curves) on the geometry which will facilitate the meshing process later by allowing control of the mesh density on critical (faces) surfaces. This was done by creating forward and backward dome as well as the central cylinder and intermediate cone parts as independent entities, and later connecting them to create the final solid model of the central bullet as in Figure 5.13 (b).
3. Draw a 2D streamwise cross-section of the inner swirler vane. Locate this on the bullet surface and extrude radially to match the inner swirl annulus height. Copy and rotate the single vane created by  $45^\circ$  about the z-axis to create eight inner swirl vanes (as shown in Figure 5.13 (c) already attached to the central bullet).

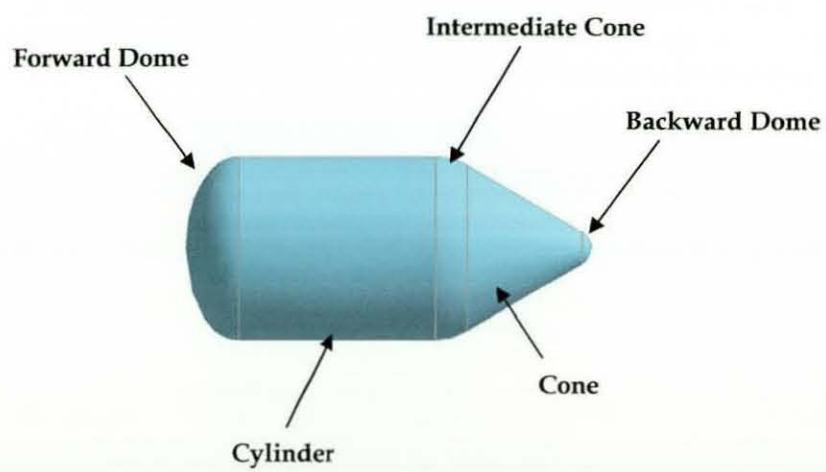


4. Assemble the swirler parts by locating each component in its right position and unite these to create a single solid model. The object so created is the merger of Figures 5.13 (a) and (c), but has so far no vanes in the outer and dome swirler annuli.
5. Draw 2D streamwise cross-sections of the dome and the outer swirl vanes passages. Locate these on their inlet and outlet surfaces and connect to form three dimensional swirl passages; thereafter copy and rotate the 3D swirl passage every  $15^\circ$  and  $22.5^\circ$  for the dome and outer swirler respectively as in Figure 5.13 (d). Subtract the created passages (24 dome swirl passages and 16 outer swirl passages) from the solid model created in step 4 to obtain the complete swirler model as shown in Figure 5.14.
6. The final step is to create the flow physical domain by subtracting the swirler model from an outer cylinder and exit inner cylinder as shown in Figure 5.15.

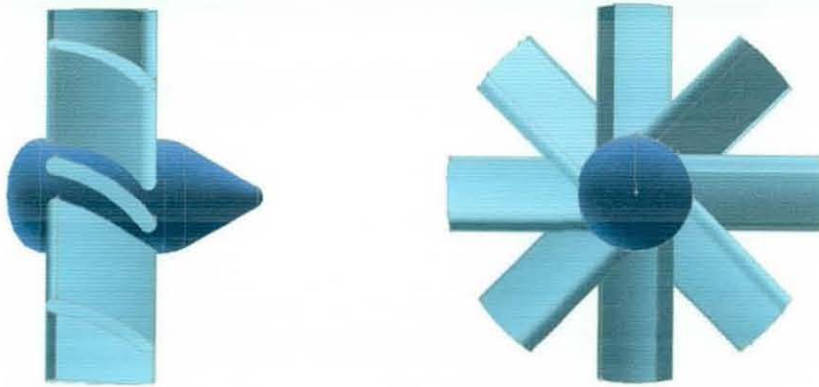
The created model possesses a periodic characteristic which can be utilized to reduce significantly the computational cost of the numerical simulation, for example a  $45^\circ$  sector of the domain can be considered to reduce the calculation time to  $1/8^{\text{th}}$  of that required for the whole domain.



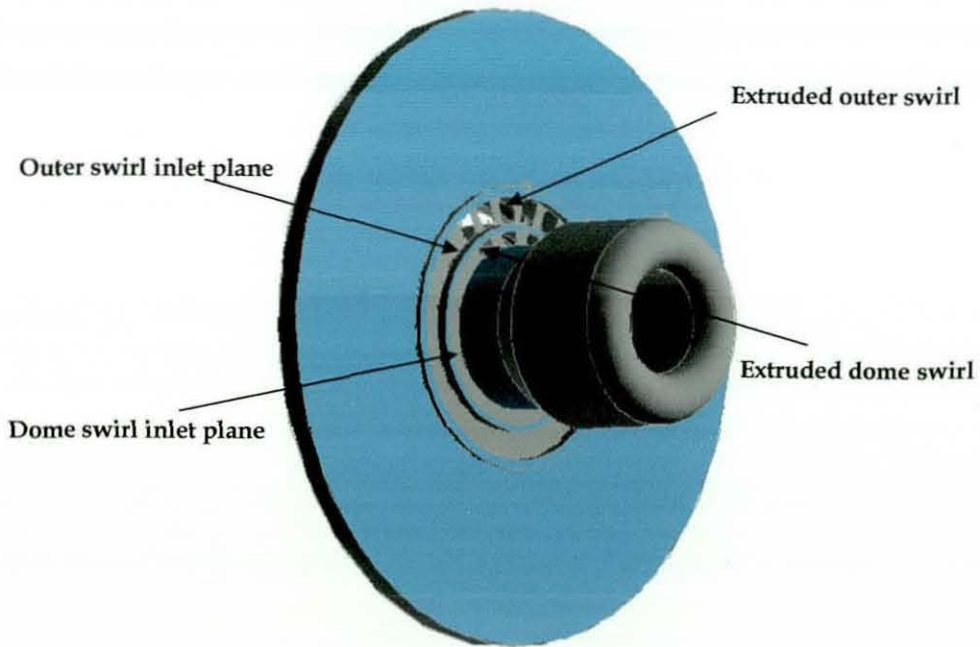
(a) Mounting plate, shrouds and inner housing solid model



(b) Central bullet solid model

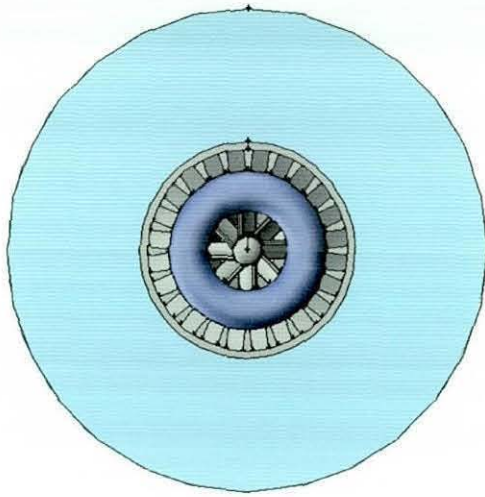


(c) Inner vanes and central bullet arrangements

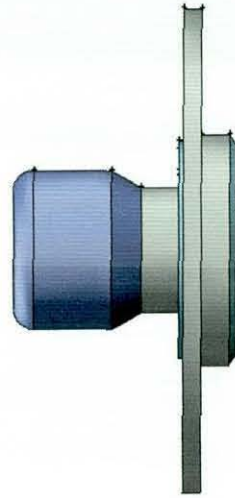


(d) Extruding the swirl passages through the solid model

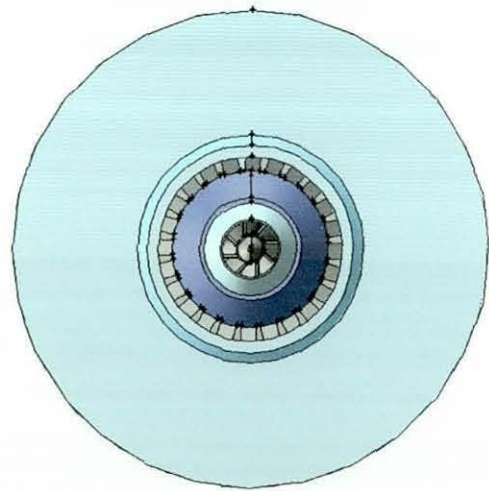
Figure 5.13 Various parts of the swirler solid model



Front view



Side view



Rear view

Figure 5.14 Swirler solid model side, rear and front views



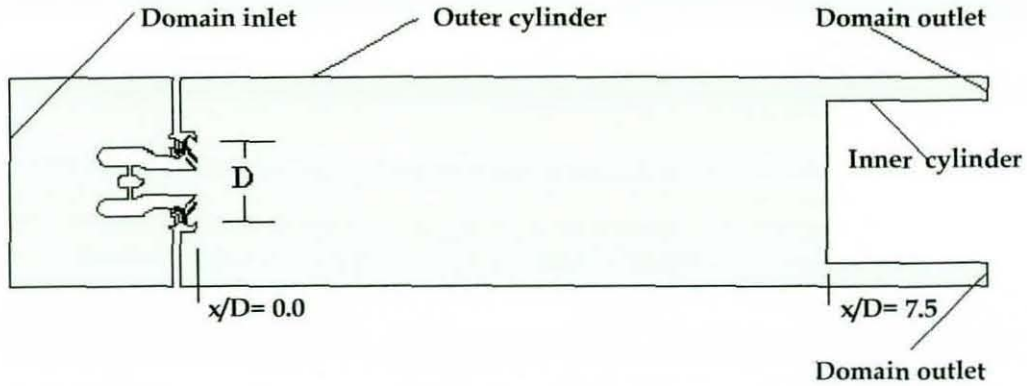


Figure 5.15 Longitudinal cross-section along the whole solid model

To generate a purely tetrahedral grid, the  $45^\circ$  sector was divided into four zones as shown in Figure 5.16. Dividing the domain into multiple zones is a common approach for handling complex geometries which facilitates an efficient grid generation process by dealing with each zone in a different manner. In order to define the rotational periodicity, a mesh hard link between the faces (surfaces) of each periodic (inlet-outlet) boundary pair has to be established prior to grid generation so that the surface grids at the inlet and outlet of each periodic pair are generated identically. Eight periodic pairs were therefore produced as a result of using four zones.

The meshing strategy now is to start with the most complex zone, which here contains the swirler (zone 4) to form the source mesh for the other zones. Initially, it is necessary to produce a high quality surface mesh on the geometry which accurately represents the solid model surfaces and establishes a base for successful volume meshing. For this purpose, in the present case an iterative process was followed to control the surface grid density and to ensure the grid captured all details of the model precisely. During this process, different sizes of surface mesh (triangles) were tried. The final mesh was passed through a comprehensive quality checking and smoothing procedure. Figure 5.17 illustrates the surface mesh of the

swirler sector. One can notice the complexity of the various surfaces specially those at the shroud ends and swirl passage spacing and steps. After establishing the surface mesh, a 3D tetrahedral mesh can be generated automatically and this also needs a further smoothing and quality checking operation. The mesh quality was quantified by the cell skewness. This property gives a measure of how far a triangle or tetrahedron is from its perfect (equilateral) form. A skewness of zero is perfect and one is poor. For the grid generated for the MSSF the mesh surface skewness was kept below 0.75, with an average value of 0.3. The interior volumetric skewness was kept below 0.85 with an average value of 0.4. A similar procedure was followed for the other three zones which are much easier than zone 4. During meshing it is important to take into consideration the common faces between the adjacent zones; any change in grid size within one zone should be accomplished smoothly and gradually starting from the common surfaces to avoid poor quality in the final mesh. An initial tetrahedral mesh of about 230,000 cells was generated for the MSSF case as shown in Figure 5.18. This was considered as a coarse mesh to be used to establish a priori knowledge of the flow and act as a base grid for further refinement.

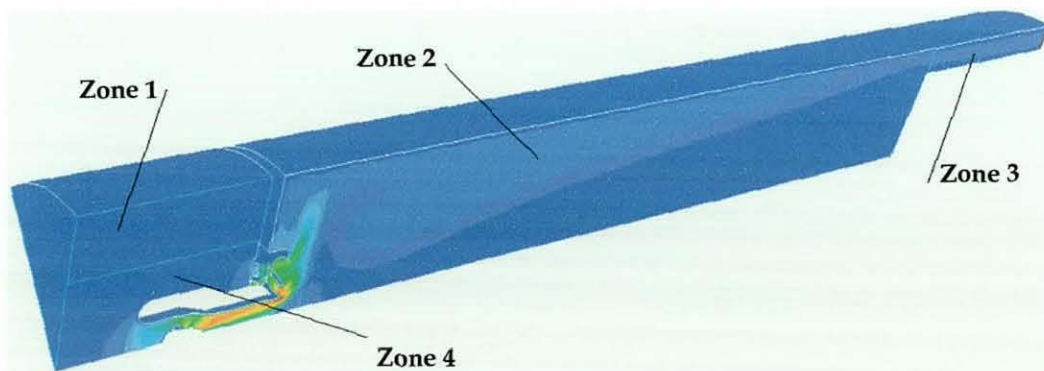


Figure 5.16 The 45° sector and the four meshing zones



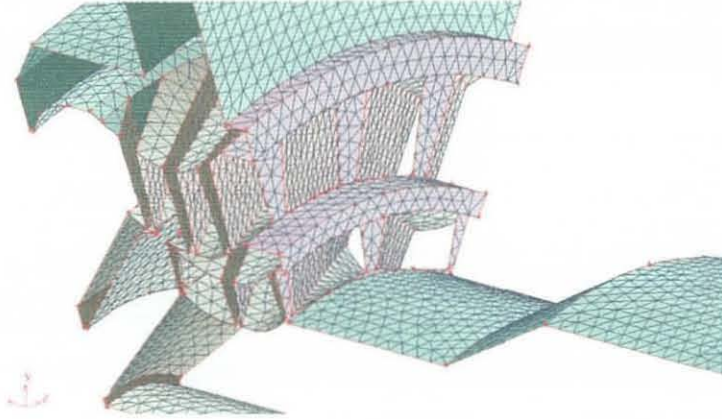


Figure 5.17 The tetrahedral surface mesh at the inlet of swirl passages

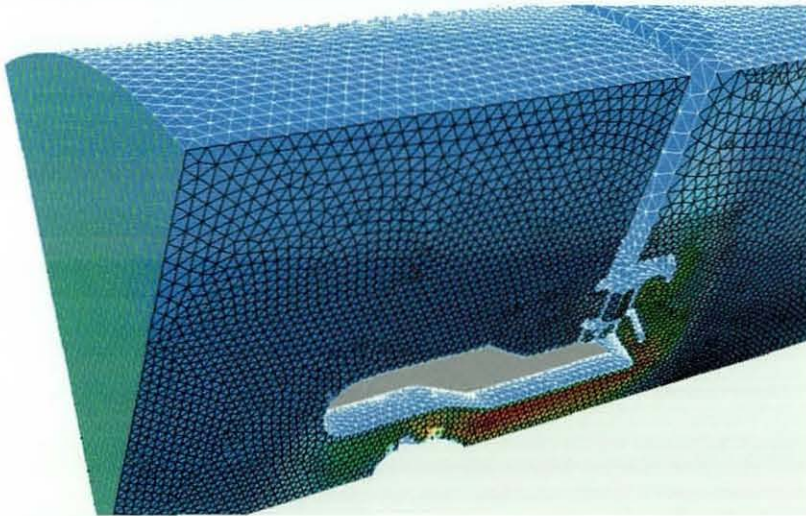


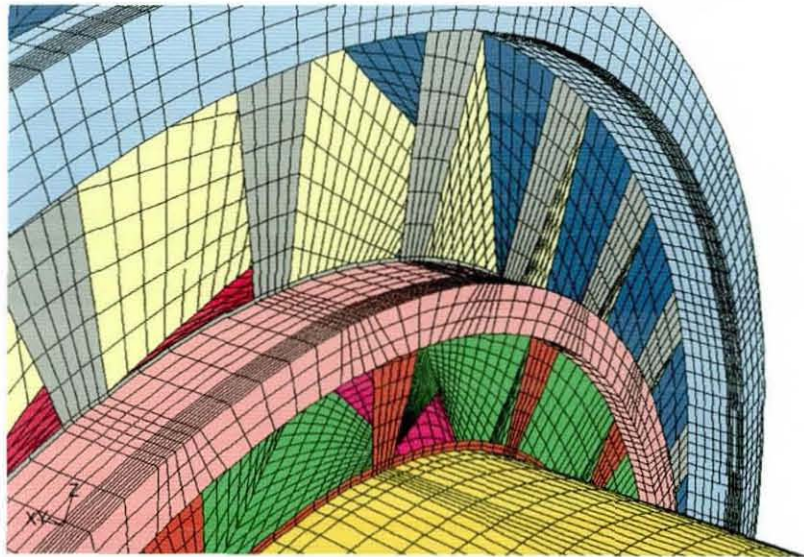
Figure 5.18 The tetrahedral computational grid

The second task in the grid generation process is to generate prismatic layers close to the solid surfaces of the model to resolve the boundary layers. A commonly used strategy for generating boundary layer meshes in commercial grid generation

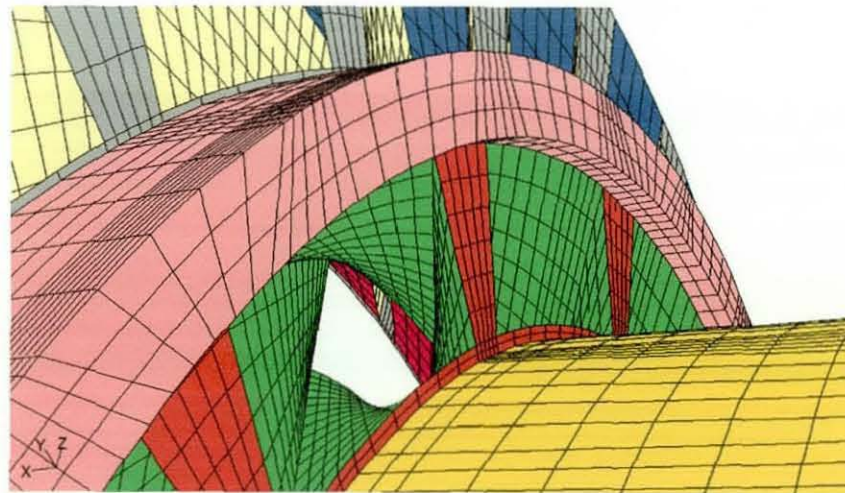
packages is the Advancing Layers Method (ALM) [159, 160]. This method starts from a surface triangulation from which the boundary layer mesh is grown. Nodes are generated along a single direction from each surface node. These nodes form the basis for creating prismatic layers on the top of each surface triangle. However, it has been found that this method may produce invalid or poor prismatic cells due to the occurrence of the following: (i) crossover of the normal directions along which nodes are placed can occur and (ii) the interference of the boundary layer mesh on intersecting surfaces [161]. Unfortunately, as was illustrated in the discussion on solid model construction the complex MSSF geometry has many intersecting, perpendicular, convex and concave surfaces which make the above two undesirable aspect very likely. The inner vane blade surfaces and their intersection with the central bullet as well as the surfaces of the curved dome/outer swirl passages are all examples of highly concave, convex, and intersected surfaces. The 3D boundary layer option in Gambit failed to produce any prismatic mesh due to lack of smooth continuity in the various surfaces which is a main constraint in Gambit boundary layer algorithm [139]. This also happened when using T-Grid which is an alternative Fluent software package used to produce prismatic layers from triangular surface meshes. ICEM-PRISM software was also tried; highly distorted prismatic layers in many regions were produced with many invalid cells. The edge collapse and face refinement operations used within the ICEM-PRISM software are included to improve the quality along the marching direction in some regions. However, these operations do not take into account the quality of the mesh in the extrusion operation which creates the prismatic layer(s) which may also then be degraded. The above shortcomings associated with ALM when used with complex geometries is one of the open issues in the field of numerical grid generation, several researchers have concluded that the restriction of growing a single set of nodes from each surface node constrains ALM and limits the quality of elements that can be created [159].



Failure to generate prismatic layers in the tetrahedral grid makes the hexahedral grid approach the only choice to simulate the current MSSF case since because of the experience gained (particularly with Hydra code) in the JICCF predictions reported in chapter 4, a purely tetrahedral grid was excluded from the beginning. ICEM-HEXA software was used to generate a purely hexahedral mesh with 2,807,124 cells. The basic approach of the ICEM-HEXA software is to create a 3D block topology model equivalent to the real geometry. With this model, blocks which completely contain the real geometry are recursively subdivided until the desired resolution is reached. The procedure of decomposing (blocking) the overall solution domain into an appropriate block topology requires considerable knowledge of meshing techniques and decomposition tools. Even an expert may experience several trials and failures before finding the best blocking strategy. With the current geometry the situation was very complicated since a large number of blocks was needed in order to capture all the geometry details accurately. This complexity is mainly due to the highly curved surfaces (central bullet, inner housing, and inner vane leading and trailing edges) as well as the steps upstream of the inlet of the swirl passages and the outer shroud edges (see grey, yellow and pink surfaces in Figure 5.19(a)) which need high resolution meshes, as can be seen in Figure 5.19. Refinement in any single block of the mesh always affects the neighbouring blocks, adding an extra number of cells to the final mesh as again can be seen from Figures 5.20 and 5.21. Successful decomposition of the MSSF solution domain into appropriate block topology required 34 blocks. The cost of this large number of blocks was high since the whole geometry had to be considered rather than a  $45^\circ$  sector. The main reason for this is a limitation of the Hydra preprocessor (*jm-54*) which only can handle up to ten periodic pairs [89]. However, blocking a periodic sector would probably be more complicated than dealing with the whole geometry and would certainly yield a number of periodic pairs larger than the maximum allowed, hence a  $360^\circ$  geometry was adopted.

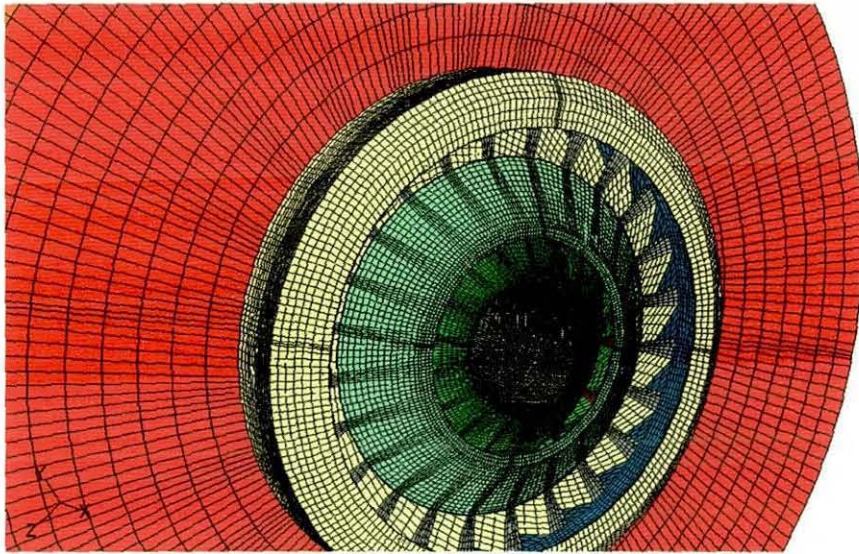


(a) Inner and outer swirls

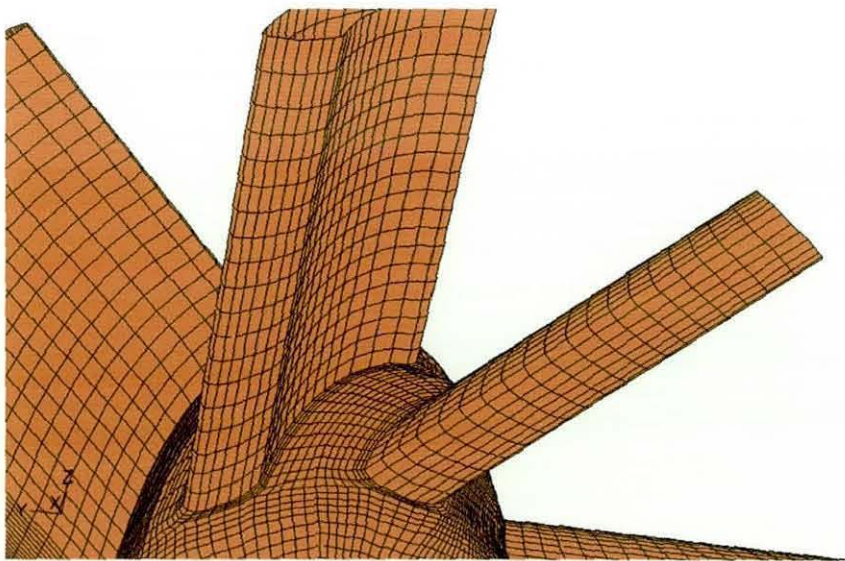


(b) Highly curved swirl passage





(c) Swirl exit shrouds and mounting plate



(d) Central bullet and inner vanes

Figure 5.19 Surface meshes of the swirler components

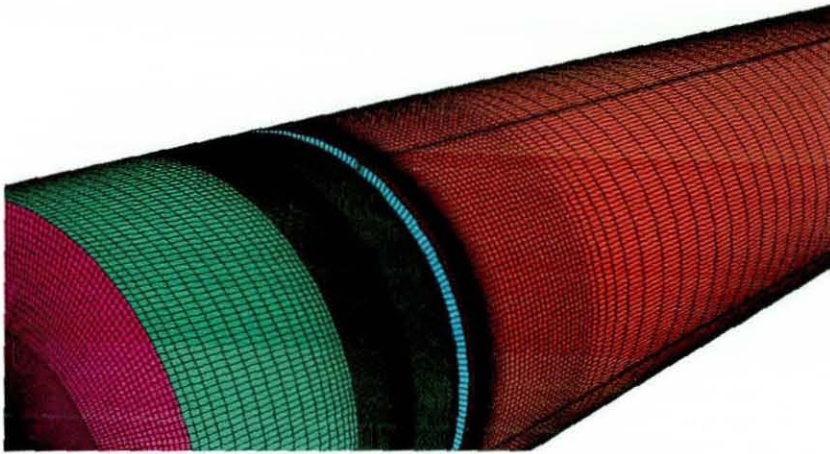
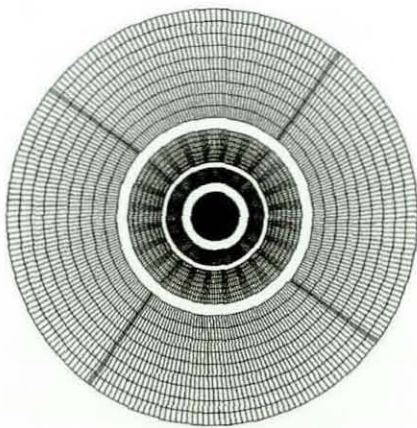
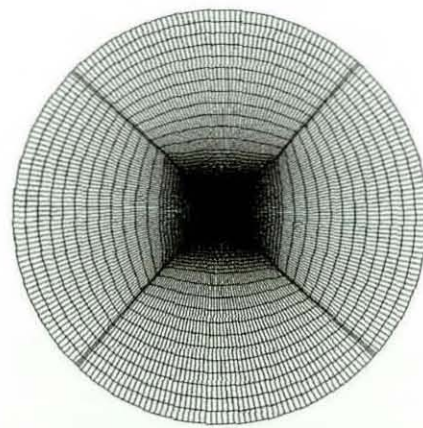


Figure 5.20 The hexahedral computational grid



(a) Exit shrouds plane  $x/D = -0.05$



(b) Swirling exit plane  $x/D = 0.0$

Figure 5.21 Axial cross-sections through the computational domain



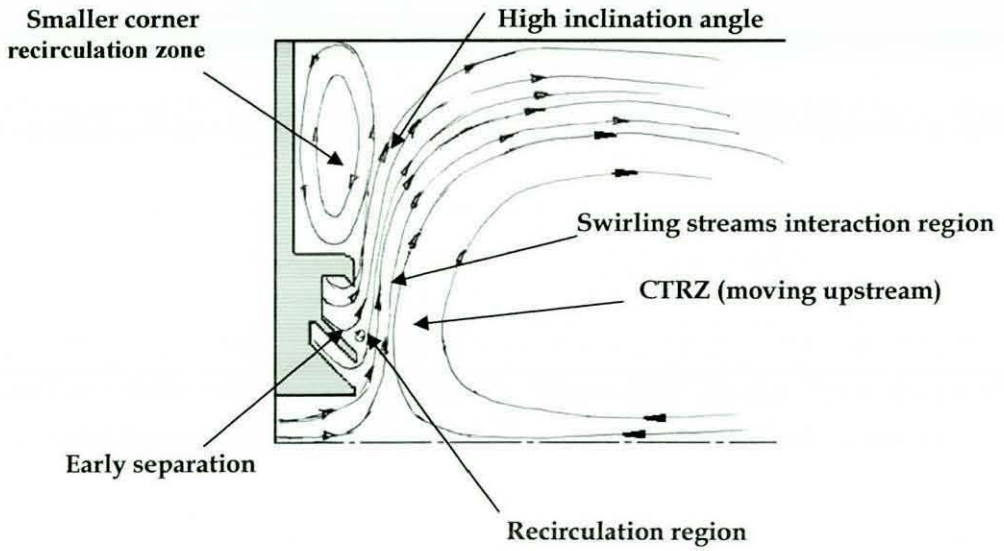
### 5.5 Unstructured Mesh Predictions, Comparisons and Discussions

Initially, the segregated solver of Fluent was used to predict the complex MSSF test case on a purely tetrahedral grid to provide quick calculations since only a 45° sector was simulated. The main goal of these predictions is to establish a solution that can provide initial information on the main flow features and also provide boundary conditions for subsequent Fluent and Hydra calculations. These initial predictions would be used to determine regions with high gradients that have to be considered for special attention during the hexahedral grid generation process. By additional grid refinement of the initial tetrahedral mesh, the ability of the *k-ε* turbulence model to predict such a complex swirling flow may also be assessed against both experimental data and the advanced RST model. In these calculations, the SIMPLE scheme was used for the pressure equation while the first order upwind scheme was used for the momentum, turbulence and stress equations. The experimentally measured flow properties were used as an inlet boundary condition as well as to initialize the computational domain. Since no measurements were carried out at the rig exit, the pressure there was adjusted through iterative calculations to maintain the experimentally measured mass flow rate. This also helps to identify exit boundary conditions which were needed for the Hydra calculations where fixing the level of the exit pressure is a common practice. To achieve best accuracy, the solution-adaptive grid capability of the Fluent solver was used, after the preliminary coarse grid calculations, to refine the grid and to examine the sensitivity of flow predictions, especially in regions with large gradients.

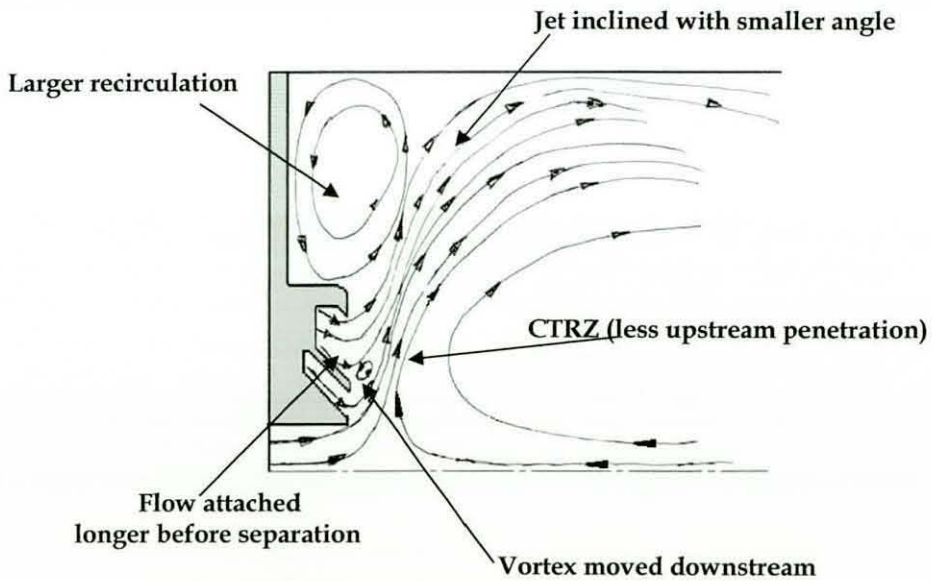
The structure of the CTRZ is one of important features of swirling flows for the validation of numerical methods. In the current case in all probability, because the test section contains a downstream blockage, the CTRZ will stretch all the way to the blockage beyond the experimental measurement limits giving less information about its structure and size, so it cannot be used in the validation. The unsteadiness noted in the measured flow is driven by a non-axisymmetric PVC structure which

reduces the utilization of the experimental data for validation of the numerical predictions, where steady state, statistically stationary turbulence models are used, but the test case was used nonetheless. Emphasis will be placed in comparing with measurements on the swirler exit region since this is where the majority of measurements were conducted. Important features include the three swirl stream interactions, the swirling jet structure and the jet spreading angle, the structure of the corner recirculation zone and the upstream part of the CTRZ. Velocity magnitude contours are used below to allow illustrative and qualitative analysis; while for quantitative analysis radial profiles of the three velocity components and turbulence levels 5 mm downstream of the swirler exit plane ( $x/D=0.05$ ) were selected. Figure 5.22 shows illustrative sketches for the flow features in the swirler exit region on different grids. Figure 5.23 and 5.24 illustrate the predicted velocity magnitude contours on the coarse and the fine grids for both the  $k-\epsilon$  and the RST models respectively. On the coarse grid, the  $k-\epsilon$  model was not able to produce the downstream inclination of the exit swirling jet presumably due to high level of numerical mixing; on the fine grid the jet was deflected more downstream and an improved conical shape was captured, see Figure 5.23. The RST model captured the conical shape of the swirling jet on both grids; a stronger jet penetration was produced on the fine grid and a slightly smaller spreading angle than that of the coarse grid as can be seen in Figure 5.24. The differently predicted penetration strength and spreading angles of the swirling jets are attributed to the ability of the turbulence models to capture small scale separation/recirculation zones on the surfaces of the swirl exit shrouds to a different degree (see Figure 5.22). For the  $k-\epsilon$  model predictions, on the coarse grid the swirling flow between the outer shroud and the dome shroud has the tendency to separate at an early stage, thus to entrain the flow vertically. However on the fine grid the flow has the tendency to remain attached longer on the surface which will delay the flow separation and modify the detailed manner in which the three separate swirl stream merge to form a single swirl jet cone, this leads to a swirl jet cone angle which impinges with a smaller spreading angle as in Figure 5.23.





(a) Coarse grid (high numerical diffusion)



(b) Fine grid (lower numerical diffusion)

Figure 5.22 Illustrative sketch for the flow features at swirl exit region

On the same coarse grid, the RST model was able to predict a spreading angle close to that predicted by the  $k-\varepsilon$  model on the fine grid. This spreading angle reduces a little in the fine grid RST model calculations as can be seen in Figure 5.24. The CTRZ has a tendency to penetrate further upstream for larger jet spreading angles and a low pressure flow is created in the centreline region. This can also be noticed from the velocity profiles in Figure 5.25 and 5.26, where the axial velocity magnitude at the centreline decreases with grid refinement. Variation of the velocity levels has a direct influence on the turbulence levels in the centreline region as may be seen in the turbulent kinetic energy profiles.

In Figure 5.25 ( $k-\varepsilon$  model predictions) the normalized axial velocity at the centreline dropped significantly from five to zero due to grid refinement while in Figure 5.24 (RST model predictions) only slight difference can be observed with grid refinement. The predicted circumferential velocities in the region immediately downstream of the inner swirl exit plane ( $r=0.0$  to  $0.015\text{m}$ ) remain mostly unchanged with grid refinement indicating low swirling flow in that region. In the region of the three stream interaction, the flow decelerated under the influence of an internal recirculation on the shroud surface induced due to the deflection of the dome swirling flow as it approaches swirler exit (see negative velocity region around  $r=0.035$  in Figure 5.25 and Figure 5.22). The flow then accelerated as the three streams were mixed producing the swirl jet conical shape. Fine grids for both turbulence models show smaller recirculation zones in this region where the flow remains attached longer before separating from the outer shroud surface.

Figure 5.27 shows comparisons between the fine grid solutions of both turbulence models and the experimental data. Both numerical solutions were able to predict the general shape of the experimentally measured velocity profiles in terms of magnitudes and peaks locations despite the high jump in the circumferential velocity and turbulence levels in the centreline region which is attributed to the flow unsteadiness noticed during the experimental testing. The slight difference in



the velocity components and the shift of their corresponding peaks within the region between ( $r=0.02$  and  $0.05\text{m}$ ) can also be attributed to the non-axisymmetric vortical structure produced by the flow unsteadiness.

In Figure 5.28, particle tracks within the flow over the whole solution domain show the different behaviour of each turbulence model on different grids in capturing the global features of the flow. This can be noticed clearly from the different sizes of the CTRZ, corner recirculation zone and swirling jet spreading angle. The  $k-\epsilon$  model has a tendency to yield more *diffusive results*. On the other hand, the RST model implies smaller diffusive effect in response to anisotropy, streamline curvature, and sudden changes in strain rate associated with swirling flows. This is due to the fact that each Reynolds-stress component has its own transport equation which improves the physical accuracy of this model.

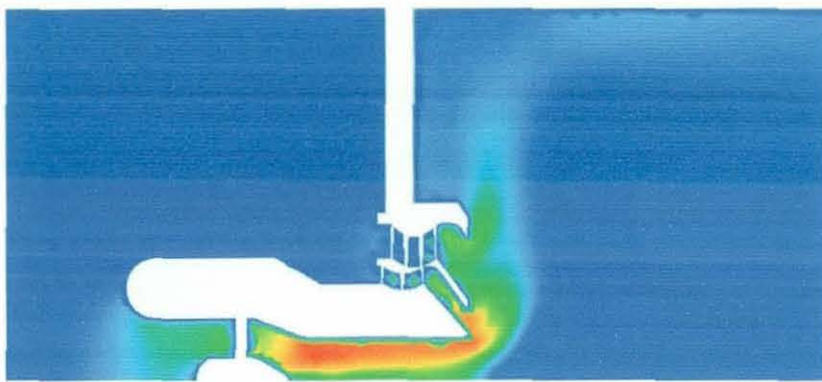
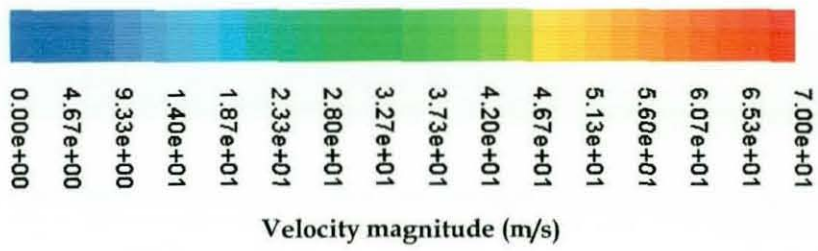
The hexahedral grid discussed in the previous section was generated based on the above tetrahedral grid predictions and within the available computational resources. The high gradient zones were refined as much as possible to capture the main flow features. The predictions obtained by both Fluent and Hydra solvers on this grid are presented in Figure 5.29 and 5.30. Both solvers were able to capture the main flow features with reasonable accuracy. Separation of the flow on the shroud surfaces at the swirl exit again plays an important role to determine the characteristics of the swirling jet thus the flow downstream. Compared to Fluent, the Hydra calculation show an earlier flow separation from the shroud wall which makes the swirling jet impinges and entrains the flow vertically allowing the CTRZ to penetrate upstream. This behaviour is similar to that noticed in the coarse tetrahedral grid predictions with the  $k-\epsilon$  model which is attributed to the numerical diffusion associated with the coarse grid solutions and can be reduced by grid refinement. On the same grid, Fluent predictions were less diffusive and able to predict the conical shape of exit swirling jet. Quantitatively, Hydra predicted the velocity and turbulent levels with reasonable accuracy compared to the



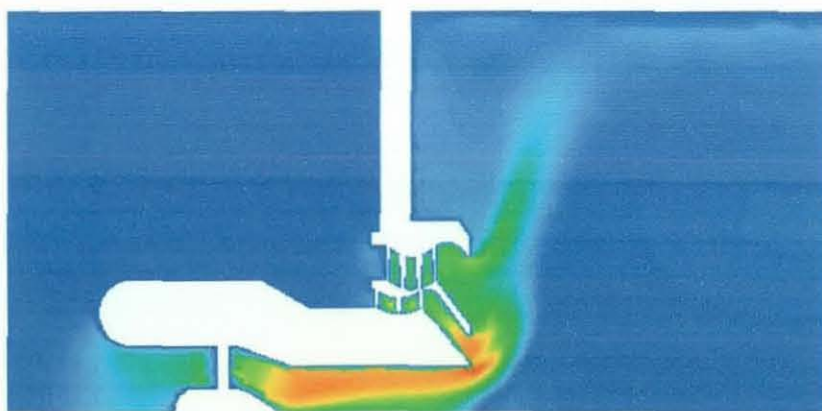
experimental data as shown in Figure 5.30. The remarkable difference in the peak values of the velocity components predicted by Hydra and Fluent compared to the experimental data is one of the main observations. Similar behavior was noticed in the JICCF calculations where on the hexahedral grid Hydra produced higher axial velocity than the experimental data. This is attributed to the flow misalignment with the grid and the numerical diffusion issues. The negative axial velocity between  $r=0.06$  and  $0.1$  and the low magnitude of the circumferential velocity indicates smaller size of the corner vortex due to the upstream propagation of the CTRZ. Despite the grid variable density and high skewness imposed by the geometry complexity in some regions, see Figure 5.31, the Hydra solver was able to predict the global structure of the flow with reasonable accuracy. From the predicted flow streamlines on Figure 5.32, the CTRZ was extended further downstream and interacts with the vortex generated on the top wall of the inner cylinder. The jet spreading was influenced by the grid quality in the swirl exit region as can be seen in Figure 5.31. Such behavior is expected since the vertex based solver of Hydra has the tendency to produce more numerical diffusion in poor grids than the Fluent cell centred solver.

Numerical diffusion as a dominant source of error in multidimensional flow has been discussed in the previous chapters. In the current case the grid quality as a major source of this error will be highlighted. To obtain maximum accuracy of the convective fluxes when using linear interpolation, the line connecting the centres of two neighbour control volumes should pass through the centre of the common face. However for the diffusive fluxes high accuracy can be achieved when the same line is orthogonal to the cell face and passes through the cell face center [12]. The hexahedral grid used in the current calculations has been generated based on multi zones as discussed before. In the interface of two zones when the grid size and/or grid orientations changed, a situation similar to that shown Figure 5.33(a) became unavoidable and will introduce more error in the convective and the diffusive fluxes calculations. The situation will be worst in the case of median dual control

volume where the angle between the normal and connected line became larger than the cell centered control volume as shown in Figure 5.33(b) and 5.33(c). This may explain the highly diffusive solution of the Hydra solver compared to the Fluent solver. Grid refinement is the easiest visible way to reduce, but not to eliminate, this kind of error. However, geometry complexity may not allow the grid refinement to take place without the high cost of extra huge number of cells.



Coarse grid predictions



Fine grid predictions

Figure 5.23 Velocity magnitude contours calculated on tetrahedral grids using Fluent solver with the  $k-\epsilon$  turbulence model



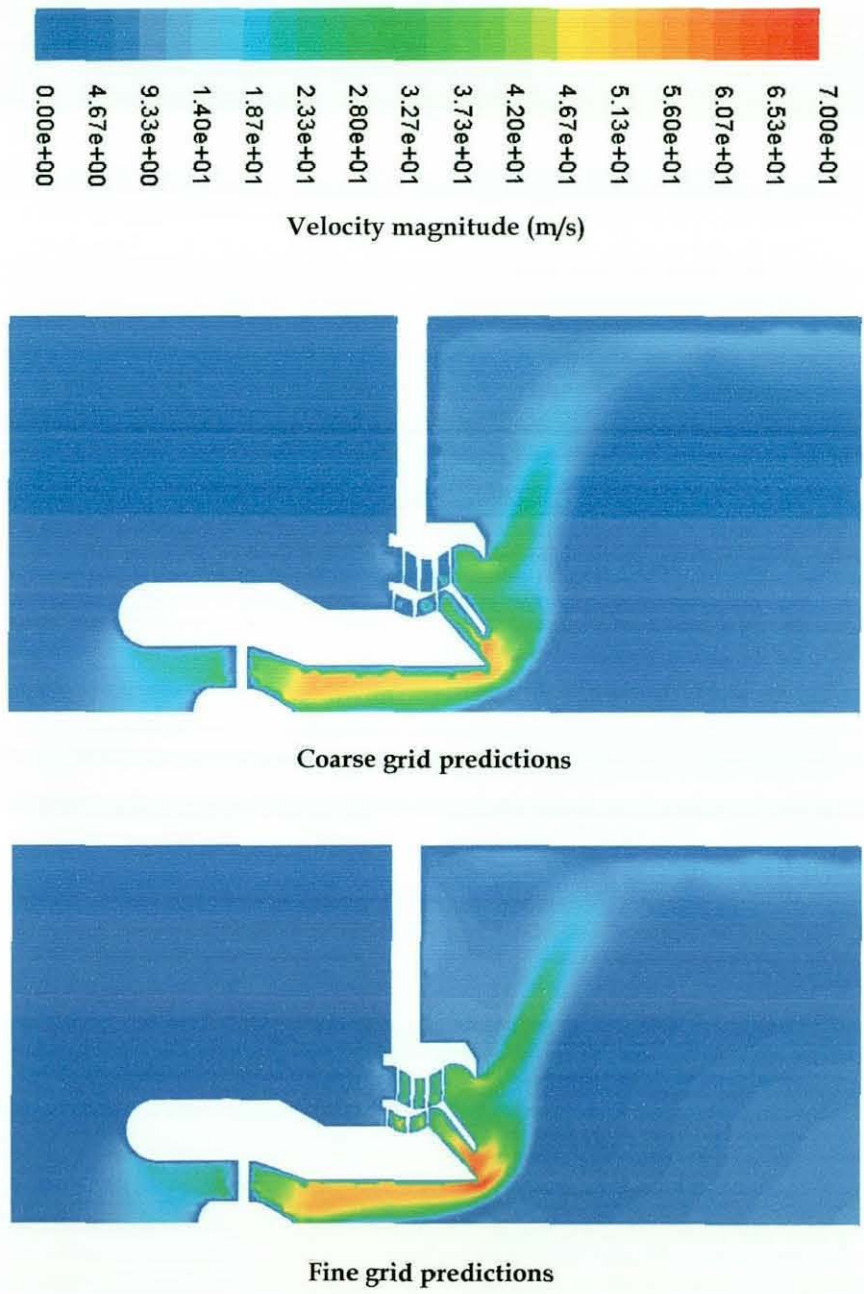
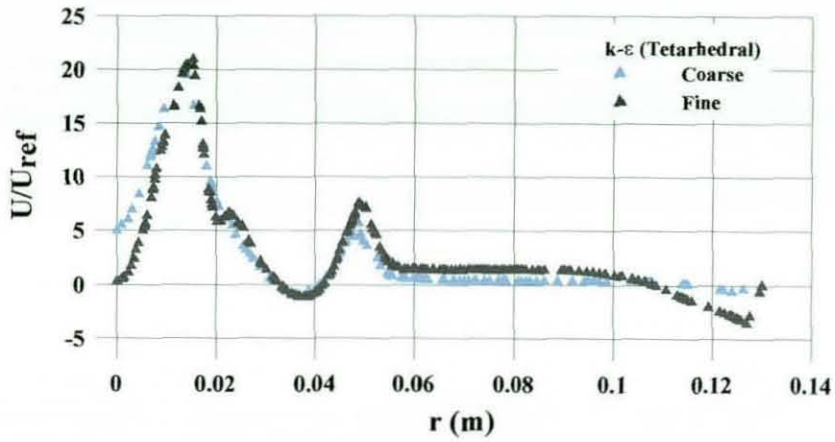
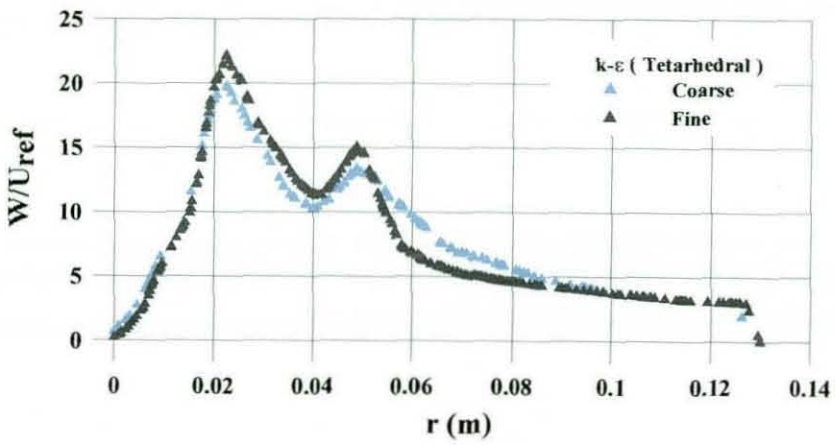


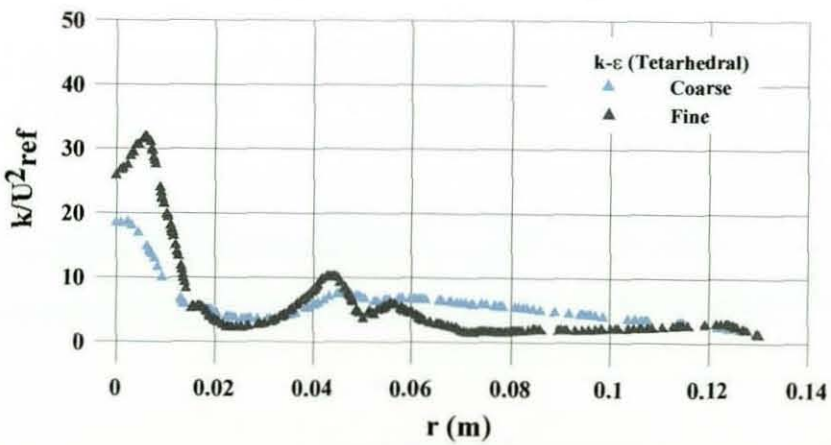
Figure 5.24 Velocity magnitude contours calculated using Fluent solver on tetrahedral grids with the RST model



(a) Axial velocity



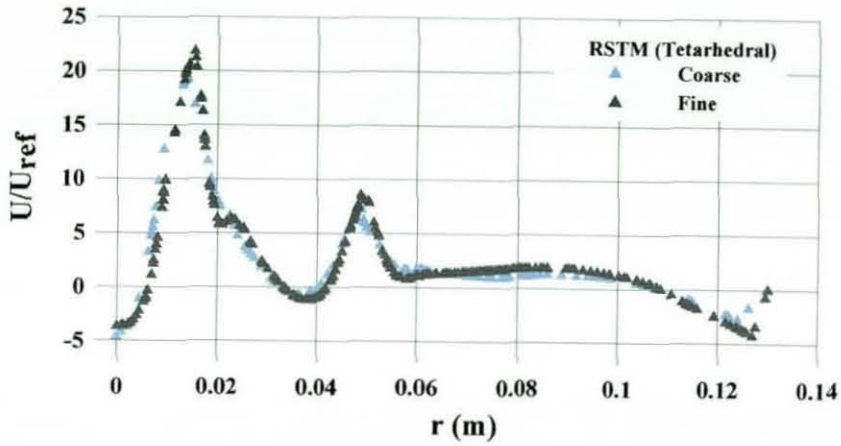
(b) Circumferential velocity



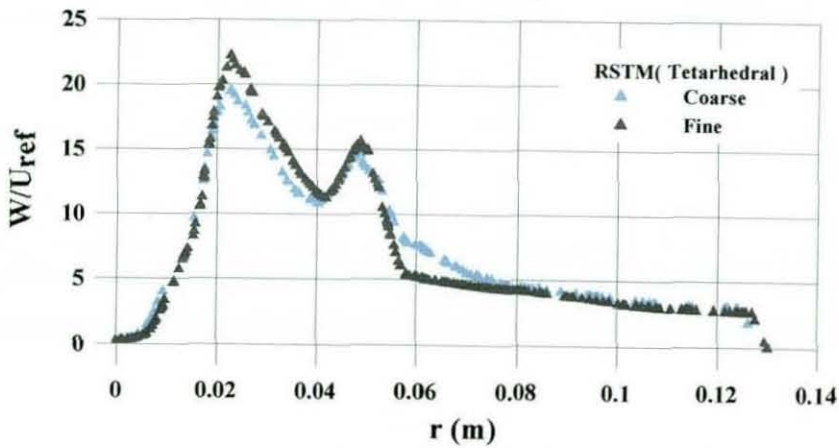
(c) Turbulent kinetic energy

Figure 5.25 Fluent predictions at  $(x/D=0.05)$  on tetrahedral grid with the  $k-\epsilon$  turbulence model

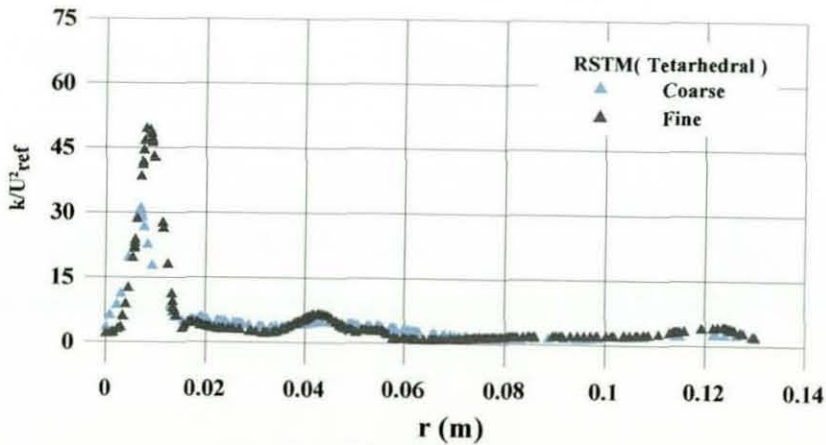




(a) Axial velocity



(b) Circumferential velocity



(c) Turbulent kinetic energy

Figure 5.26 Fluent predictions at  $(x/D=0.05)$  on tetrahedral grids with the RST model

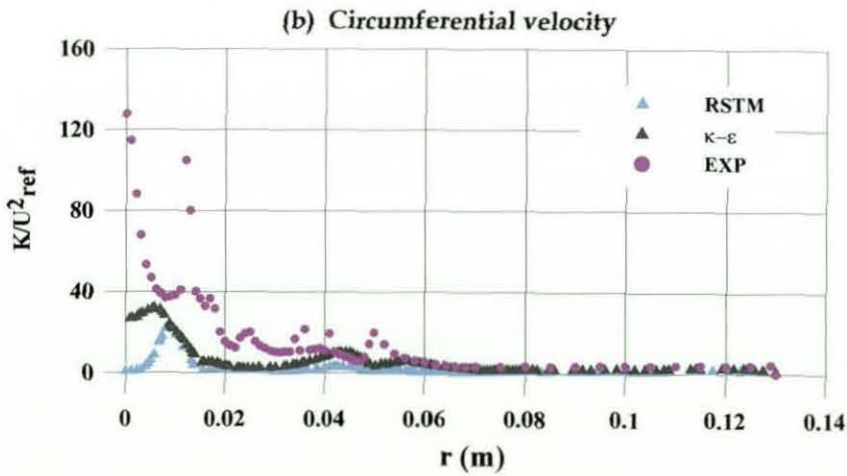
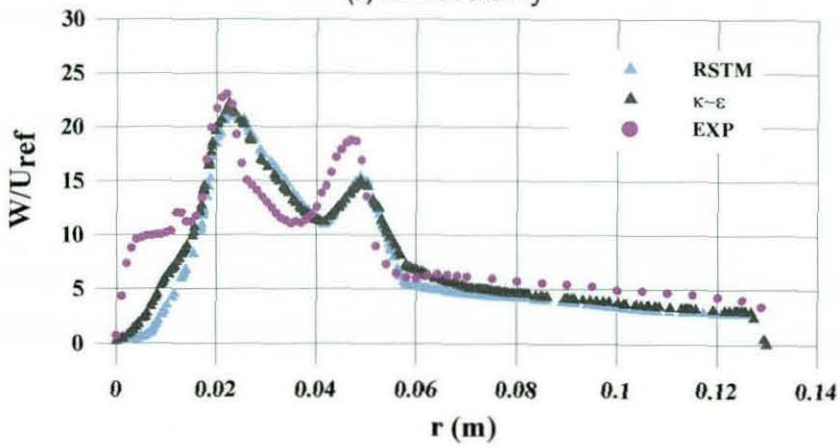
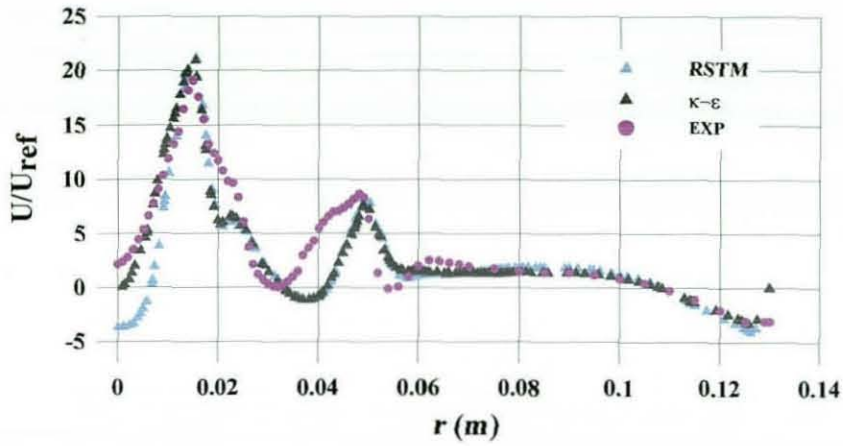
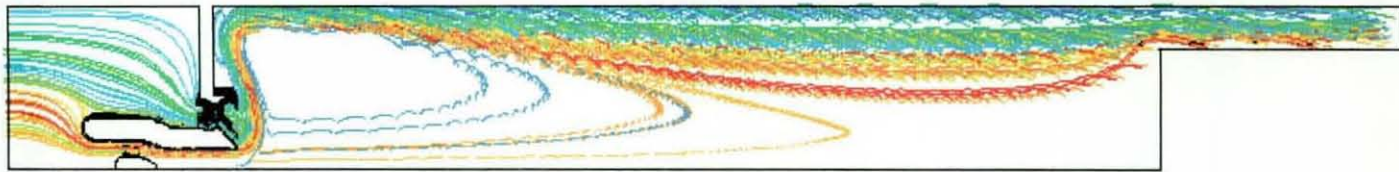
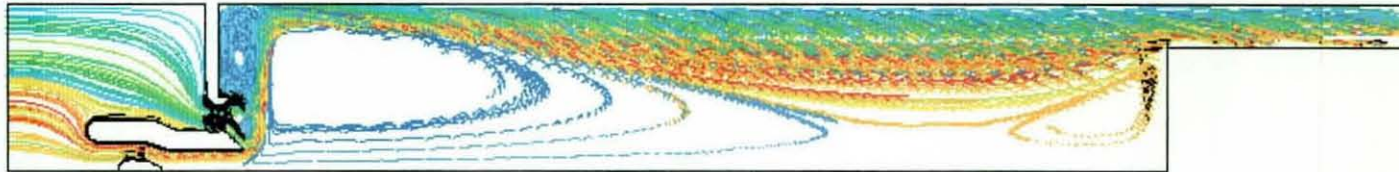


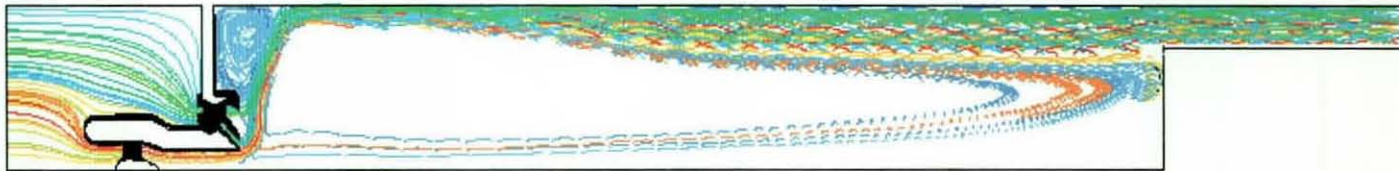
Figure 5.27 Fluent predictions on tetrahedral fine grid vs. the experimental data at  $(x/D=0.05)$



(a) The  $k-\epsilon$  turbulence model and coarse grid

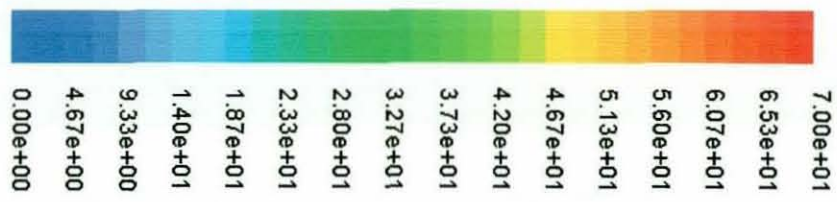


(b) The  $k-\epsilon$  turbulence model and fine grid

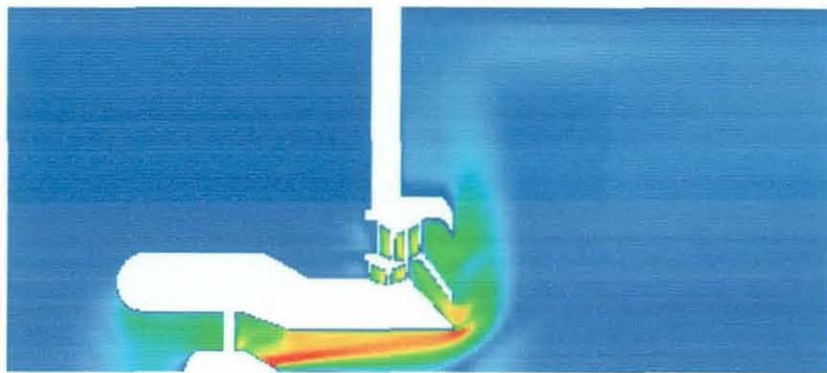


(c) The RST model and coarse grid

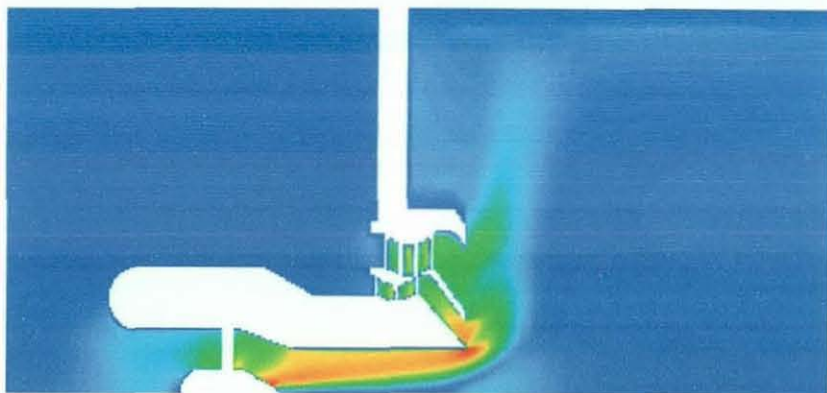
Figure 5.28 The predicted particle tracks of the flow along the computational domain



Velocity magnitude (m/s)



Hydra predictions



Fluent predictions

Figure 5.29 Velocity magnitude contours calculated on hexahedral grid



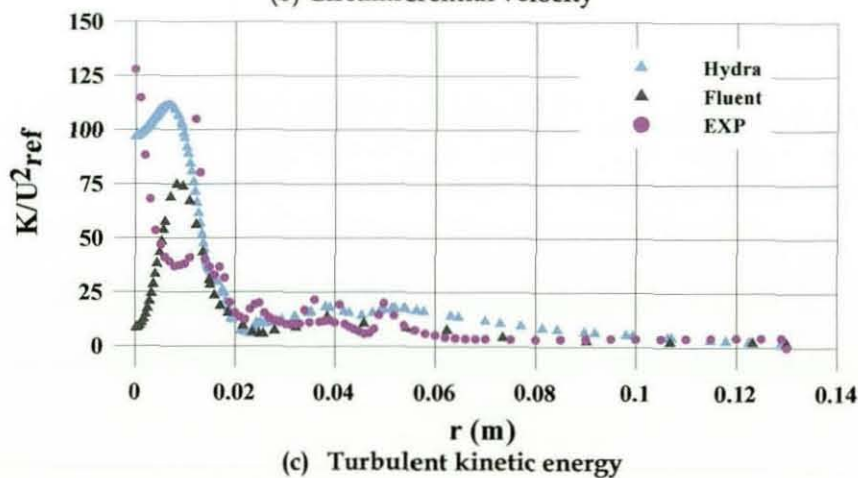
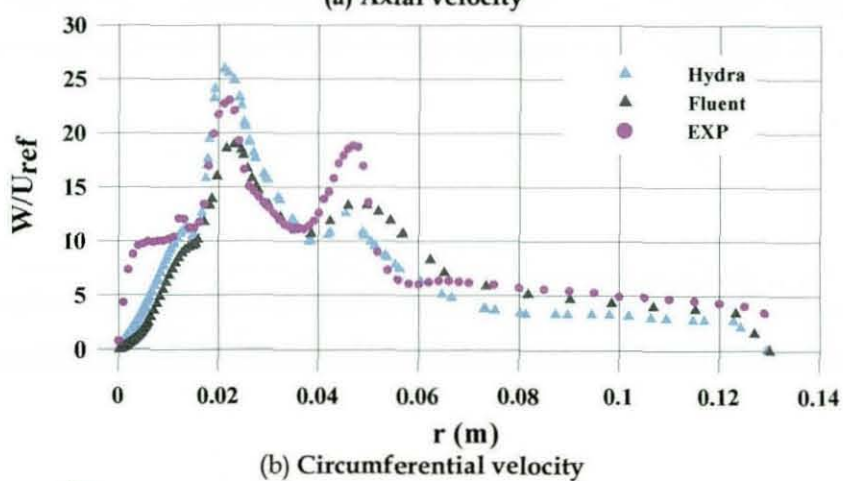
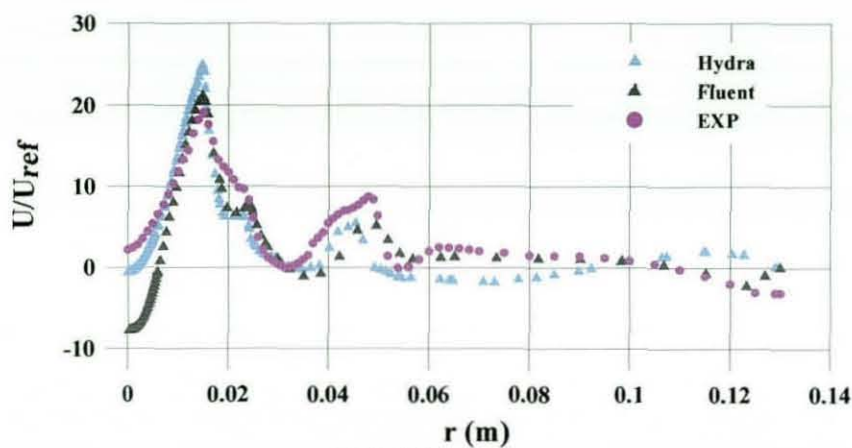
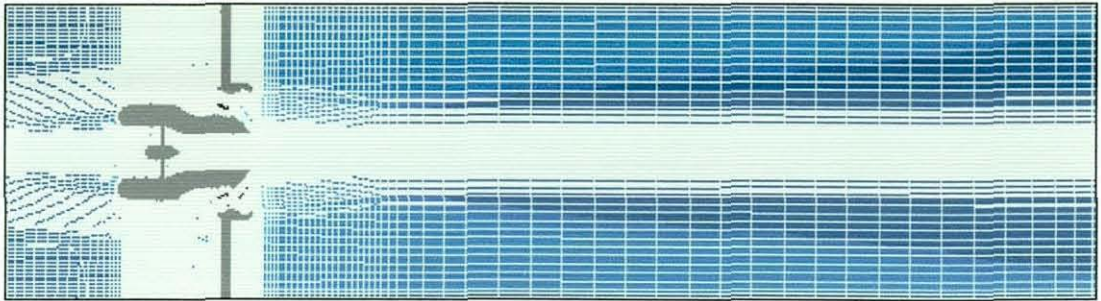
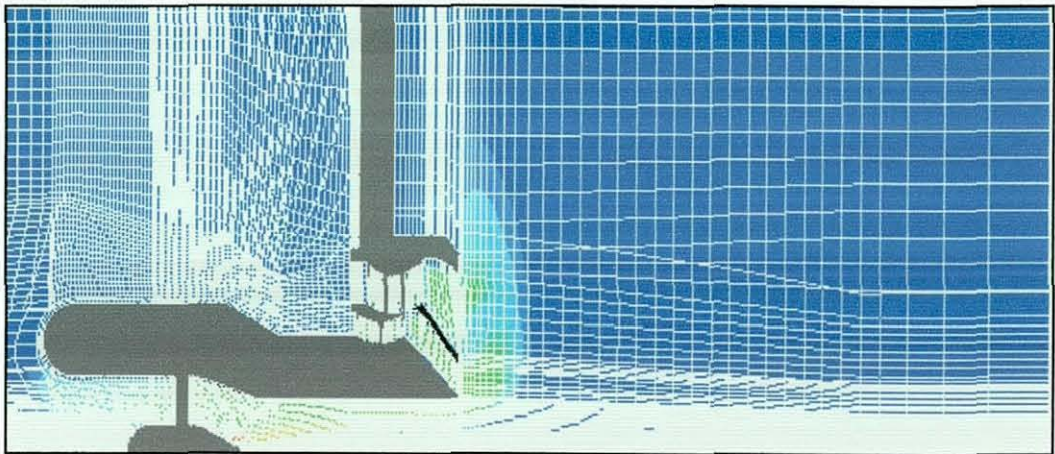


Figure 5.30 Hydra and Fluent predictions on hexahedral grid vs. the experimental data at  $(x/D=0.05)$





(a) Distribution of the grid density along the domain



(b) Grid skewness on the swirl streams and swirl exit region

Figure 5.31 Longitudinal cross-section along the hexahedral computational grid

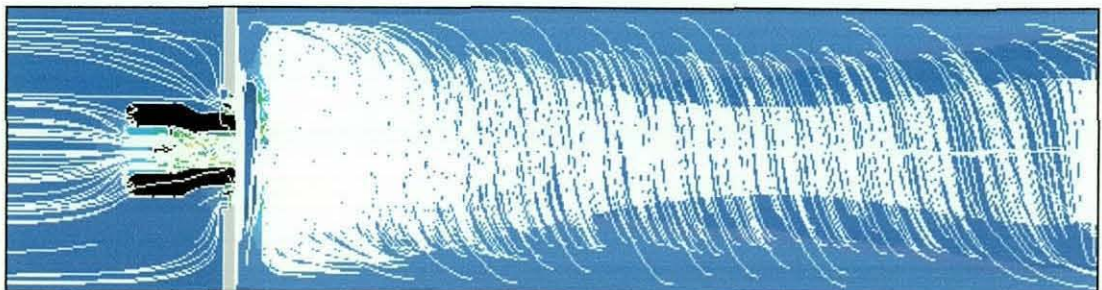
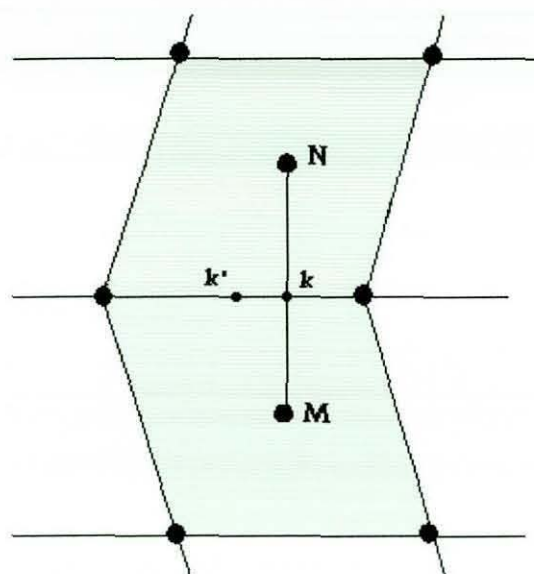
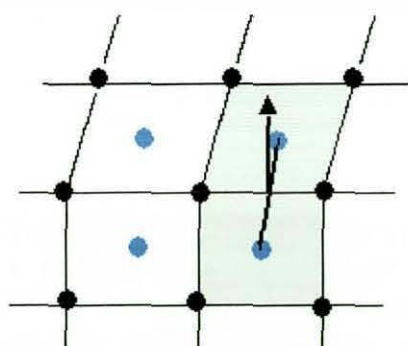


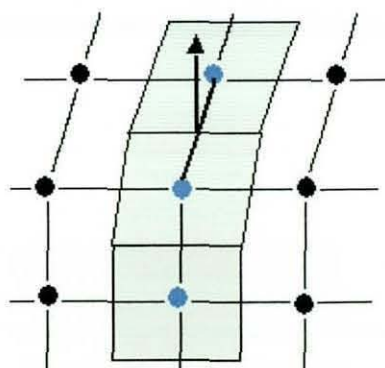
Figure 5.32 Hydra predicted streamlines along the computational domain



(a) Large distance from  $k$  to  $k'$



(b) Median dual control volume



(c) Cell centred control volume

Figure 5.33 Examples of poor grid quality

# Chapter 6

## Non-premixed Turbulent Combustion Modelling

### 6.1 Introduction

Combustion plays an essential role in most energy production processes and in the motive force needed in most of the industrial and domestic transportation applications. Nowadays, more than 80% of energy demands are met by combustion of fossil fuels such as coal, oil, and natural gas. The limited resources of fossil fuels and the destructive effect of combustion pollutant emissions on the environment demand that researchers investigate methods to increase the efficiency of combustion systems. Therefore, it is of great importance to develop reliable experimental methods and rapid predictive tools that can guide design and operation of practical combustion devices. The insights and detailed knowledge from research are transferred to industry in a continuous cycle of understanding of combustion processes, model development, numerical simulation, and validation of the numerical results with experimental data.

Since the vast majority of combustion devices operate in a turbulent flow regime, this has to influence the modeling of the many physical and thermo-chemical processes involved. To meet the requirements of efficient combustion systems and pollutant emission reduction, it is important to understand the complex combustion issues of turbulent fuel/air mixing, flame structure, and pollutant formation. Recent advances in measurement techniques for temperature and species concentration have enabled the acquisition of extensive data about the



flame interaction with the various flow field phenomena. These data are critical for understanding the above mentioned issues and for the development and validation of advanced computational models.

Turbulent combustion can be classified according to the method by which the fuel and air are supplied to the reaction zone. There are three main categories: premixed, partially-premixed and non-premixed turbulent combustion. In premixed combustion, the fuel and air are completely mixed before they are fed into the combustor. Therefore, the rate of chemical reaction is controlled by an ignition front which propagates between the hot combustion zone and the cold non-reacted region. For steady flow devices, the ignition of unburned mixture by hot burned products has to be stabilized via a continuous ignition source, often involving a recirculation region. The second category is partially-premixed combustion which occurs when fuel and air are incompletely mixed before burning. Partially mixing may result from local quenching or the frozen flow mixing before ignition; it can also occur in recirculation zone of burners. In the non-premixed combustion, fuel and air are fed separately into the reaction zone and combustion takes place simultaneously with turbulent mixing process. It is also called diffusion combustion because of the controlled mixing by diffusion of the reactants. The present study focuses on the numerical modelling of the latter type of combustion because it is utilized in most gas turbine main combustors as well as industrial furnaces and Diesel engines.

For practical use in combustion devices with large physical domains and high Reynolds numbers, RANS modelling is commonly used and is still the preferred industrial approach to reduce the complexity of the system to be described. It has been shown in chapter three that the chemical source term in the Reynolds averaged species transport equation appears in unclosed form and to achieve a closure combustion model has to be used. Several models have been proposed but many of these are only applicable to limited flow or chemistry regimes. For

example for non-premixed (or diffusion flames) a fast chemistry model may be adopted. Hence it is assumed that all chemical reactions are infinitely fast in comparison to the time-scale of the turbulent mixing process, and hence the influence of finite rate chemistry on the combustion process may be neglected [162]. The so-called Laminar Flamelet approach is assumed applicable in what is known as the "flamelet regime" where chemical reactions take place only on an interface (between unburned fuel and pure air zones) which is thinner than the smallest turbulent length scale [163]. This is only an example of a large range of combustion models of various complexity, from simple conserved scalar models (see below) to the most complex PDF transport equation type of models where a transport equation for the joint probability density function of the species composition vector is solved [164]. It is not necessary to review all these models here since the intention is to explore the introduction of a basic industry standard model into the Hydra code. Further details on combustion modelling may be found in recent reviews in [105-107].

In gas turbine main combustor modelling (in combustors as shown in Figure 1.1 of chapter 1 for example), the most successful non-premixed model is the conserved scalar approach described before. In this approach the detailed reaction rate is not modelled explicitly and species mass fraction and temperature balance equations are not required. Only the balance equations for mean mixture fraction and its variance need to be solved. The first, in combination with a combustion model describing the instantaneous thermo-chemical state, allows the fluid density (and other properties such as individual species and temperature) to be evaluated and the latter enables turbulence effects to be considered. Conserved scalar models are widely used for engineering applications because they are simpler and less time consuming than reaction rate methods and provide reasonable accuracy in predicting the temperature and species concentrations [105]. In the following section a brief description of the most commonly used conserved scalar model will be given.



## 6.2 Conserved Scalar Modelling

The concept of mixture fraction as a conserved scalar, which uniquely specifies the instantaneous thermo-chemical state, and the transport equations for its mean and variance have been discussed in chapter three in detail. The standard definition of mixture fraction used in non-premixed combustion is the fuel-stream mixture fraction  $f$  which is unity in the fuel stream and zero in the oxidizer stream. When there are more than two inflow fuel ports, an additional mixture fraction variable can be added. With the assumptions of equal diffusivity, unity Lewis number and adiabatic combustion all scalar variables such as temperature and species concentrations can be uniquely related to the mixture fraction. A thermo-chemical model is then needed to specify the relation between these scalar variables and the mixture fraction. The simplest of these models is based on the fast reaction assumption where the time required to complete the reaction is much shorter than any convection or diffusion time scales in the turbulent flame. Alternative models which relate instantaneous thermo chemistry to a single conserved scalar  $f$  have been used in numerical predictions of gas-turbine combustion and these are briefly reviewed here.

### 1. Flame sheet model

This model is also known as the "Mixed-is-Burned" model. In this model the reaction is assumed to be infinitely fast and occurs in a very thin flame sheet [165, 166]. Outside of the flame sheet no reaction takes place and combustion products are mixed with reactants. Species concentrations and temperature are calculated from algebraic equations based on the reaction stoichiometry without any information on reaction rates. Absence of radical species is one drawback of this model. The existence of intermediate radical species such as OH, O and H in the reaction zone leads to underestimation of the specific heat and therefore lower flame temperature. Due to its simplicity and low numerical cost, the flame sheet model is a reasonable choice in applications where the mean flame structure,

temperature and major species are required. Details of this model can be found in many texts, e. g. [107].

## 2. Equilibrium model

This model assumes the chemistry is fast enough for chemical equilibrium to exist at the molecular level [107]. An algorithm based on minimisation of the Gibbs free energy is used to calculate temperature and species concentrations as a function of mixture fraction. This model is widely used [105] and able to predict the formation of intermediate species without detailed knowledge of reaction kinetics. Instead of defining a specific multi-step reaction mechanism, only the important chemical species that will be present in the system need to be defined. The equilibrium model is also valid as for fast chemical reactions, i.e. Damkohler number  $D_a$  (ratio of characteristic residence time or fluid motion time scale to characteristic reaction time) much greater than unity. However, only part of the reaction processes in practical flames are fast enough to reach chemical equilibrium and slower reactions will still exist and lead to abundance of species involved in the reactions such as (OH and CO) [167]. The main drawback of the equilibrium model is the over prediction of CO levels in the fuel rich region of hydrocarbon flames.

## 3. Constrained equilibrium model

This model is a modification to the equilibrium model in order to obtain realistic levels of CO in the fuel rich mixture. The basic idea behind this model is that reactions in hydrocarbon flames occur primarily in a small zone around the stoichiometric mixture fraction. Outside of this zone the fuel will not burn if the temperature is too low or the mixture is too rich or lean. Bilger and Starner [168] developed an alternative constrained equilibrium model where the thermochemistry is described by the reaction zone at the stoichiometric mixture fraction and by a fuel break-up/pyrolysis sheet at a slightly higher mixture fraction. A portion of the hydrocarbon fuel breaks up into intermediate hydrocarbons in a one-step, irreversible and infinitely fast reaction at the fuel break-up/pyrolysis



sheet. These intermediates are considered to be consumed at the stoichiometric mixture fraction surface. The concentrations of the other species are computed from the equilibrium approximation taking into account the constraints for the fuel and the intermediate species.

All of the models described above only establish a link between the instantaneous mixture fraction and the instantaneous thermo-chemical variables (including density of the reacting gas mixture). These relationships (often captured in a tabular form in numerical simulation) do not apply between time-mean values of  $f$  and time-mean values of (say)  $T$  and  $\rho$ . Unfortunately, in a RANS approach, it is only solution of the time-averaged mixture fraction  $\tilde{f}$  which is available, and it is the time-averaged density  $\bar{\rho}$  which is needed to solve the momentum equations. The non-linear nature of the  $f_{inst} / \rho_{inst}$  relationship prevents this being used to link time-averaged equations. Instead, since it is known that  $\rho_{inst}$  is a unique function of  $f_{inst}$  then the theory of PDFs may be used to define the time-averaged value:

$$(\bar{\rho})^{-1} = \int_0^1 [\rho_{inst}(f_{inst})]^{-1} P(f_{inst}) df_{inst} \quad (6.1)$$

(N.B. the details of this relationship are influenced by the Favre-averaged nature of time-mean quantities).

To establish the pdf of mixture fraction,  $P(f_{inst})$  an assumed-shape pdf approach has become the industry standard [105]. The shape of the function is presumed to be given in terms of the mean and variance of the mixture fraction. The values of the mean and variance can be calculated from their modelled transport equations. Double delta PDF [169],  $\beta$ -PDF [170] and clipped Gaussian distribution [171] shapes have been widely used. Jones [167] concluded that the  $\beta$ -PDF and clipped Gaussian PDF predict the temperature and species mass fraction profiles accurately while double delta function gives unrealistic values in temperature profiles. The

clipped Gaussian PDF requires an iterative procedure to satisfy the bounds of the mixture fraction which is not required in the  $\beta$ -PDF implementation. The  $\beta$ -function presumed shape PDF approach is widely used in the prediction of gas-turbine combustion flows and is available as a standard non-premixed combustion model in most commercial CFD codes. In this study the  $\beta$ -PDF model will be implemented into the Hydra solver and validated against experimental data and published numerical solutions using various instantaneous thermo chemistry descriptions.

### 6.3 Implementation of the Presumed $\beta$ -PDF Model

The transport equations for the mean mixture fraction and variance are the cornerstone of most conserved scalar combustion models. The successful incorporation of these two equations and their related boundary conditions into the Hydra solver was outlined and demonstrated in chapter 3 and the good results presented there are extended in this chapter by incorporating a suitable combustion model. The selected  $\beta$ -PDF model and the thermo chemistry models described above are usually used within pressure-correction codes under the assumption of constant thermodynamic pressure and low Mach number, equal turbulent diffusivities, and unity Lewis number [105]. A typical incompressible RANS code solves the Favre-averaged balance equations for continuity (in pressure-correction form to find the local static pressure), the three momentum equations to find the average velocities, two equations for the mean mixture fraction and its variance and two equations for  $k-\varepsilon$  turbulence model [105]. The only input required during the iterative solution of these equations is the instantaneous  $\rho/f$  relationship obtained from the chemistry model and the mixture fraction probability density function constructed from the  $\beta$ -PDF shape and the locally determined values of mean mixture fraction and its variance. In the current study the suitability of the above procedure to be used within a density based code, where the energy equation and the equation of state are normally



coupled with the continuity and momentum equations, will be investigated. At low Mach numbers, the assumption of constant thermodynamic pressure is still valid since the variation of pressure is very small. A block diagram which illustrates the implementation of the procedure is shown in Figure 6.1. In the flame structure block, the relation between the mixture fraction and the other scalar variables such as density, temperature and species concentrations are stored. These may be calculated by assuming equilibrium chemistry or any other coherent combustion model using the PrePDF software available in the Fluent commercial code [172] and/or RR in-house code [173]. The relationship between the density and the mixture fraction  $\rho = \rho(f)$  is fitted as a polynomial functions input to the  $\beta$ -PDF routine when the density is required as an input for the flow solver. Other variables (e.g. temperature  $T = T(f)$  or CO mass fraction  $Y_{CO} = Y_{CO}(f)$ ) are used at the post-processing stage. The flow solver solves for the primitive variables as usual, because decoupling the governing equations is not possible, but the main concern is to obtain an accurate solution for the velocity and mixture fraction fields since the pressure is almost constant and the temperature will be obtained in the post-processing stage. In the PDF block the mean  $\tilde{f}$  and variance  $\tilde{f}''^2$  of the mixture fraction are used to construct the  $\beta$ -PDF which is used to incorporate the influence of the turbulent fluctuations as follows:

$$P(f) = \frac{f^{a-1}(1-f)^{b-1}}{\int_0^1 f^{a-1}(1-f)^{b-1} df} = \frac{f^{a-1}(1-f)^{b-1}}{\frac{\Gamma(a)\Gamma(b)}{\Gamma(a+b)}} \quad (6.2)$$

where the exponents  $a$  and  $b$  are given by:

$$a = \tilde{f} \left[ \frac{\tilde{f}(1-\tilde{f})}{\tilde{f}''^2} - 1 \right] \quad (6.3)$$



$$b = (1 - \tilde{f}) \frac{a}{\tilde{f}} \quad (6.4)$$

$P(f)$  is a density-weighted function and therefore the Favre averaged mean values are given as follows:

$$\tilde{\phi} = \int_0^1 \phi(f) P(f) df = \frac{\Gamma(a+b)}{\Gamma(a)\Gamma(b)} \int_0^1 \phi(f) f^{a-1} (1-f)^{b-1} df \quad (6.5)$$

$$\bar{\phi} = \bar{\rho} \int_0^1 \frac{\phi(f)}{\rho(f)} P(f) df \quad (6.6)$$

and

$$\bar{\rho} = \left[ \int_0^1 \frac{P(f)}{\rho(f)} df \right]^{-1} \quad (6.7)$$

The mean density  $\bar{\rho}$  is fed into the flow solver at every iteration to obtain new values of the mean and variance and the corresponding probability density functions till convergence is obtained. Thereafter, the temperature and the species mass fraction can be calculated using equation (6.6).

The integration in the above equations (e.g. 6.6) is evaluated using Simpson's method [174]. The function  $P(f)$  is singular at  $f=0$  if  $a < 1$  and singular at  $f=1$  if  $b < 1$ , this singularity is eliminated according to the method suggested by Chen et al. [175] where the integration is approximated by:

$$\int_0^1 \phi(f) f^{a-1} (1-f)^{b-1} df \approx \frac{\varepsilon^a}{a} \phi(0) + \int_{\varepsilon}^{1-\varepsilon} \phi(f) f^{a-1} (1-f)^{b-1} df + \frac{\varepsilon^b}{b} \phi(1) \quad (6.8)$$

In the above equation  $\varepsilon$  is a small parameter. An effective choice of its value was found to be  $10^{-6}$  for the density calculations [14]. Another numerical difficulty is that  $a$  and  $b$  in equations (6.3) and (6.4) may approach very large magnitudes which leads to overflow in the calculation of  $P(f)$ . To overcome this problem,

Chen et al [175] suggested to limit the bigger value among  $a$  and  $b$  while keeping their ratio constant. For example, if  $a$  is a very large value, its value is reset to a modestly large value ( $\sim 500$ ). The value of  $b$  is then set to,

$$b' = \frac{b}{a} a', \quad a' = 500 \quad (6.9)$$

When  $b$  is very large,  $a$  and  $b$  rest to

$$a' = \frac{a}{b} b', \quad b' = 500 \quad (6.10)$$

A better way to prevent overflow problem while qualitatively preserving the shape of the beta pdf function is suggested by Liu et al. [176] as follows:

$$b' = \frac{a' - 1 - f_{\max}(a' - 2)}{f_{\max}}, \quad a' = 500 \quad \text{if } a \text{ is very large} \quad (6.11)$$

and

$$a' = \frac{1 + f_{\max}(b' - 2)}{1 - f_{\max}}, \quad b' = 500 \quad \text{if } b \text{ is very large} \quad (6.12)$$

where

$$f_{\max} = \frac{1}{1 + (b-1)/(a-1)} \quad (6.13)$$

The above procedure of Liu et al. has been adopted in the current work, typical shapes of  $\beta$ -PDF are displayed in Figure 6.2 which are observed to mimic quite correctly real mixture fraction pdfs in a variety of cases.

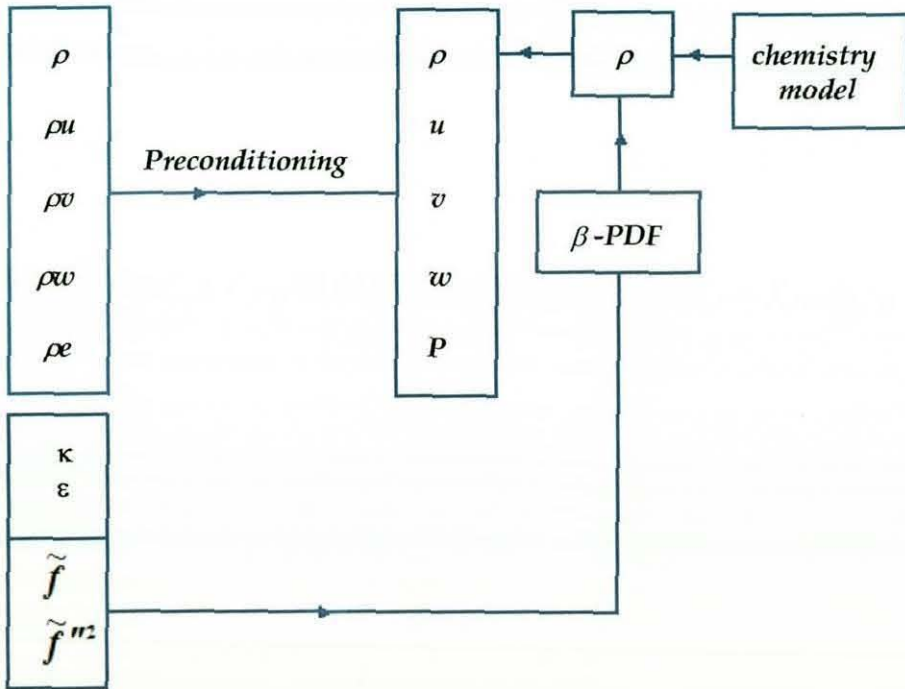
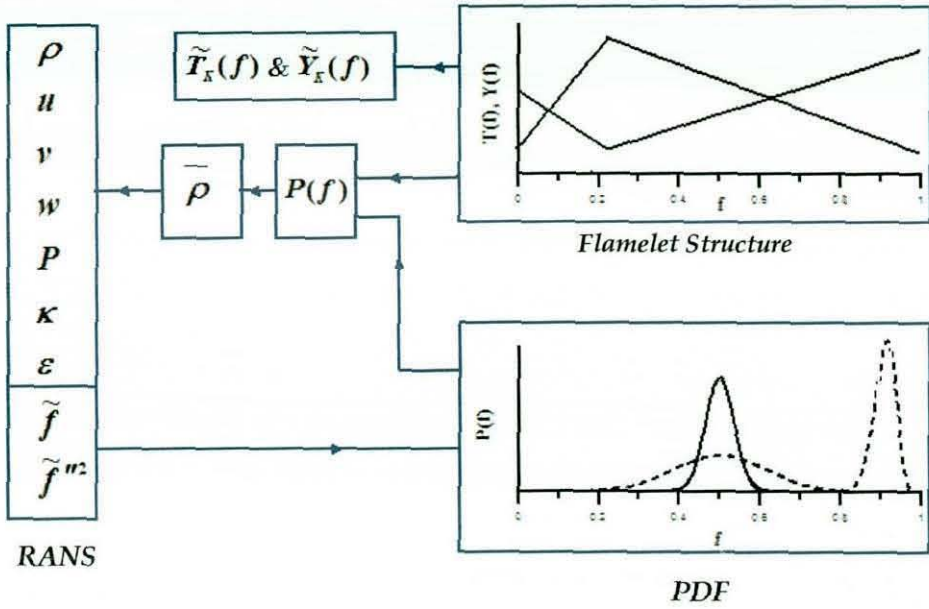


Figure 6.1 The main blocks of the implementation procedure

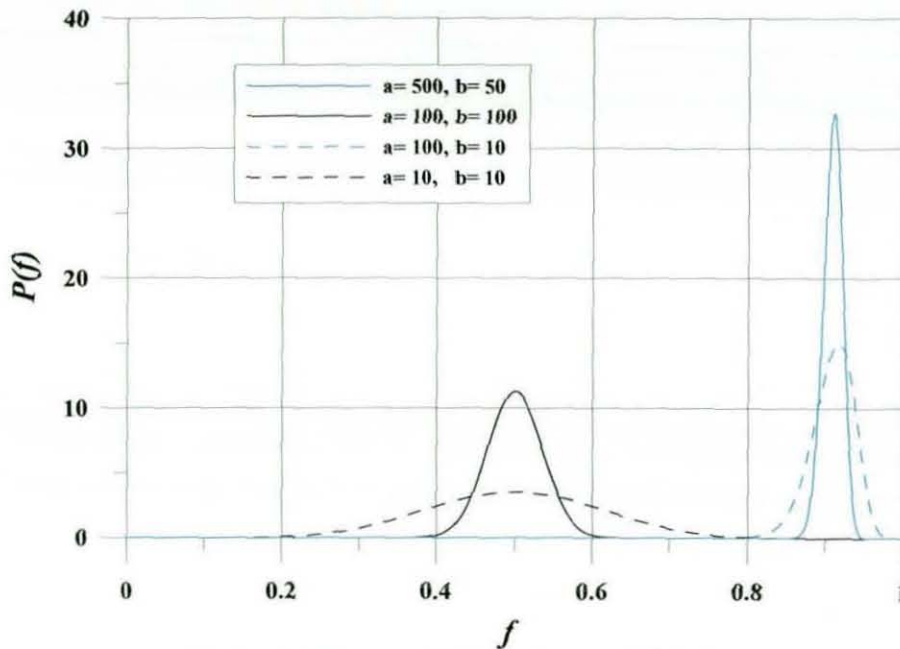


Figure 6.2 Shapes of the calculated  $\beta$ -PDF

#### 6.4 Model Testing and Validation

The experimental test case used for the validation of the current simulation is the coaxial jet combustor configuration of Owen et al. [54]. This experiment was chosen for its relatively simple geometry and boundary conditions and the availability of detailed measurements of the velocity field, mixture fraction, temperature, and species within the combustor. This experiment has been selected for use in both RANS combustion model validation [177] and also more reacting LES validation [178]. Figure 6.3 shows a schematic of the combustor and the flame configuration observed in the experiment. The cylindrical combustor had a relatively large diameter ( $R_3 = 61.15$  mm), low velocity central fuel port ( $V_{\text{fuel}} = 0.9287$  m/s), with higher velocity, nonswirling air in a surrounding annulus ( $V_{\text{air}} = 20.63$  m/s). The combustor was 1000 mm in length, with the central pipe radius ( $R_1$ ) and the annular outer radius ( $R_2$ ) as 31.57 mm and 46.85 mm respectively. The air was preheated to 750K, and the combustor pressure was 3.8 atm. Porous-metal discs were installed in the fuel injector and air entry section



to provide uniform inlet flows. The walls of the combustor were water-cooled to maintain a constant wall temperature of roughly 500K. The fuel used in the experiment was natural gas but for the present investigation pure methane was assumed. The species concentrations were measured using a traversing gas sampling probe, temperature was measured by a traversing thermocouple and axial velocity by LDV [54, 178]. Due to the high air/fuel velocity ratio, a strong central recirculation zone is formed directly downstream of the fuel port, which appears to the surrounding air stream almost as a bluff body. The recirculating combustion products provide a continuous ignition source for the relatively cold incoming reactants, thereby stabilizing the flame.

*For numerical comparisons the two investigations carried out by Jones and McGuirk (RANS) [177] and Pierce and Moin (LES) [178] for the above experiment will be used. In the first study, the predictions were based on finite volume solution of the RANS form of the governing equations of mass, momentum, together with the transport equations of the turbulence model and the mixture fraction mean and variance. The influence of the local turbulent fluctuations in the mixture strength was accounted for by the presumed  $\beta$ -PDF model, assuming a full chemical equilibrium combustion model. In the study of Pierce and Moin various combustion models based on mixture fraction assumptions were used to predict the reacting flow using the LES approach. Simulations were performed using the steady flamelet, fast chemistry and progress variable (PVA) combustion models. These various predictions provide an important source of data to assess the reacting flow simulation of the current study against different combustion models and numerical approaches. In the above calculations the computational domain started at a distance of  $1R$  ( $R = R_2$ ) upstream of the combustor and continued until a combustor length of  $8R$  was reached.*

In the current study, using an assumption of chemical equilibrium calculations were performed on a  $60^\circ$  sector of the combustor. The solution domain was



initialised with the air inlet flow variables and therefore zero mixture fraction mean and variance. During the first few iterations this led to the solution diverging due to the large decrease in density at the fuel inlet boundary condition to values less than the fuel density. To avoid this problem the density was kept equal to the fuel density whenever it fell below the fuel density during the initial part of the iterative process. Figure 6.4 shows the predicted axial velocity contours in comparison with the Jones and McGuirk [177] predictions and the experimental data [54]. The size of the central and upper corner recirculation zones and the maximum negative velocity predicted by the current calculations using the modified Hydra code are in much better agreement with the experimental data compared to the calculations of Jones and McGuirk where they were underpredicted. The most likely reason for this is that the Jones and McGuirk predictions were carried out on a coarse grid (20 x 20) and using first order upwind differencing. The current Hydra predictions (on a 3D mesh of 53968 cells and with second order differencing) are therefore much more numerically accurate, less numerical diffusion, giving rise to lower rates of momentum transfer and larger central recirculation. The size and strength of the central recirculation has a great influence on the fuel/air mixing process and therefore the flame shape and properties. The penetration of the high velocity annular air jet is better reproduced in the current solution. Comparisons of the predicted temperature and CO levels profiles with experimental data and the previous numerical calculations of [177, 178] are shown in Figures 6.5 and 6.6. The predicted low temperatures and high concentrations of CO compared to experimental data are mainly attributed to the equilibrium chemistry model which has the tendency to produce such results in fuel-rich mixtures. The scatter of the experimental data points in these two figures (and the following figures below) is due to the reflection about the centreline of data points taken on the opposite side of the combustor [179].

The LES predictions of Pierce and Moin [178] for the same test case provide more data for axial velocity, mixture fraction, temperature and CO concentrations, which

therefore serves to establish a better comparison basis for the current Hydra calculations. Figure 6.7 shows the axial velocity profiles at three different axial locations ( $x/R=0.14$ ,  $0.38$  and  $1.27$ ) for (i) the current chemical equilibrium predictions with Hydra, (ii) the experimental data, and (iii) the three different chemistry models used in the LES calculations (see [178] for more discussions on the chemistry models). The general level of agreement between Hydra predictions, LES predictions and the experimental data is relatively good. The development in the shape of the profiles from the flat topped high velocity inlet annulus at low  $x/R$  to the more mixed out peaky shape downstream is reproduced as well by the Hydra RANS calculations as the LES solutions. The details of the chemistry model do not seem to influence the velocity profile shape significantly. One contribution to the disagreement with experimental data may be due to the fact that fully developed pipe and annular inflow conditions were assumed in the calculations, whereas in the experiment flow conditioning devices were located only a short distance upstream of the jet orifice. In the third profile ( $x/R=1.27$ ) close to the upper wall, Hydra has predicted lower axial velocity levels since RANS models are known to predict a too slow recovery after a core recirculation. Figure 6.8 shows comparisons of the predicted mixture fraction profile at three axial locations ( $x/R=0.21$ ,  $3.16$  and  $3.84$ ). In the first axial location ( $x/R=0.21$ ) Hydra predictions show better agreement with the experimental data and the LES solution using the progress variable approach (PVA) while the fast chemistry and steady flamelet LES predictions predicted higher levels of mixture fraction, especially in the core region. This initial region is certainly the most sensitive to inlet conditions, so there could be some cancellation of errors here. From the other two axial locations it can be observed that the predictions of Hydra, the fast chemistry and steady flamelet models (all of which involve similar assumptions on chemistry) lead to lower mixing rates compared to the more advanced PVA approach. The Hydra RANS with chemical equilibrium and the LES steady flamelet model offer improvement over the fast chemistry approach (even with LES), but the mixing profiles are best predicted compared to experimental data by the LES with PVA model. It can be



observed that all the profiles tend toward agreement as the profile axial location is moved farther downstream, due to the fact that they all must reach the same uniform profile once mixing is complete.

Comparison of the predicted temperature profiles with experimental data and LES calculations is shown in Figure 6.9. Temperature is derived mainly from the mixture fraction and its variance (mixture fraction and progress variable in case of PVA) by assuming adiabatic walls and neglecting thermal radiation. Therefore, if mixture fraction predictions are in good agreement with experimental data, discrepancies between predicted and measured temperature profiles must be due to the breakdown of other assumptions such as the shape of the instantaneous  $T(f)$  curve, or the level of turbulent fluctuations in mixture fraction or to experimental error. Figure 6.9 shows that the RANS with equilibrium model predicting temperature very close to LES with steady flamelet and fast chemistry approach. It is also interesting to note that, whereas the LES PVA calculation gave the best agreement with the measured mixture fraction, it gives poorer agreement than other models for the gas temperature, which must be due to the instantaneous chemistry description. Another source of uncertainty is the effect of the assumption of adiabatic walls in the simulations. Since the experiment had isothermal, water-cooled walls at roughly 500K, thermal boundary layers would be expected to develop, affecting the temperature close to the wall. Since different chemistry models were used and the predicted mixture fraction values are not identical, discrepancy in the temperature profiles is expected. Figures 6.10 and 6.11 show the relationship between the mixture fraction and the temperature for equilibrium, steady flamelet and fast chemistry models. It can be noted that equilibrium chemistry predicts much lower temperatures than fast chemistry in the fuel-rich region and that a slight increment in mixture fraction can lead to a large increase in the temperature in this region. This may explain the low temperature levels predicted by Hydra in the low  $x/R$  regions where richer mixtures are observed. Finally, the CO mass fraction comparisons are shown in Figure 6.12. Hydra, as

expected from an equilibrium model, produced high concentrations of CO. Due to a low dissipation rate in the fuel-rich interior region of the flame, the steady flamelet model picks out near-equilibrium flamelet solutions, which have low temperatures and high concentrations of CO in fuel-rich mixtures. It is not the main purpose of the work reported here to discuss the details of chemistry models, but rather to demonstrate that RANS reacting flow solutions can be generated using a density-based approach after modification following the idea outlined in chapter 3 the above predictions clearly demonstrate this.

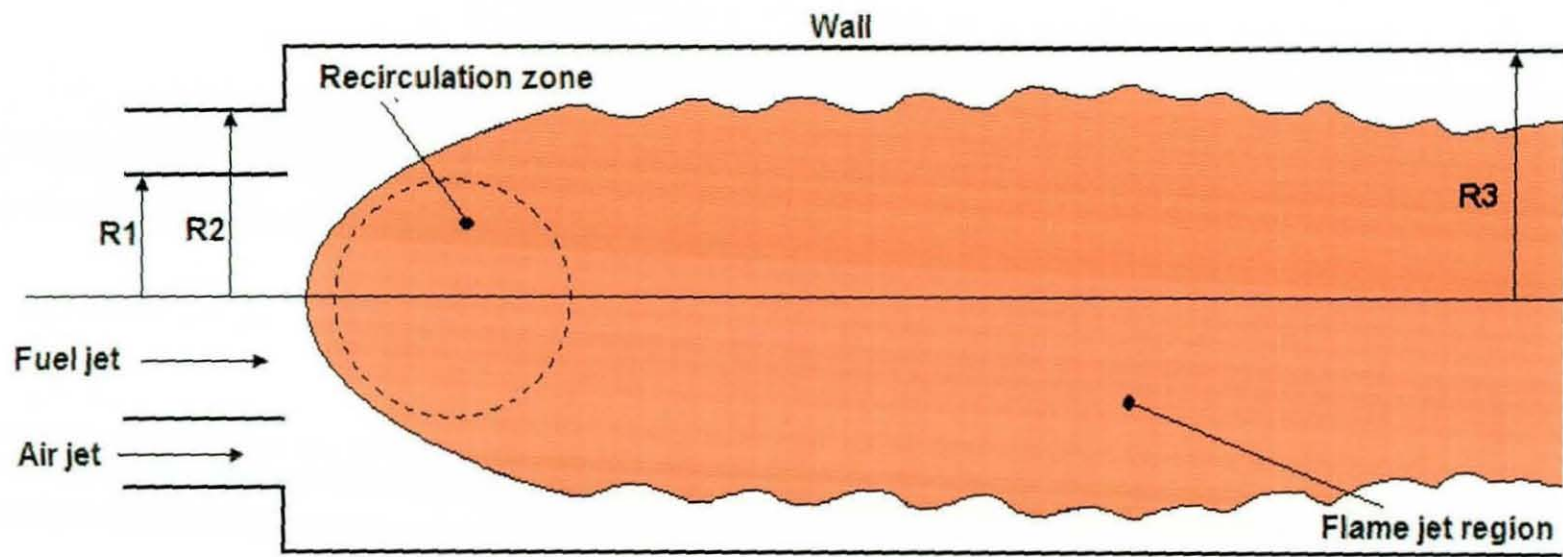
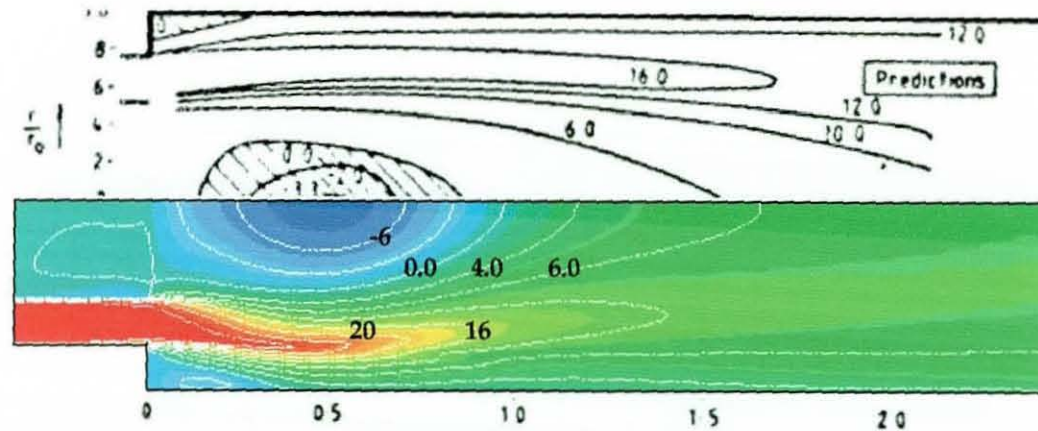
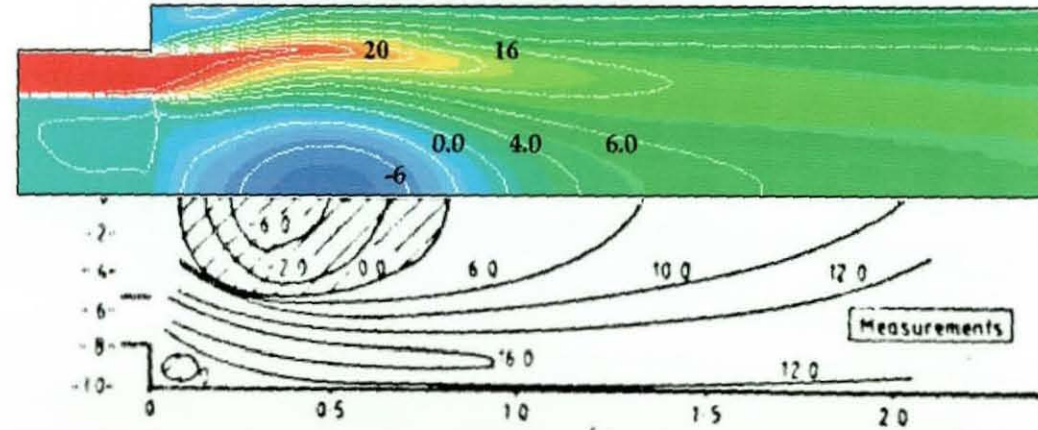


Figure 6.3 Schematic of the coaxial jet combustor experiment





(a) Hydra (bottom contours) vs. Predictions [177]



(b) Hydra vs. Experimental [54]

Figure 6.4 Hydra predictions of the axial velocity contours in comparisons with the previous predictions and the experimental data

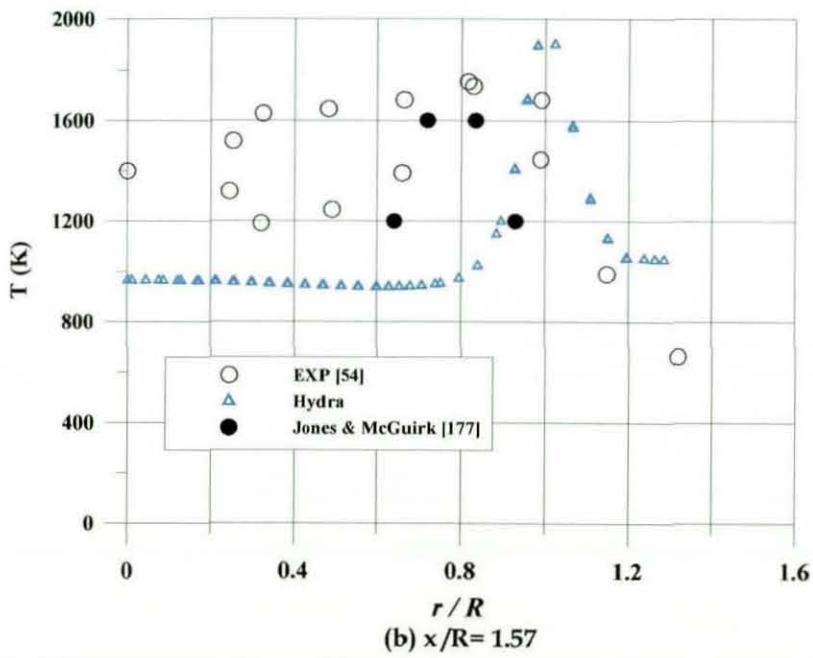
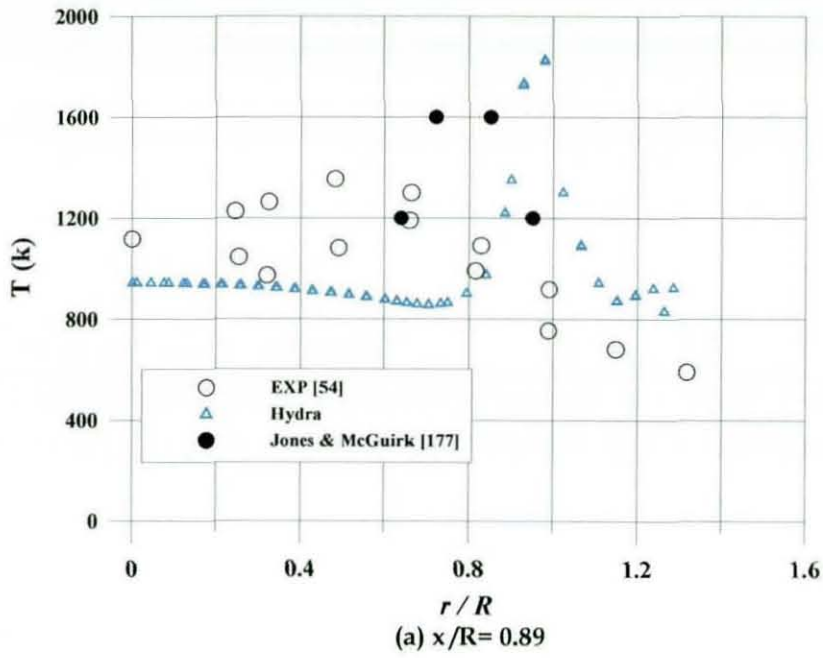


Figure 6.5 Radial profiles of temperature

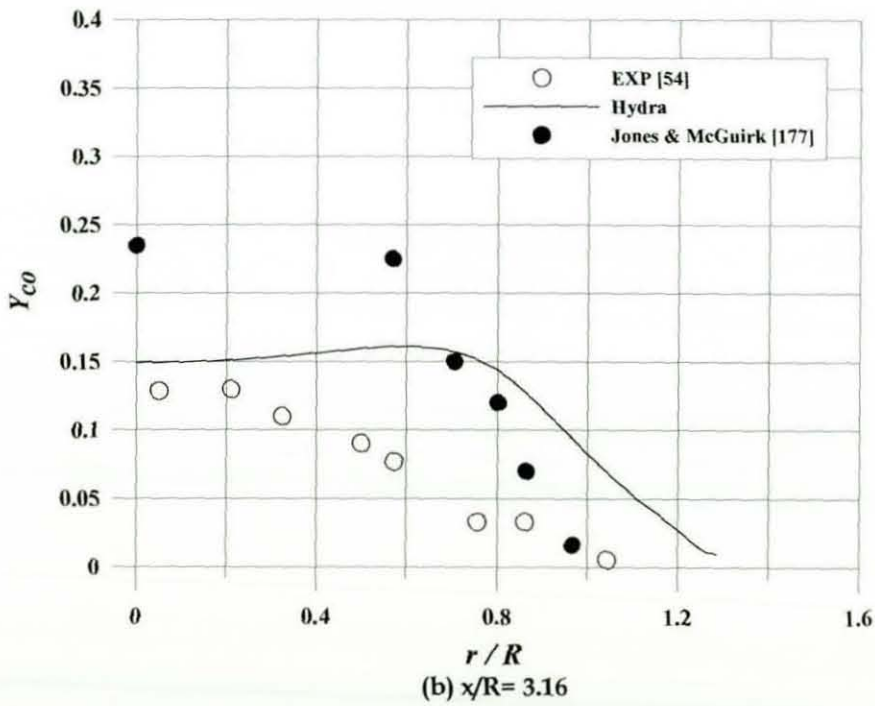
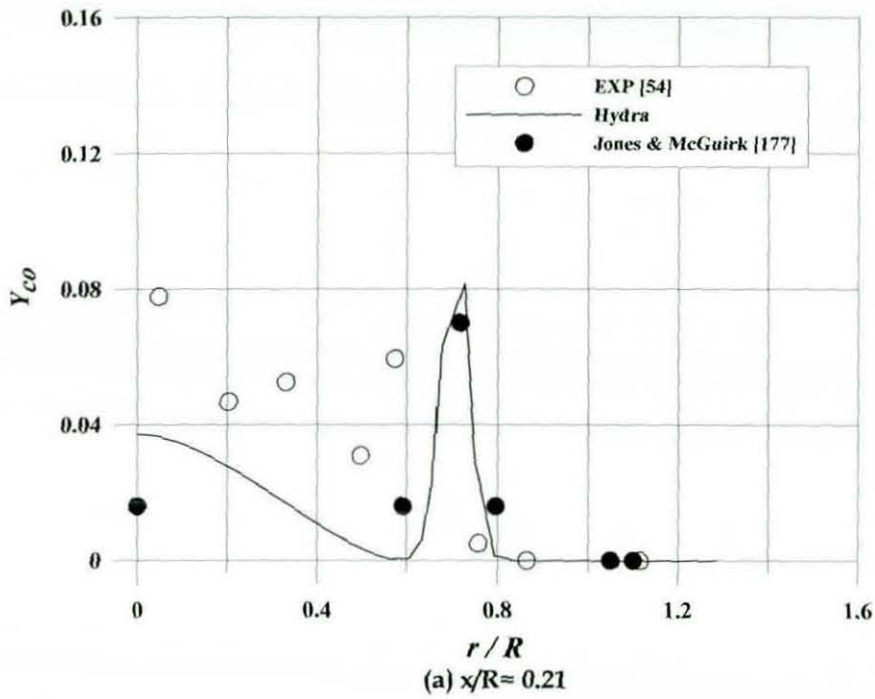


Figure 6.6 Radial profiles of CO mass fraction

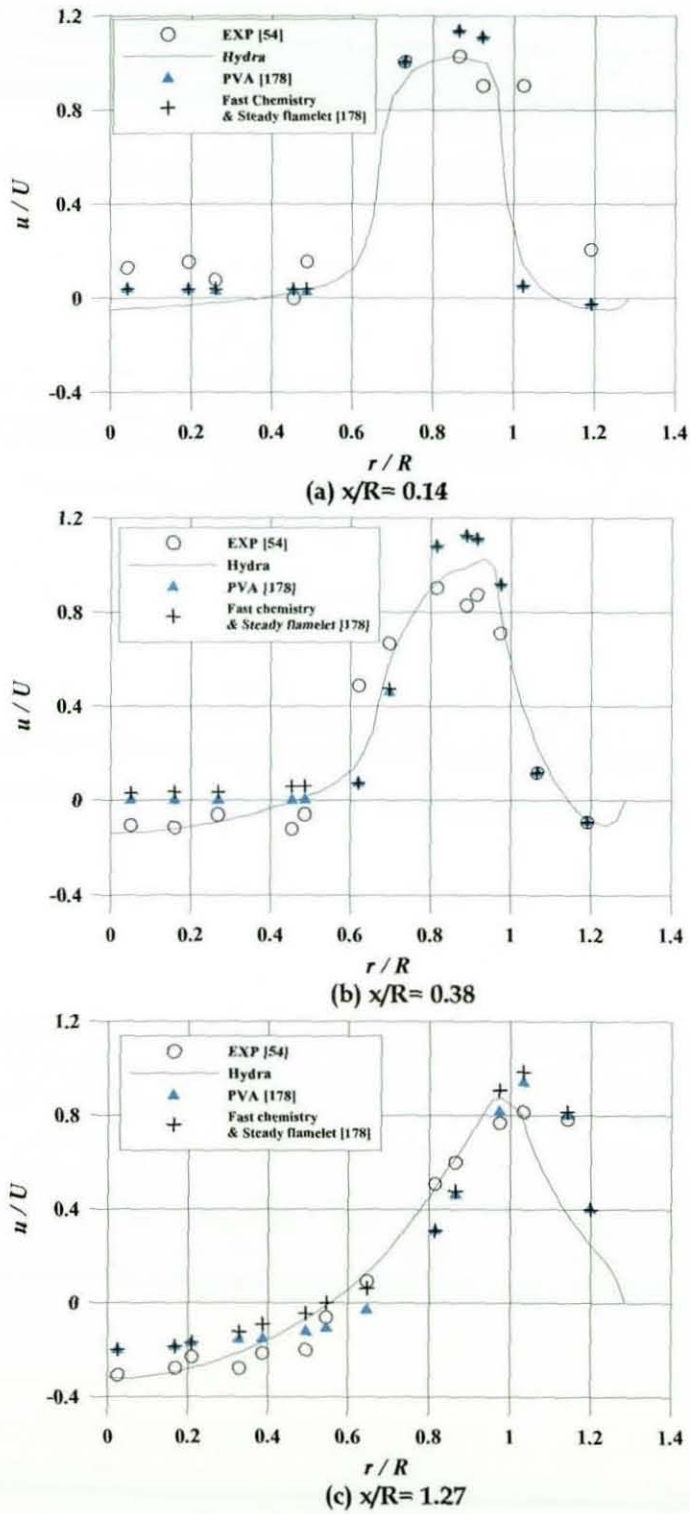
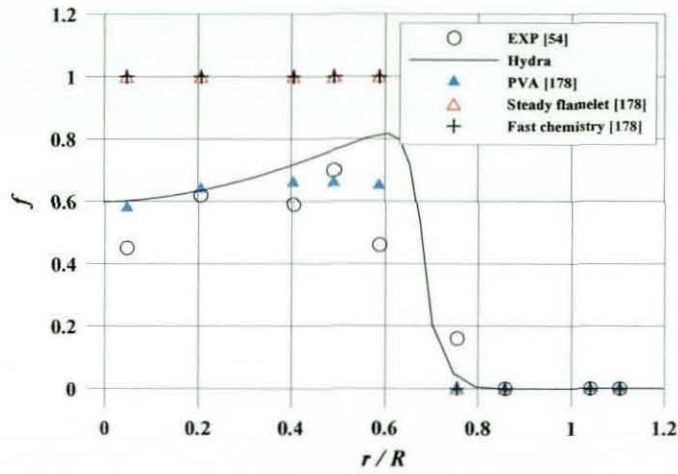
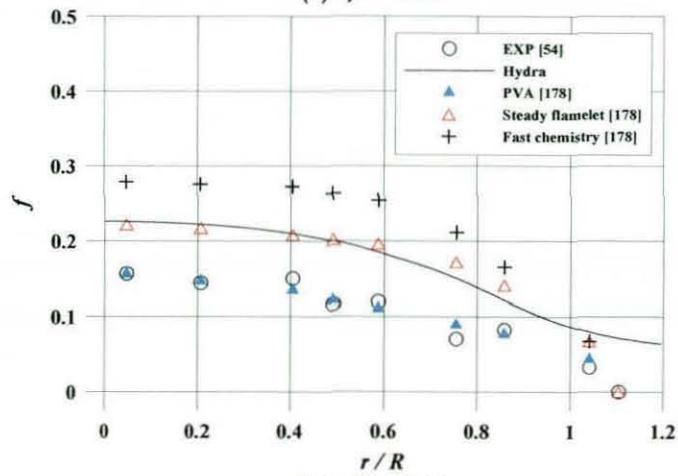


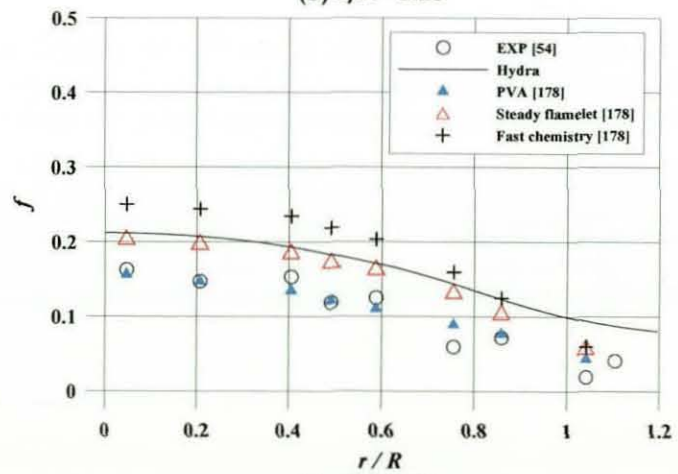
Figure 6.7 Radial profiles of axial velocity



(a)  $x/R = 0.21$



(b)  $x/R = 3.16$



(c)  $x/R = 3.84$

Figure 6.8 Radial profiles of mixture fraction



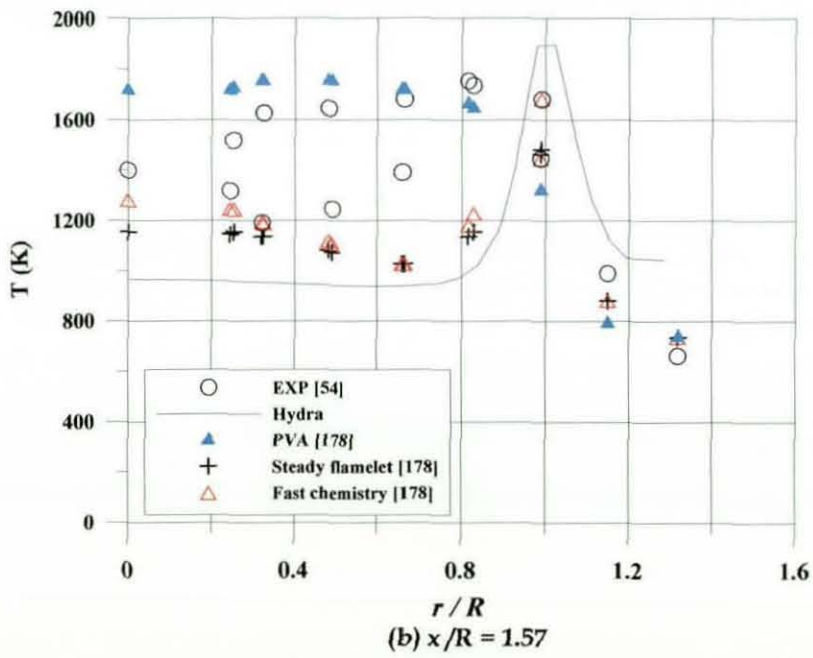
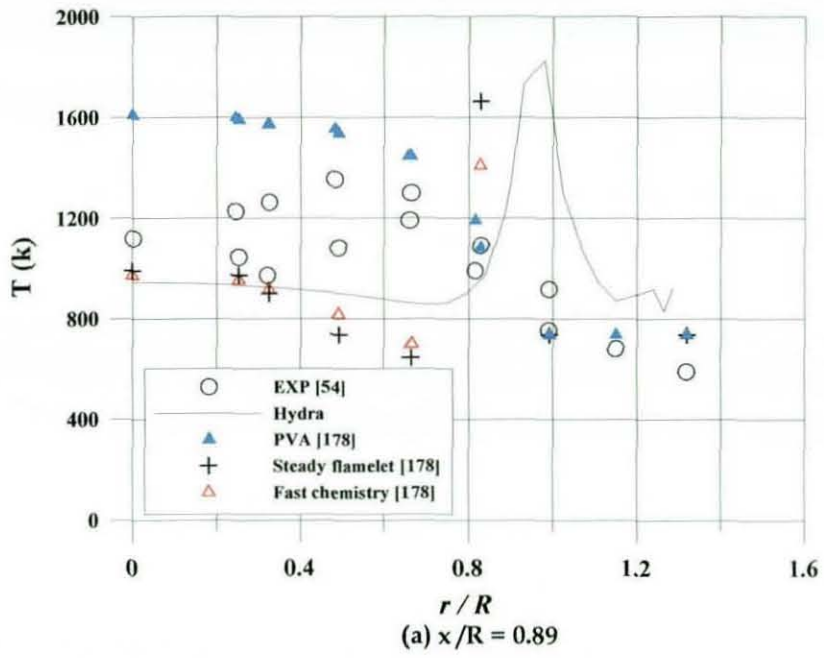


Figure 6.9 Radial profiles of temperature

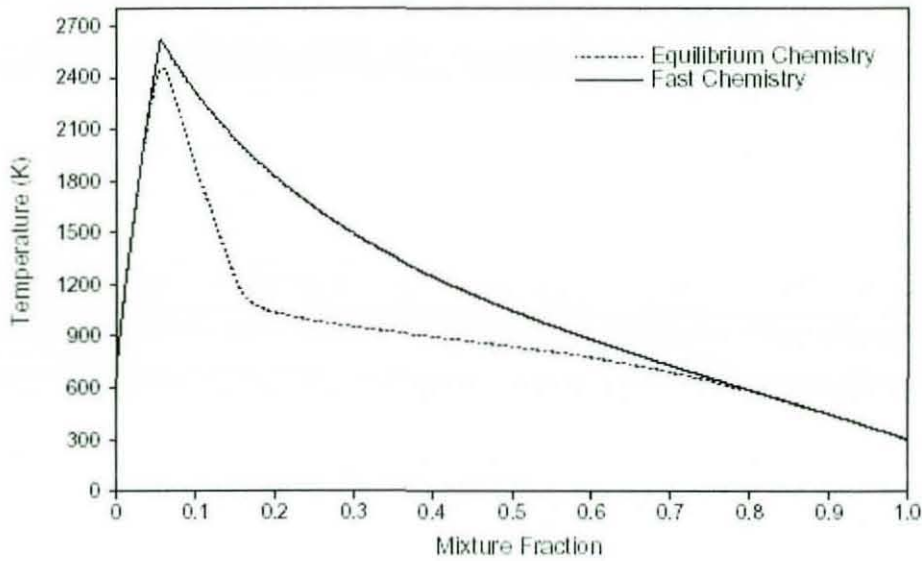


Figure 6.10 Temperature as a function of mixture fraction from equilibrium and fast chemistry state relationships [179]

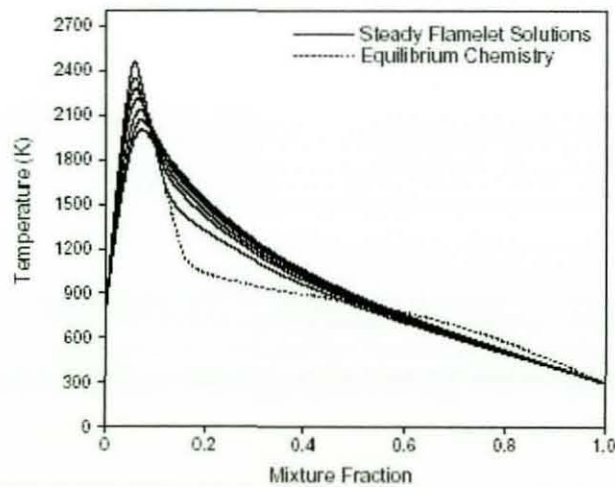


Figure 6.11 Temperature as a function of mixture fraction from equilibrium and steady flamelet solutions relationships [179]

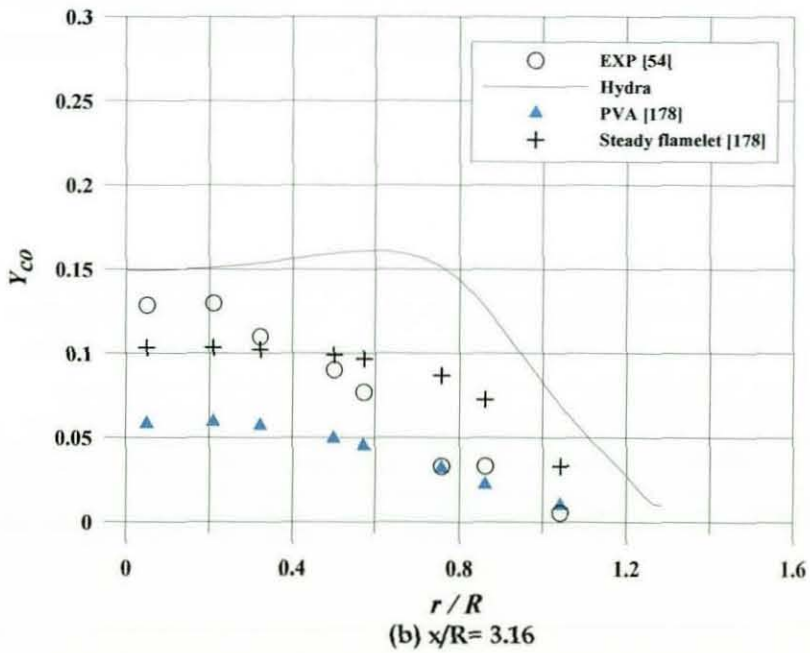
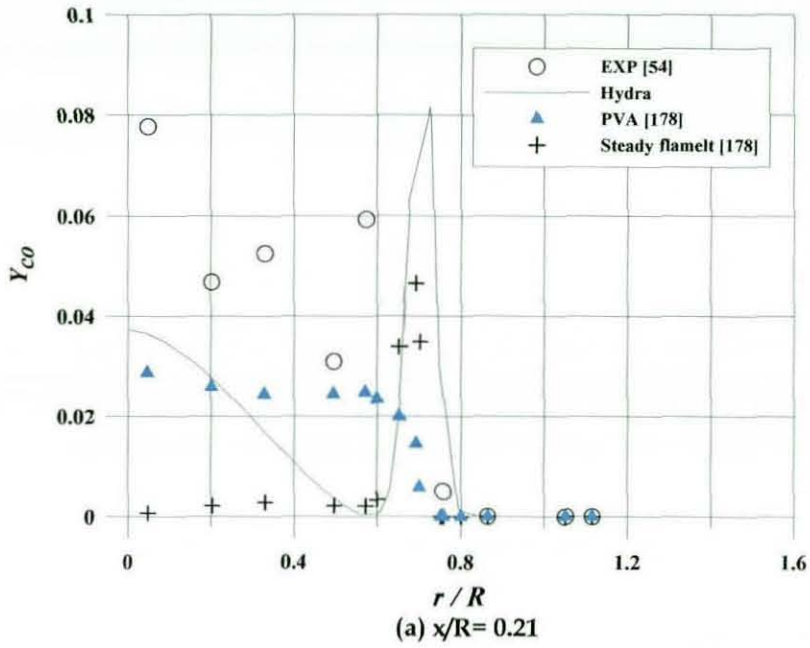


Figure 6.12 Radial profiles of CO mass fraction

# Chapter 7

## Conclusions and Recommendations

### 7.1 Summary of Results

The main goal of the present work as stated in chapter 1 was to explore the use of a density-based RANS CFD algorithm as typical of 'best-practice' turbomachinery predictions when applied to combustor relevant flow problems and to extend the solver capability to simulate reacting flows typical of main gas turbine combustor flows. The above goal has been achieved in this study through three stages. The first stage was to identify those areas of the algorithm (as represented in the Rolls-Royce Hydra code) which required modifications to allow application to combustion relevant flows. The second stage was to introduce the necessary modifications into the solver and validate these modifications against simple test cases. The third stage was to demonstrate the performance of the modified solver using a series of flow problems selected from a literature review as contributing important flows in current gas-turbine combustor applications. The basic Rolls-Royce Hydra code, a typical modern and widely-used RANS code based on an unstructured density-based algorithm, was identified as needing modifications due to the following reasons:

- The classical high Mach number flow boundary conditions used in Hydra (fixed total pressure-total temperature and flow angles at inlet, fixed static pressure at outlet) are not suitable for combustor flow applications where fixed velocity at the various inlets to the combustor is more typical in order to fix the flow split.

- The type of periodic boundary condition coded into Hydra was restricted in its application to turbomachinery flow cases. In particular it did not allow for the presence of a centreline because turbomachinery flows are typically configured as an annulus between two cylindrical bodies extending from blade root to the outer casing.
- The existing code was limited to simulation of non-reacting flows.

Hence, the following modifications were introduced into the solver:

- Two different velocity inlet boundary conditions were added to the code. These were verified against a simple convergent-divergent nozzle case and showed very good agreement with analytical results. The method based on non-reflecting Riemann invariants (RINV) was selected to be used in the rest of the study because it was found to provide a significantly faster convergence rate compared to the method based on fixed inlet velocity and temperature (VIN).
- A centreline boundary condition was added to the solver to enable the use of a periodic boundary condition treatment when the geometry contains periodic boundary plane pairs which coincide at a centreline (as typically found and used in swirling flow for example).
- A non-premixed turbulent combustion model based on a conserved scalar approach was selected, using the current industry standard approach adopted in all pressure-based solvers to simulate the non-reacting flow relevant to the main gas-turbine combustor. The incorporation of this model into the density-based solver was accomplished through the following three steps:
  1. Identification of a reliable version of the discretisation practice for the convective term of a conserved scalar transport equation by investigation of the numerical diffusion associated with the discretisation of this term and the influence of various possible



numerical schemes and mesh types on a simple single scalar variable convection test case. Centred differencing was unstable as expected and produced non-physical oscillations (unbounded solution) on coarse grids although gave good accuracy on grids fine enough to smear the oscillations. The introduction of smoothing to achieve a first order upwind differencing was observed (as expected) to preserve boundedness but at the cost of accuracy. To combine the advantages of high accuracy and boundedness a switch was used to balance a blend of both second order and fourth order smoothing terms that appeared in the convective term discretisation. Four types of grids were investigated. The hexahedral grid showed better performance in terms of accuracy compared to the triangulated grids, where the extent of increase in numerical error was found to be dependant on the alignment of median dual control volume diagonals with the flow direction. However a suitable blend of smoothing parameters did show that an acceptable accuracy of conserved scalar solutions could be achieved.

2. Introduction of two transport equations for the conserved scalar (mixture fraction) mean and variance and their corresponding boundary conditions into the solver. These equations were introduced as a separate block, similar to the treatment of turbulence model equations. These modifications were tested by simulating the case of two coaxial jets of equal density issuing into a circular concentric duct for different Craya-Curtet numbers and demonstrating acceptable validation against previous experimental data and numerical solutions showing good agreement.
3. Addition of a turbulent combustion model based on the full chemical equilibrium assumption (to provide the link between the instantaneous mixture fraction and the instantaneous

thermo-chemical variables) and a presumed probability density function ( $\beta$ -PDF) constructed by using the computed mean and variance of the mixture fraction (to account for the influence of the local turbulent fluctuations on the mixture strength).

In the final stage of the work, the modified code performance was demonstrated on three test cases, a jet in confined cross flow, a multi-stream swirler flow and a turbulent confined diffusion flame. The first two cases represent the main flow features associated with the complex primary zone of combustors such as recirculation zones due to swirling motion and jet impingement and interaction with the core cross flow. Hydra as a density-based code was compared to a pressure-based unstructured solver by simulating the same cases with the Fluent commercial code. Various numerical aspects associated with the unstructured approach were investigated. The third test case was investigated to indicate the success of the modified code to predict reacting flows. The main conclusions of the studies are:

1. In the JICCF calculations, a strong coupling between the jet flow and mainstream flow was known to exist. This coupling could not be easily captured by specifying the commonly used uniform jet velocity boundary conditions for core-only calculations. Therefore, the only way to accurately predict the combustor flow fields is to include both the interior (core) and exterior (annulus) flows into the CFD analysis. Similarly, in the MSSF the simulation of the whole domain was found to be of great importance to accurately predict the flow features. Unstructured mesh approach provides more flexibility to deal with the complex geometries produced due to coupling various regions.
2. Hydra predicted the flow characteristics of the JICCF case reasonably well compared to the experimental data. With the standard  $k$ - $\epsilon$  model all flow major structures observed experimentally were captured with different levels of accuracy. Using different type of grids, Hydra predictions showed different behaviour especially in high gradient

regions. Purely tetrahedral meshes were found to be not suitable to predict such flows since they produce inaccurate solutions in regions with high gradients such as boundary layers. Alternatively, a prismatic layer near walls and tetrahedral grid in the other regions was found to be a reasonable solution to this problem. On the other hand, generating prismatic layers was hard to accomplish in regions where the complex interaction of the geometry surfaces such as in the MSSF case. Purely hexahedral meshes were found to produce solutions with better accuracy. However, they were found to be very complex and time-consuming to generate.

3. The different behaviour of various meshes is mainly attributed to numerical diffusion arising due to the one-dimensional interpolation practices being employed in multi-dimensional cases especially when the flow is oblique to the grid lines and when there is a nonzero gradient of the dependent variable in the direction normal to the flow direction. Due to flow complexity of the combustor relevant cases, neither tetrahedral nor hexahedral grids were able to provide best grid alignment with flow direction all over the domain and it was difficult to generate a grid that would satisfy the grid alignment at every part of the domain. Grid refinement was found to reduce the numerical diffusion and improve the solution accuracy. In the absence of an adaptive solution procedure grid refinement currently is expensive.

## 7.2 Recommendations for Future work

The findings of the present work have raised some important issues that need further investigations in order to improve the code capabilities. Some of these can be summarised as follows:

- The requirement to improve the numerical algorithm particularly the discretisation method of the smoothing terms in order to increase the

accuracy of the predictions when purely tetrahedral grids are used. Such grids are easy to generate especially for complex geometries.

- The requirement to develop an adaptive technique to increase the code efficiency and to reduce the numerical cost. The full potential of unstructured methods can only be realised when including an adaptive solution procedure.
- The requirement to examine the efficiency of the code compared to pressure-based methods.
- Developing an LES version of the code to investigate the unsteady features such as PVC and explore their influence on the predictions accuracy.
- More reacting flow cases (diffusion flames) need to be tested using different thermo-chemistry models. Also the ability of the code to simulate high Mach reacting flows relevant to gas turbine flows need to be explored.
- The requirement to explore use of the same CFD algorithm for integrated coupled calculations of e.g. compressor/combustor/turbine should be considered.

# Appendix A

## Matrices for Flux and Preconditioner Calculations

The definitions of the various matrices employed in the calculations of the inviscid and viscous fluxes along with the preconditioner matrix are defined here. The

inviscid flux Jacobian matrix  $A_y = \frac{\partial F^I}{\partial Q}$  introduced in section 2.4.2 is defined as

follows:

$$A_y = (T\Lambda T^{-1})_y$$

where  $T$  is the eigenvector matrix:

$$T = (r1 | r2 | r3 | r4 | r5)$$

$$r3 = \begin{pmatrix} n_x \\ un_x \\ vn_x + cn_x \\ wn_x - cn_y \\ \frac{1}{2}q^2 n_x + c(vn_z - wn_y) \end{pmatrix}, \quad r4 = \begin{pmatrix} n_y \\ un_y - cn_z \\ vn_y \\ wn_y - cn_x \\ \frac{1}{2}q^2 n_y + c(wn_x - un_z) \end{pmatrix}$$

$$r3 = \begin{pmatrix} n_z \\ un_z + cn_y \\ vn_z - cn_x \\ wn_z \\ \frac{1}{2}q_n^2 n_z + c(un_y - vn_x) \end{pmatrix}, \quad r2 = \begin{pmatrix} 1 \\ u + cn_x \\ v + cn_y \\ w + cn_z \\ H + cq_n \end{pmatrix}, \quad r1 = \begin{pmatrix} 1 \\ u - cn_x \\ v - cn_y \\ w - cn_z \\ H - cq_n \end{pmatrix}$$

$T^{-1}$  is the inverse of eigenvector matrix:

$$T^{-1} = \frac{1}{c^2} (I1 | I2 | I3 | I4 | I5)^T$$



$$I1 = \begin{pmatrix} \frac{1}{2} \left( (\gamma - 1) \frac{q^2}{2} + cq_n \right) \\ -\frac{1}{2} ((\gamma - 1)u + cn_x) \\ -\frac{1}{2} ((\gamma - 1)v + cn_y) \\ -\frac{1}{2} ((\gamma - 1)w + cn_z) \\ \frac{1}{2} (\gamma - 1) \end{pmatrix} \quad I2 = \begin{pmatrix} \frac{1}{2} \left( (\gamma - 1) \frac{q^2}{2} - cq_n \right) \\ -\frac{1}{2} ((\gamma - 1)u - cn_x) \\ -\frac{1}{2} ((\gamma - 1)v - cn_y) \\ -\frac{1}{2} ((\gamma - 1)w - cn_z) \\ \frac{1}{2} (\gamma - 1) \end{pmatrix}$$

$$I3 = \begin{pmatrix} \left( c^2 - (\gamma - 1) \frac{q^2}{2} \right) n_x + c(w n_y - v n_z) \\ (\gamma - 1) u n_x \\ (\gamma - 1) v n_x + c n_z \\ (\gamma - 1) w n_x - c n_y \\ -(\gamma - 1) n_x \end{pmatrix}$$

$$I4 = \begin{pmatrix} \left( c^2 - (\gamma - 1) \frac{q^2}{2} \right) n_y + c(u n_z - w n_x) \\ (\gamma - 1) u n_y - c n_z \\ (\gamma - 1) v n_y \\ (\gamma - 1) w n_y + c n_x \\ -(\gamma - 1) n_y \end{pmatrix}$$

$$I5 = \begin{pmatrix} \left( c^2 - (\gamma - 1) \frac{q^2}{2} \right) n_z + c(v n_x - u n_y) \\ (\gamma - 1) u n_z - c n_y \\ (\gamma - 1) v n_z - c n_x \\ (\gamma - 1) w n_z \\ -(\gamma - 1) n_z \end{pmatrix}$$

and  $\Lambda$  is the eigenvector matrix

$$\Lambda = \begin{pmatrix} |q_n - c| & 0 & 0 & 0 & 0 \\ 0 & |q_n + c| & 0 & 0 & 0 \\ 0 & 0 & |q_n| & 0 & 0 \\ 0 & 0 & 0 & |q_n| & 0 \\ 0 & 0 & 0 & 0 & |q_n| \end{pmatrix}$$

where  $q^2 = u^2 + v^2 + w^2$

The viscous contribution to the block-Jacobi preconditioner that was introduced in section 2.7 consists of the 5x5 matrix  $B_{ij}$  and the inverse  $M^{-1}$  of the Jacobian matrix of the transformation  $M$  from conservative to non-conservative variables. The matrix B is therefore given by:

$$B = (c1|c2|c3|c4|c5)$$

$$c1 = \begin{pmatrix} 0 \\ 0 \\ 0 \\ 0 \\ \frac{\mu_l + \mu_t}{\rho^2} \\ \frac{-P\gamma}{\Pr_l} \frac{\mu_l + \mu_t}{(\gamma - 1)} \end{pmatrix}, c2 = \begin{pmatrix} 0 \\ (\mu_l + \mu_t) \\ 0 \\ 0 \\ u(\mu_l + \mu_t) \end{pmatrix}$$

$$, c3 = \begin{pmatrix} 0 \\ 0 \\ (\mu_l + \mu_t) \\ 0 \\ v(\mu_l + \mu_t) \end{pmatrix}, c4 = \begin{pmatrix} 0 \\ 0 \\ 0 \\ (\mu_l + \mu_t) \\ w(\mu_l + \mu_t) \end{pmatrix} \text{ and } c5 = \begin{pmatrix} 0 \\ 0 \\ 0 \\ 0 \\ \frac{\mu_l + \mu_t}{\rho} \\ \frac{\gamma}{(\gamma - 1)} \frac{\mu_l + \mu_t}{\Pr_l} \end{pmatrix}$$

The transformation matrix and its inverse are given by:

$$M = \frac{\partial Q}{\partial V} = \begin{pmatrix} 1 & 0 & 0 & 0 & 0 \\ u & \rho & 0 & 0 & 0 \\ v & 0 & \rho & 0 & 0 \\ w & 0 & 0 & \rho & 0 \\ \frac{q^2}{2} & \rho u & \rho v & \rho w & \frac{1}{\gamma-1} \end{pmatrix}$$

$$M^{-1} = \begin{pmatrix} 1 & 0 & 0 & 0 & 0 \\ -u/\rho & 1/\rho & 0 & 0 & 0 \\ -v/\rho & 0 & 1/\rho & 0 & 0 \\ -w/\rho & 0 & 0 & 1/\rho & 0 \\ \frac{q^2(\gamma-1)}{2} & -u(\gamma-1) & -v(\gamma-1) & -w(\gamma-1) & \frac{1}{\gamma-1} \end{pmatrix}$$

where  $Q$  and  $V$  are the conservative and non-conservative variables vectors given as follows:

$$Q = \begin{pmatrix} \rho \\ \rho u \\ \rho v \\ \rho w \\ \rho e_t \end{pmatrix} \quad \text{and} \quad V = \begin{pmatrix} \rho \\ u \\ v \\ w \\ p_t \end{pmatrix}$$

## References

1. <http://civil.rolls-royce.com/Trent-900-jet-aero-engines/>
2. Jameson A., "Steady State Solution of the Euler Equations for Transonic Flow," *Transonic, Shock, and Multidimensional Flows: Advances in Scientific Computing*, No. 47, Academic Press, New York, pp.37-70, 1982.
3. Steger J. and Warming R., "Flux Vector Splitting of the Inviscid Gasdynamic Equations with Application to Finite Difference Methods," *Journal of Computational Physics*, Vol. 40, No. 2, pp. 268-293, 1981.
4. Wilcox D. C., "Turbulence Modeling for CFD," DCW Industries, La Canada, California, 1993.
5. Durbin P. and Petterson B., "Statistical Theory and Modeling for Turbulent Flow," John Wiley & Sons Ltd, Chichester, 2001.
6. Webster M. F., Keshtiban I. J. and Belblidia F., "Computation of Weakly-Compressible Highly-Viscous Liquid Flows," *Engineering Computations*, Vol. 21 No. 7, pp. 777-804, 2004.
7. Guillard H. and Viosat C., "On the Behaviour of Upwind Schemes in the Low Mach Number Limit," *Computers and Fluids*, Vol. 28, pp. 63-86, 1999.
8. Van Leer B., Lee W. T., and Roe P. L., "Characteristics Time Stepping of Local Preconditioning of the Euler Equations," AIAA paper 91-1552, 1991.
9. Turkel E., "Preconditioned Methods for Solving the Incompressible and Low Speed Equations," *Journal of Computational Physics*, Vol. 72, pp. 277-298, 1987.

10. Weiss J. M. and Smith W. A., "Preconditioning Applied to Variable and Constant Density Flows," AIAA Journal, Vol. 33, No. 11, 1995.
11. Patankar S. V., "Numerical Heat Transfer and Fluid Flow," McGraw Hill, New York, 1980.
12. Ferziger J. H. and Peric M., "Computational Methods for Fluid Dynamics," Springer-Verlag, Berlin, 2002.
13. Shyy W., Chen M. and Sun C., "Pressure-Based Multigrid Algorithm for Flow at All Speeds," AIAA Journal, Vol. 30, No. 11, 1992.
14. Rhie M. C., "Pressure-Based Navier-Stokes Solver Using the Multigrid Method," AIAA Journal, Vol.27, No.8, 1989.
15. Ansari A. and Strang W. Z., "Large-Eddy Simulation of Turbulent Mixing Layers," AIAA Paper 96-0684, 1996.
16. Moin P., "Numerical and Physical Issues in Large Eddy Simulation of Turbulent Flows," JSME International Journal, 1998.
17. Dawes W., "The Simulation of 3-dimensional Viscous Flow in Turbomachinery Geometries Using a Solution-Adaptive Unstructured Mesh Methodology," Journal of Turbomachinery-Transactions of the ASME, Vol. 114, No., pp 528-537, 1992.
18. Kwon O. and Hah C., "Solution of the 3-D Navier-Stokes Equations with a Two-Equation Turbulence Model on Unstructured Meshes Applied to Turbomachinery," AIAA paper 1994-1833, pp 238-254, 1994.
19. Su K. and Zhou C., "Numerical Modeling of Gas Turbine Combustor Integrated with Diffuser," NHTC'0012229, Proceedings of NHTC'00, 34th



- National Heat Transfer Conference, Pittsburgh, Pennsylvania, August 20-22, 2000.
20. Mongia H., "Aero-thermal Design and Analysis of Gas Turbine Combustion Systems-Current Status and Future Direction," AIAA paper 1998-3982, AIAA/ASME/SAE/ASEE Joint Propulsion Conference and Exhibit, 34th, Cleveland, OH, July 13-15, 1998.
  21. Shluter J., Apte S., Kalitzin E., Weide J., Alonso J., and Pitsch H., "Large Scale Integrated LES-RANS Simulations of a Gas Turbine Engine," Center for Turbulence Research Annual Briefs, Stanford University, 2005.
  22. Reynolds W. C., Alonso J., and Fatica M., "Aircraft Gas Turbine Engine Simulations," 16<sup>th</sup> AIAA Computational Fluid Dynamics Conference, Orlando, FL, AIAA paper 2003-3698, 2003.
  23. Shluter J. and Kim S., "Integrated Simulations of a Compressor/Combustor Assembly of a Gas Turbine Engine," ASME Turbo Expo 2005, ASME paper GT2005-68204, 2005.
  24. Lytle J., Follen G., and Lopez I., "Computing and Interdisciplinary Systems Office Review and Planning Meeting," NASA/TM-2003-211896, 2003.
  25. Salman H., "Numerical Simulation of Streamwise Vorticity Enhanced Mixing" Ph.D. thesis, Loughborough University, 2001.
  26. Lapworth L. and Shahpar S., "Design of Gas Turbine Engine Using CFD," European Congress on Computational Methods in Applied Sciences and Engineering, ECCOMAS 2004, Jyvaskyla, July 2004.

27. Salman H., McGuirk J., and Page G., "Prediction of Lobed Mixer Vortical Structures with a  $k-\epsilon$  Turbulence Model," *AIAA Journal*, Vol. 41, No. 5, 2003.
28. Rolls-Royce Computational Fluid Dynamics Research Annual Report, Derby, 2004.
29. Rolls-Royce Computational Fluid Dynamics Research Annual Report, Derby, 2005.
30. "The jet engine," Rolls-Royce plc, 4th edition, 1986.
31. Lefebvre A., "Gas Turbine Combustion," Taylor & Francis; 2nd edition, 1998.
32. Saravanamuttoo H., Rogers G., and Cohen H., "Gas Turbine Theory," Prentice Hall, 5th edition, 2001.
33. Shyy W., Braaten M., and Burrus D., "Study of Three-Dimensional Gas-Turbine Combustor Flows," *International Journal of Heat Mass Transfer*, Vol. 32, No. 6, pp. 1155-1164, 1989.
34. Shyy W., Correa S. M., and Braaten, M., "Computation of Flow in a Gas Turbine Combustor," *Combustion Science and Technology*, Vol. 58, pp. 97-117, 1987.
35. Koutmos P., and McGuirk J., "Isothermal Flow in a Gas Turbine Combustor - A Benchmark Experimental Study," *Experiments in Fluids*, Vol. 7, pp 344-354, 1989.

36. Koutmos P., and McGuirk J. **"Isothermal Modeling of Gas Turbine Combustor: Computational Study,"** Journal of propulsion, Vol. 7, No. 6, pp 1064-1071, 1991.
37. Bazdidi-Tehrani F., and Jahromi M., **"Three-Dimensional Numerical Simulation of the Flow Inside a Model Gas Turbine Combustor,"** Proceedings of the Eleventh Annual Conference of the CFD Society of Canada (CFD 2003), Vancouver, BC, Canada, May 28-30, 2003.
38. Stevens S.J., and Carrotte J.F., **"Experimental Studies of Combustor Dilution Zone Aerodynamics, Part I: Mean Flowfields"** Journal of Propulsion, Vol.6, No.3, pp. 297-304, 1990.
39. Holdeman J.D., **"Mixing of Multiple Jets with a Confined Subsonic Crossflow,"** Progress in Energy and Combustion Science, Vol. 19, pp. 31-70, 1993.
40. Gulati A., Tolpadi A., VanDeusen G., and Burrus D., **"Effect of Dilution Air on the Scalar Flowfield at Combustor Sector Exit,"** Journal of Propulsion and Power, Vol. 11, No. 6, pp. 1162-1169, 1995.
41. Anacleto P., Heitor M., and Moreira A., **"The Mean and Turbulent Flowfields in a Model RQL Gas-Turbine Combustor,"** Experiments in Fluids, Vol.22, pp. 153-164, 1996.
42. Doerr T., Blomeyer M., and Hennecke D., **"Optimization of Multiple Jets Mixing With a Confined Crossflow,"** Journal of Engineering for Gas Turbines and Power, Vol. 119, pp. 315-321, 1997.

43. Blomeyer M., Krautkremer B., Hennecke D., and Doerr T., "Mixing Zone Optimization of a Rich-Burn/Quick-Mix/Lean-Burn Combustor" *Journal of Propulsion and Power*, Vol. 15, No. 2, pp. 288-295, 1999.
44. Ahmed, S.A., "Velocity Measurements and Turbulence Statistics of a Confined Isothermal Swirling Flow," *Experimental Thermal and Fluid Science*, Vol. 17, pp. 256-264, 1998.
45. Tsao J., and Lin C.A., "Reynolds stress modelling of jet and swirl interaction inside a gas turbine combustor , " *International Journal for Numerical Methods in Fluids*, Vol. 29, Issue 4, pp. 451-464, 1999.
46. Spencer A., "Gas turbine combustor port flows," Ph.D. thesis, Loughborough University, 1998.
47. McGuirk J., and Spencer A., "Coupled and Uncoupled CFD Prediction of the Characteristics of Jets from Air Admission Ports," Paper presented at ASME conference. Paper No. ASME 00-GT-0125, pp. 1-11, 2000.
48. Hughes N., "Computational and Experimental Study of a Multi-Stream Swirler," Ph.D. thesis, Loughborough University, 2003.
49. Xia J., Yadigaroglu G., Liu Y., Schmidli J. and Smith B., "Numerical and Experimental Study of Swirling Flow in a Model Combustor," *International Journal of Heat Mass Transfer*, Vol. 41, No. 11, pp. 1485-1497, 1998.
50. Liu N., "On the Comprehensive Modeling and Simulation of Combustion System," AIAA 2001-0805. 39<sup>th</sup> AIAA Aerospace Sciences Meeting & Exhibit, NV, 2001.

51. Veres J., "Overview of High-Fidelity Modeling in the Numerical Propulsion System Simulation (NPSS) Project Activities," NASA/TM-2002-211351, 2002.
52. Davoudzadeh F. and Liu N., "Numerical Prediction of Non-Reacting and Reacting Flow in a Model Gas Turbine Combustor," NASA/TM-2005-213898, 2005.
53. "The HYDRA User's Guide," Version 0.03, Rolls-Royce plc, March 2004.
54. Owen F., Spadaccini L., and Bowman C., "Pollutant Formation and Energy Release in Confined Turbulent Diffusion Flames," Proc. Combustion Institute, Vol. 16, pp. 105-117, 1976.
55. Jones W., and McGuirk J., "Mathematical Modeling of Gas-Turbine Chambers," Imperial College, London, 1980.
56. Peirce C., and Moin P., "Progress-Variable Approach for Large-Eddy-Simulation of Non-Premixed Turbulent Combustion," Journal of Fluid Mechanics, Vol. 504, 2004, pp 73-79.
57. Crumpton P., Moinier P., and Giles M., "An Unstructured Algorithm for High Reynolds Number Flows on Highly Stretched Grids," 10<sup>th</sup> International Conference on Numerical Methods for Laminar and Turbulent Flow, 1997.
58. Moinier P., "Algorithm Developments for an Unstructured Viscous Flow Solver" Ph.D. thesis, University of Oxford, UK, Trinity Term 1999.
59. "The HYDRA Programmer's Guide," Version 0.02, Rolls-Royce plc, March 2004.



60. Jones W. and Launder B., "The Prediction of Laminarization with a Two-Equation Model of Turbulence," *International Journal of Heat and Mass Transfer*, Vol. 15, pp 301-314, 1972.
61. Hoffman K. and Chiang S., "Computational Fluid Dynamics for Engineers-Volume I," Engineering Education System, Wichita, USA, 1993.
62. Morton K. and Suli E., "Finite Volume Methods and their Analysis," *IMA Journal of Numerical Analysis*, Vol. 11, No. 2, pp 241-260, 1991.
63. Barth T., "Aspects of Unstructured Grids and Finite-Volume Solvers for the Euler and Navier-Stokes Equations In Computational Fluid Dynamics Lecture," Series 1994-05, von Karman Institute for Fluid Dynamics, March 1994.
64. Mavriplis D., "Unstructured Mesh Algorithms for Aerodynamic Calculations," *Proceeding of 13th International Conference on Numerical Methods in Fluid Dynamics, Lecture Notes in Physics*, Vol. 414, pp. 57-77, Springer Verlag, Heidelberg, Germany, 1992.
65. Vinkatakrishnan V., "Convergence to Steady-State Solutions of the Euler Equations on Unstructured Grids with Limiters," *Journal of Computational Physics*, Vol. 118, No. 1, pp. 120-130, April 1995.
66. Roe P., "Error Estimates for Cell-Vertex Solutions of the Compressible Euler Equations," *ICASE Report No. 87-6*, January 1987.
67. Haselbacher A., "A Grid-Transparent Numerical Method for Compressible Viscous Flows on Mixed Unstructured Grids," Ph.D. thesis, Loughborough University, 1999.

68. Roe P., "Approximate Riemann Solvers, Parameter Vectors, and Difference Schemes," *Journal of Computational Physics*, Vol. 43, pp 357-372, 1981.
69. Anderson W. and Bonhaus D., "An Implicit Upwind Algorithm for Computing Turbulent Flows on Unstructured Grids," *Journal of Computers Fluids*, Vol. 23, No. 1, pp. 1-21, 1996.
70. Ashford G., "An Unstructured Grid Generation and Adaptive Solution Technique for High-Reynolds-Number Compressible Flows," PhD Thesis, University of Michigan, 1996.
71. Kunz R. and Lakshminarayana B., "Explicit Navier-Stokes Computation of Cascade Flows Using the k- $\epsilon$  Turbulence Model," *AIAA Journal*, Vol. 30, No 1, pp. 13-22, 1992.
72. Stolcis L. and Johnston L., "Compressible Flow Calculations Using a Two-Equation Turbulence Model and Unstructured Grids," In *Proceedings of the 7<sup>th</sup> International Conference on Numerical Methods for Laminar and Turbulent Flow*, pp. 852-862, Pineridge Press, 1991.
73. Mavriplis D. and Martinelli L., "Multigrid Solution of Compressible Turbulent Flow on Unstructured Meshes Using a Two-Equation Model," AIAA paper 91-0237, 1991.
74. Hirsch C., "Numerical Computation of Internal and External Flows, volume 1," John Wiley & Sons, New York, 1988.
75. Gear C., "Numerical Initial Value Problems," Prentice Hall, Englewood Cliffs, 1971.

76. Lambert J. "Numerical Methods for Ordinary Differential Systems: the Initial Value Problem," Wiley, Chichester, NY, 1991.
77. L. Martinelli L., "Calculations of Viscous Flows with a Multigrid Method," Ph. D. thesis, Princeton University, Princeton, NJ, October 1987.
78. Hosseini K. and Alonso J., "Optimization of Multistage Coefficients for Explicit Multigrid Flow Solvers," AIAA paper 2003-3705, 2003.
79. Carpenter M. and Kennedy C., "Fourth-Order 2N-Storage Runge-Kutta Schemes," NASA Technical Memorandum 109112, 1994.
80. Huy F., Hussaini M. and Manthey J., "Low-Dissipation and -Dispersion Runge-Kutta Schemes for Computational Acoustic," ICASE Report No. 1994-102, 1994.
81. Spalart P. and Allmaras S., "A One-Equation Turbulence Model for Aerodynamic Flows," AIAA Paper 92-439, 1992.
82. Moinier P. and Giles M., "Preconditioned Euler and Navier-Stokes Calculations on Unstructured Meshes," 6th ICFD Conference on Numerical Methods for Fluid Dynamics, 1998.
83. Wesseling P., "An Introduction of Multigrid Methods," John Wiley, 1992.
84. Mavriplis D. and Venkatakrishnan V., "A Unified Multigrid Solver for the Navier-Stokes Equations on Mixed Element Meshes," AIAA paper 95-1666, 1995.
85. Mavriplis D. and Venkatakrishnan V., "A 3D Agglomeration Multigrid Solver for the Reynolds-Averaged Navier-Stokes Equations on Unstructured Meshes," AIAA paper 95-0345, 1995.

86. Crumpton P. and Giles M., "Implicit Time Accurate Solutions on Unstructured Dynamic grids," *International Journal of Numerical Methods in Fluids*, Vol. 25, pp 1285-1300, 1997.
87. Jones W., "Turbulence Modelling-In Introduction to the Modelling of Turbulence," Lecture Series 1997-03, von Karman Institute for Fluid Dynamics, March 1997.
88. Mohammadi B. and Puigt G., "Wall-Laws for High Speed Flows over Adiabatic and Isothermal Walls," INRIA Report No. 3948, May 2000.
89. Muller J., "A user's guide to hip," Version 1.13.13, Oxford University Computing Laboratory, January 2001.
90. Haines B., "VISUAL 3 User's & Programmer's Manual," Version 2.35, Massachusetts Institute of Technology, 1998.
91. Sturgess G. and Syed S., "Importance of Inlet Boundary Conditions for Numerical Simulation of Combustor Flows," AIAA paper -83-1263, 1983.
92. Darmofal D., Moinier P., and Giles M., "Eigenmode Analysis of Boundary Conditions for the One-Dimensional Preconditioned Euler Equations," *Journal of Computational Physics*, Vol. 160, pp 369-384, 2000.
93. Slater J. "Verification Assessment of Flow Boundary Conditions for CFD Analysis of Supersonic Inlet Flows," AIAA paper 3882, 2001.
94. Ferlauto M., Iollo A., and Zannetti L., "Set of Boundary Conditions for Aerodynamic Design," *AIAA Journal*, Vol. 42, No. 8, August 2004

95. Caraeni M. and Fuchs L., "Investigation of Non reflective Boundary Conditions for Computational Aeroacoustics," AIAA Journal, Vol. 44, No. 9, 2006.
96. Loh C. and Jorgenson P., "A Robust Absorbing Boundary Condition for Compressible Flows," NASA/TM-2005-213654, AIAA-2005-4716, 2005.
97. Yee H., "Numerical approximation of boundary conditions with applications to inviscid equations of gas dynamics," Technical Memorandum 81265, NASA, 1981.
98. Private communication, Dr. Leigh Lapworth, Aerothermal Methods, Rolls-Royce, Derby.
99. Patankar S., "Numerical Heat Transfer and Fluid Flow," Hemisphere Publishing Corporation, 1981.
100. Peric M., "A Finite Volume method for the prediction of three-dimensional fluid flow in complex ducts," PhD thesis, Imperial College, University of London, 1985.
101. Smith R. and Hutton A., "The numerical treatment of advection: A performance comparison of current methods," Numerical Heat Transfer, vol. 5, 1982.
102. Roe P., "Optimum Upwind Advection on A Triangular Mesh," NASA CR-187459, ICASE Report No. 90-75, 1990.
103. Jiang D., McGuirk J. and Page G., "Influence of Mesh Type and Grid Quality on Spurious Mixing in Unstructured Mesh CFD Predictions of Scalar Mixing Layers," ECCOMAS CFD, Swansea, UK, pp 1-10, 2001.



104. Jameson A., "Numerical Solution of the Euler Equations for Compressible Inviscid Fluids," Numerical Methods for the Euler Equations of Fluid Dynamics, edited by F. Angrand, et al. , SIAM, 1985, pp. 199-245.
105. Poinso T. and Veynante D., "Theoretical and Numerical Combustion," R.T. Edwards Inc, 2001.
106. Fox R., "Computational Models for Turbulent Reacting Flows," Cambridge University Press, 2003.
107. Kuo k., "Principles of Combustion, 2nd Edition", John Wiley & Sons, Inc., 2005.
108. Burke S. and Schumann T., "Diffusion Flames," Industrial Eng. Chem. Vol. 20, pp 998, 1928.
109. Spalding D., "Concentration Fluctuations in a Round Turbulent Free Jet," Chemical Engineering Science, Vol.26, pp. 95, 1971.
110. Elgobashi S., Pun W., and Spalding D., "Concentration fluctuation in isothermal turbulent confined coaxial jets," Chemical Engineering Science, Vol. 32, pp. 161-166, 1975.
111. Becker H., Hottel H., and Williams G., "On the light-scatter technique for the study of turbulence and mixing," Journal of Fluid Mechanics, Vol. 30, pp259-284, 1967.
112. Torrest R. and Ranz W., "Concentration fluctuations and chemical conversion associated with mixing in some turbulent flows," AIChE Journal, Vol. 16, pp 930-942, 1970.

113. Carrotte J. and Stevens S., "The Influence of Dilution Hole Geometry on Jet Mixing," ASME Journal of Engineering for Gas Turbines and Power, Vol. 112, pp. 73-79, 1990.
114. Kamotani Y. and Gerber I., "Experiments on Confined Turbulent Jets in Cross Flow," NASA CR-2392, 1974.
115. Atkinson K., Khan Z., and Whitelaw J., "Experimental Investigation of Opposed Jets Discharging Normally into a Cross-Stream," Journal of Fluid Mechanics, Vol. 115, pp 493-504, 1982.
116. Holdeman J., "Perspective on the Mixing of a Row of Jets with a Confined Crossflow," NASA TM 83457, AIAA paper 83-1200, 1983.
117. Andreopoulos J., "Measurements in a Pipe Flow Issuing Perpendicular into a Cross Stream," J. Fluids Eng., Vol. 104, pp. 493-499, 1983.
118. Andreopoulos J. and Rodi W., "Experimental Investigation of Jets in a CrossFlow," Journal of Fluid Mechanics, Vol. 138, pp 93-127, 1984.
119. Andreopoulos J., "On the Structure of Jets in a Crossflow," Journal of Fluid Mechanics, Vol. 157, pp 163-197, 1985.
120. Lilley D. "Lateral Jet Injection into Typical Combustor Flow fields," NASA CR 3997, 1986.
121. Demuren A. "Modeling Jets in Cross Flow," ICASE Report No. 94-71, 1994.
122. Achayara S., Tyagi M., and Hoda A. "Flow and Heat Transfer Predictions for Film Cooling," Analysis of the New York Academy of Science, Vol. 934, pp 110-125., 2001.

123. Holdeman J., Liscinsky D., and Bain D., "Mixing of Multiple Jets with a Confined Subsonic Crossflow Part II - Opposed Rows of Orifices in Rectangular Ducts," NASA TM 107461, 1997.
124. Sykes R., Lewellen W. and Parker S., "On the Vorticity Dynamics of a Turbulent Jet in a Crossflow," *Journal of Fluid Mechanics*, Vol. 168, pp 399-413, 1986.
125. Kim S. and Benson T., "Fluid Flow of a Row of Jets in Crossflow-A Numerical Study," *AIAA Journal*, Vol. 31, No. 5, May 1993.
126. Muldoon F. and Acharya S., "Dynamics of Large-Scale Structures for Jets in Crossflow," NASA CR 1998-206606, 1998.
127. Patankar S., Basu D. and Alpay S., "Prediction of the Three-Dimensional Velocity Field of a Deflected Turbulent Jet," *Journal of Fluids Engineering*, Vol. 99, pp 758-762, 1977.
128. Jones W. and McGuirk J., "Computation of a Round Turbulent Jet Discharging into a Confined Crossflow," *Turbulent Shear Flows 2*, Springer, pp 233-245, 1980.
129. Demuren A. "Characteristics of 3D Turbulent Jets in Crossflow," NASA TM 104337 ICOMP-91-05, 1991.
130. Claus R. and Vanka S., "Multigrid Calculations of a Jet in Crossflow," *Journal Propulsion and Power*, Vol. 8, pp 185-193, 1992.
131. Barata J., Durao D., and McGuirk J., "Numerical Study of a Single Impinging Jets through a Crossflow," AIAA paper 89-0449, 1989.

132. Bain D., Smith C., Liscinsky D., and Holdeman J., "CFD Mixing Analysis of Axially Opposed Rows of Jets Injected Radially into Confined Crossflow," NASA TM 7106179 -AIAA-93.2044, 1993.
133. Demuren A., "Calculations of 3D Impinging Jets in Crossflow with Reynolds Stress Models," Proceedings, International Symposium on Heat Transfer in Turbomachinery, Marathon, Greece, 1992.
134. Pathak M., Dewan A., Dass A., "Computational Prediction of a Slightly Heated Turbulent Rectangular Jet Discharged into a Narrow Channel Crossflow Using Two Different Turbulence Models," International Journal of Heat and Mass Transfer Vol. 49, pp 3914-3928. 2006.
135. Kim S., and Benson T., "Calculation of a Circular Jet in Crossflow with a Multiple-Time-Scale Turbulence Model," International Journal of Heat and Mass Transfer, Vol. 35, No. 10, pp 2357-2365, 1992.
136. Baker S. and McGuirk J., "Multi-jet Annulus/Core-flow Mixing - Experiments and Calculations", Transactions of the ASME Journal of Engineering for Gas Turbines and Power, Vol. 115, pp 473-479, 1993.
137. Bain D., Smith C., Liscinsky D., and Holdeman J., "Flow Coupling Effects in Jet-in-Crossflow Flow fields," NASA TM107257, AIAA paper 96-2762, 1996.
138. Hollis D. "Particle Image velocimetry in gas turbine combustor flow fields," Ph.D. thesis, Loughborough University, 2004.
139. GAMBIT User's manual, Version 2.4, 2004.

140. Wang Z., Chen R., Hariharan N., Przekwas A., and Grove D., "A 2<sup>nd</sup> Tree Based Automated Viscous Cartesian Grid Methodology for Feature Capturing," AIAA paper 99-3300, 1999.
141. Gnoffo P. and White J., "Computational Aerothermodynamic Simulation Issues on Unstructured Grids," AIAA paper 2004-2371, 2004.
142. FLUENT User's Manual, Version 6.2, 2004.
143. Gupta A., Lilley D., and Syred N., "Swirl flows," Taylor & Francis, 1984.
144. Gore R. and Ranz W., "Back Flows in Rotating Fluids Moving Axially Through Expanding Cross Sections," A.I.Ch.E. Journal, Vol. 10, pp. 83 - 88. 1964.
145. Chigier N. and Chervinsky A., "Experimental Investigation of Swirling Vortex Motion in Jets," Journal of Applied Mechanics, Vol. 34, pp. 443-451, 1967.
146. So R., Ahmed S., and Mongia H., "An Experimental Investigation of Gas Jets in Confined Swirling Air Flow," NASA C. R. 3832, 1984.
147. Syred N. and Beer J., "Combustion in Swirling Flows: A Review," Journal of Combustion and Flame, Vol. 23, pp. 143-201, 1974.
148. Lilley D., "Swirl Flows in Combustion: A Review," AIAA Journal, Vol. 15, pp. 1063-1078, 1977.
149. Jones W. and Pascau A., "Calculation of Confined Swirling Flows with a Second Moment Closure," Journal of Fluids Engineering, Vol. 111, pp. 248-255, 1989.
150. Ramos J., "Turbulent Non-reacting Swirling Flows," AIAA Journal Vol. 22, No. 6, pp 846-848, 1984.



151. Vu B., and Gouldin F., "Flow Measurement in a Model Swirl Combustor," AIAA Journal, Vol. 20, pp. 642-651, 1982.
152. Habib, M. A. and Whitelaw, "Velocity Characteristics of Confined Coaxial Jets with and without Swirl," Journal of Fluids Engineering, Vol. 102, pp. 47-53, 1980.
153. Sharif M. and Wong Y., "Evaluation of the Performance of Three Turbulence Closure Models in the Prediction of Confined Swirling Flows," Journal of Computers and Fluids, Vol. 24, No. pp. 81-100, 1995.
154. Crocker S., Nickolaus D., and Smith C., "CFD Modelling of a Gas Turbine Combustor from Compressor Exit to Turbine Inlet," ASME Paper No. 98-GT-184. 1998.
155. Widmann J., Charagundla S., and Presser C., "Characterization of the Inlet Combustion Air in NIST's Reference Spray Combustion Facility: Effect of Vane Angle and Reynolds Number," NISTIR Report No. 6458, 2000.
156. Guo B., Langrish T., and Fletcher D., "CFD Simulation of Precession in Sudden Pipe Expansion Flows with Low Inlet Swirl," Applied Mathematical Modelling, Vol. 26, No. 1, pp. 1-15, 2002.
157. Fudihara T., Goldstein L., and Mori M., "The Three-Dimensional Numerical Aerodynamics of A Movable Block Burner," Brazilian Journal of Chemical Engineering, Vol. 20, No. 04, pp. 391 - 401, 2003.
158. Beér J. and Chigier N., "Combustion Aerodynamics," Applied Science Publishers Ltd., 1974.

159. Garimella R. and Shephard M. "Boundary Layer Meshing for Viscous Flows in Complex Domains," 7th International Meshing Roundtable, pp. 107-118, 1998.
160. Thompson D., Chalasani S., and Soni B. "Generation of Volume Meshes by Extrusion from Surface Meshes of Arbitrary Topology," Proceedings of the 9th International Meshing Roundtable, Sandia National Laboratories, pp. 385-393, 2000.
161. Chalasani S. and Thompson D., "Quality improvements in extruded meshes using topologically adaptive generalized elements," International Journal for Numerical Methods in Engineering, Vol. 60, pp. 1139-1159, 2004.
162. Bilger R. and Beck R., "Turbulent Diffusion Flames," Annual Review of Fluid Mechanics, Vol. 21, pp. 101-135, 1989.
163. Peters N., "Laminar Diffusion Flamelet Models in Non-premixed Turbulent Combustion," Progress in Energy and Combustion Science, Vol. 10, pp. 319-339, 1984.
164. Pope S., "The Probability Approach to the Modelling of Turbulent Reacting Flows," Journal of Combustion and Flame, Vol. 27, pp. 299-312, 1976.
165. Elghobashi S. and Pun W., "A Theoretical and Experimental Study of Turbulent Diffusion Flames in Cylindrical Furnaces," In Fifteenth Symposium (International) on Combustion, The Combustion Institute, pp. 1353-1365, 1974.

166. Lockwood F., El-Mahallawy F., and Spalding D., "an experimental and theoretical investigation of turbulent mixing in cylindrical furnace," *Journal of Combustion and Flames*, Vol. 23, pp. 283-293, 1974.
167. Jones W. "Models for turbulent flows with variable density and combustion," *Prediction Methods for Turbulent Flows*, pp. 423-458 Hemisphere Publications, 1980.
168. Bilger R. and Starner S., "A simple model for carbon monoxide in laminar and turbulent hydrocarbon diffusion flames," *Journal of Combustion and Flame*, Vol. 51, pp. 155-176, 1983.
169. Khalil E., Spalding D., and Whitelaw J., "The Calculation of Local Flow Properties in Two-Dimensional Furnaces," *International Journal of Heat and Mass Transfer*, Vol. 18, pp. 775-791, 1975.
170. Jones W. and Priddin C., "Predictions of the Flow Field and Local Gas Composition in Gas Turbine Combustors," *Seventeenth Symposium (International) on Combustion*, The Combustion Institute, pp. 399-409, 1978.
171. Lockwood F. and Naguib A., "The Prediction of the Fluctuations in the Properties of Free, Round-Jet, Turbulent, Diffusion Flames," *Journal of Combustion and Flame*, Vol. 24, pp. 109-124, 1975.
172. prePDF User's Manual, Version 4, 1996.
173. Laminar flamelet library generation code, Rolls-Royce in house code.
174. Jeffreys H. and Jeffreys B., "Methods of Mathematical Physics," 3rd edition, Cambridge, England: Cambridge University Press, p. 286, 1988.

175. Chen C. and Chang K., "Application of Robust  $\beta$ -pdf Treatment to Analysis of Thermal NO in Nonpremixed Hydrogen-Air flame," *Journal of Combustion and Flame*, Vol. 98, pp. 375-390, 1994.
176. Liu F., Guoa H., Smallwood G., Gülder L., and Matovic M., "A Robust and Accurate Algorithm of the  $\beta$ -pdf Integration and its Application to Turbulent Methane-Air Diffusion Combustion in a Gas Turbine Combustor Simulator," *International Journal of Thermal Sciences* Vol. 41, pp. 763-772, 2002.
177. Jones W. and McGuirk J., "Mathematical Modelling of Gas-turbine Combustion Chambers," AGARD Conference proceedings No. 275, 1980.
178. Pierce C. and Moin P., "Progress-Variable Approach for Large-Eddy Simulation of Non-premixed Turbulent Combustion," *Journal of Fluid Mechanics*, Vol. 504, pp. 73-97, 2004.
179. Pierce C., "Progress Variable Approach for Large Eddy Simulation of Turbulent Combustion," Ph.D. Thesis, Stanford University, 2001.

